UNIVERSITÀ DEGLI STUDI DI CATANIA

DIPARTIMENTO DI SCIENZE BIOLOGICHE, GEOLOGICHE E AMBIENTALI

XXIX cycle - Ph.D. in:

Scienze Geologiche, Biologiche e Ambientali

SABRINA GRASSI

Characterization of active tectonic structures of the Etna volcano, through geophysical surveys, analysis of site response and deformation.

PH.D. THESIS

Advisor

Prof. S. Imposa

Co-advisor

Prof. G. De Guidi

PhD coordinator: Prof. A. Di Stefano

Table of contents

Introduction

The earthquakes that have affected the Italian territory in the last decade, and the tragic events connected with them, have contributed to stimulate interest in research and development of all those actions that can help to mitigate the seismic risk.

The problems of seismic risk has increased exponentially since the last century, in relation to an increasing of urbanization, which often does not take into account the geological and structural characteristics of the territory. The action planning aimed at the mitigation of seismic risk, which affect a territory, lays its foundations on the studies that allow an improvement of technical-scientific knowledge of the area as well as the assessment of all those parameters which can increase the local seismic hazard.

It is important to study the local and surface geological structures because they determine the site effects, generated by the propagation near the Earth's surface of the seismic waves. It is now widely recognized that local seismic effects can have a significant influence on the extent and distribution of seismic motion and damage during earthquakes.

The local seismic response evaluation is directed to the identification of possible ground motion amplification phenomena that occur when the surface geology is characterized by strong seismic impedance contrasts.

The site effects, are determined primarily by the impedance contrast (defined as the product of the velocity to the density of the medium, in which the wave propagates) that is caused by the seismic wave passage through the rock-soil interface; however, the seismic response varies according to geometrical and mechanical characteristics of the subsoil that are represented by shallow and deep morphological irregularities, vertical and lateral heterogeneity, non-linear and dissipative behavior of ground.

Where are present tectonic structures, it is very important to identify all parameters that contribute to the definition of the seismic response, such as the

structures geometry, the stratigraphy, the dynamic characteristics of surface soils and the spectral content of a seismic input; these factors contribute to the change in amplitude, duration and frequency content of the ground motion.

The study and monitoring of deformations occurring in seismogenic areas is essential to have a complete picture of the dynamics of these areas. In fact, from the results derived from the study of coseismic or time dependent deformation along shear structures, it is possible to deduce what was the shear event of deformation mechanism and the reaction of the surrounding area, after it occurred.

The studies and the geological and geophysical surveys conducted so far in the Etnean area have highlighted how the subsoil is characterized by considerable lateral-vertical variability of the seismic wave velocity, probably related to the different accumulation geometries of Etnean products; contextually, the different geo-lithological characteristics and the presence of active tectonic structures, strongly influence the local seismic response. Particularly, the Etnean eastern slope is characterized by the presence of numerous active shear structures that present different kinematic characteristics and different modes of strain energy release (coseismic deformation and aseismic creep). These structure can be subdivided into three main fault systems, with different geometry and kinematic (Pernicana Fault System, Timpe Fault System, Tremestieri-Trecastagni-San Gregorio-Acitrezza Faut System), which accommodate the extensional regional dynamic (nearly EW).

I focused the present research on a fault system, considered as "laboratory structure", selected for the different kinematic characteristics and different modes of strain energy release, that characterized the fault segments, identified in Trecastagni-Tremestieri-San Gregorio-Acitrezza Fault System. In the northernmost portion, this system has a kinematic behavior of normal fault and releases energy during coseismic deformation, while in the southernmost portion presents a kinematic behavior of a right-lateral strike-slip fault with releases energy during aseismic creep. Furthermore, this fault system, which can be considered the southern boundary of the sliding of Etnean eastern slope, was less studied than the northern sliding boundary (Pernicana

Fault system; Alparone et al., 2013; Acocella and Neri, 2005; Siniscalchi et al., 2010, 2012; Bonforte et al., 2007; Currenti et al., 2010; Guglielmino et al., 2011) and very little is known about the depth geometry of its fault segments.

This thesis reports the results of multidisciplinary measurements carried out along the Tremestieri-Trecastagni-San Gregorio-Acitrezza fault system with the aim to provide additional insightful about its geometry and kinematics; also, additional geophysical surveys were performed at various sites of the municipalities most affected by the fault segments in order to obtain information on site response.

The surveys were performed after an analysis of the data relating to surface geology and to morphological, structural, stratigraphic, geophysical and seismological aspects; these detailed surveys have confirmed and highlighted a variety of geological and geomorphological conditions that can determine the occurrence of different stress following the occurrence of an earthquake.

After have performed a detailed structural survey, the project has planned the collection and analysis of many ambient noise acquisitions, and of other geophysical surveys, undertaken within the municipalities affected by the passage of the fault segments, increasing the surveys near the fault. All this in order to reconstruct the resonance frequency distribution and detect the possible presence of areas affected by amplification effects.

Moreover, in some areas, the surface deformation process was characterized through the design, implementation and installation, across the fault segments, of a geodetic monitoring network, in order to obtain information on the fault kinematics and on the local stress field.

The integration of the results obtained from structural, geological and geophysical surveys, with a complete literature review has provided important information on the development in depth of the fault segments; it was thus possible to reconstruct a 3D model of geometry that characterized the southern boundary of Etnean eastern slope sliding.

Various deformation data such as GPS displacements, InSAR images, level data and measures with extensometers suggest that the slip along the fault system is not uniform, but can be better described by a distribution of dislocation sources along the fault surfaces. In order to model the slip distribution along the fault surfaces, an inverse modeling of DInSAR deformation data was carried out.

This project was aimed to the recognizing site effects, that characterize the studied areas, in order to highlight the seismo-stratigraphic and tectonic behavior of subsoil, as well as to the characterization of the deformation field related to the fault segments, through the implementation of a new geodetic monitoring network (GEO-UNICT geodetic network).

The results allowed to obtain important information on all parameters that can increment the local seismic hazard; all these different but converging approaches, have permitted a complete study of the investigated area. This study providing essential information for a proper land use planning, having as main objective the mitigation of risks that can affect the population.

In addition to the introduction and the conclusions the thesis consists of seven chapters. In the first chapter it is described the geological and tectonic framework of eastern Sicily and the tectonic evolution of the Mount Etna volcano; it is also analyzed the seismicity of the Etnean area, and described the structural framework of the eastern slope of Etna. In the second chapter, the concept of site response is explained and the seismic ambient noise characteristics are discussed; finally it is explained the HVSR (Horizontal to Vertical Spectral Ratio) method and the possibility to obtain information on the seismo-stratigraphic structure of the subsoil.

The third chapter reviews the main geodetic-topographic monitoring techniques, the satellite systems and the geodetic reference systems, as well as the main networks of GNSS permanent stations. In the fourth chapter are explained the basic SAR (Synthetic Aperture Radar) principles and is briefly examined the space-borne SAR systems evolution; finally it is explained the Differential Synthetic Aperture Radar Interferometry (DInSAR) technique and its importance for the study of the surface

deformation. The chapter five describes in detail the structural characteristics of the different fault segments belonging to the studied fault system.

In the sixth chapter, for each investigated area are presented the surveys done on the field, the data elaborations and results, both for structural and geophysical surveys and for geodetic monitoring. In the seventh chapter, it is explained how was built the depth geometric model of the fault system and the numerical inversion process used to obtain the modelling of the slip distribution along the fault planes.

Chapter I

1.0. Geologic and tectonic framework of Eastern Sicily

The Mount Etna is located in eastern Sicily within the complex geodynamic context of the central Mediterranean area. The resulting tectonic frame is characterized by different structural domains resulting by Neogene-Quaternary convergence of Europe -Africa tectonic plates.

The consequent collision led to the formation of Appennines-Maghrebian orogen. The chain extends roughly in the east-west direction, through the Southern Apennines, the Calabrian Arc, Sicily and North Africa, with south-southeastern vergence (Fig. 1.1).

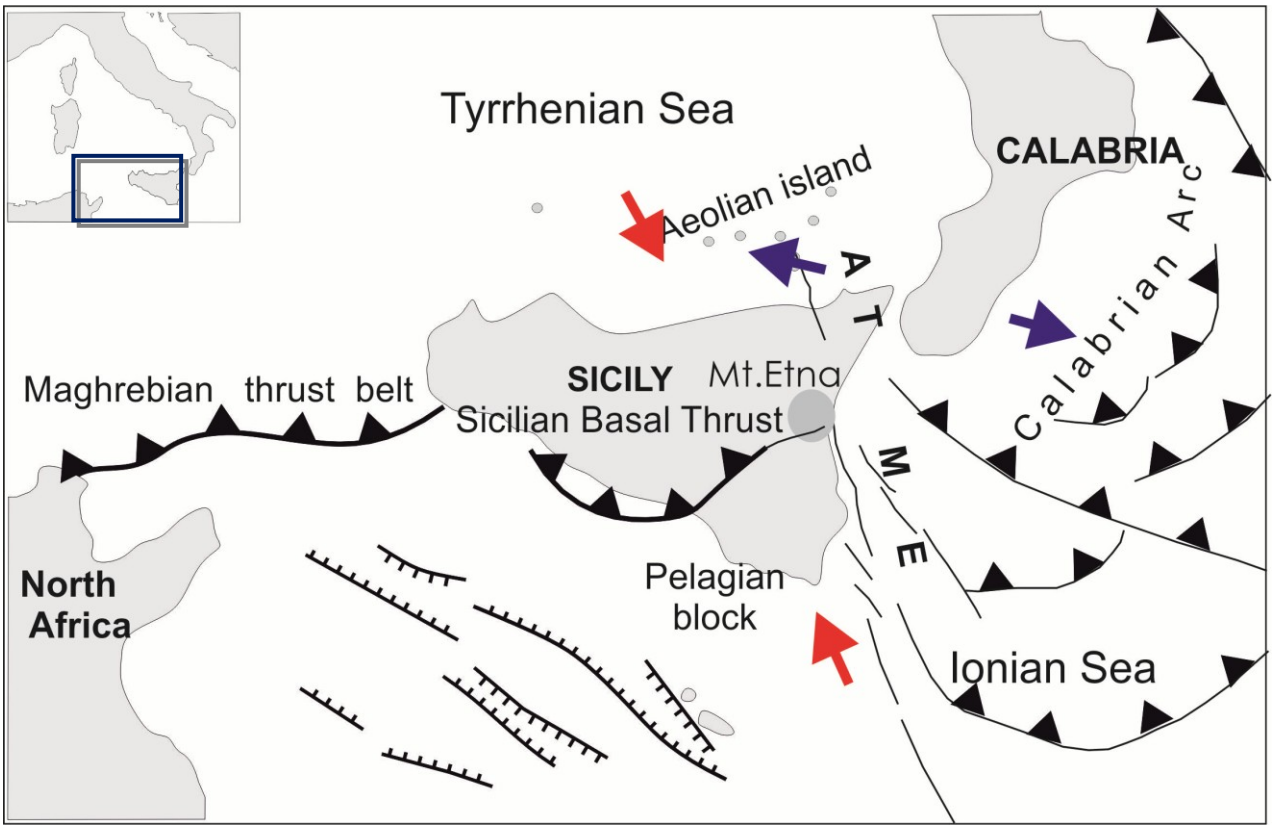

Fig. 1.1. Geodynamic setting of the central Mediterranean; the arrows show the principal stress direction (red arrows: compressive stress – blue arrows: extensional stress.

Fig. 1.2. Main structural domains of Eastern Sicily.

The structural setting of Eastern Sicily (Fig. 1.2) is characterized by three different domains: the foreland domain, the orogenic domain and the Tyrrhenian Basin (Fig. 1.3).

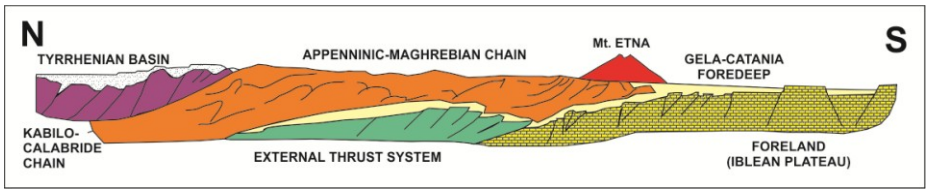

Fig. 1.3. Schematic N-S profile (passing through Mount Etna) of the main structural domains of Eastern Sicily (Lentini et al., 1996, modified).

1.1. Foreland domain

It consists of undeformed portions of the Afro-Adriatic tectonic plates, particularly the Apulian Block and the Pelagian Block are characterized by thickness of about 30 km continental crust. The Apulian Block consists of Meso-Cenozoic carbonate sequences, the Pelagian Block is characterized by slightly thinned crust consisting of Meso-Cenozoic carbonate and volcanic sequences. Between theese blocks is the Ionian Basin, characterized by 11 ÷ 16 km-thick Permo-Triassic oceanic crust, covered by pelagic basin sediments (Finetti, 2005). The foreland domain is represented, in eastern Sicily, from the emerged portion of the Pelagian Block known as Plateau Ibleo; to the east this latter is separated by the Ionian Basin through the Malta Escarpment. It is composed by 300 km-long NNW-SSE oriented normal fault system, extending from Malta up to the southeastern slope of Mount Etna.

Along the foreland northern edge there is the Gela-Catania foredeep, a structural depression formed as a consequence of foreland's margin collapse under the chain. The foredeep is composed by a Neogene-Quaternary sequence of basin deposits that are progressively involved in the orogenic process (Branca et al., 2011).

The orogenic domain includes areas characterized by intense deformation, it is divided into three different structural units, the external Thrust System (Carbone and Lentini 1988), the Appenninic-Maghrebian and Kabilo-Calabride Chain, the last two units together make up the allochthonous unit. The deformation process of the external Thust System and the overlap contact of the allochthonous unit, is referred to Upper Miocene-Pleistocene.

The external Thrust System named Sicilian Basal Thrust by Lavecchia et al. (2007) is located along deformed edge of the African-Adriatic plates. It presents a duplex structure involving sequences similar to those of the carbonatic foreland (Lentini et al., 1996; Finetti et al., 1996); its formation, dating Upper Miocene-Pleistocene, is connected to the Tortonian continent-continent collision and to the opening of Tyrrhenian Basin. In this period begins the deformation and the detachment of sedimentary carbonatic coverages of the Pelagian Block margin, earlier inflected under the allochthonous units.

The Apennine-Maghrebide Chain, formed in Sicily the Nebrodi Mountain, and represents the outermost of allochthonous orogenic domains. It is composed of the superposition of sedimentary sequences from the paleogeographic domains originally located between the European and the African Adriatic plates. The Oligo-Miocene orogenic transport was responsible of Chain staking. At the botton of this structural domain, it is possible to observe basinal successions, called Ionidi (Finetti, 2005c), characterized by oceanic crust and ascribable to a branch of the Ionian paleo basin (Finetti et al, 2005a, b; Lentini et al. 2006).

Above the Ionidi Units are present the Panormidi Units composed by Meso-Cenozoic sequences of carbonate platform, characterized by thinned continental crust. Finally, at the sequence roof, represents the Sicilide Units characterised by oceanic crust and consist of Alpino-Tetidee pelagic successions.

The Kabilo-Calabride Chain was originated from the delamination of the European margin, consists of base layers of Proterozoic Paleozoic age, that have superimposed during the Upper Eocene-Lower Oligocene, and by the remains of

sedimentary coverages of Meso-Cenozoic age. The overthrust of this structural domain above the Apennine-Maghrebide Chain coincided with the rotation of the Sardo Corso Block, dating Oligocene-Miocene. In Sicily the Kabilo-Calabride Chain constitutes the frame of Peloritani Mountains.

The orogenic domain overthrusts the Foreland domain areas; its differential feed, gave origin, from Serravallian, on the back of the chain (in inland areas of orogen), to an extensional process, which led to the formation of the Tyrrhenian Basin. The maximum extension has taken place for the basin areas located on the back side of the most advanced orogen portions (Ben Avraham et al., 1990). This differential extension has been accommodated by right lateral strike-slip fault system, arranged en-échelon, oriented NW-SE, then orthogonal to the direction of extension of the chain, known with the name of South Tirrenic System (Finetti and Del Ben, 1986; Finetti et al., 1996). The gradual disappearance of the extension process to the south, along this system, has enabled the advancement of orogenic units of the Calabrian-Peloritan Arc (Lentini et al., 1995) through the Ionian oceanic crust, and the moving back of its slab.

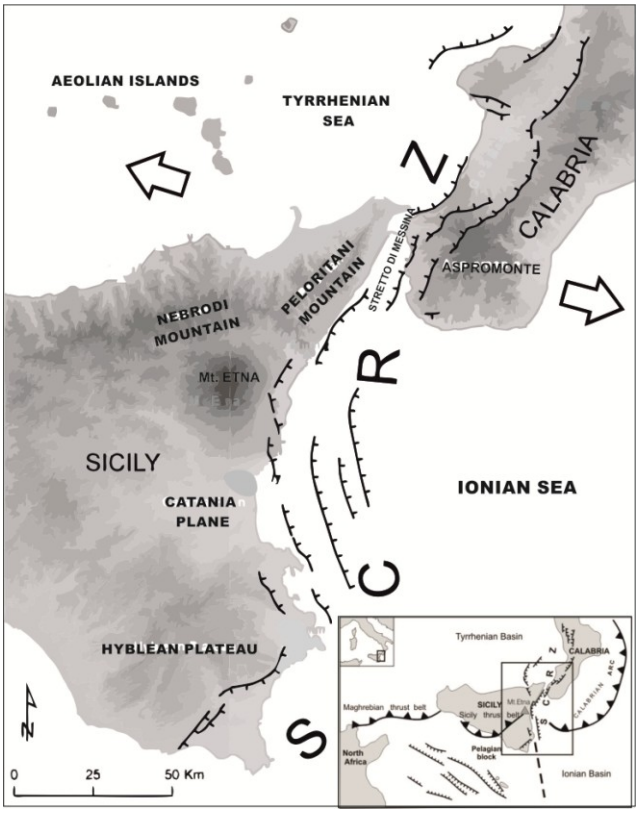

Fig. 1.4. Tectonic Map of eastern Sicily and southern Calabria. The black lines are the main fault segments that make up the Siculo-Calabrian Rift (SCRZ system); the white arrows show the main extension direction of SCRZ system.

The eastern Sicily is subject to a complex tectonic characterised by the coexistence of two different stress schemes, one compressive NNW-SSE direction, associated to the slow convergence between European plate and African plate, and one extensional stress, that affects the Ionian margin of Sicily and the Calabrian Arc. This extensional zone has about an WNW-ESE orientation (Fig. 1.4) and it is linked

to the presence of a fault system known as Siculo-Calabrian Rift Zone (Monaco et al., 1997; Catalano et al., 2008.; De Guidi et al., 2013). This complex system of transtensive faults, characterized by segments of variable length from 10 to 50 km, is long about 370 km; it extends from Calabria's Tyrrhenian coast to reach the Eastern Iblei and the area around the island of Malta (Tortorici et al.; 1995; Monaco and Tortorici, 1995; Monaco et al., 1997; Monaco and Tortorici, 2000). At the Siculo-Calabrian Rift Zone system belong: the fault segments of Maltese Escarpment, the normal faults with right component, localized at the eastern slopes of Etna and the Taormina-Messina fault system.

1.2. Mount Etna: volcano-tectonics evolution

The Etna volcano is located in the convergence area between the European and African plates, along the east coast of Sicily, at the front of the Apennine-Maghrebide Chain and at the footwall of the Malta Escarpment fault system (Monaco et al., 1997), lithospheric discontinuity which, as mentioned earlier, separates the foredeep domain and Hyblean foreland from Ionian domain. With an elevation of about 3330 m and an areal coverage of about 1200 km^2, the Mt. Etna is the largest active volcano on the European continent and one of the largest volcanoes in the world. The current Etna structure is the result of a complex interaction between magmatic processes and regional tectonic (Monaco et al., 2010; De Guidi et al., 2012; Azzaro et al., 2013). Another aspect that make complex the structural setting of Etna is related to the variability of the basement on which the Volcano rests; the northern part rests on tectonic units of Apennine-Maghrebide orogen, the southern sector, instead, rests on infra-Pleistocene clay units that fill the Gela-Catania foredeep.

The physical characteristics of Etnean lavas, including thickness and viscosity (Walker, 1967), the chemistry of emission products, initially to tholeitic affinity and subsequently alkaline sodium affinity (Cristofolini and Romano, 1982) and the differentiation trend (Corsaro and Cristofolini, 1996; 1997), set the volcano Etna

within an extensional geodynamic context, that presents WNW-ESE orientation and which is manifested in the Siculo-Calabrian Rift Zone (Tapponnier, 1977; Ellis and King, 1991; Mazzuoli et al., 1995; Monaco and Tortorici, 1995).

The first emission episodes occurred, at the northern edge of the African plate, from the late Miocene (5.3 Ma), they were characterized by extensive lava effusions, with prevailing fissural character, that from the Iblei mounts was subsequently extended to current south-eastern margin of Mount Etna (Branca et al., 2004, 2008, 2011b).

Evidences of the first manifestations of volcanic activity in the Etnean area (pre-Etnean stage: 500-200 ka), are observable at south-eastern margin of the volcano, these are predominantly submarine fissure eruptions, the chemistry of emitted products is transactional tholeiitic (Romano, 1982; Gillot et al., 1994; Monaco et al., 1995).

The complex Etnean volcanic succession is characterized by alternating several sequences of lavas and pyroclastic products, originate from numerous eruptive centers that over time have undergone a migration from ESE to WNW (Lo Giudice et al., 1982). The identification within the volcanic succession of strong discontinuities related to the eruptive style change have allowed to distinguish in the evolutionary history of Etna four major phases of activity (Fig. 1.5): Basal Tholeiitic, Timpe, Valle del Bove, Stratovolcano (Branca et al., 2011a, b).

The Mt. Etna presents a complex structure, characterized in the lower part by a shield structure and in the higher-layer by a stratovolcano. To the northwest of the central part of the volcano, the sedimentary basement emerges to 1000 m of altitude s.l.m, consequently, the maximum thickness of the volcanic products in the top portion exceeds 2000 m (Branca and Ferrara, 2013).

The Etnean region is at the center of a complex tectonic system. In the southwestern portion the superficial and profound evidences of a compressive tectonic are visible, with main compressive stress axis oriented approximately NNW-

SSE; this trend appears to be active in the late Quaternary with even current evidence (Monaco et al., 2008; De Guidi et al. 2014, 2015; Ristuccia et al. 2013).

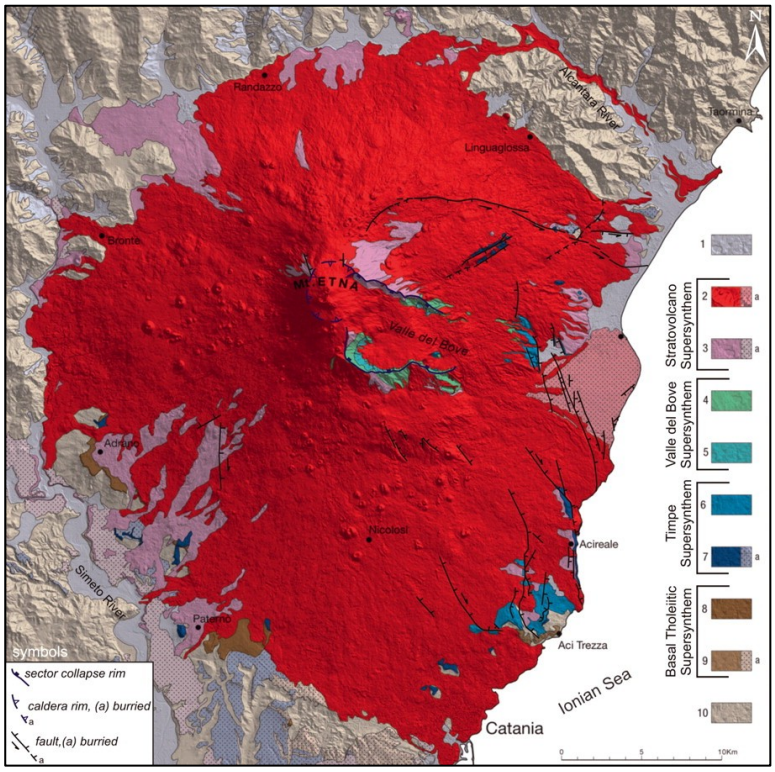

Fig. 1.5. Geological map of synthems (Branca et al., 2011):
1) Present and recent covers;
2) Il Piano Synthem
a) sedimentary deposits;
3) Concazze Synthem
a) sedimentary deposits;
4) Zappini Synthem;
5) Croce Menza Synthem;
6) S. Alfio Synthem;
7) Acireale Synthem
a) sedimentary deposits;
8) Adrano Synthem;
9) Aci Trezza Synthem
a) sedimentary deposits;
10) Sedimentary and metamorphic basament.

The compressive tectonic engenders trust and fold systems with axis approximately east-west (Fig. 1.6); strike-slip faults oriented NNW-SSE accommodate these structures. The rates of shortening in this area are of the order of 5 mm/a in both directions, causing uplift rates, recorded for the Catania anticline, on the order of cm/a (De Guidi et al. 2015). In the eastern sector are evident extensional structures, linked to a regional dynamics with main stress axis oriented approximately east-west; these structures consist mainly of normal faults with horizontal component (right).

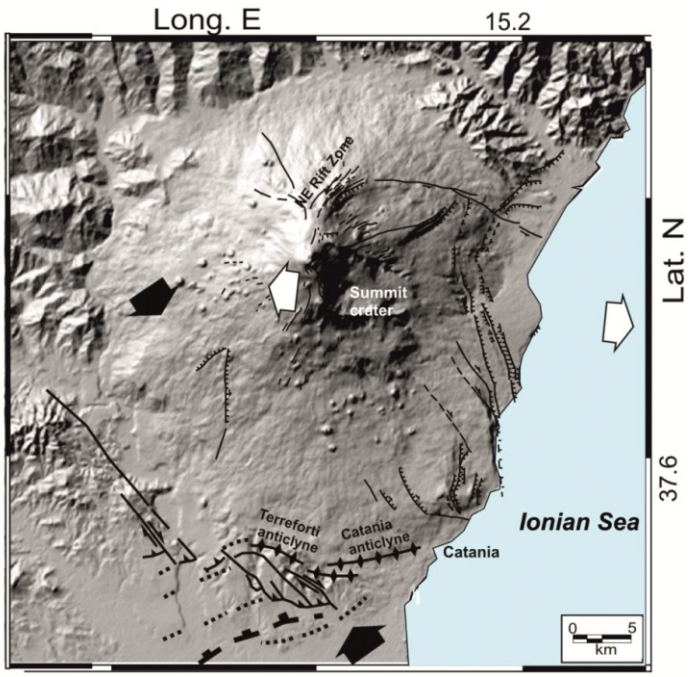

Fig. 1.6. Representation of stress patterns active in Etnean area; the black arrows show the direction of compressive stress, the white arrows show the direction of extensional stress.

1.2.1. Seismicity of the Etnean area

The Etnean area is characterized to an intense seismic activity, connected with the volcano dynamics and the tectonic structures presented therein; also, the Etna region is strongly subject to the effects of the strong tectonic earthquakes at regional character. Among the strongest crustal events, which caused destructive effects in the Etnean area, despite not having hypocenter in this area, there are the earthquakes of 1169 and 1693, with an epicenter in the south-eastern sector of the Hyblean area, and the seismic event occurred in the Straits of Messina in 1908; these events with maximum magnitude of about 7.4, have caused more destructive effects in the eastern side areas (IX-X MCS), and affected less the western and northern areas.

The earthquakes with epicenter in the Etnean area are characterized by a much lower energy content than a regional events, with a magnitude which does not exceed the value 4.9, and hypocentral depths that rarely exceed 10 km, except for the seismic event occurred in 1818, with epicenter in the Aci Sant'Antonio area (CT), of magnitude M = 6.2. This seismic event caused destruction over a wide area of Catania, on the slopes of Etna and in the countries of the Ionian coast, with permanent deformation along some fault zones, liquefaction phenomena, landslides and tsunamis (Boschi e Guidoboni, 2001).

The Etna earthquakes while presenting a energy from low to moderate, because of the extreme shallowness of the source, are capable of causing strong damage to residential areas next to the epicenter; the main effects are recorded in small area (2-5 km long and 1-2 km wide) near the tectonic structure that generated the earthquake (Lo Giudice and Rasà 1992; Gresta et al. 1997; Azzaro, 2004).

A recent scientific paper of De Guidi et al. (2015) highlights a clear deepening trend of hypocenters from shallow depths (0-12 km), in the southern sector of the volcano, to 35 km in NNW sector (Fig. 1.7); this work analyze the seismicity of western and southern sector of the volcano, considering 1900 earthquakes, of magnitude from low to moderate ($1.0 \leq ML \leq 4.8$), recorded by the INGV local network between 1999 and 2012.

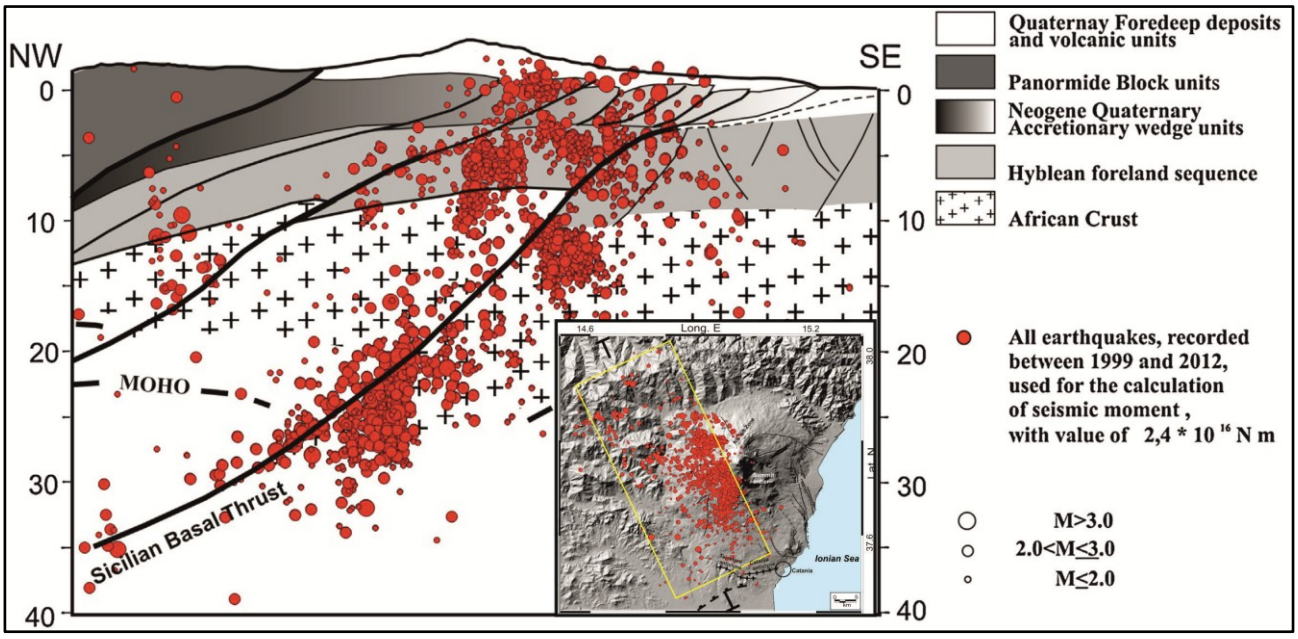

Fig. 1.7. Projection of the hypocentre distribution, relating to the seismic events shown in the lower box on the right (by De Guidi et al. 2015).

The computed focal mechanisms for the main recorded events, in order to characterize the movement type of the seismogenic source and the stress fields actives in the area, has allowed the identification of three areas with different strike-slip regimes.

The deepest zone located to the north of the volcanic edifice is subject to a principal stress σ1 oriented in NNW-SSE direction; the central sector, between 0 and 9 km depth, is characterized by a σ1 oriented E-W; the southern portion, between 10 and 15 km depth, is characterized by a σ1 axis oriented NE-SW (Fig. 1.8).

It is possible be say that, in the west sector of the volcano, at greater depths, the seismicity is strongly influenced by the regional dynamic related to the collision between the African and the European plates, which present the stress axis oriented NW-SE (Cocina et al 1998; Patanè et al. 2003; Scarfì et al., 2013); instead, the seismicity relating to the shallow and middle areas (up to 10-15 km) is affected by local processes, probably related to the volcano dynamics (Latora et al., 1999).

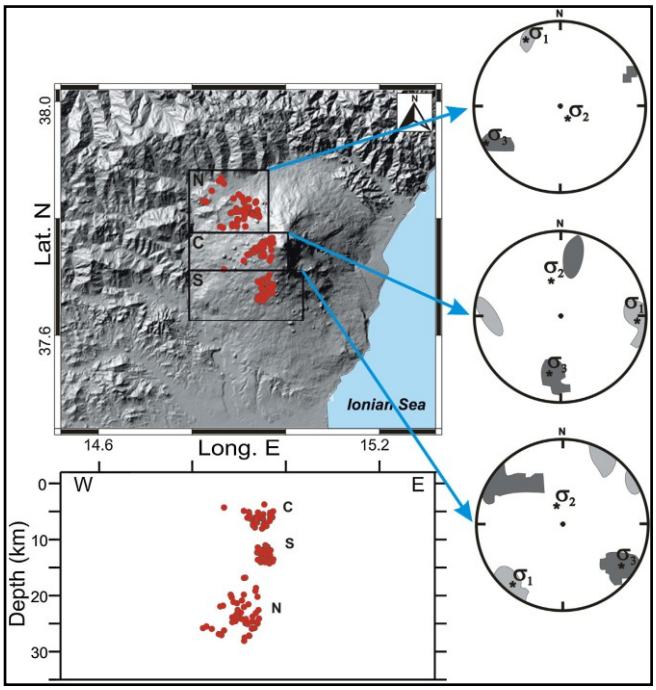

Fig. 1.8. Orientation of stress axes for earthquakes cluster with hypocentres at different depth (by De Guidi et al., 2015).

Looking at the earthquakes distribution, with a magnitude greater than 3, which occurred from 1990 to 2016 in the Etnean area (Database Isis), it is possible to note that the greatest number of seismic events is localized in the eastern sector of the volcano (Fig. 1.9).

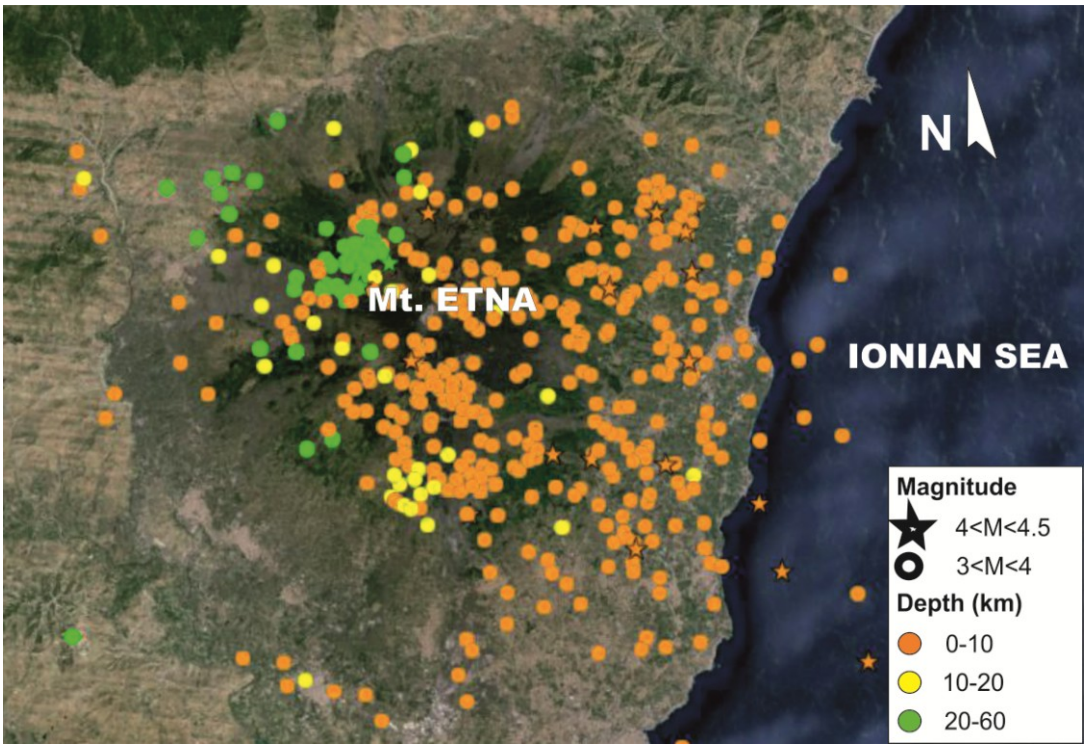

Fig. 1.9. Distribution map of earthquakes with M>3, which occurred from 1999 to 2016 in the Etnean area (Database ISIDe – Italian Seismological Instrumental and Parametric Data-Base).

The seismic events that occur in the eastern portion of the volcano, conversely to those that occur in the west sector, are characterized by hypocenters localized at shallow depths, which in most cases does not exceed 5 km (Gresta et al., 1998); many of the earthquakes that occur in this sector of the volcano can be connected to the activity of surface extensional structures that control the deformation of the Etnean eastern side (Alparone et al., 2013; Azzaro et al., 2013).

The earthquakes of the lower-middle eastern slope of Etna, despite having reduced hypocentral depths, conversely to those that occur in the western portion, are mainly related to regional tectonics, correlated to the extensional regime oriented WNW-ESE to which is subject the east coast of Sicily (Azzaro, 1999; Bousquet and Lanzafame, 2004; Monaco et al., 2005).

The tensile stress to which is subjected this area is differentiated by some authors in regional tensile stress field and local stress field, the latter induced by the gravitational sliding of the slope (Lo Giudice and Rasà, 1992; Walter et al., 2005); in other cases, both regional and local stresses are connected to the opening of the Sicilian-Calabrian Rift (Catalano et al., 2008).

1.2.2. Tectonic structures of the Etnean eastern slope

The eastern side of Etna is characterized by the presence of many fault systems that are the result of iteration between volcanic processes, that take place on a local scale and the complex regional geodynamic pattern, that affect this area with a extensional dynamic oriented ~N100°E (Lo Giudice et al., 1982; Lo Giudice and Rasà, 1986; McGurie and Pullen, 1989).

This domain is confine to north and south by strike-slip shear structures, respectively to north with left movement (the Pernicana system) and to south with right movement, Tremestieri-Trecastagni system (Lo Giudice and Rasà, 1992; Solaro et al., 2010), to west by the North-East Rift (Kieffer, 1975), oriented NE-SW, and by the Southern Rift (Kieffer, 1975), with direction from NS to NNE-SSW (Fig. 1.10).

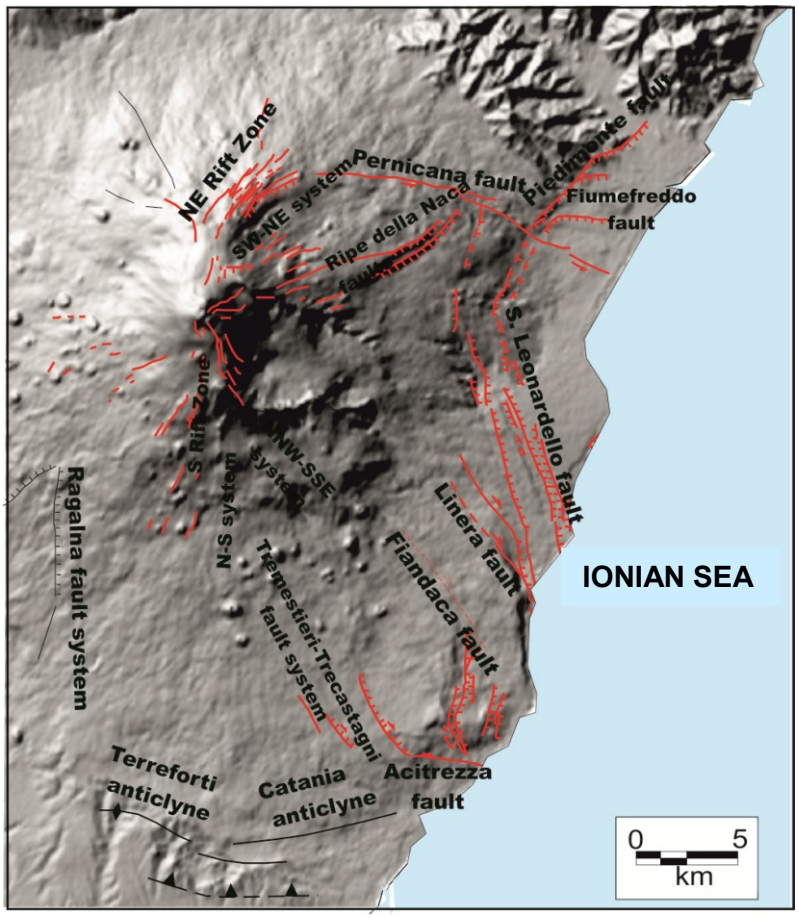

Fig. 1.10. Main structural lineaments of the eastern side of Etna.

The Pernicana Fault System (Monaco et al., 1997; Azzaro, 1999) extends for approximately 20 km in E-W direction, from Piano Provenzana until the Ionian coast; the fault system shows an extensional character at the surface, while in depth it is characterized by a compressive kinematic due to the overlap of the Apennines on the Hyblean block. To confirm the hypothesis of a compressive regime, under this structure, there is an outcrop of the Quaternary marine deposits at higher altitudes above 700 m, which cannot be justified by the kinematics of the coastal fault systems that lower to east towards the Ionian basin. In the eastern portion this system is characterized by structures with en-échelon trending and development about parallel to each other and with ESE direction, that arriving near the coast. The structure known as Fiumefreddo Fault belongs to this fault system, it extends about in E-W direction and has a left-lateral strike-slip movement (Azzaro et al., 1998a; Tibaldi and Groppelli, 2002). The seismic sequence that preceded the early stages of the eruptive

activity generated along the northeastern rift, in October 2002, can be related mainly to the activation of the Pernicana Fault, in its westernmost segment, and it is precisely in this area that the most energetic events (M = 4.2) have been located. The fault throws observed in that occasion were of the order of 20-25 cm for vertical ones and 10-15 cm for horizontal ones. The eastern sector of the fault system is well identifiable due to fracturing phenomena of road surface, walls and various artifacts, affected by phenomena of aseismic creep with left-lateral transtensional movement of the order of 2 cm/a (Rasà et al., 1996; Groppelli and Tibaldi, 1999; Azzaro et al., 2001).

The Rift System of the southern slope, ends along a cutting area with right-lateral movement, known as Trecastagni-Tremestieri System, which consists of a series of segments arranged en-échelon, with NW-SE direction (Monaco et al., 1997). The Trecastagni and Tremestieri structures are two normal faults with right-lateral component, characterized by evident morphological escarpments sometimes obscured by the presence of slag cones and recent lava flows. In the Trecastagni Fault have been observed coseismic displacements of the fault scarp both during the seismic sequence of September 1980, both in consequence of the earthquake of 11/21/1988.

As a consequence of this seismic events it was possible to observe subsidence of the soil, cracks along the SP 8/III walls and on buildings (Azzaro, 1999). By some SAR interferometry studies made by Froger between 1996 and 1998, were estimated displacements to year of about 4-6 mm, but with the eruption crisis of the 2001-2003, as observed for the Pernicana Fault System, has been registred a growth of fracturing on manufactured and an increase of the annual movements that have become from millimetric to centimetric.

The south-central area of the lower east side of Etna is characterized by the presence of a major fault system that extends for about 30 km, known as Timpe system. This system consists of normal faults, with right lateral component, oriented NNW-SSE/ NW-SE, which dip to the east; these structures create steep morphological jumps with vertical throws that in some cases exceed the hundred

meters. A number of major segments belong to the Timpe system (Fiandaca, Acireale, Santa Tecla, Moscarello and San Leonardello), some of these have been responsible for well-known destructive earthquakes that occurred in the area: S. Tecla-Linera Fault for the earthquake of 1914, Moscarello Fault for the seismic events of 1865 and 1911, Macchia Fault for the earthquake of 1989, Fleri Fault for the seismic event that occurred in 1984 and Santa Venerina Fault for the earthquake of 2002.

From a morphostructural point of view this system is composed of juxtaposed primary structures from synthetic and antithetic faults that, in some cases, form "graben" structures, as in the case of the San Leonardello Fault.

The northernmost area of the lower east side of Etna is characterized by the presence of a further fault system oriented NNE-SSW, connected with the Timpe system, known as Piedimonte system; it consists of some normal faults, which dip towards east. Three are the main segments that belong to this system: Piedimonte Fault, Calatabiano Faults and Ripe della Naca Fault. The first two structures, oriented respectively, WSW-ENE and NE-SW, are interpreted as regional tectonic lineaments (Finetti et al., 2005; Lentini et al., 2006). The Ripe della Naca Fault is composed by a pair of escarpments, with height between 80 and 120 m (Azzaro et al., 2013), oriented WSW-ENE. The Ripe della Naca and Piedimonte structures are buried by Holocenic lava flows and interrupted by the Pernicana Fault (Azzaro et al., 2012).

Structural analyses of different fault segments on the eastern Sicily and geodetic measurements allowed to determinate the mean direction of extension (~N115°E) and an opening velocity of 3.6 ÷ 0.6 mm/a (Monaco et al., 1997; Monaco and Tortorici, 2000; D'Agostino and Selvaggi, 2004; Catalano et al., 2008).

In the Etnean eastern slope single fault segments and volcano-related processes make more complex the overall tectonic setting (Catalano et al., 2004; Catalano and De Guidi 2003; De Guidi et al., 2014; Scudero et al., 2015). An uplift rate of 2.5–3.0 mm/a has been estimated for the last 6–7 ka along the eastern coastal slope of Etna (Branca et al., 2014). The general process of uplifting is only locally interrupted by

subsidence related to flank sliding of the volcanic edifice, measured at manmade structures, and by up rise acceleration along the hinge of an active anticline and at the footwall of an active fault (Branca et al., 2014). GPS and PSInSAR data show a more marked subsidence, (Bonforte and Puglisi 2006; Bonforte et al., 2011).

Many authors have interpreted the Etnean tectonic structures as the boundaries of some independent blocks moving consequently to the gravitational spreading of the eastern flank of the volcano (Borgia et al., 1992; Rasà et al., 1996; Rust and Neri, 1996; Froger et al., 2001; Tibaldi and Groppelli, 2002; Neri et al., 2007; Palano et al., 2008; Palano 2016).

Other authors indicate different causative factors (regional stress, gravity forces and dike-induce drifting, or a combination of these) to explain the slow sliding of eastern and south-eastern flanks (Bonforte et al., 2013). Branca et al. (2014), highlight that the sliding-related subsidence clearly involving the northern eastern sector of Etna has only recently affected the southeaster sector of the slope, where it failed to counteract the effects of the volcano-tectonic uplifting. The time–space boundaries of the lateral sliding, which is probably much younger and shallower than is generally stated and differentially involves distinct blocks, remains to be constrained more accurately.

Chapter II

2.0. Site response

The mechanical and physical properties of subsoil as well as their stratigraphic and morphologic features influence the seismic ground motion recorded at the free surface. The seismic shaking U(t) can be considered the results of the superposition of three different factors: the source mechanism S(t), the seismic wave propagation from the bedrock to the site A(t) and the site effects G(t).

$$U(t)= S(t)*A(t)*G(t)$$

The first two factors define the kind of seismic input whereas the third represents all modifications that can occur as a consequence of the interaction between seismic waves and local features of the site.

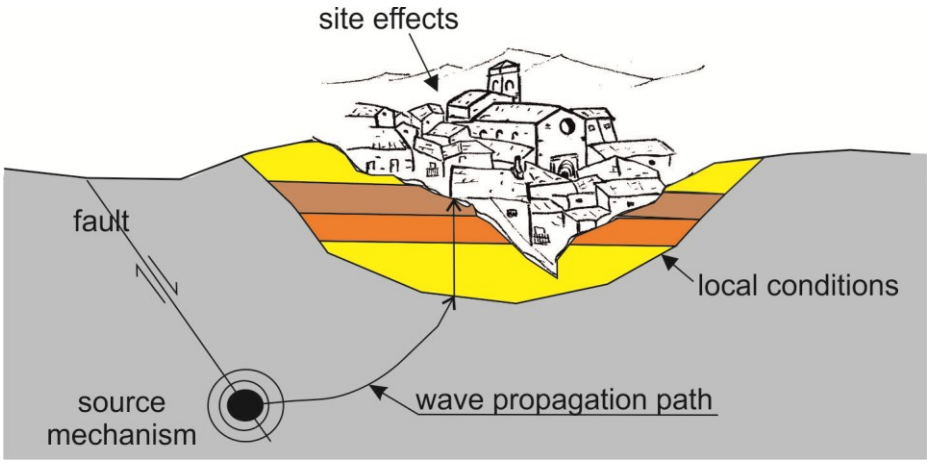

Fig. 2.1 . Factors which determine the seismic motion at the site.

It is well known that the seismic waves undergo a first change of spectral composition during the source-bedrock path (attenuation function), and a second, when they cross the layers between the bedrock and the free surface; the latter is known as “local seismic response”.

The site effects are determined primarily by the impedance contrast (Z), defined by the equation:

$$Z=V*\rho$$

were V is the seismic wave velocity and ρ is the density of the medium in which the wave propagates; it is a parameter closely related to the amplification of seismic vibrations that is caused by the passage of seismic wave through the interface between rocks with different physical and mechanical characteristics. The seismic response varies according to geometrical and mechanical characteristics of the ground: superficial and deep morphological irregularities; vertical, horizontal and lateral heterogeneities; non-linear and dissipative behavior of the soil.

The local conditions, such as the different mechanical properties of the subsoil linked with the presence of discontinuities, fractures or heterogeneities, as well as the geometry of shallow layers and the surface topography affect the propagation of seismic waves causing several physical phenomena as diffraction, multiple reflections, resonance etc. This phenomena can cause local seismic amplification effects, linked to changes of seismic motion and its frequency content.

The local seismic response determines the different damage distribution in various areas affected by the same seismic event.

The site seismic response can be evaluated by experimental method using the records of seismic signals generated by ambient seismic noise.

2.1. Seismic ambient noise

The seismic ambient vibrations are constantly present on Earth's surface; they are characterized by seismic waves of low energy and amplitudes of the order of 10^{-4} - 10^{-2} mm (Okada, 2003).

The seismic noise is originated by a series of different sources, often not related and continuous, distributed spatially. For these reasons the noise is compared to a stationary stochastic process, which is devoid of a well-defined phase spectrum (Bormann and Wielandt, 2002).

The seismic ambient noise sources can be natural or anthropogenic, this subdivision is carried out as a function of their frequency.

Natural sources essentially act at low frequencies (<1 Hz) and anthropogenic ones at high frequencies (>1 Hz). The vibrations with low frequencies (<1 Hz) are called microseisms, while those at high frequencies (>1 Hz) are known as microtremors.

The microtremor sources are largely due to cultural activities such as industrial, agricultural, and traffic noise. They energize the soil mainly with surface waves, which lessen within a few kilometers, both on the surface and at depth (McNamara and Buland, 2004).

Signals below 0.3 Hz are primarily caused by oceanic waves, winds and other meteorological sources (Bonnefoy-Claudet et al., 2006a). The interaction between marine wave and coasts induce the propagation of elastic waves within the continental crusts.

Ambient noise has a temporal variability (Okada, 2003) linked to the different types of sources generating it; at frequencies below 1 Hz, it is linked to the succession of meteorological phenomena, while at higher frequencies ambient noise is frequently affected by anthropic activity. The amplitude of the noise does not particularly vary in a few hours, but seems variable for samplings made on different days (Okada, 2003)

Seismic ambient noise can be considered the result of the interaction of several unrelated seismic sources (Lachet and Bard, 1994; Tokimatsu, 1997; SESAME, 2003). Many authors assume that ambient noise consists mainly of seismic surface waves (Ohmachi and Umezono, 1998; Chouet et al., 1998; Yamamoto, 2000; Arai and Tokimatsu, 1998, 2000; Cornou, 2002; SESAME, 2003) and that the proportion between the wave types depends on the site conditions and the impedance contrast (Bonnefoy-Claudet et al., 2008).

Ambient noise has, in recent years, become widely used for site amplification studies.

The vertical seismic component is conditioned by the Rayleigh waves, while the horizontal components are influenced simultaneously by Rayleigh and Love waves

(Aki and Richards, 2002; Lay and Wallace, 1995). The H/V ratio can therefore be considered indicative of Rayleigh waves ellipticity (Bonnefoy-Claudet et al., 2006a, b), and the ellipticity curve shows a peak corresponding to the site fundamental frequency (Lachet and Bard, 1994; Kudo, 1995; Bard, 1998).

The presence of Love waves does not alter this interpretation, since the Airy phase that occurs at a similar frequency to the fundamental frequency, acting on the horizontal components, strengthens the peak (Arai and Tokimatsu, 2000). The propagation of Love waves in the environmental seismic noise controls the HVSR amplitude (Bonnefoy-Claudet et al., 2008).

2.2. HVSR

The "passive seismic single-station" method provides information on the local seismic response and it is based on the acquisition of environmental seismic noise.

The main advantage of this methodology is related to its non-invasiveness and quick execution, since it does not require any artificial energization.

The analysis of the record of seismic noise can be carried out by several methods; among these, the technique known as H/V Spectral Ratio is the most used. This technique allows identifying the frequency at which ground motion is amplified due to resonance effects, related to the presence of tectonic and stratigraphic discontinuities as well as the topography (Dal Moro, 2012), by calculating the spectral ratio between the average of the horizontal components on the vertical component of the ground motion.

The HVSR technique, applied for the first time by Nogoshi and Igarashi (1970), was analyzed and made widespread by Nakamura (1989). The frequency of the maximum H/V amplitude corresponds to the fundamental SH resonance frequency of the site. Indeed, the peaks occurring in the H/V spectra indicate the resonance frequencies proper of the site, while their amplitude gives information about the minimum expected seismic amplification at the site in case of earthquake.

It is known that stratigraphy, topography (surface and buried morphology) and geotechnical characteristics (static and dynamic properties of the subsoil) of a site, may play an important role on the site effects linked to earthquakes, by locally attenuating or amplifying the expected ground motion at the surface compared to the reference bedrock (Albarello and Castellaro, 2011).

The HVSR peak is linked to an impedance contrast in the subsoil with varying amplitude depending on the degree of this contrast. Although the relationship between the two variables is nonlinear, the higher the values of the impedance contrast between different rock types, or between portions of the same lithotype with different mechanical characteristics, the greater the amplitude of the spectral peak. Many authors (Yamanaka et al., 1994; Duval et al., 1995; Goula et al., 1998; Bodin and Horton, 1999; Zhao et al., 2000; Giampiccolo et al., 2001; Panou et al., 2005; Pappalardo et al., 2016) have shown how the HVSR technique is well suited to identifying the impedance contrasts created at the transition between rock types with different physical–mechanical characteristics.

The records of ambient noise, through the H/V spectral ratio technique, can supply information on the mechanical behaviour of buried structures under seismic stress. This technique can be considered an important tool for a preliminary characterization of the local seismic response, since it allows highlighting the main seismic refractors (Spizzichino et al., 2013).

Each peak in the H/V graph corresponds to a possible reflector (seismo-stratigraphic level) that presents an impedance contrast compared to the neighbour levels. Since the impedance contrast may be related to stratigraphic variations (Amorosi et al., 2008), and the stratigraphy of a rock sequence may consist of alternation between intact and fractured layers (Gross, 1995), the H/V single-station technique could provide information also about changes in the degree of fracturing of the rock sequence. In this case, the impedance contrast occurs between layers with different geomechanical properties (Pappalardo et al., 2016).

In a simple two-layer system of soft sediment, with a shear-wave velocity Vs and a thickness H, covering a hardrock basement, the equation (1) links the resonance frequency "f" to the thickness "H" of the resonating layer, depending on the shear waves velocity:

$$f = n\ Vs/4\ H \quad (1)$$

where n (= 1, 3, 5...) indicates the order of the mode of vibration (fundamental, first superior, etc.), Vs and H represent the shear waves velocity and the thickness of the resonating layer respectively.

Equation 1 allows understanding how the H/V technique can also provide information on stratigraphic features. Starting from a noise measurement providing f, once known the Vs of the coverage, the depth of the main seismic reflectors or vice versa can be estimated.

In recent years, this method has been widely used to obtain information on the subsoil stratigraphy (Field and Jacob, 1993; Lachet and Bard, 1994; Lermo and Chavez-Garcia, 1993; Bard, 1998; Ibs-von Seht and Wohlenberg, 1999; Delgado et al., 2000; Parolai et al., 2002; Imposa et al., 2013, 2016a,b; Pappalardo et al., 2016; Tarabusi and Caputo, 2016).

It is reasonable to consider that the waves velocity within the investigated medium increases with depth due to a greater consistency of the material, associated with increasing load. This relationship can be expressed by the following function (Ibs-von Seht and Wohlenberg, 1999):

$$V_s(z) = V_0(1 + z)^{\alpha} \quad (2)$$

where:

Vs(z)= shear wave velocity

V_0= shallow shear wave velocity

z= depth

α= proportionality coefficient between depth and velocity.

Knowing the velocity change with depth, determined experimentally, it is possible to obtain the parameters V_0 and α for which there is the minimum error between the experimental Vs - depth profile and curve fitting these data. Substituting these two parameters in the formula of Ibs-von Seht and Wohlenberg (1999), it is possible to convert the frequency values in depth values:

$$h = \left[\frac{V_0(1-\alpha)}{4f} + 1\right]^{1/(1-\alpha)} - 1 \qquad (3)$$

This process enables reconstructing the impedance contrast sections that show the distribution of the amplitude values of the H/V spectral ratio in the subsoil.

In order to detect the presence of directional effects on HVSR peaks, the spectral ratio must be calculated along various directions (Albarello, 2005), turning the NS and EW components of the motion with azimuthal intervals of 10°, proceeding from 0° (north) to 180° (south).

Chapter III

3.0. Geodetic-topographic monitoring

In a geodetic monitoring network, the area or object under investigation is usually represented by points which are permanently monumented or marked. All these points are observed from two to several times in different time epochs.

A geodetic network can be a terrestrial network, a Global Positioning Satellite (GPS) network or a combination of these network types.

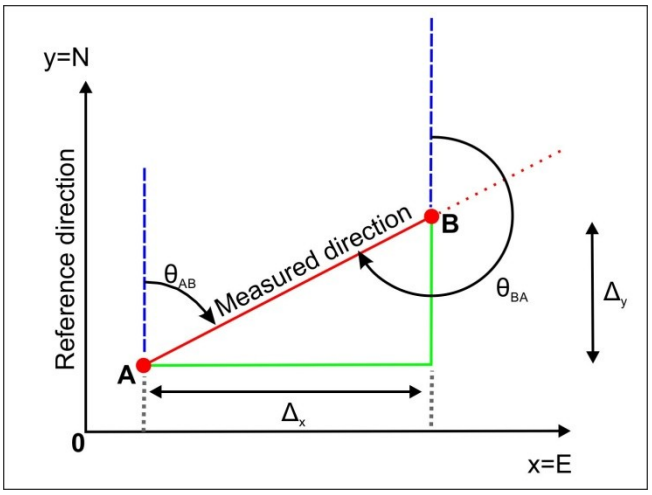

Fig. 3.1. Direction angle

In topographic monitoring the changes are measured and analyzed over time, in terms of direction, distance and difference in height, among points, identified as targets.

The measure of direction is defined by three different angles: direction angle, azimuth angle and zenith angle. The direction angle is the angle between reference direction and the measured direction. Considering a Cartesian coordinate system, where the coordinates of two points A and B are known (Fig. 3.1), we define "angle of the direction of B with respect to A (θ_{AB}) or (AB)", the angle made by the clockwise rotation of an axis parallel to the Y axis, passing through the reference A, to overlap the direction AB. θ_{BA} is the reciprocal of θ_{AB}.

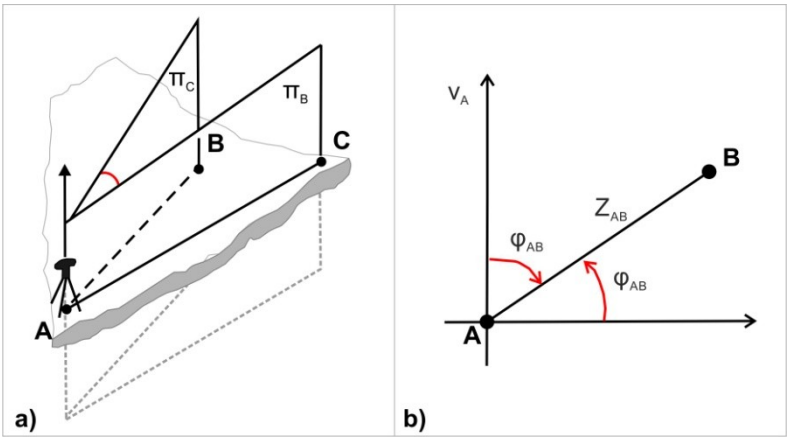

Fig. 3.2. a) Azimuth angle; b) Zenith angle

Considering three points A, B, C (Fig. 3.2a) the azimuth angle is the dihedral angle formed by the plane containing the verticals passing through A and B with the plane containing the verticals passing through A and C.

The zenith angle φ_{AB} is the angle between the direction of the vertical passing through ν_A and the considered direction Z_{AB} (Fig. 3.2b).

The angle unit is the "radiant" [rad], defined as "the angle subtended by an arc equal in length to the radius"; it follows that the angle α_r is expressed in radians as $\alpha_r = l / R$, where l is equal to the length of the arc subtended and R is equal to radius circumference. In the centesimal system the unit is the "centesimal degree" [gon], defined as 1 gon = π / 200 rad. In the sexagesimal system the angle unit is the "degree sexagesimal" [°], defined as 1° = π / 180 rad.

Defining the position of a discrete series of points, with high accuracy, is the basis of a good topographic monitoring, because all the measures will be related to the position of those reference points. This points are called vertices (benchmarks); they allow to properly insert the land survey in a defined reference system (local or national).

The main network represents the structure within which are located other subnets that allow a detailed topographic survey; this network defines the local reference system to which the other subnets are linked. The main network is determined with redundant measurements, for allowing statistically strong controls. The coordinates of its points are identified as reference (are considered fixed), because the main network is considered as infinitely precise.

Secondary networks and those of detail can also be calculated and compensated independently, in their own system of reference, and later incorporated into the general system of local survey with appropriate transformations.

The construction of the main reference network is carried out through the triangulation method; to determine the coordinates of an inaccessible point, the network of known points, through the basic triangulation, can be thickened with the operations of forward intersection and reverse intersection.

In the topographic survey called simple polygonal, the coordinates of the intermediate vertices of a broken line, formed by "n" segments, are determined starting from two known endpoints (belonging to the main monitoring network or derived from that network through forward intersection or reverse intersection).

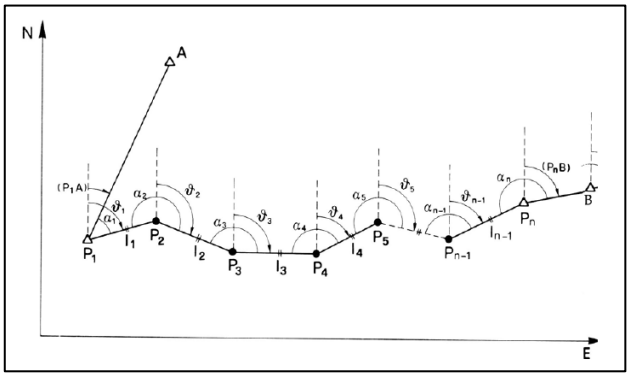

Fig. 3.3. Open traverse

The coordinates of the intermediate vertices are determined by measuring their mutual distances and angles formed by the segments that join them. In order to perform a polygonal, between two points on the reference network, it is necessary to choose and materialize on the ground the points "P" which represent the vertices.

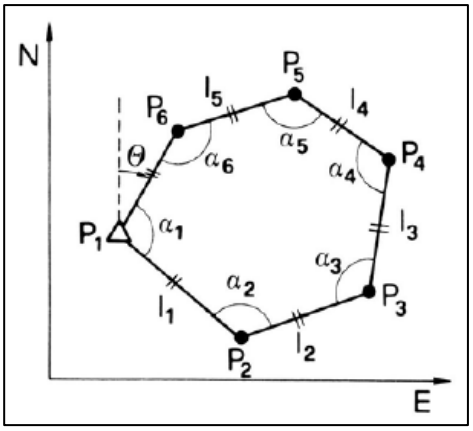

Fig. 3.4. Closed traverse

The scheme of the open traverse bound to extremes (Fig. 3.3) shows two extreme vertices (A-B) with known position (for example, determined by GPS measurement), the position of intermediate vertices is determined measuring all sides and all angles, in every point of the polygonal it is measured the previous point and the next point.

The scheme of the closed traverse (Fig. 3.4) shows that in this case the last side is coincident with the first.

3.1. Tacheometry or quick measurement

Tacheometry is a method of measuring both horizontal distance and vertical elevation of a point in the distance; it represents the last phase of the topographic survey because it allows to identify the detail points. In order to carry out the survey

with this method are necessary a theodolite and a diastimeter. The methods discussed above are used to determine the vertices of a monitoring network; in the tacheometric survey the points to be detected may correspond to architectural elements, such as edges or manmade details.

The survey is made in a reference system bound to the coordinates of two vertices used, one for positioning the theodolite (station point) and the other as orientation (Fig. 3.5). By collimating the sequence of vertices to be determined it is possible to define the coordinates of these vertices by measuring azimuth, zenith and distance.

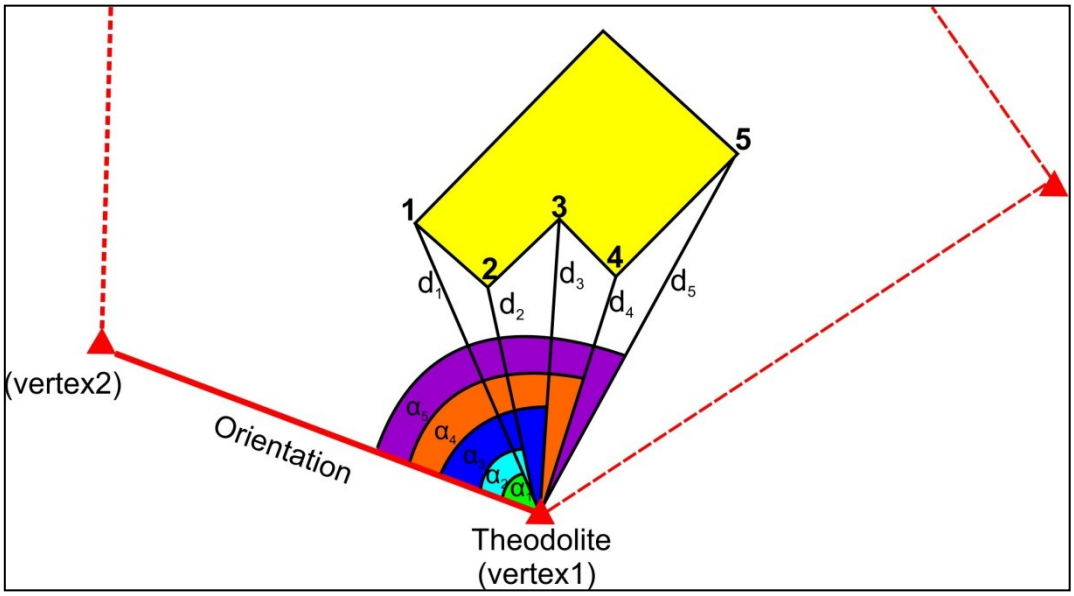

Fig. 3.5. Scheme of tacheometry surveying

3.2. GNSS

GNSS (Global Navigation Satellite System) (Fig. 3.6) is a satellite system that is used to pinpoint the geographic location of a user's receiver anywhere in the world. It is based on the emission of electromagnetic signals which allow to obtain information related to time and distances between satellites and a receiving station. Through the reception and interpretation of such signals by small electronic receivers, located on the earth's surface or in the atmosphere, it is possible to determine the position in a

predetermined reference system (longitude, latitude and altitude). Two GNSS systems are currently fully in operation.

NAVSTAR GPS (Navigation Satellite Timing And Ranging Global Positioning System) is a spatial navigation system developed by the United States Department of Defense, capable of accurately estimating the position, velocity and time in a common reference system. The constellation is formed by 24 satellites, located on 6 orbits, tilted 55° to the equator and designed to allow the visibility of up to 12 satellites at the same time, from any location on Earth, at any time of day or night.

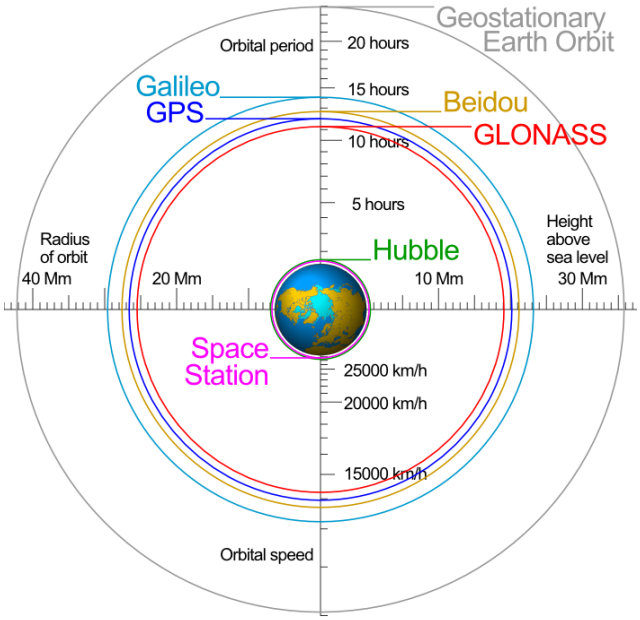

Fig. 3.6. Orbital information about GNSS and other systems

GLONASS (Global Navigation Satellite System) is a spatial navigation system of the Russian Federation. It is composed by 14 satellites simultaneously visible on the horizon.

A third, the European Galileo, is slated to reach full operational capacity in 2020; as of May 2016 the system has 14 satellites in orbit. When Galileo will be fully operational, there will be 30 satellites in Medium Earth Orbit (MEO). Ten satellites will occupy each of three orbital planes inclined at an angle of 56° to the equator.

The positioning can be performed using two different techniques: the "Point Positioning", which consists in the absolute positioning of a single point in the assigned reference system, this method determine the position with an uncertainty of the order of tens of meters; the “Differential Positioning” or “Relative Positioning” method determines the position of a point with respect to another, considered as known, with a precision of the order of a few millionths of the distance. In particular, the vector relative position of the "baseline" between the two points is determined in

its three components with respect to an assigned Cartesian tern. In order to utilize this second technique two receivers (base + rover) located on two different points and operating simultaneously for the entire duration of the measurement session are necessary. The time of the measurement session is variable depending on the distance between the two receivers and the accuracy required.

The positioning is carried out through distance measures between the satellites, with known position, and the monitoring points on the earth's surface; the measurement accuracy depends on various factors, such as the number and geometry of satellites tracked, observation time, ephemeris, ionospheric and tropospheric conditions, multipath etc…

The main acquisition methods utilized for geodetic-topographic monitoring with GNSS systems are: static, kinematic and real time kinematic (RTK).

In the static method the measures have a variable time from 30 minutes to several hours, in this case the receivers are kept fixed on the ends of the baseline to be determined; this method provides high accuracy data (3 mm in the horizontal component, 5 mm in the vertical component).

In the kinematic method one of the two receivers (base) is maintained on a fixed position and the second (rover) is moved over the points that must be measured, following a path with continuity, the determination of position is performed at regular time intervals.

These two methods require a post-processing phase of the measures.

In the RTK method, similar to the operating mode of the kinematic method, the determination of the points position is performed in real time, at the moment when the point is occupied by the mobile receiver. The fixed receiver (normally placed on a known position) communicates its position and the satellite data to the mobile receiver; the latter calculates in real time, its position relative to the fixed receiver, based on the above data.

3.2.1. Geodetic datum

A geodetic datum or geodetic system is a coordinate system, and a set of reference points, used to describe the location of unknown points on the Earth. These networkss are periodically measured and calculated.

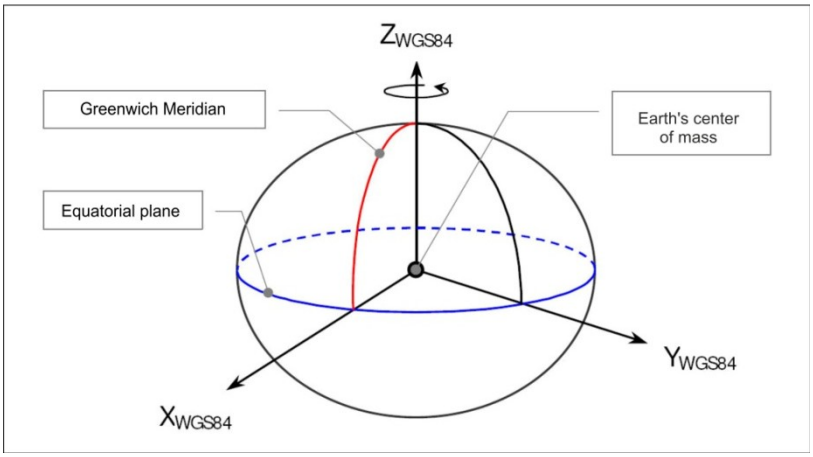

Fig. 3.7. Geodetic datum used for G.N.S.S.

The datum used for G.N.S.S. is valid for all the Earth or for entire continents; it is based on a geocentric Cartesian tern XYZ, which is associated with a geocentric ellipsoid, having its origin in the Earth's center of mass, the Z axis is directed according to Earth's rotation axis and X and Y lie on the equatorial plane (Fig. 3.7). In the geocentric system, the G.N.S.S. satellite orbits are determined as a function of time (ephemeris).

For the management of the GPS system, the datum used is the WGS84 (World Geodetic System 1984). There are different geodetic datum such as: ITRS (International Terrestrial Reference System) and ETRS (European Terrestrial Reference System).

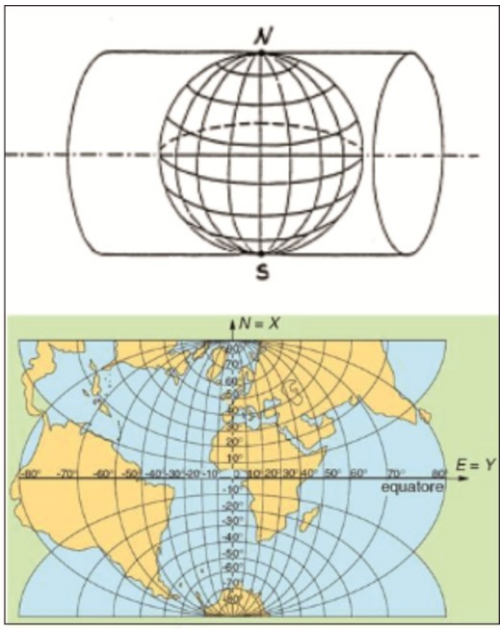

Fig. 3.8. Gauss rapresentation

The coordinates of a point can be expressed in ellipsoidal geographic coordinates φ, λ and h (latitude, longitude and ellipsoidal height, respectively) or/and geocentric Cartesian coordinates X,Y,Z. Instead of geographic coordinates, are often used the plane

coordinates- In Italy it is currently used the Gauss representation (Fig. 3.8), in the Gauss-Boaga version (associated to Roma 40 datum) or UTM (associated to WGS84-ETRF89).

3.2.2. GNNS permanent stations

The GNSS permanent stations are capable of acquiring in a continuous manner; the installations consist of a Satellite receiver of geodetic type with appropriate characteristics, placed in undisturbed areas (far away from electromagnetic sources and radio wave emissions), where the signals reception is good at any time of the day and in any period of the year. The installation point is known and calculated with great precision.

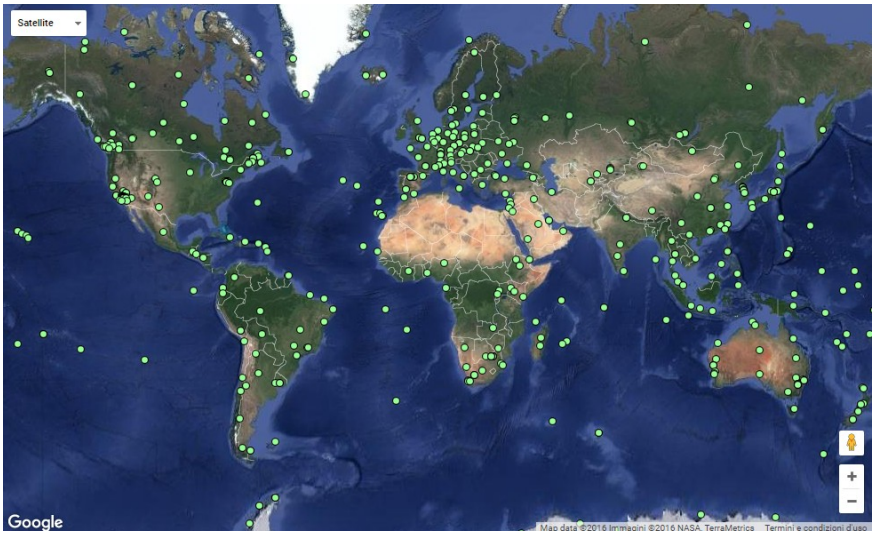

Fig. 3.9. IGS network

Fig. 1.10. Dynamic National Network, RDN

Some GNSS permanent stations have the ability to make public their data, at least in the 30 sec decimation for post processing. These stations almost always belong to a network created for geodetic (eg. IGS, EUREF, ...), geodynamic (eg. RING) or other purposes. The IGS network (International GPS Service for Geodynamics) calculates and distributes,

for scientific applications, i) the precise ephemeris of GPS and GLONASS satellites, ii) the parameters of the Earth's rotation, iii) the corrections of the GNSS satellite clocks, iv) the coordinates and velocities of the ITRF stations (International Terrestrial Reference Frame), v) the tropospheric and ionospheric information and vi) a series of information on the satellites (constellations, time series of the networks and the subnets calculated by various analysis centers (AC)).

Fig. 3.11. RING network

The IGS network at present includes more than 350 stations around the world (Fig. 3.9), managed by different authorities and with different monumentations. Their stations provide free rough data of precise orbits in ASCII files, with 30 sec acquisition rate and sp3 format.

RDN (National Dynamic Network) consists of 99 permanent GPS stations (Fig. 3.10) belonging to public authorities, they observe continuously the GNSS satellite signals and transmit them electronically to a Computing Center set up at the IGM Geodetic Service. The stations are evenly distributed throughout the national territory, with an average spacing of 100-150 km. In the network are included all stations on the national territory, already calculated in ITRS and IGS international networks.

RING (National Integrated Network GPS) is a network of about 140 permanent stations located on the national territory (Fig. 3.11), managed by INGV. The data with 30 sec acquisition rate, are available to the public on FTP, with daily files in RINEX format.

NetGEO is a network consisting of 200 GNSS permanent stations realized by Geotop, equipped with GPS + GLONASS receivers. The receivers continuously acquire the signals emitted by visible satellites and transmit them to a control center that processes data, from all stations of the network, to make them available to users in Rinex format, with acquisition frequency of 1 sec. NetGeo is geo-referenced in the ETRF2000-RDN reference system, defined by IGM.

Chapter IV

4.0. Basic SAR principles

In Remote Sensing scenarios the Synthetic Aperture Radar (SAR) sensor plays a significant role. It is a coherent active microwave remote sensing system which permits to generate high spatial resolution imageries, independently from weather conditions and during both day and night time by operating in the microwave spectrum region. SAR sensors have been largely employed to monitor the Earth surface.

A radar system is formed by a transmitting antenna that illuminates the surrounding space with electromagnetic waves. The transmitted energy is partially absorbed by the Earth's surface and partially scattered in all directions. A portion of the incident radiation is scattered back to the antenna, that is also equipped for the reception.

A radar system after an accurate measure of the time delay between the transmitted and the received echoes, knowing that the pulse travels at the speed of light, is able to figure out the distance (called slant range) between the sensor position, along its flight direction, and the illuminated targets on the ground.

The antenna directivity (the selectivity in the lighting the surrounding space) used for transmitting and receiving the radar signal enables the location of the object along the other dimension (called azimuth) (Fig. 4.1)

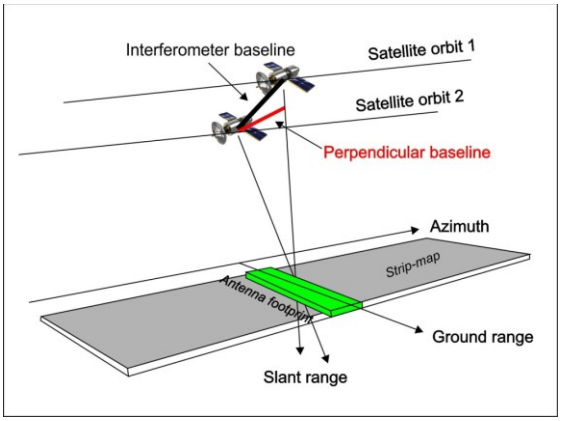

Fig. 4.1. Radar system geometry

The motion of the sensor along its flight path causes the illuminated area to shift in the azimuth direction. The refracted pulses are captured and processed by the radar, thus obtaining a two-dimensional imagery of the surface. Combining in a coherent way the data acquired by the sensor in successive positions and taking into account amplitude and phase of the SAR signal, it is possible to synthesize a fictitious large antenna, defined synthetic aperture. This process allows to obtain a high resolution even in the azimuth direction (Norwood, 1991).

The antenna is mounted on a satellite moving at a constant altitude with a velocity v with respect to the Earth; its flight direction is called azimuth. The radar illuminates along the direction perpendicular to the flight path, slant range, with an inclination ϑ (look angle-off nadir) with respect to the vertical. The planar projection of the slant range direction is called ground range; the antenna footprint is the dimension of the illuminated area at the Earth's surface. The direction of the line joining the satellite and the radar target, perpendicular to the orbit, is called range or line of sight (LOS).

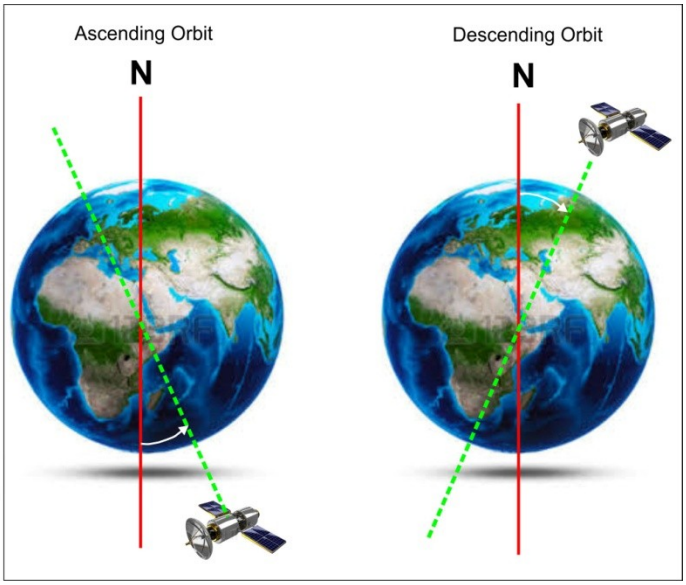

Fig. 4.2. Ascending and descending orbit of a SAR sensor

The distance measured by the sensor is that of radar beam, this is the length of the beam along the view direction (Line Of Sight - LOS) between antenna and object: this direction is called slant range.

The geometric resolution is the capability of the sensor to discriminate echoes return from separated targets; the resolution length is then the minimum distance between two objects to be considered as separate entities.

SAR sensors acquire data during both the ascending and descending orbit (Fig. 4.2), in the first case the sensor moves from south to north and illuminates the ground

area from west to east; in the descending orbit the sensor moves from north to south and illuminates the ground area from east to west. The time interval between two successive passages of the satellite on the same portion of territory is called revisiting time.

4.1. Satellite systems

The space-borne SAR systems evolution during the last 25 years has enabled the acquisition of a huge dataset (Fig. 4.3).

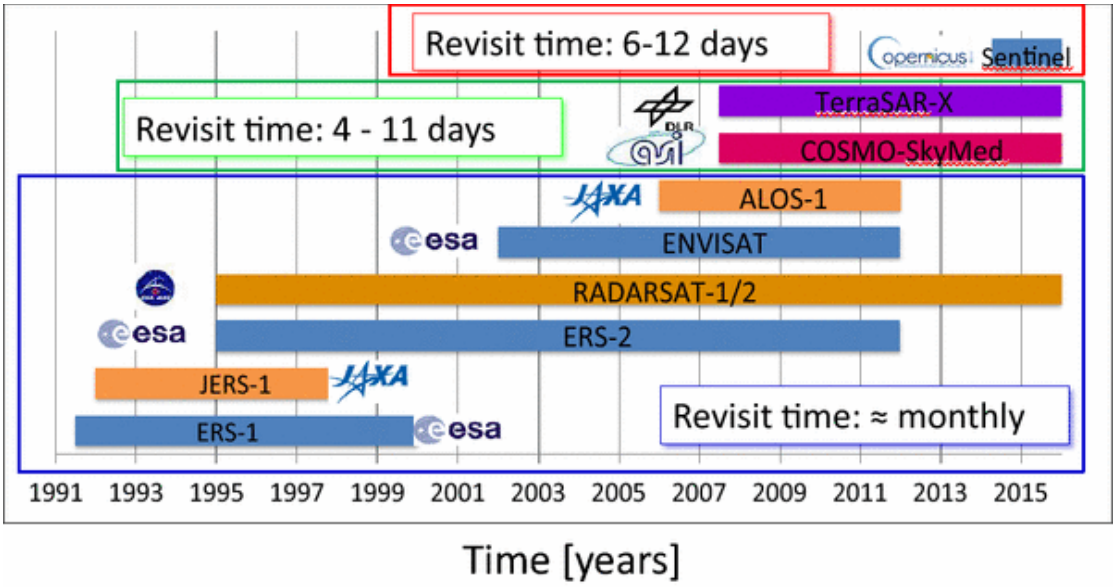

Fig. 4.3. Space-borne SAR systems evolution

The SAR sensors are characterized by different acquisition periods, operating frequencies, spatial resolutions and coverage; in the new generation SAR sensors it is possible to note a reduction of the revisiting time.

The main characteristics of some of the most important satellite systems are summarized in table 4.1.

SATELLITE	ERS1-ERS2	ENVISAT	RADARSAT-1/2
SPACE AGENCY	ESA (European Space Agency)	ESA (European Space Agency)	CSA (Canadian Space Agency)
ACQUISITION PERIOD	ERS1-from 1992 to 2001 ERS2-from 1995 to 2001	From 2002 to 2012	From 1995 to now
OPERATING FREQUENCIES	c-band (5.33 GHz)	c-band (5.33 GHz)	c-band (5.33 GHz)
REVISITING TIME	35 days	35 days	24 days
AZIMUTH RESOLUTION	5 m	5 m	5 m
RANGE RESOLUTION	8 m	9.5 m	5 m (fine beam) – 9.5 m (standard beam)
GROUND RANGE RESOLUTION	20 m	25 m	20 m
Θ OFF-NADIR	23°	variable	variable

Table 4.1. Main characteristics of ERS1-ERS2, ENVISAT, RADARSAT-1/2 satellite systems

The COSMO-SkyMed system is a constellation of four SAR satellites, developed by ASI (Italian Space Agency) in cooperation with Italian Defence Ministry. The platforms host an X-band SAR, capable of operating in all visibility conditions at high resolution and in real time, with right and left looking imaging capabilities, an incidence angle range of 20°–60°; the orbital cycle is 16 days.

The COSMO-SkyMed system have a high revisit frequency offered by the four X-band SAR spacecraft, with a maximum revisit time of 12 hours. The constellation is fully operational since the 2008.

4.2. DInSAR

One of the major applications of the SAR technology is represented by the SAR Interferometry (InSAR) technique. The use of Differential Synthetic Aperture Radar Interferometry (DInSAR) techniques has become crucial to the satellite measurement of surface deformation phenomena. The satellite deformation maps can cover large areas with a very high spatial resolution. Thanks to the dense areal coverage it is possible to monitor and analyze large-scale phenomena even in areas not accessible to land-based surveillance networks. From the comparison of one or more pairs of satellite imageries acquired from slightly different positions (spatial baseline) and at different times (temporal baseline) it is possible to detect deformations of the soil

occurred between two successive passages of the satellite (Gabriel et al., 1989; Massonet and Feigl, 1998; Rosen et al., 2000; Berardino et al., 2002).

The radar imageries obtained with coherent systems are made up of amplitude (or module) and phase. The amplitude detects the incident electromagnetic field share per target illuminated reflected back to the sensor. The phase encloses, instead, the information relating to the distance between sensor and target. The interferometric analysis studies the phase differences between two separate acquisitions. Unlike typical radar applications, which store only the amplitude information, the SAR interferometry uses the amplitude and phase informations. This technique uses the phase measurements to obtain the differential range (difference between the distances perceived by the radar sensor at the same target from two different points of view) and the change range (difference between two pairs of imageries, sign that it is occurred a displacement of the target between two subsequent acquisitions) in the SAR acquisitions relating to the Earth's surface, while the amplitude is crucial for the co-registration of the imageries.

The interferometric datum is obtained by performing the cross product between two imageries, of which one is taken as reference (usually the first in chronological order), called master, and the second is defined slave. The product is carried out on the characteristic complex value of the individual pixels ($A_1e^{i\phi}$) for the complex conjugate of the second ($A_2e^{i\phi}$), relative to the same pixels on the ground. The result will have amplitude ΔA equal to that of the first image multiplied by the second, while the phase will be the difference between the two.

The determination of geometrical parameters is very important for the interferometric analysis. The accuracy with which they are determined influences the estimation of the pulse path from the target to the sensor on the satellite, and thus indirectly also the phase. The distance between the two satellites at the time of the survey, in the plane perpendicular to the orbit's direction, is defined interferometer baseline; the component of the latter projected on the direction orthogonal to the line of sight of the slave image of slant range is called perpendicular baseline (Fig. 4.4).

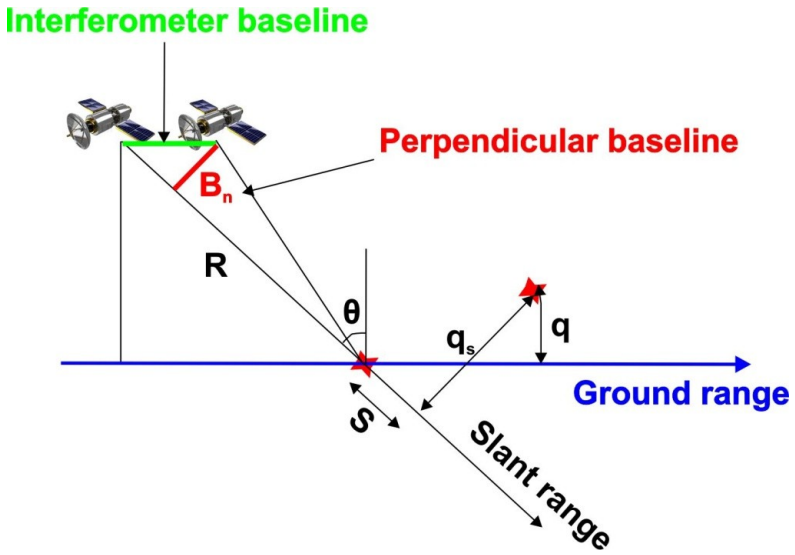

Fig. 4.4. Geometrical parameters of InSAR system

The DInSAR technique is often used to detect ground deformation by comparing two different imageries acquired on the same area, in a discrete time interval. More specifically, the DInSAR technique exploits the phase difference between SAR imagery pairs acquired at different times but with the same illumination geometry and from sufficiently close flight tracks (Franceschetti and Lanari,1999) and provides a measurement of the ground deformation projection along the radar LOS.

In order to study the deformation it is important to choose pairs of imageries with a small baseline. The greater is the perpendicular baseline, the less accurate is the calculation of the deformation. For this reasons, among the variety of DInSAR techniques that have been developed over the years, a very popular approach is represented by the Small Baseline Subset (SBAS) algorithm (Berardino et al., 2002; Mora et al., 2003; Lanari et al., 2004). In order to mitigate the decorrelation errors and to obtain very accurate deformation measurements this algorithm imposes constraints on the maximum temporal and spatial baselines and it focuses on the use of appropriate combinations of interferograms, characterized by small baselines.

The SBAS technique allows to detect the temporal evolution of Earth's surface deformation; it is based on the use of a large number of SAR acquisitions and implements an easy combination of the multilook DInSAR interferograms computed from these data.

Chapter V

The numerous active shear structures that characterize the Etnean eastern slope can be grouped in three main fault systems (Pernicana fault system, Timpe fault system, Tremestieri- Trecastagni-San Gregorio-Acitrezza faut system). These fault systems accommodate the extensional regional dynamic, they present different geometry and kinematic characteristics and different modes of strain energy release (coseismic deformation and aseismic creep). The Pernicana fault system is considered the northern boundary of the sliding of Etnean eastern slope, it is characterized by a left-lateral kinematic; the Timpe fault system is characterized by numerous active east-dipping normal faults, oriented about NNW-SSE.

The Trecastagni-Tremestieri-San Gregorio-Acitrezza fault system can be considered the southern boundary of the sliding of Etnean eastern slope, it was less studied than the northern boundary of sliding and very few is known about the depth geometry of its fault segments; it is identified by different kinematic characteristics and different modes of strain energy release. In the most northern portion, this system has a kinematic behavior of normal fault and releases energy for coseismic deformation, while in the most southern portion presents a kinematic behavior of a right-lateral strike-slip fault with releases energy for aseismic creep. Such tectonic structure can be therefore considered as representative of all different kinematics and different strain energy release modes that characterize the active shear structures of the Etnean eastern slope. For this reasons the research was focused on Trecastagni-Tremestieri-San Gregorio-Acitrezza fault system, considered as "laboratory structure".

5.0. Tremestieri-Trecastagni-San Gregorio-Acitrezza fault system

The right-lateral fault system named Tremestieri-Trecastagni-San Gregorio-Acitrezza borders and accommodates, to the south, the eastern flank instability of Mt. Etna. This system extends approximately NW-SE to E-W for about 13 km across the municipalities of Tremestieri, Trecastagni, San Giovanni La Punta, San Gregorio and

Acitrezza. It is marked by both long-term developed fault scarps and deformation bands that in the urban areas are emphasised by the occurrence of damage on buildings and other manmade structures.

The fault segments that compose this system (Fig. 5.1), from the west to the east, are: Tremestieri Fault (TMF), Trecastagni Fault (TCF), San Gregorio-Acitrezza Fault (SG-ATF), San Gregorio-Northern Fault (SGNF), Nizzeti Western and Eastern Faults (NZWF and NZEF) and finally by Acitrezza Southern Fault (ATSF).

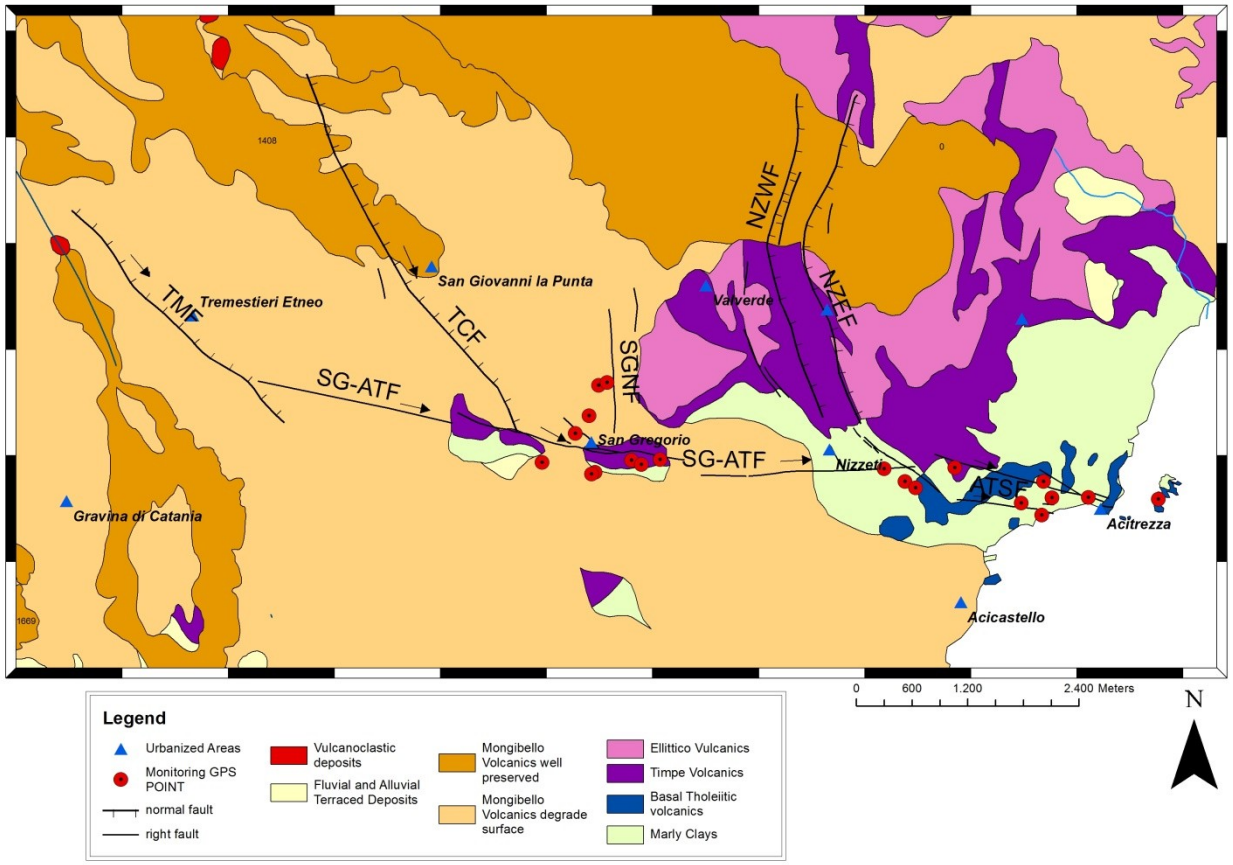

Fig. 5.1. Structural elements of Tremestieri-Trecastagni-San Gregorio-Acitrezza Fault System; geologic map (modified after Monaco et. al., 2010 and Branca et al., 2011)

The Tremestieri Fault is about 3 km-long; in its northern portion it is characterized by a 10 m-high scarp, while in the sector crossing the Tremestieri town it shows poor morphological evidence, though several structures are damaged by recent activity (Monaco et al., 2010). As reported by Azzaro (2004), the Tremestieri Fault extends towards NW as far as Nicolosi, without morphological evidence («hidden fault»). Evidence of coseismic ground rupture are visible south of Nicolosi,

with a system of NNW-striking tensional cracks (Silvestri, 1886; Arcidiacono, 1901; Azzaro et al., 1989b; Azzaro, 1999; 2004), about 0.9 km-long**.** Ground fractures at the bottom of the scarp along the northern sector of the fault have been associated to very shallow seismicity (Martelli, 1911; Lo Giudice and Longo, 1986; Azzaro, 1999), characterized by oblique-dextral motion (Rasà et al., 1986). Aseismic creep episodes are reported during the 1883 eruptive event (Silvestri, 1883), and during the 1984 and 1986 seismic events (reactivation of the Fiandaca and Acireale faults) (Rasà et al., 1996).

The Trecastagni Fault, shows a NNW-SSE trend and a morphological scarp reaching the maximum height of 10 m. The fault kinematics is mainly normal and the slip mainly occurs aseismically even though, sometimes a very shallow seismicity affects the area. The fault crosses the Trecastagni town causing damage at manmade structures. The analysis of InSAR data, acquired from 1994 to 2009, documents a subsidence of the fault hanging-wall (eastern side) with a mean rate of about 10 mm/a on the southernmost part and a slip-rate of about 4 mm/a that was as high as 7.0 mm/a during the October 2009-January 2010 period (Bonforte et al., 2013). The measurements made using extensimeters, from 2005 to 2010, revealed a continuous opening trend of the fault, at a rate of about 2-3 mm/a (Gambino et al., 2011; Bonforte et al., 2013).

Three different segments compose the San Gregorio-Acitrezza Fault System, with an E-W trend and a total length of about 10 km. The kinematics is predominantly right-lateral with poor or absent morphological evidences, the deformation belts are visible on buildings and in other manmade infrastructures damaged by the recent activity. The western fault segment consists of very scattered lineaments which link the southern tip of the Tremestieri Fault and the southwestern tip of the Trecastagni Fault, for a length of about 2.5 km. The second fault segment extends for about 5 km from the southwestern tip of the Trecastagni Fault to the southern tip of the Nizzeti Fault. The morphological evidences are poor except for a very small scarp. The San Gregorio fault has been accurately mapped based a

detailed survey of the damage to artefacts and infrastructures caused by the almost continuous fault creep (Imposa et al., 2015). The displacement along the structure occurs aseismically (Bella et al., 1996; Gresta et al., 1997; Azzaro, 1999).

The Nizzeti Fault shows a NNE to NNW trend (Monaco et al., 1997), it is characterized by a linear cumulative scarp up to 100 m-high and it is associated with a minor parallel conjugate structure upslope truncating the Timpe 47olcanic, represented in this area by 120 ka-old (Branca et al., 2008) lava flows capping Eutyrrhenian (Marine Isotope Stage-MIS 5.5) marine conglomerates (Kieffer, 1971; Monaco et al., 2002).

The Valverde Fault has been seismically active in historical times (Imbò, 1935) and it was recently the site of aseismic creep that caused the development of ground fractures and faults with centimetric offset and damage on buildings along a NW-SE trending belt, 500 m-long and 70-80 m-wide, in the San Nicolò area (Azzaro et al., 1989b).

In the following chapter I will describe the accurate and detailed field survey of fractures and damage to artefacts and infrastructures, caused by the fault creep (Imposa et al., 2015), which allowed to accurately map the fault segments already known, and a new fault segment extending roughly N-S in the urban area of San Gregorio di Catania (SGNF-Fig. 5.1). Furthermore, this original survey has identified second-order features for the Acitrezza Fault extending for about 1200 m in an E-W direction, about 400 m south of SG-ATF eastern segment.

Chapter VI

6.0. Multidisciplinary surveys in the studied areas

The effects of surface faulting, caused by coseismic ruptures and aseismic creep, contribute significantly to increase the risk to towns and villages and their related infrastructures. Fault zones could be assessed with several direct or indirect approaches, but seldom a variety of techniques is applied at the outcrop scale (Similox-Tohon et al., 2006; Štěpančíková et al., 2011). The integration of direct superficial observation with indirect methodologies able to investigate at depth allows a careful assessment of fault zone geometry and therefore to identify the artifacts potentially subject to structural damage. The collection and analysis of observational and experimental data represent the main tools for assessing the presence and the extent of phenomena that can increment the local seismic hazard.

In this chapter I will present and discuss a series of multidisciplinary data, acquired by means of detailed field geological and geomorphological campaigns, as well as geophysical and geodetic surveys. In particular, the latter investigations were focused along a narrow zone across the Tremestieri-Trecastagni-San Gregorio-Acitrezza Fault System. Moreover, additional ambient noise seismic records and other geophysical surveys were acquired in the municipal areas of San Gregorio di Catania, Tremestieri and Aci Castello.

6.1. Surveys in San Gregorio di Catania area

The study area is characterized by volcanic products of different ages, covering a sedimentary substrate that outcrops only locally. The 200 ka volcanics outcrop along a structural high oriented approximately E–W and probably controlled by the presence of the San Gregorio di Catania Fault. Subsequently, lava flows related to the most recent phase of the eruptive activity (<15 ka) covered most of the area (Fig. 6.1). The San Gregorio di Catania Fault is characterized by a morphological scarp

with downthrown side to the north, and variable drop. The maximum height is in the westernmost portion, where the scarp reaches 5 m; moving to the east, the scarp narrows until it completely disappears in the central part, and then appears again in the easternmost part, with height between 2 and 3 m.

Morphological features are absent in the central area probably because the progressive urbanization have caused the alteration of the original morphology. Instrumental seismicity related to San Gregorio di Catania Fault was not recorded, but creep episodes were reported following seismic events along the Trecastagni Fault (1988), along the Timpe system (2002) and during a seismic crisis occurred in 2009 in the area of Ficarazzi-Acitrezza (Monaco et al., 2010).

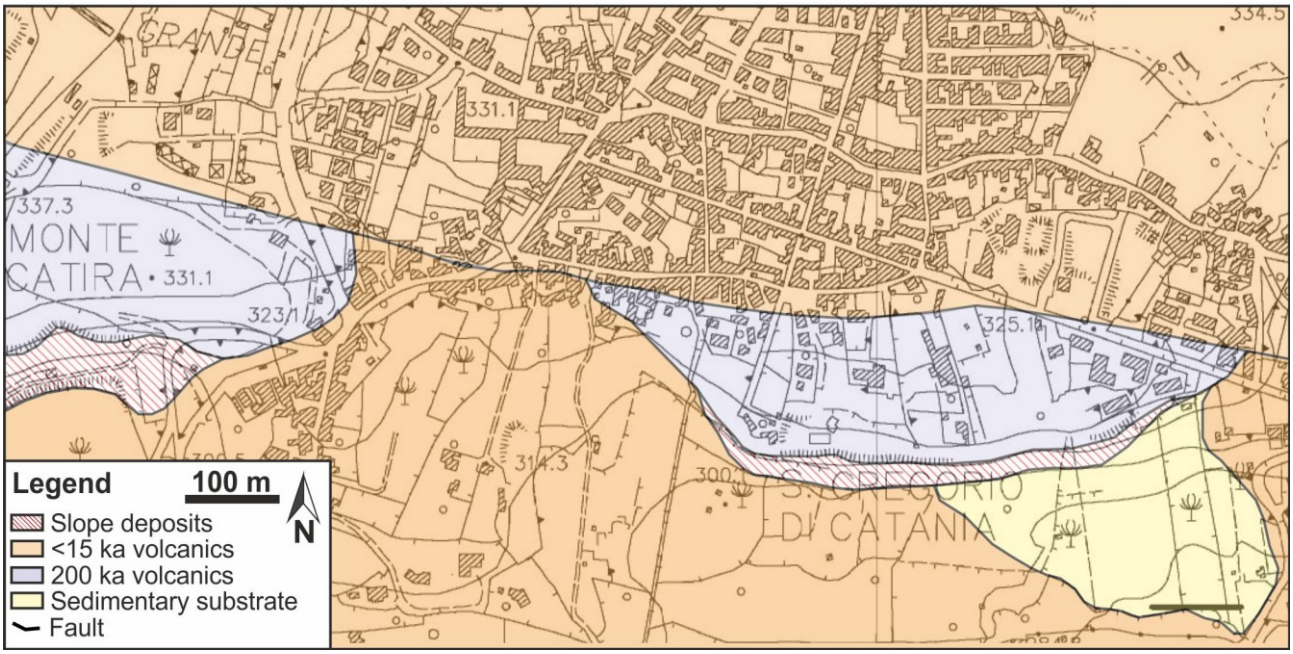

Fig. 6.1. Geologic map (modified after Branca et al., 2011) and trace of San Gregorio di Catania fault segment

6.1.1. Structural survey: mapping of the fracture zone

The fracture zone connected to the section of the fault within the urban area has been mapped with precision on the basis of an accurate and detailed survey of damage to artefacts and infrastructures caused by the fault creep (Imposa et al., 2015a,b).

For each fracture and/or deformation identified has been filled a form (Table 6.1), specifically prepared, containing the following information:

- Date;
- GPS coordinates;
- Type of fracture (fracture to the ground or fracture on buildings or manmade structures);
- Locality/address;
- ID (fracture identification number);
- Photo;
- Description;
- Direction;
- Length;
- Opening/ fracture throw;
- Marker reliability (choose between Low, Middle and High);
- Note.

Also, the exact position and the ID of every fracture have been reported on a topographic map.

Date	15/10/2014		**GPS Coord.**	37° 33.826'N / 15° 7.089'E	
Type (fracture to the ground / on building / etc..)	fracture to the ground		**Locality/Address**	Via Rua di sotto, 148	
ID	192		**Photo**	158	
Description are visible deformations and fractures on the ground and on the curb; the deformation strip is about 7 m wide					
Direction	~ N 135° E		**Length**		
Opening/ fracture throw					
Marker reliability	**L**	**M**		**H**	X
Note curb displaced of about 40 cm					

Table 6.1. Example of fracture survey form

The fractures mapping has documented that the trace of the main fault zone extends for about 1.6 km within the urban area across the entire town center with an average direction N100°E (Imposa et al., 2015a). The damages mainly consist of shallow to deep cracks affecting the walls of buildings (both infilling and bearing walls), fractures and rotations of retaining walls, sidewalks, curbs and pavings (Fig. 6.2).

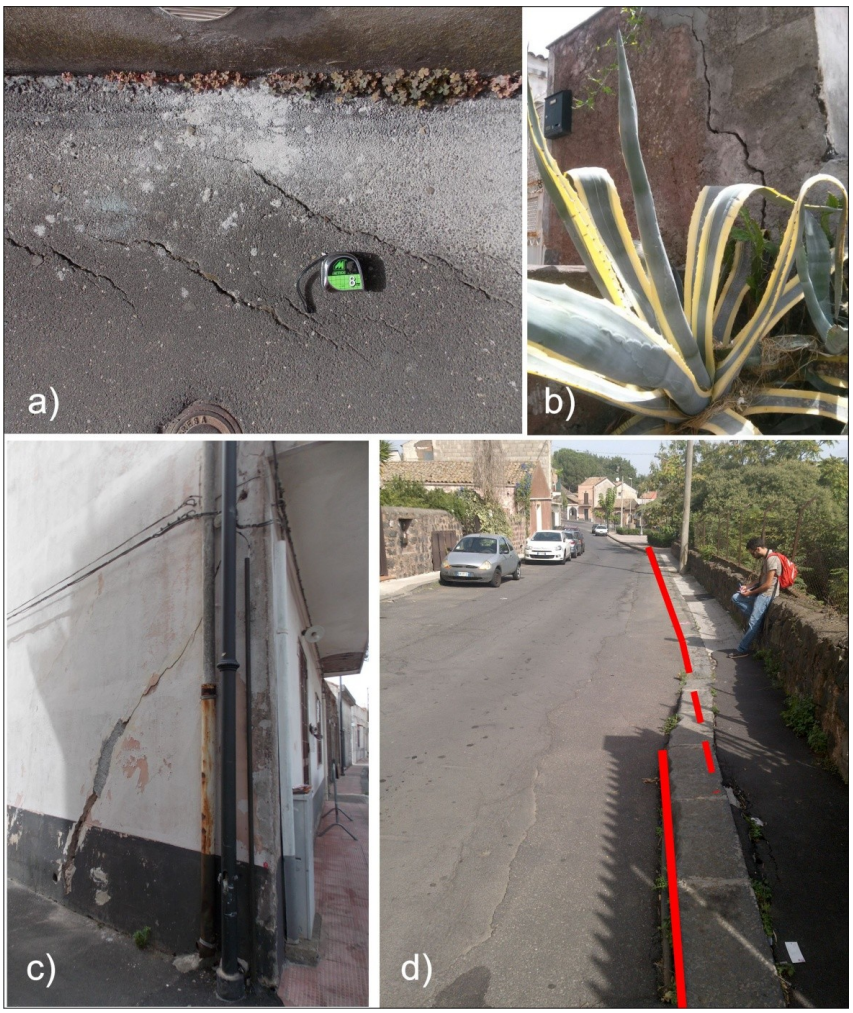

Fig. 6.2. Effects of the displacement along the San Gregorio fault zone; a) extensional fractures with en-echelon arrangement striking at about 45° from the main right-lateral shear zone direction; b) and c) fractures on walls of buildings; d) right-lateral slip (40 cm) highlighted by the displace curb (modified after Imposa et al., 2015a).

The width of fracture zone is highly variable usually ranging between 5 and 10 m (Fig. 6.3), but it was more than 40 m in the central portion. The maximum offset observed is ~30 cm and it is probably the result of several creep episodes.

The fractures orientation, systematically arranged provides important information on the kinematics of the main fault zone. The measured fractures have been interpreted as Riedel's R- or T-type fractures in a right lateral shear zone (Fig. 6.3) (Riedel, 1929; Mercier and Vergely, 1996). The average direction of T-type cracks is N140°, consistent with the shear zone oriented ~N100°. In the central portion, where the fracture zone is wider, extensional fractures systematically ~N10° oriented have been identified. They are kinematically consistent with an isolated block defining a negative flower structure.

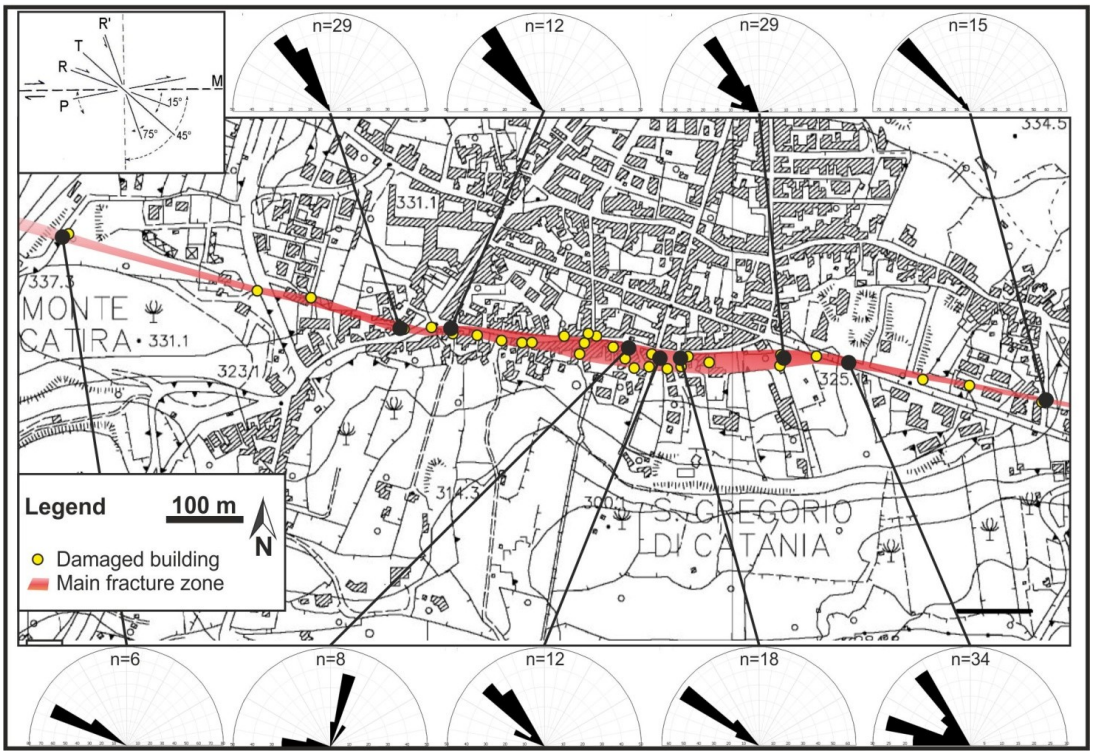

Fig. 6.3. Trace of San Gregorio di Catania fault zone detected by the structural survey (modified by Imposa et al., 2015a); frequency diagrams of the surveyed fracture network are showed: the kinematics of the system is compatible with a right-lateral shear zone (see inset) (modified after Imposa et al., 2015a).

Within the urban area of San Gregorio di Catania, the field survey has allowed to identify a secondary fracture zone that extends roughly N-S (Imposa et al., 2015b); it is long about 1080 m (Fig. 6.4) and the zone is approximately 10 m-wide. Even if with poor morphological evidence, this fracture zone shows a prevailing extensional kinematics. The fracture zone is wider in the hanging-wall than that in the footwall.

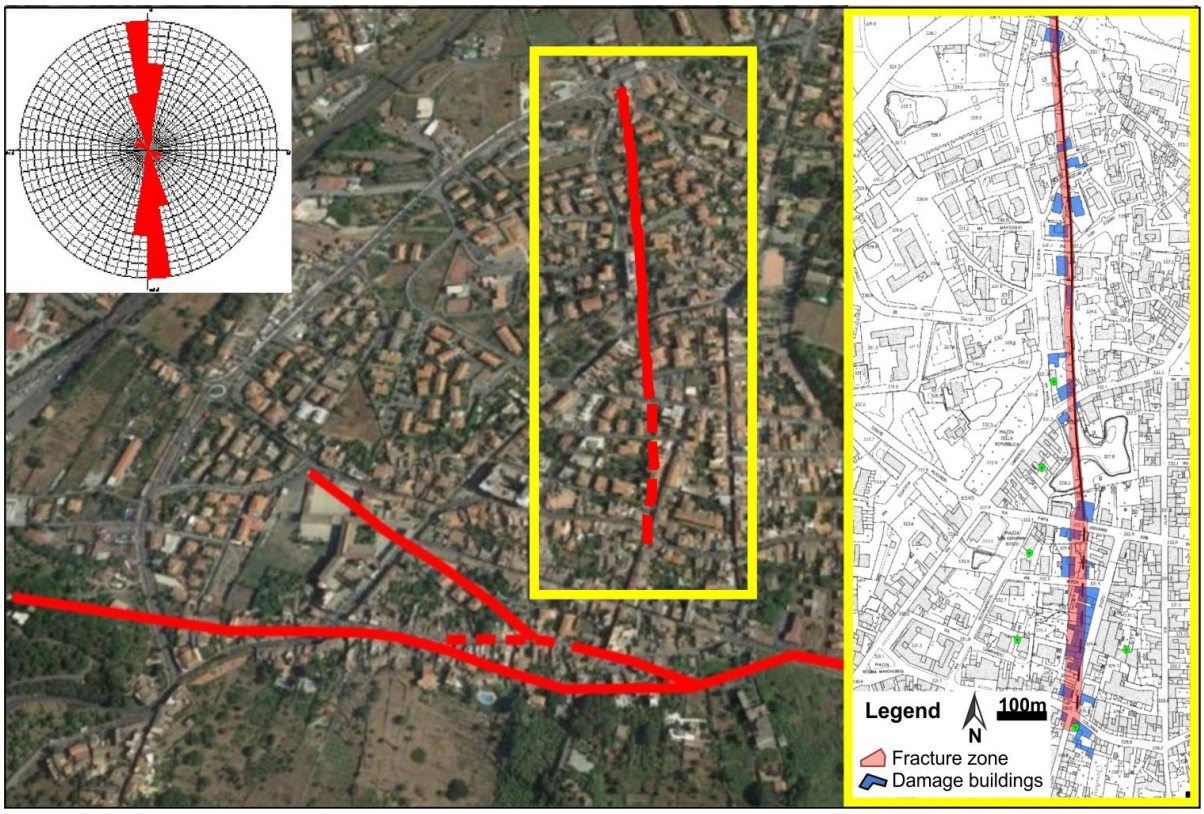

Fig. 6.4. Trace of the secondary fracture zone detected in the San Gregorio di Catania urban area by the structural survey; diagram of the azimuthal direction of the surveyed fracture network

6.1.2. Geophysical surveys to reconstruct the 3D geological structure of a selected portion of the San Gregorio Fault

Geophysical surveys are able to detect the variations of physical and mechanical characteristics in the subsoil; these properties of the rock type are influenced by the presence of mechanical discontinuities either joint or shear fractures.

Where major damage to infrastructure has been reported and where the fault zone is wider, three different geophysical techniques (G.P.R., sesmic tomography and Re.Mi.) have been applied in order to investigate the shallow geological structure (Imposa et al., 2015a) (Fig. 6.5). The variations of the properties of host rocks (i.e. seismic wave velocity) have been correlated with the occurrence of the fault zone.

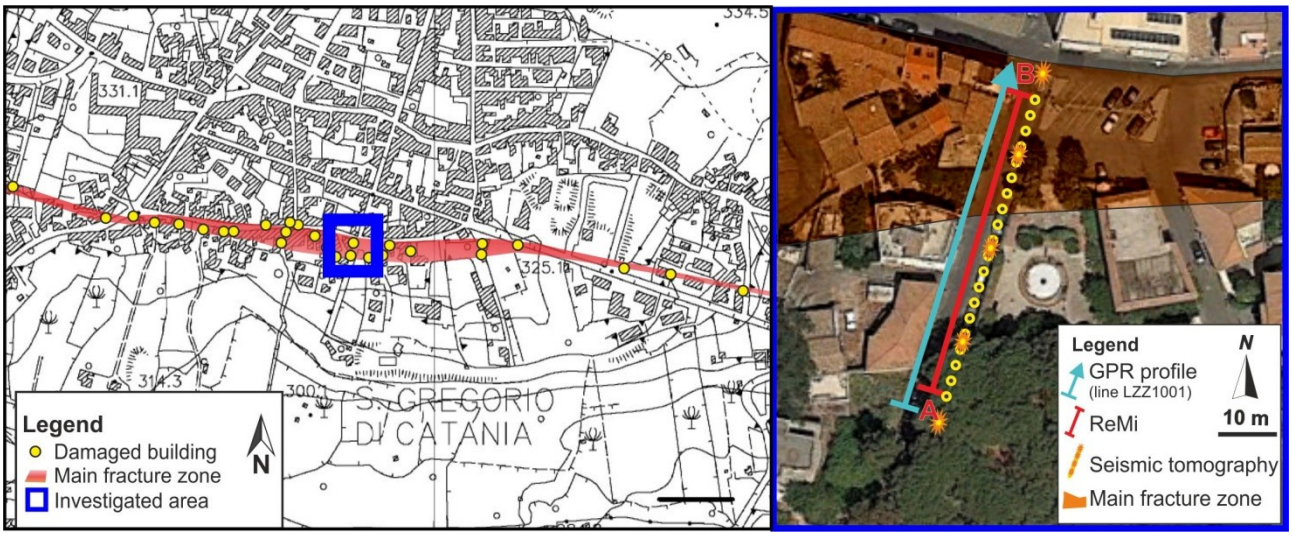

Fig. 6.5. The box at left shows the location of the investigated area; the box at right shows the location of G.P.R., ReMi and seismic tomographic surveys (modified after Imposa et al., 2015a).

6.1.2.1 G.P.R. survey

Ground penetrating radar is a non-invasive surveying method that uses the propagation of electromagnetic waves to investigate the conditions of the subsoil. The instrumentation consists of a control unit that generates an electromagnetic pulse of a few nanoseconds (ns) and relays it to an antenna which in turn transforms it into an impulse of higher amplitude that is irradiated into the ground. Any transition between materials with different electrical and magnetic properties causes the reflection of a part of the energy. The radar signals reflected by the subsoil is then detected by a receiver that relay them to the control point to produce a radargram.

The GPR (Ground Penetrating Radar) survey was carried out by using an IDS Ris FM Hi-Mod GPR system, equipped with two different frequency antennas of 200 and 600 MHz, respectively. The device worked in a monostatic mode with a constant antenna separation of 0.2 m (common-offset profiling) and sampling windows between 0.1 and 256 ns during which data were correctly recorded and a number of individual traces (A-Scan) were stacked (10 stacks per trace). Resulting B-scans were processed by using GRED 3D software (version 02.01.029 IDS, Ingegneria dei Sistemi S.p.A.) and adopting common GPR processing techniques.

A ~N-S oriented line was acquired on asphalt road crossing the ~W-E oriented damage zone detected with the structural analysis previously carried out (Imposa et al., 2015a). The most representative radar section is the 70 m-long, 200 MHz-derived line LZZ1001 with a max depth penetration of 3.5 m (Fig. 6.6).

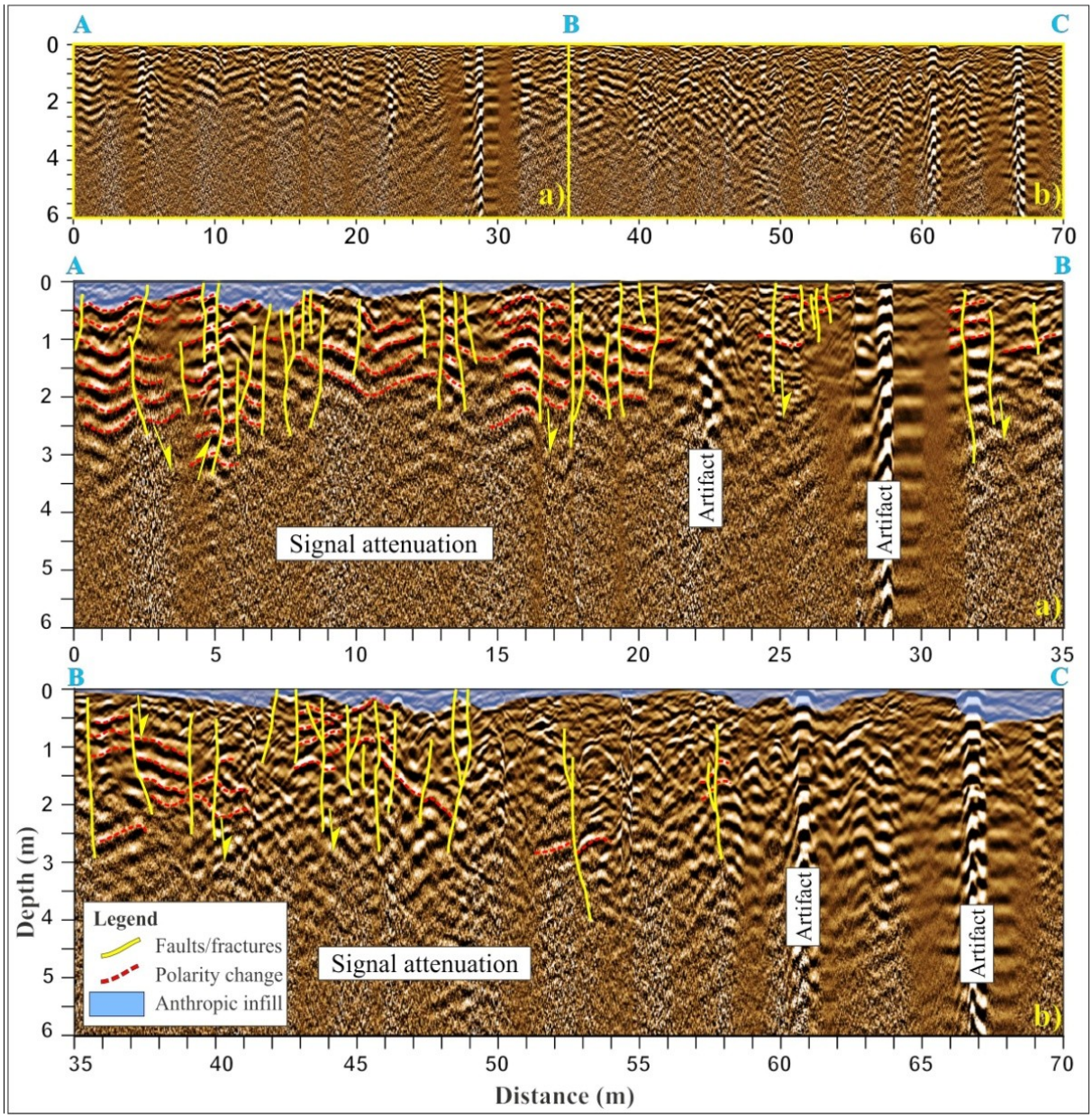

Fig. 6.6. GPR section and details of the southern (AB) and northern (BC) portion respectively (modified after Imposa et al., 2015a).

The entire line exhibits continuous to semi-continuous, high-amplitude parallel reflections resembling bedded electromagnetic facies which have been interpreted, according to field data, as distinct lava flow units. In particular, between 0-55 m it is possible to observe some truncations and displacements of the reflectors

accompanied by abrupt changes in seismic facies. Based on displaced reflectors, truncations have been interpreted as fault branches or fractures. They mainly consist of sub-vertical, tightly–spaced (0.5-1 m) fault planes with opposite dipping that appear to reach the topographic surface. Fault-truncations are often accompanied by along trace, strong-to-moderate, signal attenuation and they frequently juxtapose distinct electromagnetic facies. As regards fault movements, we used polarity changes (positive vs negative) as marker lines to estimate the vertical offset for each fault segment. In general, faults exhibit displacements in the range of 20-40 cm, but frequently they give rise only to a distortion of reflectors near them without a clear vertical offset.

According to the dipping of most planes and to the observed offsets, faults mainly consist of extensional and rare reverse dip-slip structures, whereas near-plane distortions could indicate also an along-strike lateral movement. As a whole, detected tectonic structures are confined within a ~55 m-wide damaged zone that, according to the deduced fault kinematics, can be interpreted as a transtensional wrench zone.

The GPR survey has confirmed the presence of, and allowed delimiting below ground level, the fracture zone detected also by the structural survey.

6.1.2.2 Seismic tomography

The seismic refraction tomography has been performed with the aim of collecting information about the possible extension of fracture zones at depth and understand if such fractures affects the elastodynamic properties of the rock types, in terms of variations in the velocity of elastic waves, which is closely related to the physical and mechanical properties of the subsoil (Imposa et al., 2015a). By studying the velocity distribution within the investigated medium, it is possible to detect the presence of physical and mechanical heterogeneities and to reconstruct with good approximation the subsurface stratigraphy.

The survey was carried out using a multi-channel seismograph (MAE A6000-S to 24 channels), equipped with two Purex multipolar seismic cables, each with 12 takeouts with an interval of 5 m; 20 vertical geophones with a frequency of 14 Hz and relative floor supports (perforated metallic plates to ensure the verticality and the good contact of the geophone with the ground); 10 kg hammer with trigger and alufer shot plate; extension cord starter and power system (Fig. 6.7a, b).

Even in this case the acquisition geometry has been calibrate so as to locate geophone alignment on the wider fracture zone. The geophones were arranged in an approximately NNE–SSW direction, with a spacing of 3 m, for a total coverage of 57 m. Five shots were performed, 2 external to the array, 5 m away from the first and the last geophone, 2 intermediate and one at the center of the alignment, in order to have a sufficient number of seismic data between shot points and geophones. The survey thus covered a total length (shot to shot) of 67 m (Fig. 6.7a, c). During the acquisition phase, in order to increase the signal/noise ratio, more shots were performed at the same point (Corrao and Coco, 2009).

The seismic data acquired have been inverted using the GSAO (Generalized Simulated-Annealing Optimization) method (Pullammanappallil and Louie, 1994).

In order to obtain the seismic tomography section two softwares by Optim LLC were used (SeisOpt ®Picker and SeisOpt ® 2D). The first one allows to run the manual picking of the first arrivals of longitudinal waves, while the second one allows searching for a theoretical model as similar as possible to the model observed and geologically compatible with the investigated area.

The tomography survey allowed investigating the subsurface down to a maximum depth of 15 m. From the obtained seismostratigraphic model between 39 and 57 m (Fig. 6.7c), an area characterized by velocity values Vp ≈ 400 m/s (bounded in figure by the red dashed line) is evident. It tends to decrease with increasing depth; this area can be observed down to the maximum depth reached by the tomography (~15 m). Laterally, many seismic layers are visible with different thicknesses and inclinations, which show an increase in Vp values with depth. The first seismic-layer

(from 0 to m ~3 m) has a subhorizontal trend and is characterized by low velocity values (~Vp = 400 m/s). Below we observe an increase of Vp, with values of ~850 m/s found from ~3.5 m-depth downwards; in the central area of the alignment, between 29 and 38 m, these values are detectable down to the maximum depth reached by the tomographic section. In the final part of the section, this seismic-layer has an inclined trend with a thickness of ~4 m. In addition, two areas with high Vp values (1100–1600 m/s) located respectively between 11 and 24 m and between 55 and 67 m from the start of the alignment are also visible.

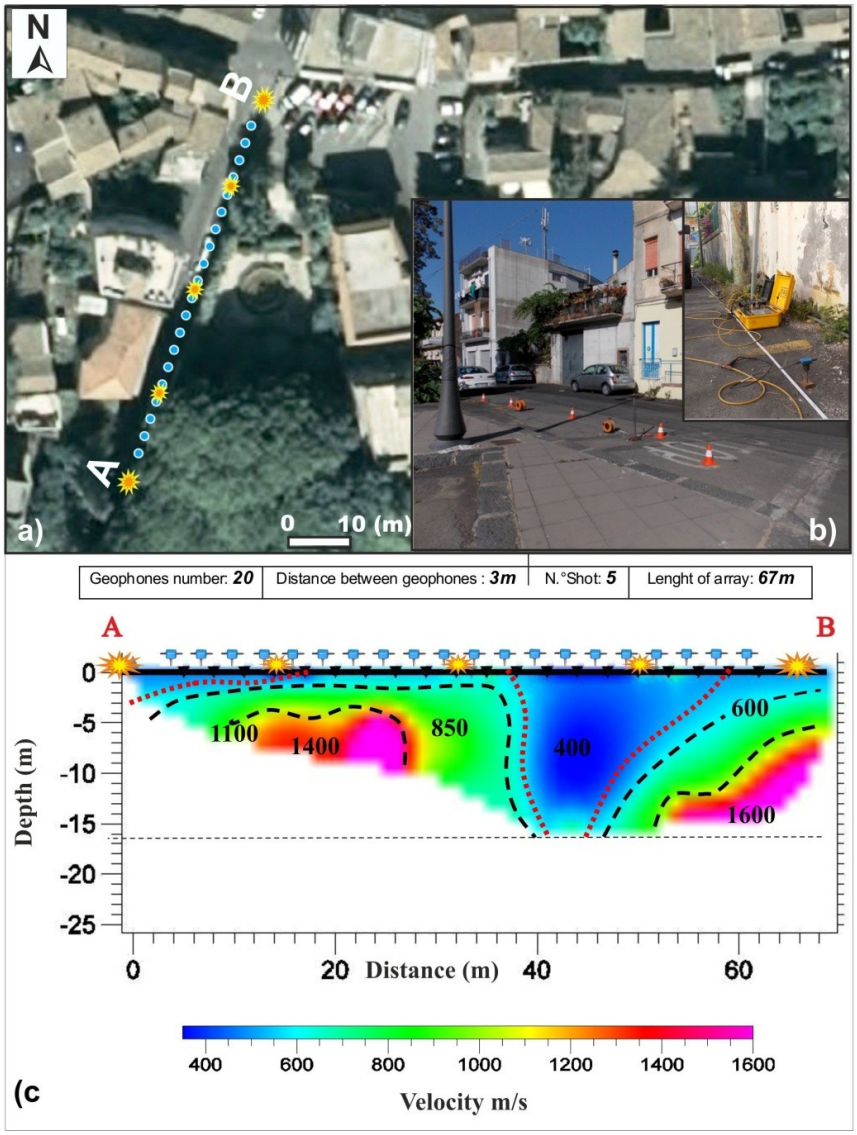

Fig. 6.7. a) Location of seismic tomography; b) photograph of the instrumentation used (seismograph, hammer and seismic array) c) seismic tomography section with acquisition geometry (shot points and geophones) and velocity distribution (modified after Imposa et al., 2015a).

Considering the orientation of the tomographic section with respect to the fracture zone detected by the structural survey, the low velocity area (Vp ≈ 400 m/s), could be associated with the volume of rock affected by tectonic disturbance linked to the San Gregorio Fault that caused the fracturing and thus the worsening of the geomechanical properties of the rocks investigated by the geophysical survey. The high Vp values (1100–1600 m/s) found in two different areas of the section might indicate the presence of an unevenly cracked rocky substrate.

6.1.2.3 ReMi

The passive refraction microtremor (ReMi) method (Louie, 2001) allows to extrapolate information on the dynamic characteristics of the subsurface to greater depths than the active geophysical surveys; the energizing source is represented by the ambient noise from unknown and assumed isotropic sources.

Based on the inversion process of the dispersion curve of the surface waves (Rayleigh) (Tokimatsu et al., 1992; Yuan and Nazarian, 1993), the ReMi method allows identifying the shear wave velocity profile (Vs) of the investigated subsoil, that depends on the characteristics of the medium and its vertical variations.

The ReMi survey was performed by placing the geophones alignment parallel to that of the tomographic survey; the equipment was the same as that used previously but with geophones at a different frequency (4.5 Hz), set 3 m apart, for a total length of 57 m. Ten recordings of ambient noise were carried out, each consisting of 20 s windows with sampling frequency at 500 Hz and sample rate of 2 ms.

The acquired data were processed using the software SeisOpt ® ReMi (Optim L.L.C., 2003). After obtaining the power spectrum p–f (slowness–frequency), the picking was performed (Fig. 6.8a) on the border between signal and the inconsistency of the noise, 16 triplets of values (f–p-apparent velocity) were thus selected.

The data selected from the p–f spectrum were then plotted on a graph which includes a dispersion curve calculated from an initial Vs model (Fig. 6.8b). By

varying the number of layers, their velocity and density, the theoretical dispersion curve has been modified to make it as similar as possible to the experimental one obtained by picking (Fig. 6.8b).

A 1D Vs profile was thus obtained, representing the trend of variations of the shear wave velocities with increasing depth, characterized by the presence of 8 seismic-layers in a 35 m depth range (Fig. 6.8c). The first seismic-layer reaches a depth of 2 m and has a velocity of 185 m/s, may indicate the presence of incoherent material. In the next seismic-layer (2–5.6 m) there is an increase in Vs of up to 297 m/s, correlated to the presence of levels of slag and volcanic breccias. From 5.6 m, there was a further increase in velocity values, reaching values equal to 410 m/s, probably associated with the presence of fractured and/or cracked lavas. Below this layer, the values of Vs continue to increase steadily with greater depth.

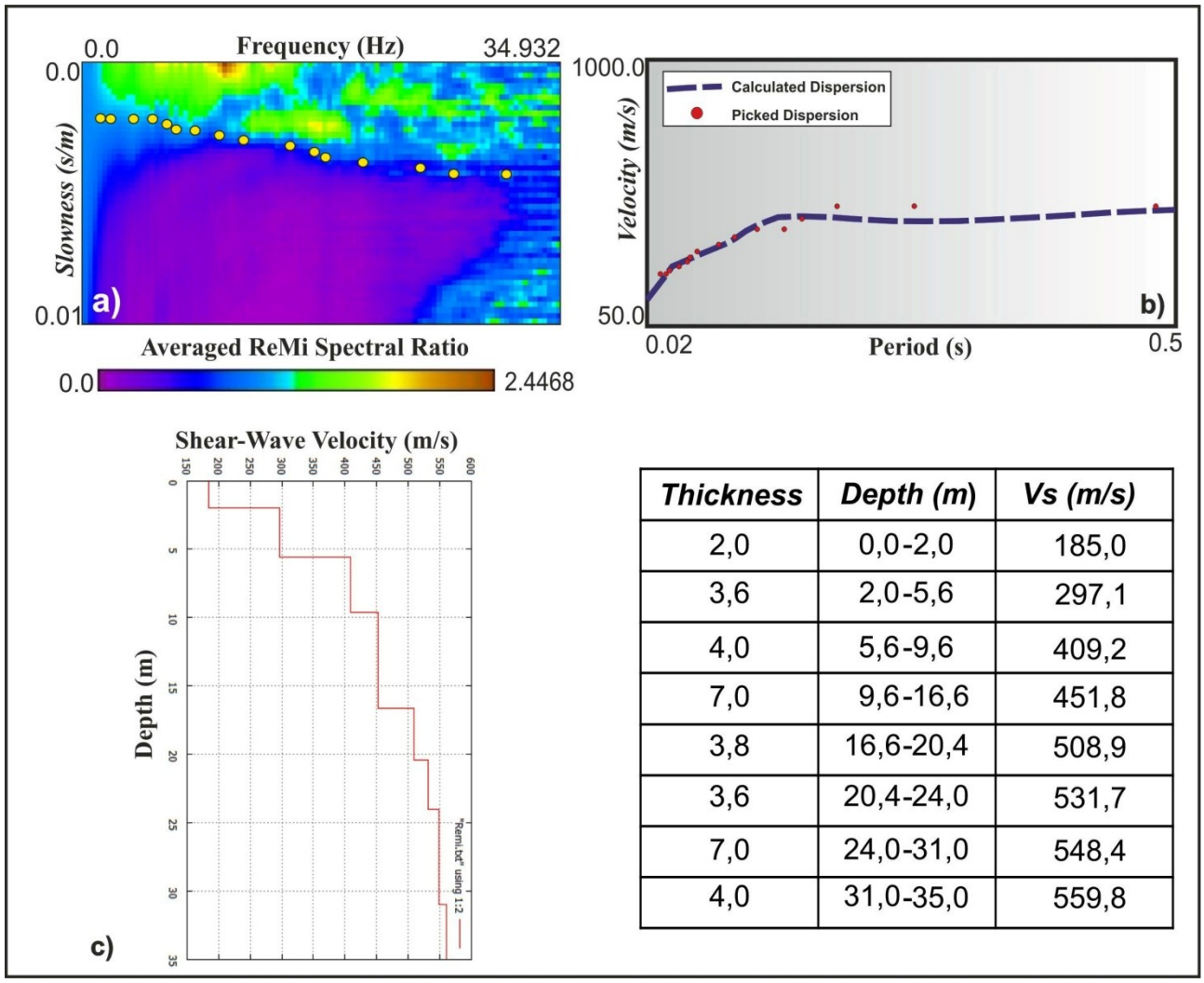

Thickness	Depth (m)	Vs (m/s)
2,0	0,0-2,0	185,0
3,6	2,0-5,6	297,1
4,0	5,6-9,6	409,2
7,0	9,6-16,6	451,8
3,8	16,6-20,4	508,9
3,6	20,4-24,0	531,7
7,0	24,0-31,0	548,4
4,0	31,0-35,0	559,8

Fig. 6.8. a) Power spectrum; b) dispersion curve (red dots is experimental and blue dotted line is theoretical; and c) 1D velocity-depth profile (by Imposa et al., 2015a).

For a detailed as possible model of the investigated section, the recordings of the 20 channels were divided in 5 subgroups (Raines et al., 2011) in order to develop a ReMi section. Each subgroup consists of the datasets from 8 channels, chosen so that each subgroup is superimposed with the adjacent one by at least 60% (1–8; 4–11, 7–14; 10–17; 13–20) (Fig. 6.9a) to ensure a good fit of the data. The dataset of each subgroup was processed with the same procedure to establish the one-dimensional Vs profile. Five power spectra, five dispersion curves and five one-dimensional profiles were defined; given the limited number of channels constituting each subgroup, the method allowed reaching a depth of about 15 m (Corrao and Coco, 2009; Dal Moro, 2012). Finally, from the obtained one-dimension profiles (Fig. 6.9b), a representative

section of the calculated Vs distribution was extracted by a process of contouring and smoothing, to which a color scale has been added indicating the Vs velocity ranges.

The obtained section is 36 m-long and 15 m-deep; the first and last one-dimension profiles are located respectively between geophones 1–8 and 13–20, at a distance of 10.5 m from the ends of the geophonic array, while the intermediate profiles, 7–14, 10–17 and 13–20, are located respectively at 19.50, 28.50 and 37.50 m (Fig. 6.9a; Table 6.2).

Geophone Series	Distance interval along array(m)	Plot position on 2D image(m)
G1 – G8	0 - 21	10.5
G4 – G11	9 - 30	19.5
G7 – G14	18 - 39	28.5
G10 – G17	27 - 48	37.5
G13 – G20	36 - 57	46.5

Table 6.2. Geophone groups and the relative distances of the ReMi section (by Imposa et al., 2015a).

The section shows 5 areas characterized by different Vs values (Fig. 6.9a); between 36 and 46.5 m from the origin of the geophones alignment, an area characterized by velocity values Vs ≈ 250 m/s down to a depth of 5 m is visible. Another area characterized by values of Vs≈350 m/s is present in two different sectors of the profile, between 10.5 m and 27 m from the origin of the alignment to a depth of 1.5 m with a sub-horizontal trend and between 31 and 46 m, with a thickness of about 5 m with a slight slope that reaches toward the final part the maximum investigated depth (15 m). An area, characterized by Vs values of about 450 m/s, can be observed in the whole section; in the first meters of the section this area has a sub-horizontal trend and thickness of about 5 m, between 30 and 36 m, it slopes down and presents a thickness of 1.5 m, reaching the maximum depth investigated, between about 36 and 46.5 m.

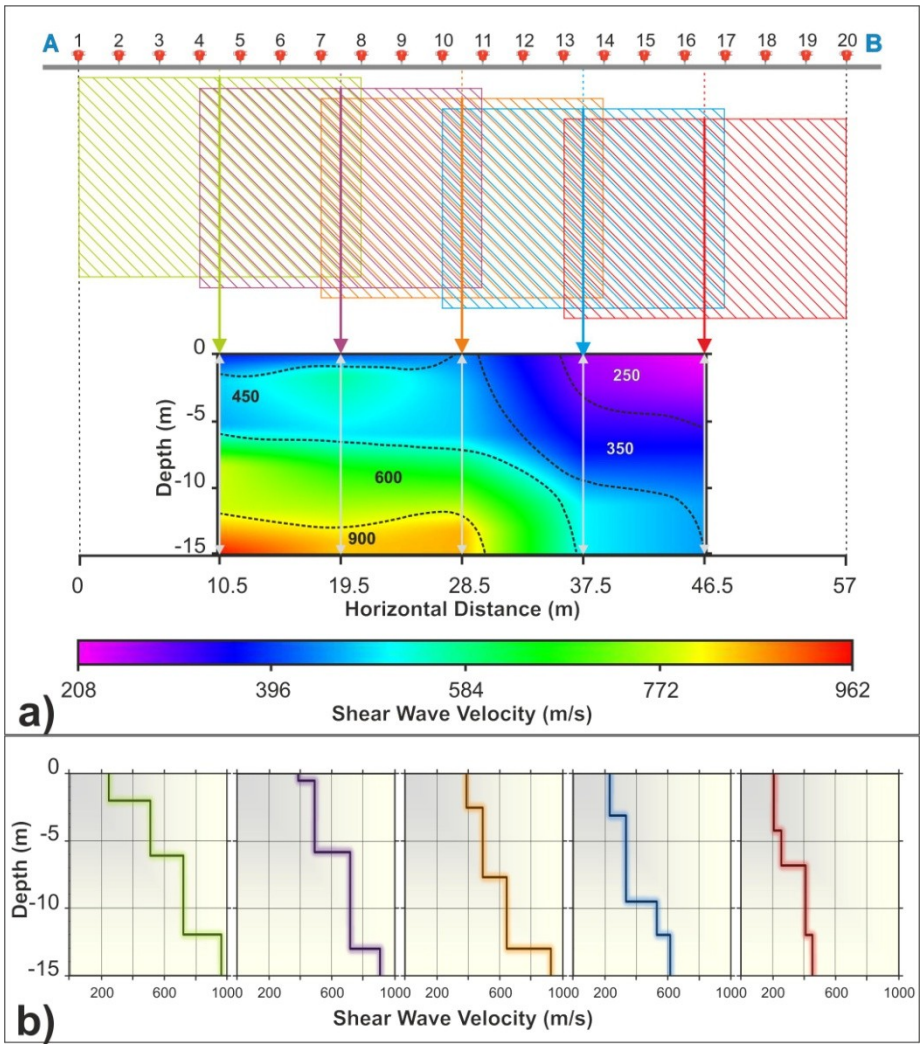

Fig. 6.9. a) ReMi section and Vs distribution; b) 1D velocity models for the five subgroups (Table 6.2) (by Imposa at al., 2015a).

As increasing depth, there are two additional sectors in the section with increasing velocity: the first, observable between 10.5 m and 36 m and to a depth ranging from 6 to 12 m, with Vs≈600 m/s, has a sub-horizontal trend that tends to widen toward the final part, down to 15 m depth. Underlying this seismic-layer an area can be observed characterized by higher Vs that reaches the maximum value of about 960 m/s; this area, located in the alignment approximately between 10.5 m and 30 m, has a thickness of about 3 m with a sub-horizontal trend.

6.1.2.4 Results integration

All the geophysical surveys have highlighted the presence of anomalies in the mechanical and elastic characteristics of rocks at depth that are ascribable to the fault zone observed at surface. The boundaries between faulted rock volume and the surrounding sound rock is clearly detectable and well correlate with the development of the fracture zone.

By comparing the tomographic section with the one obtained from the ReMi survey, it is possible to observe how in both cases there are lower velocity values in the first meters of depth. This may be correlated to the high degree of fracturing observed at the surface and documented at shallow depth by the GPR survey; lower velocities are also observed at greater depths and down to the maximum investigation depth. In both sections, there is also an increase in velocity with depth moving away from the fractured zone; this phenomenon may be indicative of a reduction in the degree of fracturing and an improvement of the physico-mechanical and elastic properties of the rock types.

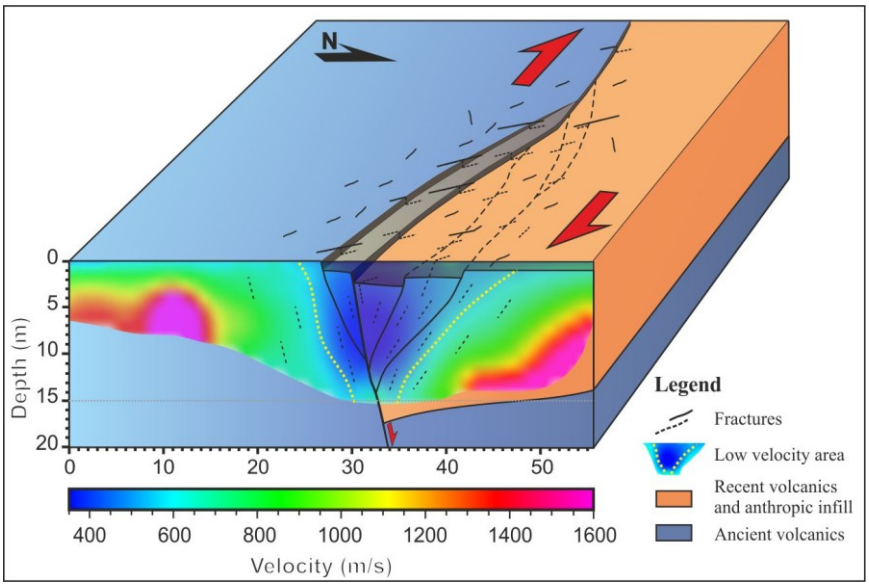

Fig. 6.10. Schematic illustration showing the geological structure of the study area. The area can be interpreted as a meso-scale negative flower associated with themain, right lateral shear zone (by Imposa et al. 2015a).

By integrating the results, it has been possible to accurately define the width of the fracture zone and its continuation at depth (Imposa et al., 2015a). In the area where the investigations were carried out, the fracture zone is 40 m-wide and the subsurface geometry of the fault zone is consistent with a negative flower structure (Fig. 6.10). The block between the two main branches of the fault extends to a depth of about 20 m, and is intensely fractured and

crushed by the continuous displacement occurring between the two fault blocks. This rock volume corresponds to the low velocity areas of the sections (Figs. 6.7c, 6.9a).

6.1.3. HVSR surveys in San Gregorio area

Seismic ambient noise recordings were acquired in 618 different sites in the municipal territory of San Gregorio di Catania, in order to identifying the frequency at which ground motion is amplified due to resonance effects, related to the presence of tectonic and stratigraphic discontinuities; some of these recordings were repeated at different times in order to verify the repeatability of the acquired data.

In particular, 518 ambient seismic noise recordings were carried out, along 23 profiles (Fig. 6.11), with constant spacing of 5 m between each measurement; 19 of these profiles were performed perpendicular to the fault traces identified by the structural survey. The position of the other 100 acquisitions has been defined in order to have a uniform coverage of the entire municipality area (Fig. 6.12).

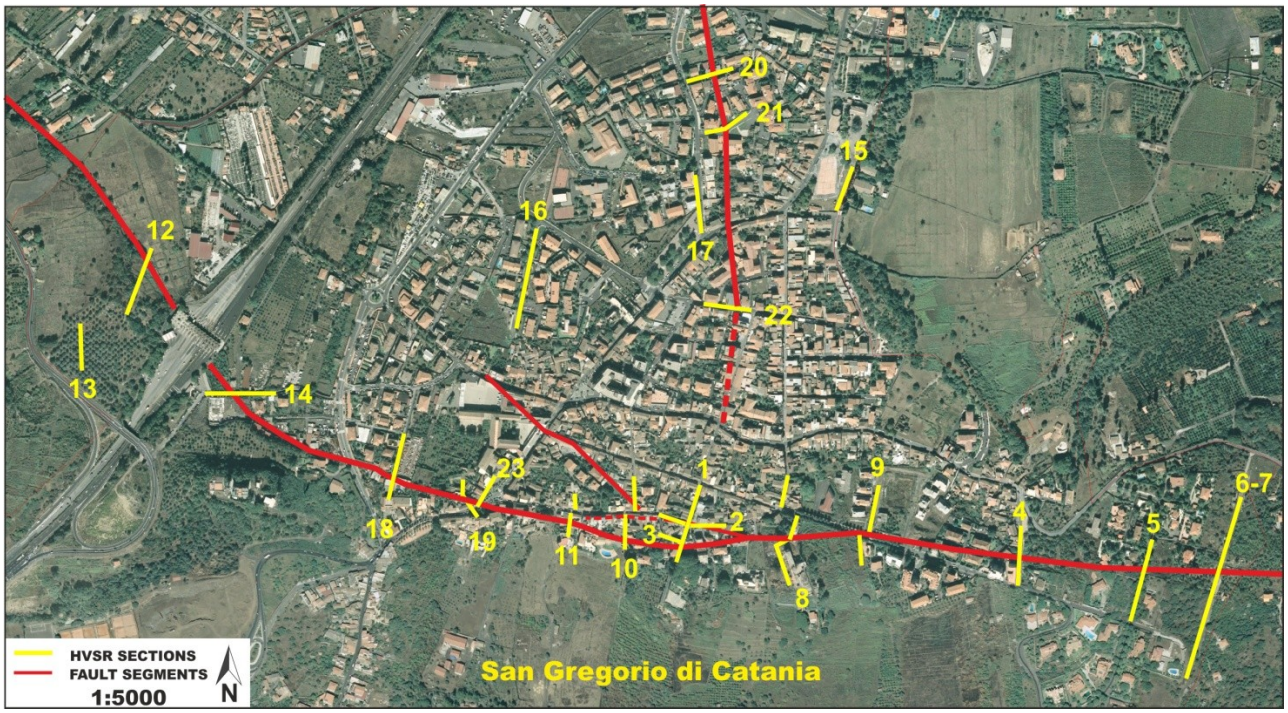

Fig. 6.11. Location of 23 HVSR sections performed in the San Gregorio di Catania urban area

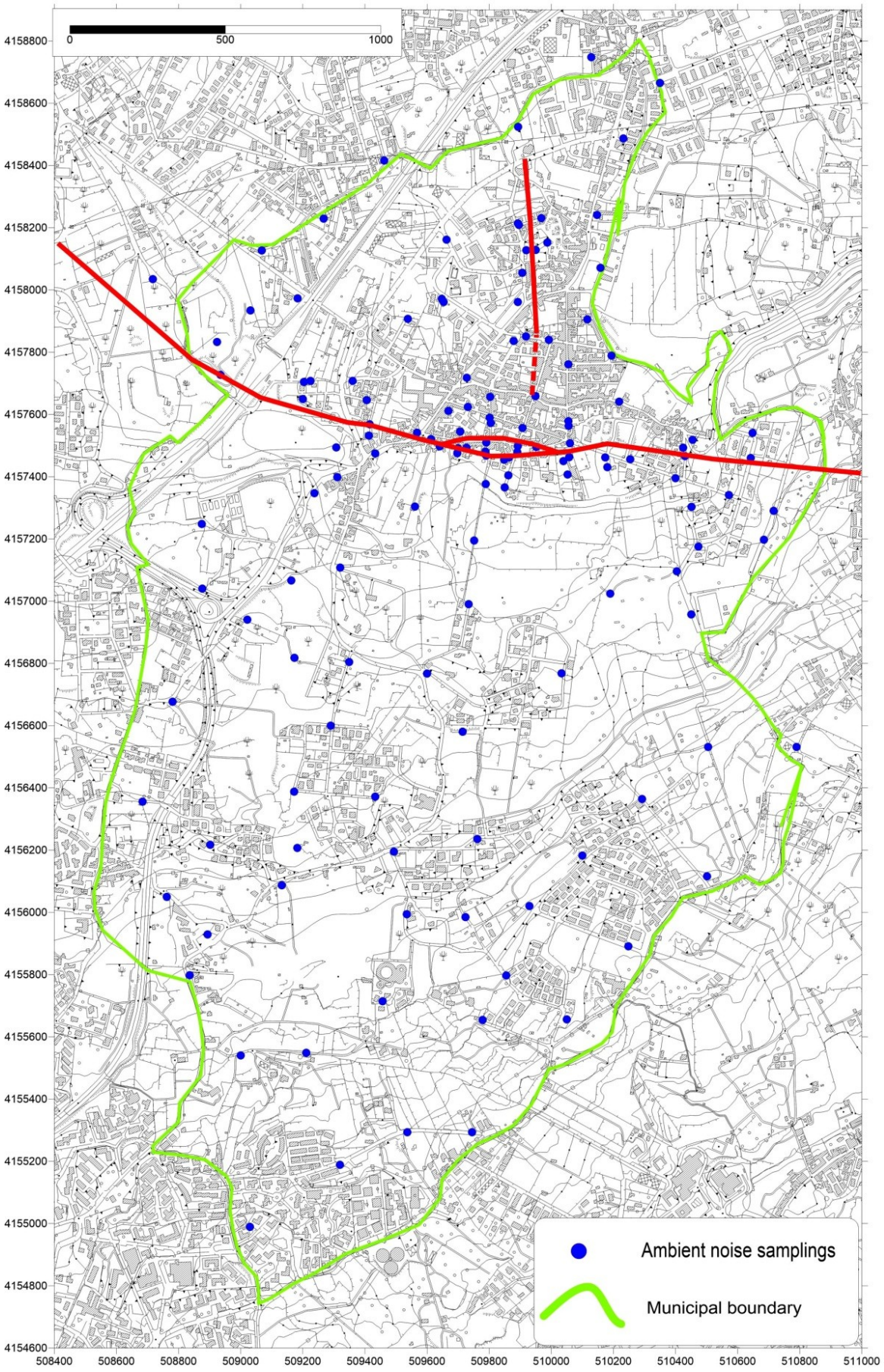

Fig. 6.12. Location of HVSR surveys, the red lines represent the fault segments

The ambient seismic noise samplings were performed using 4 MoHo—Tromino tromograph (http://www.tromino.eu) (Fig. 6.13), very compact (1 dm^3 and 1 kg weight) portable digital three-components seismographs, with high sensitivity and resolution (2200 V/(m/s), 24 dB, 0.1250 Hz); at each measuring station, the environmental seismic noise has been recorded for 20 min, so to ensure the signal stationarity, with a sampling frequency of 128 Hz.

Fig. 6.13. Three-components seismographs (Tromino)

During the field surveys, forms were compiled, with information related to: date, registration number, name, reference of GPS coordinates, location or address, time start of recording, weather conditions and any notes; in addition, for the acquisitions carried out along profiles, has been reported the profile number, the spacing between recordings and the total length (Fig. 6.14).

Località: San Gregorio										Profilo **11**: NNW-SSE
Frequenza di campionamento (Hz): 128 Hz										
Data: 27/01/2014										Lunghezza tot.: 92 m
Durata registrazione: 20 minuti										
Profilo	Int.	Grilla	Numero	Nome misura	Lat° N	Long° E	Via o Contrada	Ora inizio	Condizioni metereologic	Note
11		05(524)	1	F1	WP. 253		Vico Catalano	09.34	leggermente coperto/ vento debole	Etna in attività
	5 m	33(19)	2	G1			Vico Catalano n°2			
	5 m	36(221)	3	H1			Vico Catalano			tra G3 e H1 frattura
	5 m	23(491)	4	N1	WP. 254		Vico Catalano n°4			
	5 m	06(604)	5	F2			Vico Catalano n°6	10.04		F2 a 2,5 m da N3
	5 m	34(510)	6	G2			Vico Catalano			tra N1 e N2 dislivello circa 1,5 m;
	5 m	37(367)	7	H2			Vico Catalano n°8			
	5 m	24(891)	8	N2			Vico Catalano (fine strada)			F2-G2-H2-N2 su sabbia
		07(84)	9	F3			Vico Catalano	10.36		F3 a 2,5 m da F1
		35(130)	10	G3			Vico Catalano			G3 a 2,5 m da G1
		38(665)	11	H3			Vico Catalano			H3 a 2,5 m da H1
		25(224)	12	N3			Vico Catalano			N3 a 2,5 m da N1
		26(34)	13	N4			vialetto civico 47 (via Marciano)	11.05		N4 a 12 m da F1
	5 m	39(722)	14	H4			vialetto civico 47 (via Marciano)			tra H5 e N4 dislivello circa 1 m
	5 m	36(404)	15	G4			vialetto civico 47 (via Marciano)			
	5 m	08(842)	16	F4			vialetto civico 47 (via Marciano)			
	5 m	27(95)	17	N5			vialetto civico 47 (via Marciano)	11.29		
	5 m	40(231)	18	H5			vialetto civico 47 (via Marciano)			

Fig. 6.14. Example of ambient noise acquisition form

In each measurement site the instrument has been positioned taking into account the magnetic north direction, identified by means of a compass, in order to evaluate

the possible presence of directional effects; serious attention has been paid to provide a good coupling between the instrument and the measurement site.

The environmental noise recordings have been processed through the H/V spectral ratios technique (Nakamura, 1989). The decision was made to develop the entire track for each acquisition, dividing it into time windows of 20 s, to which a smoothing equal to 10% of the centre frequency with a triangular windows function was applied. The signal was analyzed, using the Grilla software, in the frequency range 0–64 Hz, in relation to the adopted sampling frequency of 128 Hz and cleaned by removing transients. Furthmore, the spectral ratio was calculated along various directions, turning the N-S and E-W components of the motion with azimuthal intervals of 10°, proceeding from 0° (north) to 180° (south), in order to detect the presence of directional effects on HVSR peaks. For each recording, the statistical tests result was verified (SESAME guidelines 2005), which showed that all measurements meet the criteria of execution goodness, analysis and reliability, while the main resonance peaks were not always significant and clear for all six criteria analyzed.

Considering the high number of measurements was not possible to show in this thesis all acquired spectra. Some spectra are shown in figure 6.15 related to ambient noise recordings done near the fault segments and within the municipal area.

Based on the obtained results, it is possible to position the resonant frequency values, observed in the H/V spectra, within three main frequency ranges. In particular, for the acquisitions made in the southeastern portion of the municipal area, the resonance frequencies fall within a range approximately between 0.5 and 5 Hz. Those acquired in the western sector fall within a frequency range between 3 and 8 Hz, while in the northwestern sector the resonance frequency values fall within a range approximately between 9 and 16 Hz.

In some cases, two or three peaks are present in the spectra, some of which at higher frequency values. These peaks are associated with different oscillation frequencies, connected with stratigraphic discontinuities located at different depths,

from site to site. The lowest frequencies of amplification are probably related to deep geological characteristics of the study area, conversely the higher frequencies can be associated to the presence of surface disturbances such as rubble deposits.

The stronger directional effects were observed for the recordings performed near the new fault segment (with N-S orientation) detected by the structural survey; the identified directional effects appear to be orthogonal to the fractures azimuthal direction; these recordings were further elaborated with the DHVPOR technique (see paragraph 6.1.4). Directional effects are also detected, although less strong, in the acquisitions made near the main fault segment that crosses the area in the E-W direction; in this case the identified directional effects appear to be parallels to the fractures azimuthal direction detected by the structural survey.

The different directional effects detected could be connected to the different kinematics of the two fault segments; in particular, the directional effects are parallel to the direction of the fractures, for the fault segment with oblique-dextral strike-slip kinematics. On the contrary, this effect appears to be perpendicular to the direction of the fractures, for the segment fault with normal kinematic.

As above mentioned, the recordings were carried out all over the area of San Gregorio Municipality with a denser grid near the fault zone. In order to reconstruct the natural frequency and the associate HVSR amplitude distribution in the studied area, 61 of the recordings carried out along profiles evenly distributed in the urban area of San Gregorio di Catania and the 100 acquisition conducted in surrounding areas have been considered. For each site the coordinates, the fundamental frequency f_0 in the 0.5-20 Hz frequency range, and the corresponding H/V amplitude, have been considered. Using the kriging interpolation method included in Golden Software Surfer$^{(R)}$, a contouring of data was made. In this way the map of the resonance frequencies distribution (Fig. 6.16) and the map of HV amplitude distribution (Fig. 6.17) were thus obtained.

The variable distribution of the fundamental frequency is strictly connected with the variation at depth of the impedance contrast existing among the seismic basement

and the layers that produce the resonance. Comparing the map of the fundamental frequencies with the geological-technical map, obtained from first level microzonation study in San Gregorio municipality (Fig. 6.18), it is possible to note a good agreement between the fundamental frequency variation and the distribution of different lithotypes.

The map of HV amplitude distribution clearly show the presence of areas characterized by resonance phenomena with high values of HV amplitude, in particular near the fault traces, confirming the results of the structural survey and of the other geophysical surveys performed in the study area.

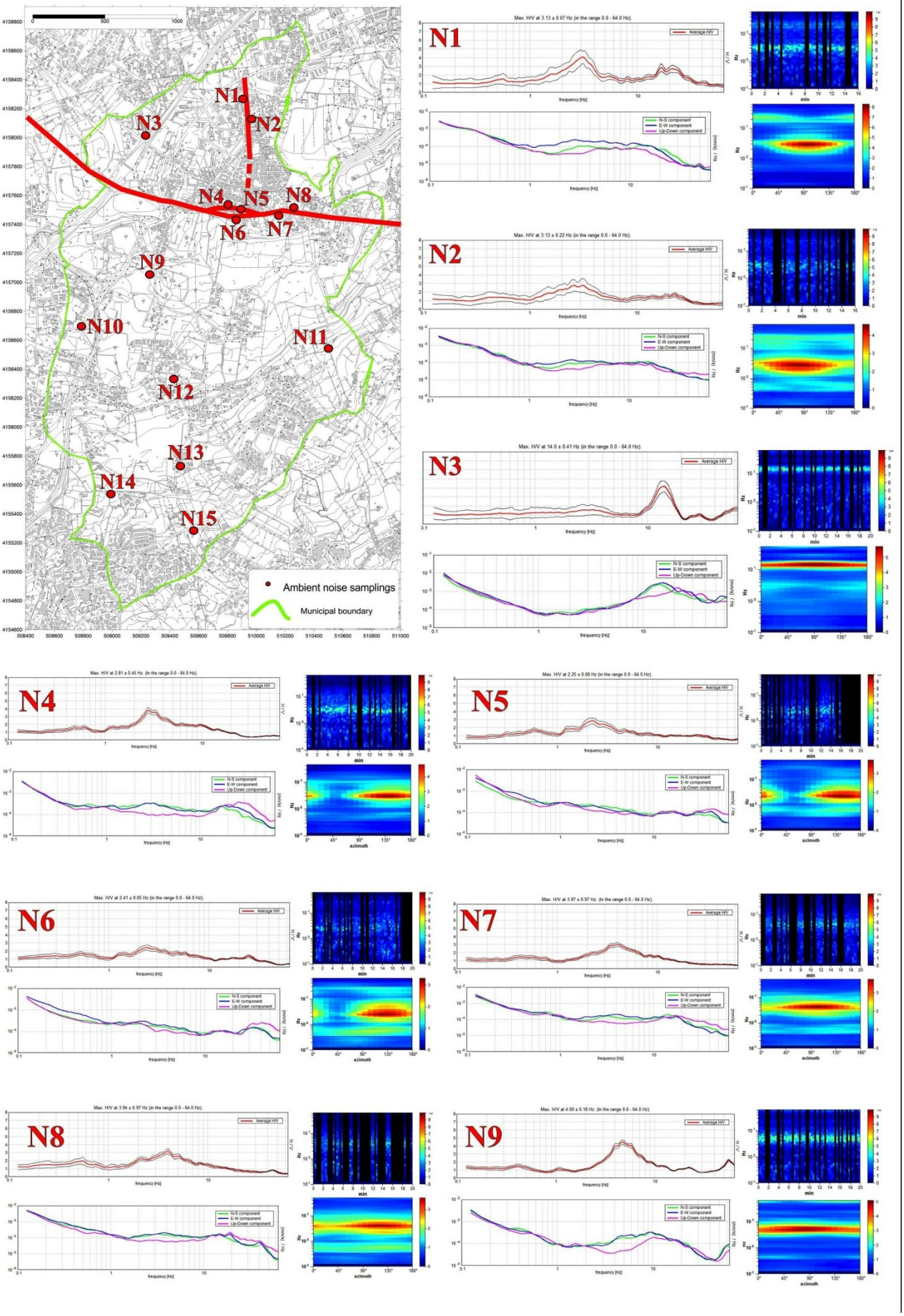
N1
N2
N3
N4
N5
N6
N7
N8
N9
N10
N11
N12
N13
N14
N15
Ambient noise samplings
Municipal boundary
Average H/V
N-S component
E-W component
Up-Down component
frequency [Hz]
min
azimuth

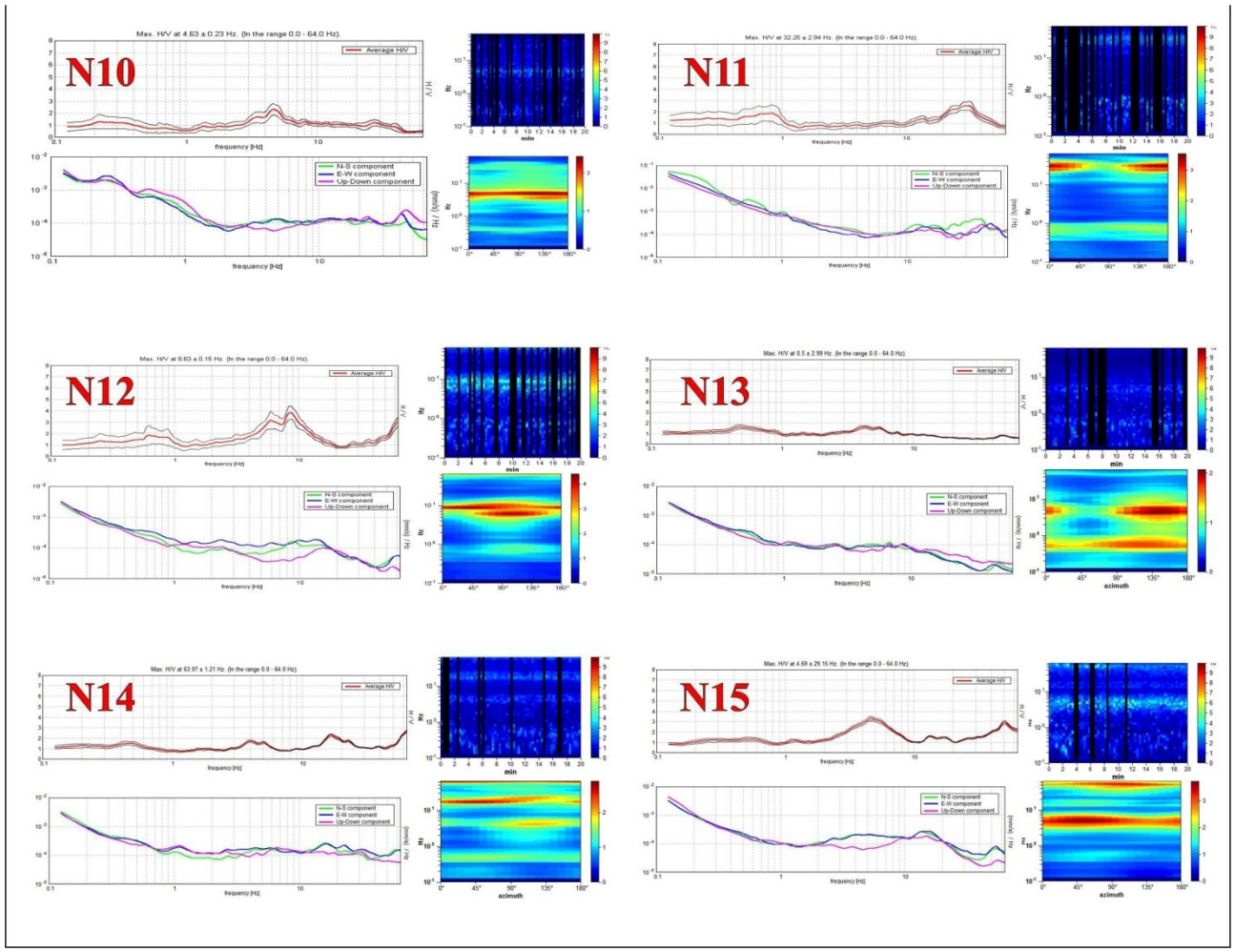

Fig. 6.15. Results of the elaborations of some ambient noise measurements performed in theMunicipality of San Gregorio di Catania (HV spectra; amplitude spectra of single components N-S, E-W, up-down; H/V stability; directional HVSR)

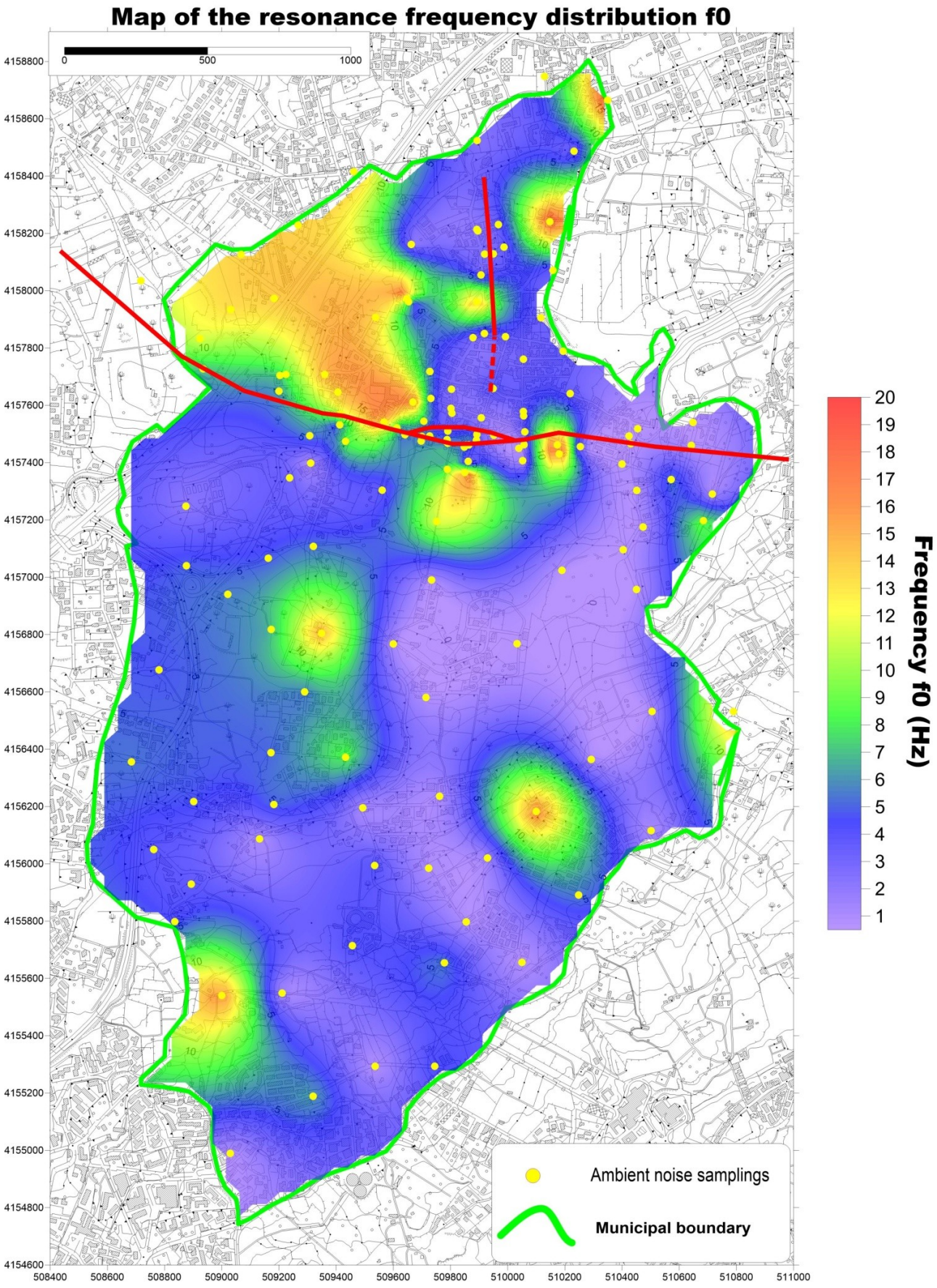

Fig. 6.16. Map of the resonance frequencies distribution

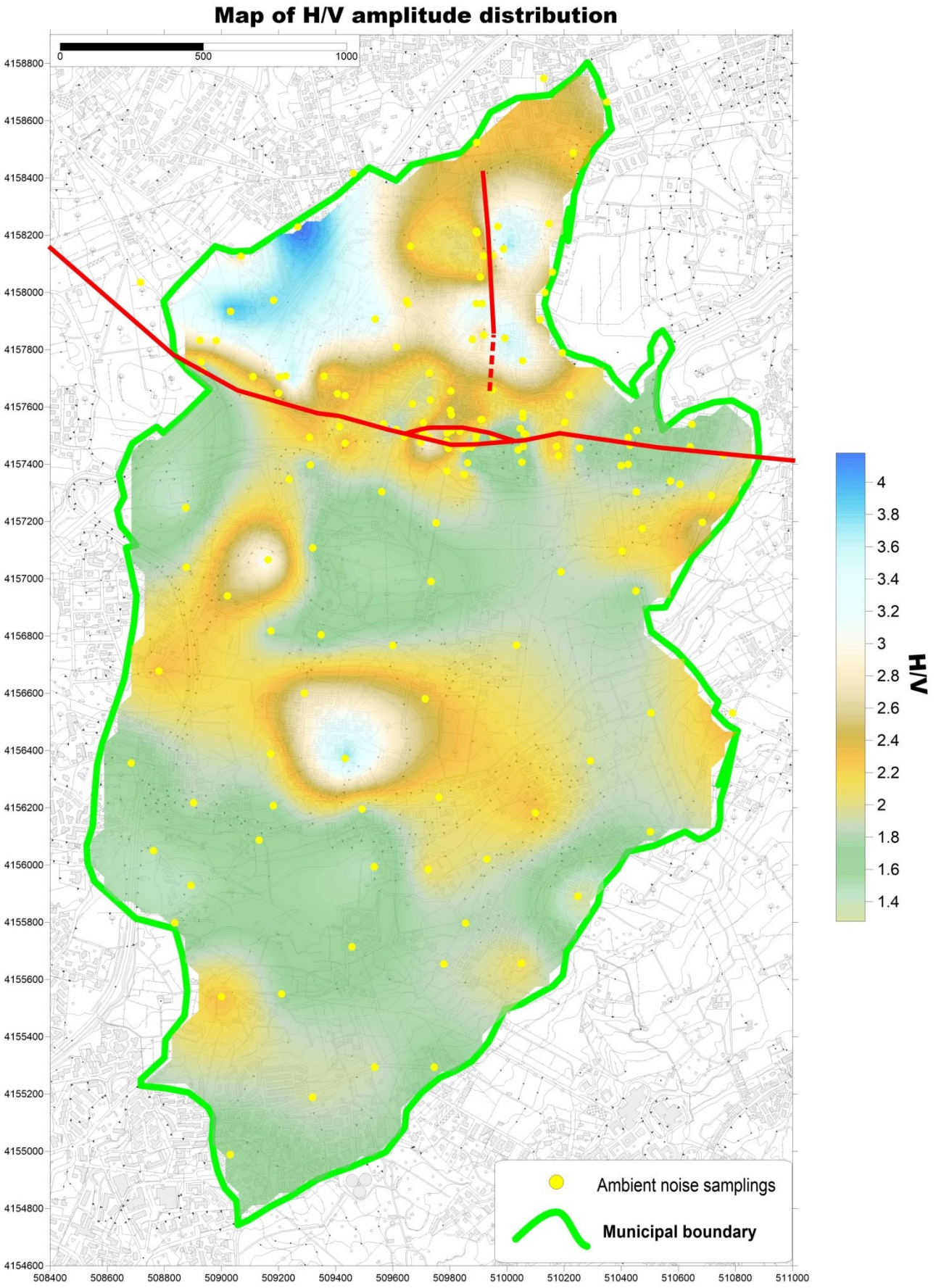

Fig. 6.17. Map of HV amplitude distribution

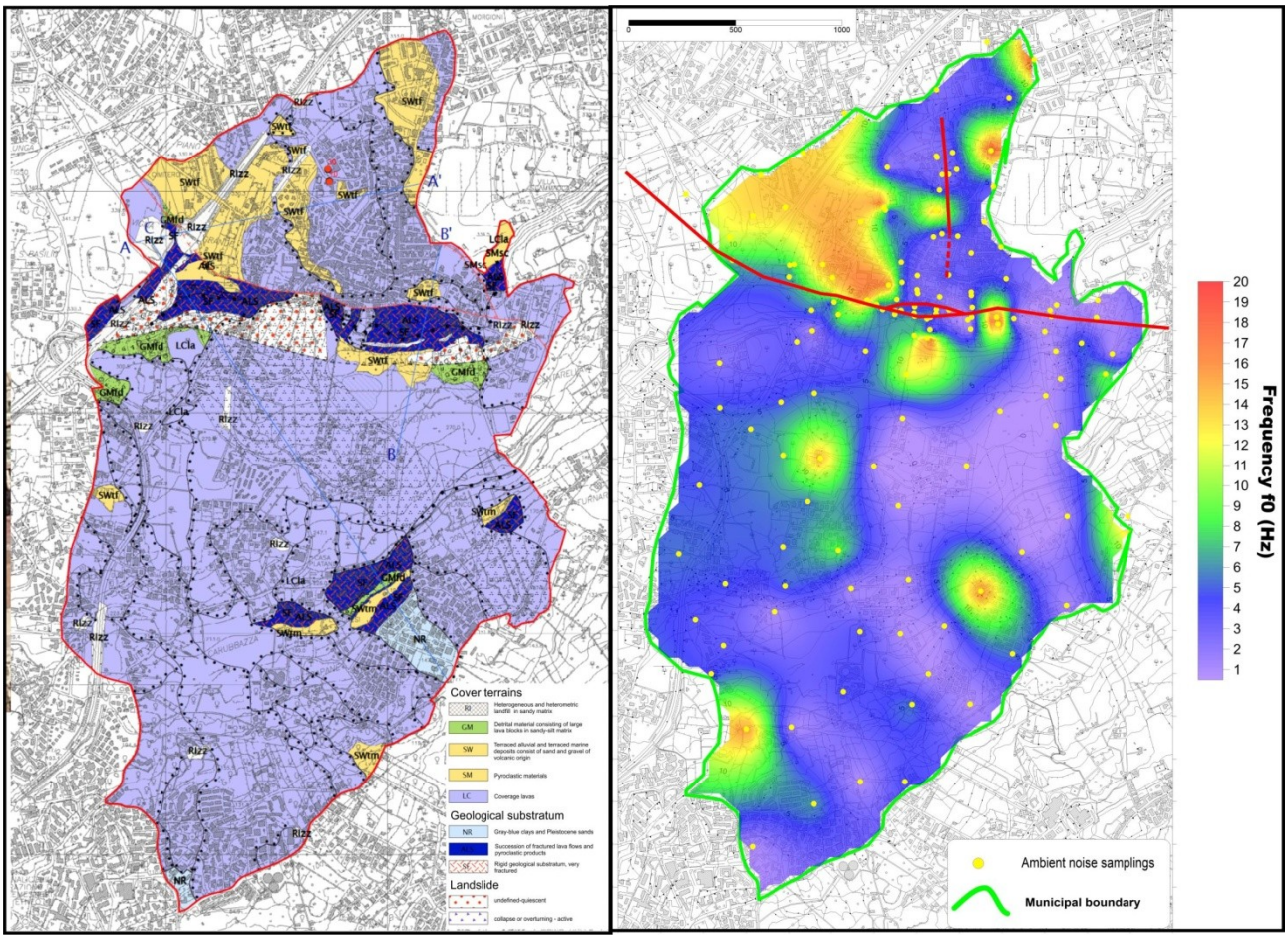

Fig. 6.18. Comparison between geological-technical map, obtained from first level microzonation study in San Gregorio Municipality (on the left), and the map of the resonance frequencies distribution (on the right)

6.1.4. DHVPOR analysis

The HVSR technique is also useful to obtain information on the directional characteristics of the seismic response. In particular, the analysis of azimuthal variations of the H/V spectral ratios can reveal the presence and the orientation of directional resonance phenomena (Del Gaudio et al., 2008).

In order to assess the possible presence of a systematic preferential orientation of the resonance peaks observed in the H/V spectra acquired near the fault segment which extends in N-S direction, the data obtained by such processing were further elaborated with the DHVPOR (Directional H/V Peak Occurrence Rates) technique (Del Gaudio et al., 2013). The DHVPOR analysis among the recording time windows enables highlighting a systematic direction in site response, through the observation of a high percentage of peaks H/V around a given frequency and a given azimuth.

The study of the occurrence rates allows detecting, with a good statistical significance level, the directional effects characterizing the survey area, closely linked to the geolithological and structural properties of the subsurface. The DHVPOR analysis was performed using a specifically designed Excel spreadsheet (Fig. 6.19). The average values of the H/V spectral ratios for azimuthal intervals of 10° and frequency intervals of 0.5 Hz were calculated. The analysis only took the significant H/V peaks into account, namely those having an H/V ratio average value greater than 2 and an H/V maximum and minimum ratio observed at the same frequency (in an orthogonal direction— with divergence no more than 30°) at least equal to 1.5.

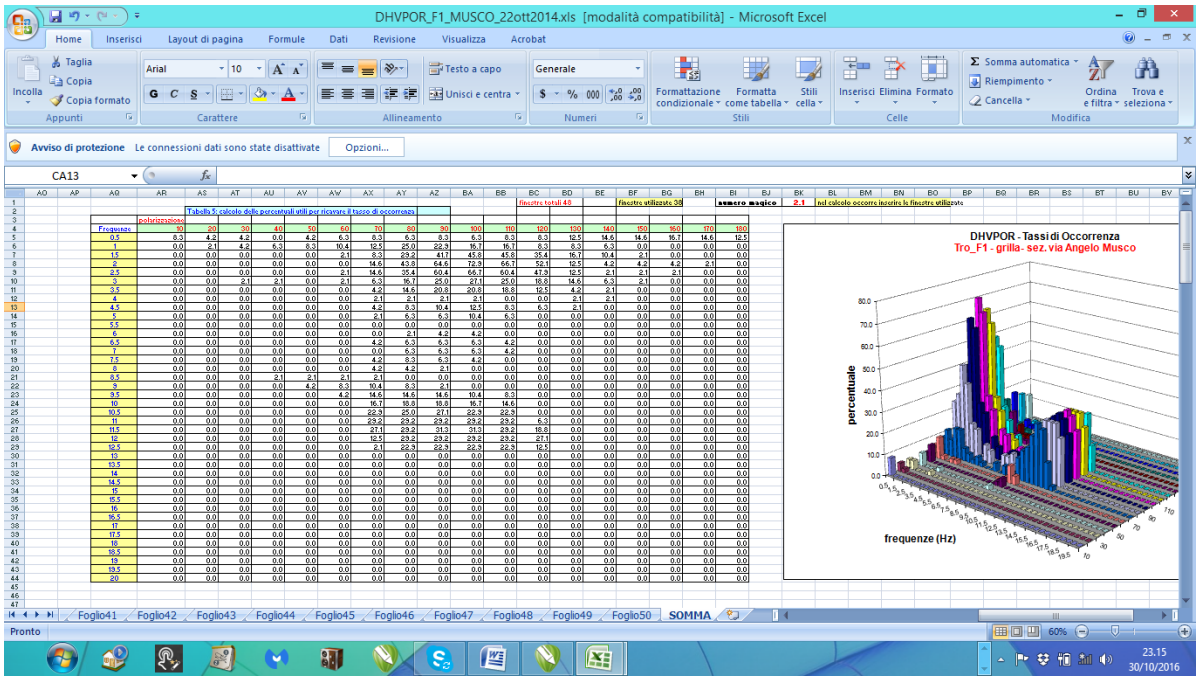

Fig. 6.19. Screenshot of the Excel spreadsheet specifically designed to perform the DHVPOR analysis

It is necessary to consider, that sometimes, the noise recordings are characterized by weakly polarized signals that do not represent the resonance properties of site. To better highlight the presence of amplification peaks at the major resonance frequencies, even when these maxima are not "visible" in the average H/V calculated over the whole recording, the average of H/V ratios is limited only to the azimuth-frequency combinations associated with significant directional peaks.

The occurrence rates were evaluated in the frequency range 0.5–20 Hz, highlighting for each analyzed recording the time windows percentages characterized by directional peaks, with a similar orientation, indicative of the site resonance properties; these percentages were plotted on 3D histograms (Fig. 6.20) where the vertical bars height, for each frequency–azimuth combination, is proportional to the occurrence rate percentage. The histograms clearly show that ambient noise is affected by a significant horizontal polarization near the studied fault segment, indeed, the percentage of occurrence rate in some case reaches 80% .

Comparing the orientation trend of fractures, roughly N-S, determined by the field survey, with the rose diagrams, that show the orientation of directional

resonance phenomena, it is possible to observe that the latter is roughly orthogonal to the average orientation of fractures (Fig. 6.20).

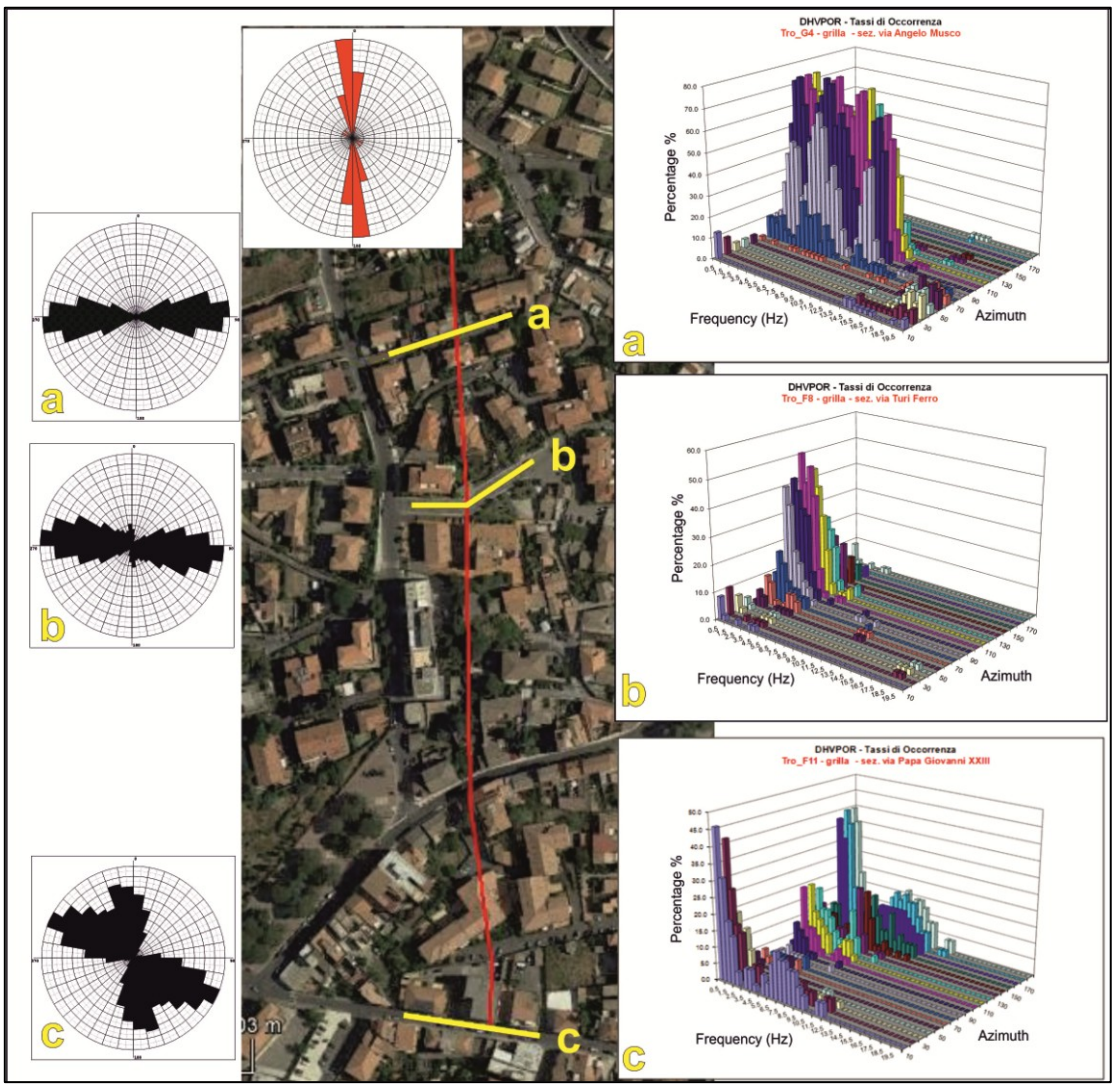

Fig. 6.20. Rose diagrams on the left show the orientation of directional resonance phenomenon for one of the acquisitions performed along the three arrays carried out orthogonally to the SGNF fault segment; on the right are show the 3D histograms obtained by the DHVPOR analysis related to the same acquisitions; the box on the top shows the orientation trend of fractures network detected by the structural survey

6.1.5. Impedance contrast sections

As previously discussed in paragraph 2.2, the HVSR method has been widely used, in the recent years, to obtain information on the subsoil stratigraphy. For this purpose it is necessary to know the velocity variations with depth. Assuming that the waves velocity increases with depth, as a consequence of the lithostatic load, the function

$$V_s(Z) = V_0(1+Z)^{\alpha} \quad \text{(see paragraph 2.2)} \quad (2)$$

shows the relationship between depth and shear waves velocity variations. In order to retrieve Vs-depth profiles, determined experimentally it was carried out a systematic search for San Gregorio area, both in the archives of the civil engineering office and contacting freelance geologists operating in the area, of the surveys previously performed within the study area (Fig. 6.21). The velocity profile obtained from the ReMi survey performed in the San Gregorio downtown, which has been discussed in paragraph 6.1.2.3, was also taken into account. A further Vs-depth profile was obtained through the conjunct fit (Castellaro and Mulargia 2009) made between a dispersion curve, obtained from a MASW survey performed in the western portion of the urban area, and a H/V spectrum relating to one of the noise recordings acquired near the alignment on the same day (see Appendix A).

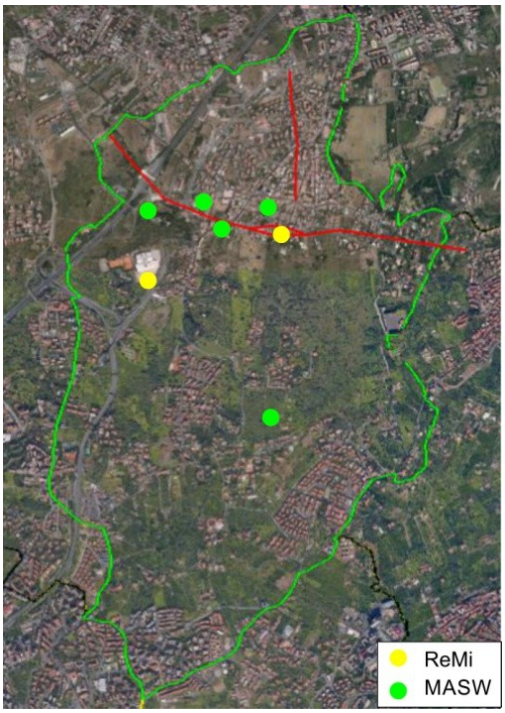

Fig. 6.21. Location of ReMi and MASW surveys in San Gregorio di Catania area

To perform the fit of the Vs-depth profiles found, the gnuplot free software (Version 4.6 - www.gnuplot.info) was used. The process starts after setting two parameters V_0 and α; through various iterations, the software modifies these parameters, until it finds those for which there is the minimum error between the experimental Vs - depth profiles and curve fitting these data (see Appendix B; Fig. 6.22).

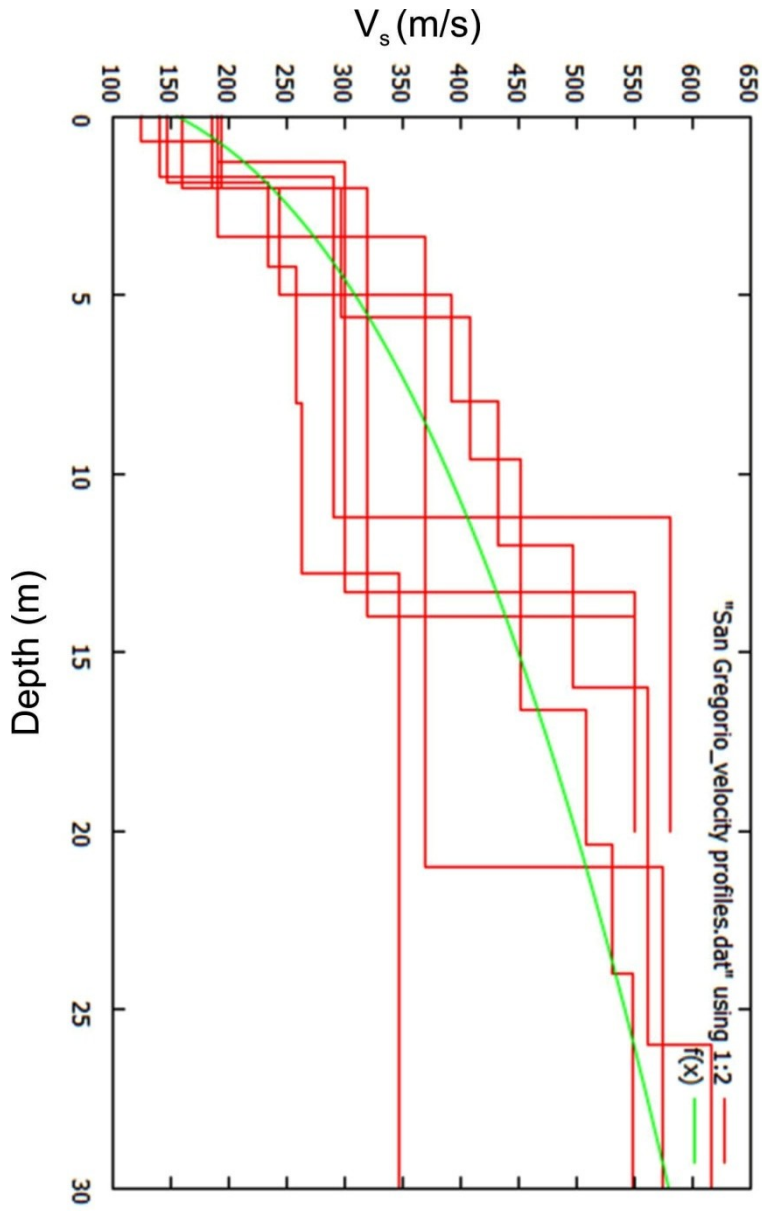

Fig. 6.22. Velocity-depth profiles: the green curve represents the function $V_s(Z) = V_0(1+Z)^{\alpha}$ that has the minimum misfit with the data of the Vs–depth profiles

The V_0 and α values, which provide a minimum misfit between the function (2) and the Vs–depth profiles, are equal to V_0 = 155.517 m/s and α= 0.383. Substituted in the formula of Ibs-von Seht and Wohlenberg (1999) (Eq. 3 - paragraph 2.2), these values enabled conversion of the frequency values, present in the spectra, into depth values, thus allowing to map the distribution of amplitude values of the H/V spectral ratio in the subsoil.

From the ambient noise records, 23 two-dimensional impedance contrast sections were reconstructed, of which 19 were performed orthogonal to the fault

traces detected by the structural survey (Fig. 6.11). These sections show the distribution of the amplitude values of the H/V spectral ratio in the subsoil, allowing distinguishing the main horizontal and vertical discontinuities.

The x-axis in these sections shows the distance between the measuring points, with spacing of 5 m, and the y-axis the depth; variations in the amplitude value of the H/V spectral ratio are represented by colors associated with a chromatic scale.

Three particularly significant impedance contrast sections (Fig. 6.23), performed orthogonally to the new fault segment (SGNF), that is approximately in a N-S direction within the town of San Gregorio di Catania, are shown in Fig. 6.23 as examples.

Observing the three sections is possible to note how the main impedance contrast, associated to the resonance peak observable in the spectra, is interrupted in correspondence of the passage point of the fault segment. It is noteworthy that in the 6.23 a and 6.23b sections this impedance contrast is dislocated probably due to the normal kinematics characterizing this fault segment.

The estimate of V_0 and α parameters, obtained for the San Gregorio Municipality, was also used to get a map that provides an indication on the seismic bedrock depth (Fig. 6.24).

The resonance frequency value, identified in the spectra relating to 161 ambient noise recordings, has been converted to depth using the following formula:

$$h = \left[\frac{155.517(1-0.383)}{4f_r} + 1\right]^{\frac{1}{(1-0.383)}} - 1$$

The contouring of obtained depth data was made using the kriging interpolation method included in Golden Software Surfer(R).

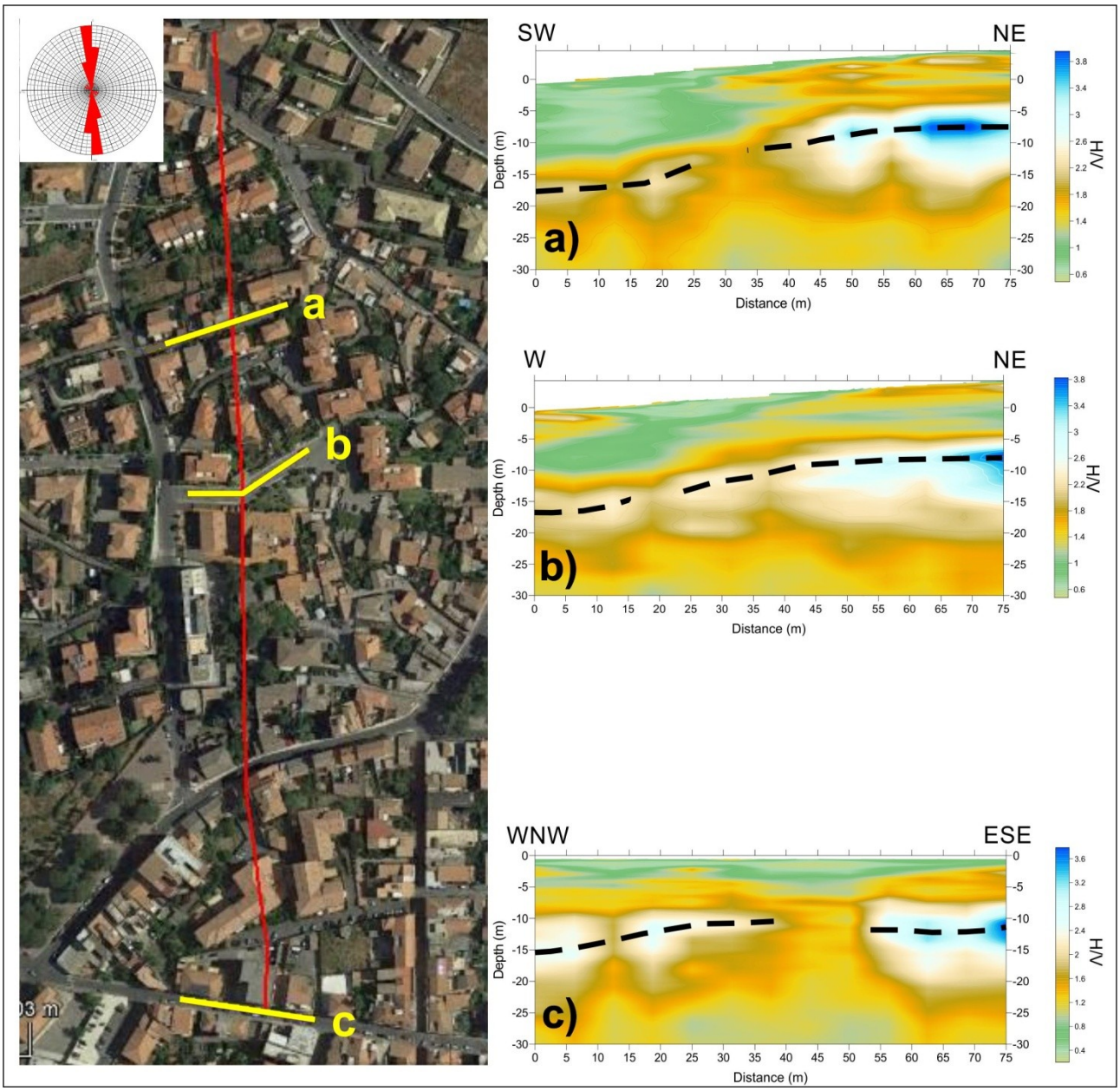

Fig. 6.23. Examples of impedance contrast sections carried out orthogonally to the SGNF fault segment

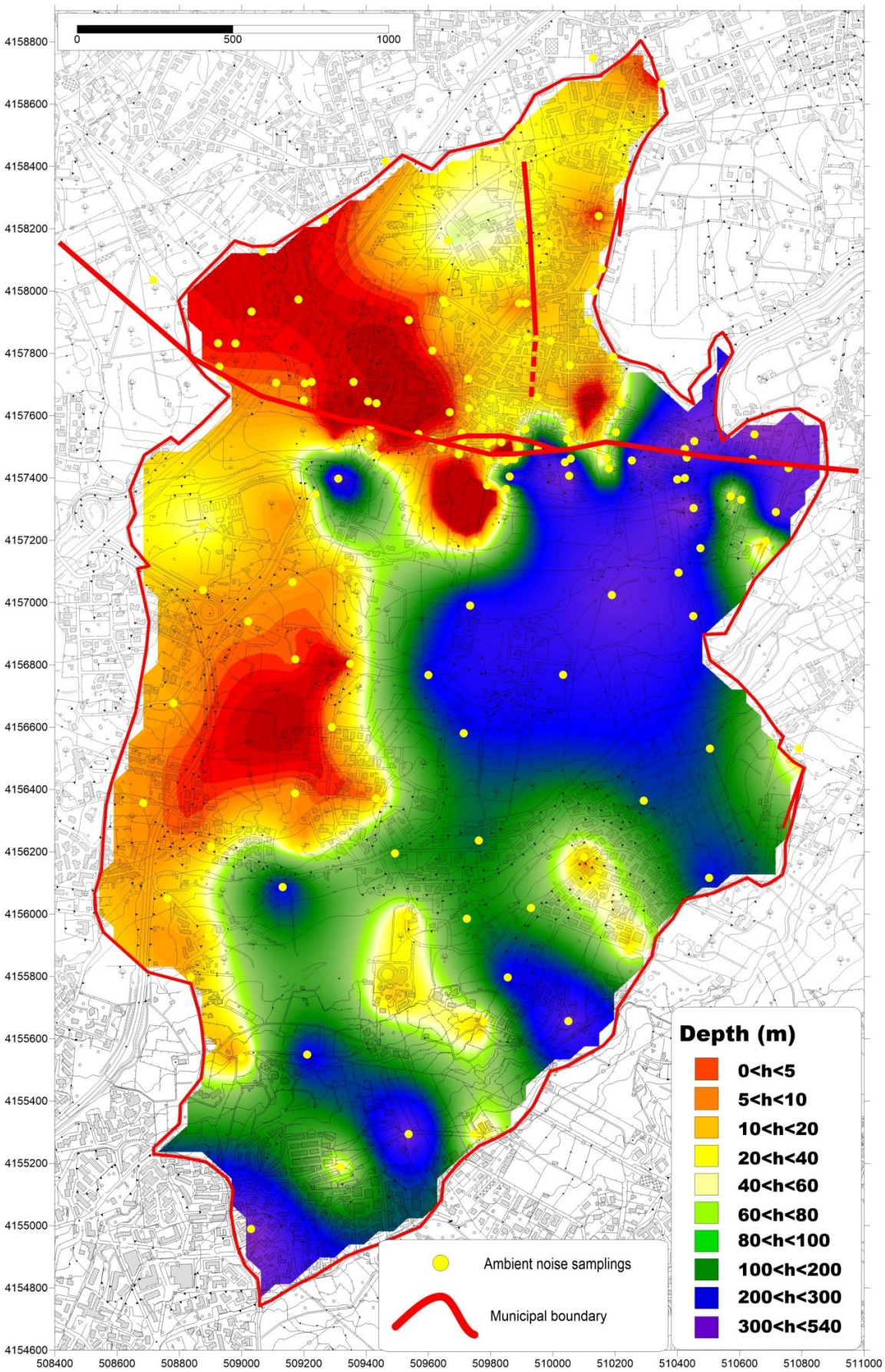

Fig. 6.24. Depth map of the interface that causes the resonance peaks

6.1.6. Topographic and geodetic surveys: monitoring network design

In order to analyze the deformation on surface and characterize the kinematic behavior of area affected by the fault segments, kinematik monitoring with geodetic and topographic survey has been designed and realized across the active deformation zones of the fault system, with an integrated system of instruments, that includes GNSS receivers and Total Station. This method allows to assess relative displacements between benchmarks georeferenced to a geographical and/or kilometric reference system.

The instruments used for the topographic and geodetic surveys consist of two dual frequency (L1+L2) satellite receivers TOPCON HiPerV (Fig. 6.25a) and a Total Station Topcon Ds-103RC (Fig. 6.25b); the latter allows to obtain distance measurement with a precision of 0.5 mm on 1000 m without the aid of reflectors prisms, the measuring range increases up to 10 km with the use of reflectors prisms.

The accuracy and precision of the measurements can be affected by weather conditions such as humidity and temperature, which affect the refraction index, increasing the average error. The measurements performed through GNSS satellite receiver have an error, on the horizontal distance, of 5 mm on 1000 m.

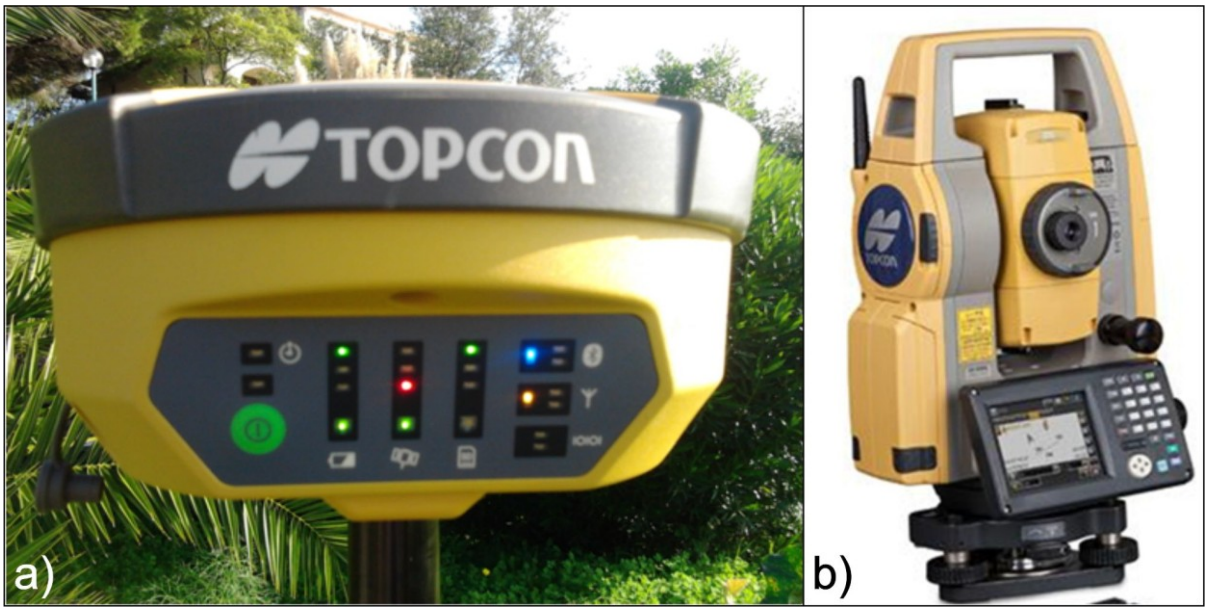

Fig. 6.25. a) Satellite receivers TOPCON HiPerV; b) Total Station Topcon Ds-103RC

The monitoring network develops within the urban area of San Gregorio di Catania village (Fig. 6.26), it was designed across the deformation zone. The installation of the monitoring network was performed by the Municipality of San Gregorio di Catania as a result of the agreement with the University of Catania.

The location of permanent monitoring points was chosen taking into account:

- the geological and structural characteristics of the area;
- the visibility between the measurement points;
- the space/time stability of monitoring points: were chosen non-deformable and stable points, constituted for example by outcrops of not fractured volcanic rock (which fall in areas not subject to future urbanization plans or to changes of intended use) or buildings with limited elevation, that do not show instability effects or structural imperfections;
- the absence of physical barriers above the positioning point of GPS antenna;
- the incidence angle in the collimation point: as a function of this parameter has been chosen whether to use target (for incidence angles ≈ 90°) or reflectors prisms (for incidence angles less than 90°);
- to obtain a high degree of precision and considering the available instruments, the distance between points, was chosen to use baselines less than 500 m.

The monitoring points are divided in permanent points of main monitoring, permanent points of secondary monitoring and points outside to the vertices of the polygonal.

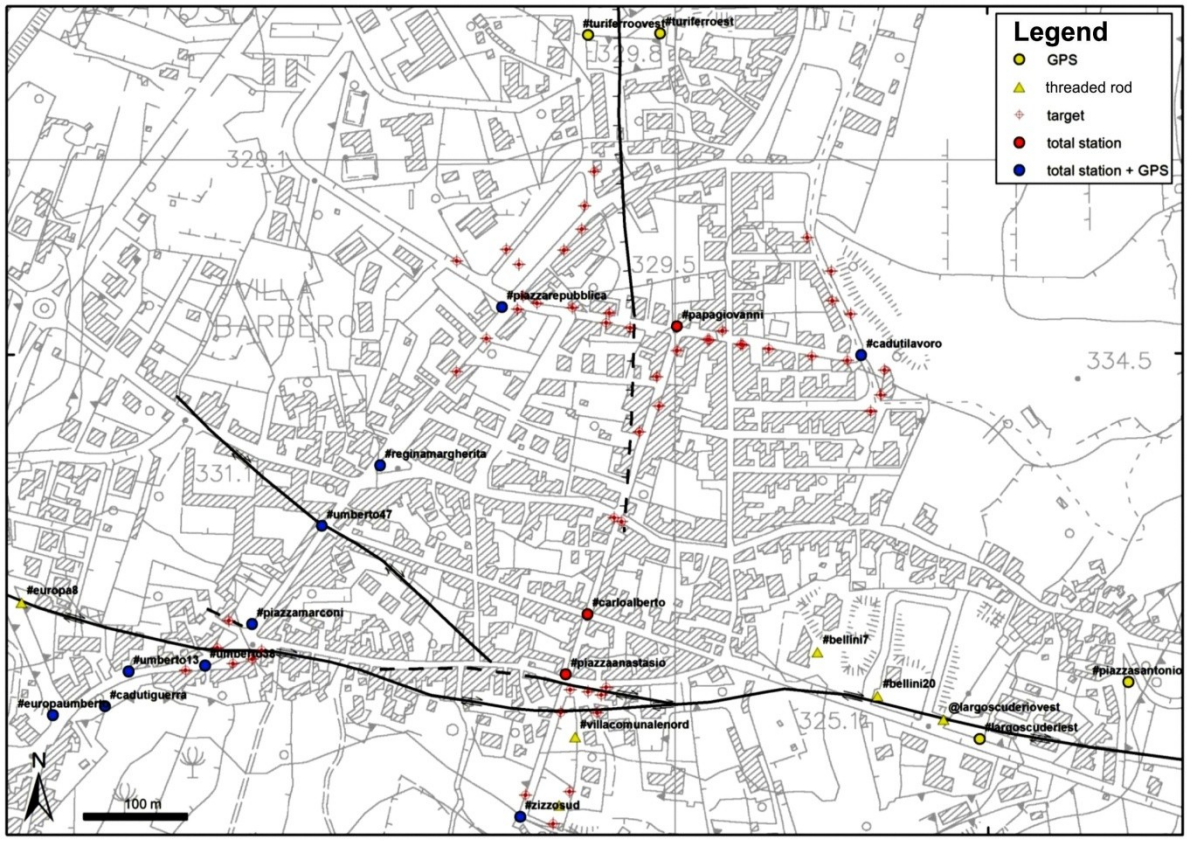

Fig. 6.26. Geodetic-topographic monitoring network developed within the urban area of San Gregorio di Catania

At main monitoring points were realized manholes to place the coupling system between the pillar (for the instrument holder-Fig. 6.27a,b,c) and the soil; this coupling system consists of a stainless steel bushing (Fig. 6.27d) with an error tolerance on the measurement of 0.1 mm.

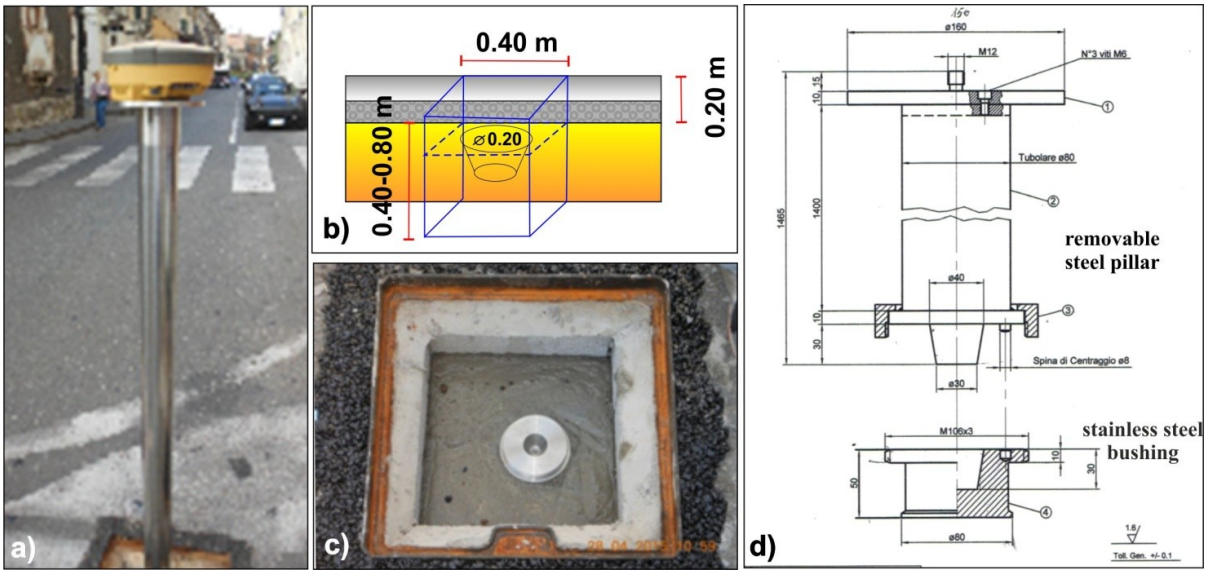

Fig. 6.27. a) One of the measuring points, can observed the pillar and the GNSS satellite receiver; b) project of manhole, to place the coupling system between the pillar and the soil; c) one of the 17 manholes realized, in urban area of San Gregorio di Catania; d) project of coupling system and pillar

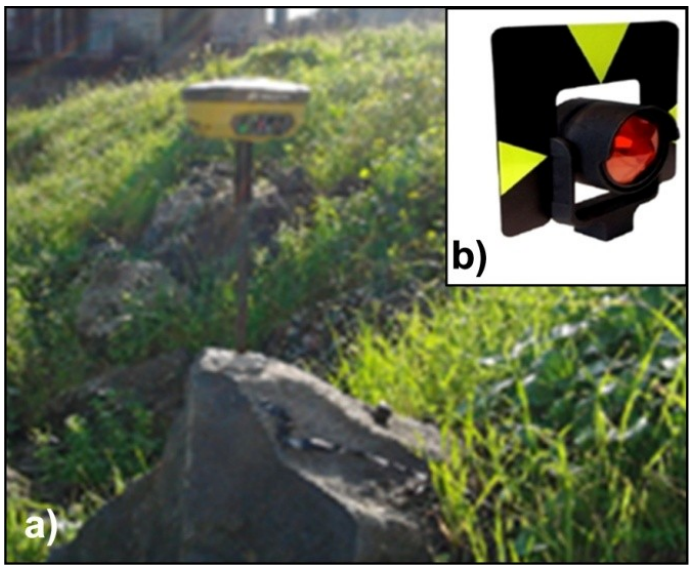

Fig. 6.28. a) Permanent point of secondary monitoring point constituted by threaded rod anchored to the rock; b) reflector prism

The permanent points of secondary monitoring consist of threaded rods anchored to the rock outcropping or to stable structures; it is possible to screw the instruments or the reflectors prisms to these threaded rods (Fig. 6.28 a,b).

The points outside at the vertices of the polygonal are materialized by reflective targets placed on buildings and road artifacts (Fig. 6.29).

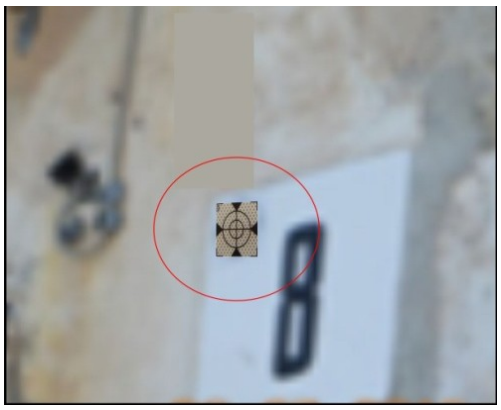

Fig. 6.29. Reflective target placed on a wall of building

The main benchmarks were located outside and sufficiently far away from the deformation zone: they are part of the main network which defines the local coordinate system, all other secondary and detail networks are connecting to it.

6.1.6.1 GNSS measures

Four GNSS measurement campaigns were carried out between June 2015 and April 2016; in the calendar of measurement campaigns are reported (Table): survey date; reference number of monitoring station; day of the year (DOY); week; day of the week (GPS weekday); receiver type (B-base, R-rover); raw data name (.tps); Rinex file name; GPS and GLONASS precise final orbits; recording time.

#	FIELD SURVEY	SURVEY DATE	ID STATION	DOY	WEEK	GPS WEEKDAY	BASE 54/ ROVER 44	TPS FILE NAME	RINEX FILE NAME	GPS FINAL ORBITS	GLONASS FINAL ORBITS	h.reg
1	giu-15	150616	02	167	1849	2	B	150616_.tps	02sg167e.15o	igs18492	igl18492	4.30
2			01				R	440616g.tps	#			#
3			03				R	440616g.tps	#			#
4			04				R	440616g.tps	#			#
5			05				R	440616g.tps	#			#
6		150617	07	168	1849	3	B	log0617fa.tps	07sg168e15o	igs18493	igl18493	4.30
7			06				R	440617f.tps	#			#
8			08				R	440617f.tps	#			#
9		150618	10	169	1849	4	B	log0618g.tps	10sg169e.15o	igs18494	igl18494	4.15
10		150623	22	174	1850	2	B	150623_.tps	22sg174e.15o	igs18502	igl18502	5.30
11		150624	15	175	1850	3	B	log0624h.tps	15sg175e.15o	igs18503	igl18503	4.00
12			16				R	440624j.tps	#			#
13			14				R	440624j.tps	#			#
14		150625	19	176	1850	4	B	log0625ga.tps	19sg176e.15o	igs18504	igl18504	4.00
15			18				R	440625g.tps	#			#
16			20				R	440625g.tps	#			#
17			21				R	440625g.tps	#			#
1	ott/nov-15	150914	02	257	1862	1	B	log0914g.tps	02sg257e.15o	igs18621	igl18621	4.30
2			08				R	440914g.tps	08sg257e.15o			4.30
3		151029	09	302	1868	4	B	log1029i.tps	09sg302e.15o	igs18684	igl18684	5.30
4			10				R	441029i.tps	10sg302e.15o			5.30
5		151030	05	303	1868	5	B	log1030i.tps	05sg303e.15o	igs18685	igl18685	5.30
6			04				R	441030ia.tps	04sg303e.15o			6.00
7		151105	16	309	1869	4	B	log1105h.tps	16sg309e.15o	igs18694	igl18694	5.45
8		151106	19	310	1869	5	B	log1106h.tps	19sg310e.15o	igs18695	igl18695	6.00
9			18				R	441106h.tps	18sg310e.15o			5.00
10		151110	03	314	1870	2	B	log1110ha.tps	03sg314e.15o	igs18702	1gl18702	6.00
11			01				R	441110ha.tps	01sg314e.15o			5.30
12		151111	21	315	1870	3	B	log1111h.tps	21sg315e.15o	igs18703	igl18703	6.00
13			20				R	441111h.tps	20sg315e.15o			5.45
14		151112	15	316	1870	4	B	log1112i.tps	15sg316e.15o	igs18704	igl18704	6.00
15			14				R	441112i.tps	14sg316e.15o			5.45
16		151113	07	317	1870	5	B	log1113g.tps	07sg317e.15o	igs18705	igl18705	6.00
17		151114	22	318	1870	6	B	log1114g.tps	22sg318e.15o	igs18706	igl18706	6.00
1	gen-16	160114	02	14	1879	4	B	log0114g.tps	02sg14e.16o	igs18794	igl18794	6.00
2			03				R	440114g.tps	03sg14e.16o			5.45
3		160115	10	15	1879	5	B	log0115h.tps	10sg15e.16o	igs18795	igl18795	6.00
4			09				R	440115h.tps	09sg15e.16o			5.45
5		160116	19	16	1879	6	B	log0116i.tps	19sg16e.16o	igs18796	igl18796	6.00
6			21				R	440116i.tps	21sg16e.16o			5.45
7		160119	22	19	1880	2	B	log0119g.tps	22sg19e.16o	igs18802	igl18802	6.00
8		160120	15	20	1880	3	B	log0120h.tps	15sg20e.16o	igs18803	igl18803	6.00
9			16				R	440120h.tps	16sg20e.16o			5.45
10		160121	7	21	1880	4	B	log0121g.tps	07sg21e.16o	igs18804	igl18804	6.00
1	mar/apr-16	160321	02	81	1889	1	B	log0321ia.tps	02sg81e.16o	igs18891	igl18891	5.15
2			03				R	440321i.tps	03sg81e.16o			6.00
3		160322	22	82	1889	2	B	log0322g.tps	22sg82e.16o	igs18892	igl18892	5.45
4		160323	22	83	1889	3	B	log0323g.tps	22sg83e.16o	igs18893	igl18893	5.30
5		160324	02	84	1889	4	B	log0324g.tps	02sg84e.16o	igs18894	igl18894	5.45
6			03				R	440324g.tps	03sg84e.16o			6.00
7		160325	19	85	1889	5	B	log0325f.tps	19sg85e.16o	igs18895	igl18895	5.30
8			21				R	440325f.tps	21sg85e.16o			5.45
9		160326	19	86	1889	6	B	log0326h.tps	19sg86e.16o	igs18896	igl18896	5.45
10			21				R	440326h.tps	21sg86e.16o			6.00
11		160329	09	89	1890	2	R	440329g.tps	09sg89e.16o	igs18902	igl18902	6.00
12			10				B	log0329f.tps	10sg89e.16o			5.45
13		160402	09	93	1890	6	R	440402e.tps	09sg93e.16o	igs18906	igl18906	6.00
14			10				B	log0402e.tps	10sg93e.16o			6.00
15		160404	15	95	1891	1	R	440404g.tps	15sg95e.16o	igs18911	igl18911	6.00
16			16				B	log0404g.tps	16sg95e.16o			5.45
17		160406	07	97	1891	3	R	440406e.tps	07sg97e.16o	igs18913	igl18913	6.00
18		160407	15	98	1891	4	R	440407f.tps	15sg98e.16o	igs18914	igl18914	6.00
19			16				B	log0407f.tps	16sg98e.16o			6.00
20		160408	07	99	1891	5	R	440408h.tps	07sg99e.16o	igs18915	igl18915	6.00
21		160512	08	133	1896	4	B	log0512f.tps	08sg133e.16o	igs18964	igl18964	6.00
22		160513	08	134	1896	5	B	log0513f.tps	08sg134e.16o	igs18965	igl18965	6.00

Table 6.3. Calendar of San Gregorio di Catania geodetic measurement campaigns

At each monitoring point the signal was acquired for a time ranging from four to six hours; the raw data acquired (.tps) was converted in Rinex (Receiver Indipendent

Exchange Format) files. The RINEX format, created to facilitate the exchange of data, is composed of two file types: the navigation data file (.nav) containing parameters for satellite orbits calculation; the observation file (.obs) containing the code and phase informations, and the header information concerning receiver and antenna type, station coordinates, antenna instrument height, observations type. The Rinex files are named according to the convention with a nomenclature of kind "nomedoys.yyx", where "nome" is the identification name of measure site, "doy" is the day of the year, "s" is the session number, "yy" is the registration year, "x" identifies the file type, can be "o" (observation) or "n" (navigation).

For the data post-processing, two types of software were used: Magnet™ Tools and GAMIT/GLOBK (supplied by INGV, Catania section). The Magnet Tools software provides a graphical and planar representation of data acquired during the geodetic-topographic monitoring.

Available GNSS raw observations, were analysed using the GAMIT/GLOBK software (Herring et al., 2010) and adopting the methodology described in Gonzalez and Palano (2014). This procedure is divided in three different phases for processing and modeling of data (Herring et al., 2006). In the first phase the software uses linear combinations of iono-free (correct of the error due to the refraction of the signal when it passes through the ionosphere) observable (measured data) double difference, L1 and L2, to generate weighted least squares solutions for each daily session (Bock et al., 1986; Schaffrin and Bock, 1988; Dong and Bock, 1989). An advantage from the double difference is that during processing of the recorded data, by comparing the observed amount with that predicted, with an automatic algorithm (AUT-CLN; Herring, 2006, King and Bock, 2000), can be identified and subsequently removed the phase jumps in the recorded data, caused by the loss of the satellite signal by the receiver (cycle slip).

Precise ephemerides and absolute antenna phase centres models provided by the IGS (www.igs.org) were used. In addition, the Saastamoinen (1972) atmospheric zenith delay models, coupled with the Global Mapping Functions (Böhm et al.,

2006) for the neutral atmosphere have been adopted. To improve the overall configuration of the network and to tie the regional measurements to an external global reference frame, data coming from the continuous GPS network operating on Mt. Etna volcano and from 8 continuously operating IGS stations (Table 6.4), were introduced in the processing.

Network	Station	City
IGS	GENO	Genova (Italy)
	GRAS	Caussols (France)
	GRAZ	Graz (Austria)
	JOZE	Jozefoslaw (Poland)
	MATE	Matera (Italy)
	MEDI	Medicina (Italy)
	NOT1	Noto (Italy)
	ZIMM	Zimmerwald (Switzerland)
ETN@NET	EBAG	Giarre
	ELAC	Isola Lachea
	ENIC	Nicolosi
	EPMN	Piedimonte E.
	EPOZ	Pozzillo
	ESAL	S. Alfio

Table 6.4. IGS and ETN@NET stations considered in the processing of GNSS data

This first phase provides an estimate of daily loose-constrain solutions (h-files) containing the stations coordinates, the orbits, the atmospheric delays, with the associated variance-covariance matrices. In the second phase the daily loose-constrain solutions were processed with GLRED modulus (in GLOBK software) in order to generate combined daily solutions of the unconstrained network. Subsequently, the daily solutions were placed in the Etn@ref reference system (Palano et al., 2010), using a Helmert transformation (estimation of 3 rotation parameters, 3 translation parameters and of 1 scale factor), in order to obtain both the time series of North, East, and Up components of each station, and the velocity field.

Etn@ref is a geodetic reference frame for Mt. Etna GPS networks, used to remove the contribution of regional deformation and highlight the contribution of local deformation (Palano et al., 2010).

Finally, with the GLORG modulus (in GLOBK software), the daily solutions, cleaned by offsets and outliers, were combined in order to estimate the deformation field (velocity- mm/a) with respect to the Etn@ref reference system.

6.1.6.2 Consideration on GNSS measurement campaigns and results

The first measurement campaign (June 2015) was performed in kinematic mode: a satellite receiver was used with basic function (1143-11554) fixed to a station for the whole survey duration and a rover receiver (1143-11544) was displaced in correspondence of several benchmarks, at constant time intervals. The data collected by the rover receiver were not processed due to technical problems probably related to malfunction of the acquisition software, so were processed only the data of the base receiver.

The other three measurement campaigns were performed in static mode, maintaining the receiver fixed on each station for 5-6 hours. These recordings were useful to test the instrumental response; the latest survey was the most rigorous, have been carried out two recordings of six hours each on two different days, in order to get a better estimate and reduce the error.

The velocity diagrams for the three components were obtained using the GLRED/ ENSUM software; in this software each daily data is processed separately and the ENSUM program simply does a linear fit of one component time series for each station. Observing the velocity diagrams for the three components N, E and Up, relating to each stations (Fig. 6.30) it is possible to note that in some of the stations for the two measurement days of the fourth measurement campaign were detected values quite different from each other; this is probably related with an increased noise in the acquisition linked to the presence of reflective surfaces (sources of errors from multipath), or to the presence of high vegetation (errors due to the poor visibility of the satellites). Between the two values obtained from the fourth measurement campaign, the velocity straight line recorded in the period under investigation, intercepts the value that best fits to its trend.

In order to have realistic measurements on the vertical component, time series of at least five years must be considered. For this reason, in relation to the limited number of measurements carried up to this moment, the data relative to the vertical component are not considered.

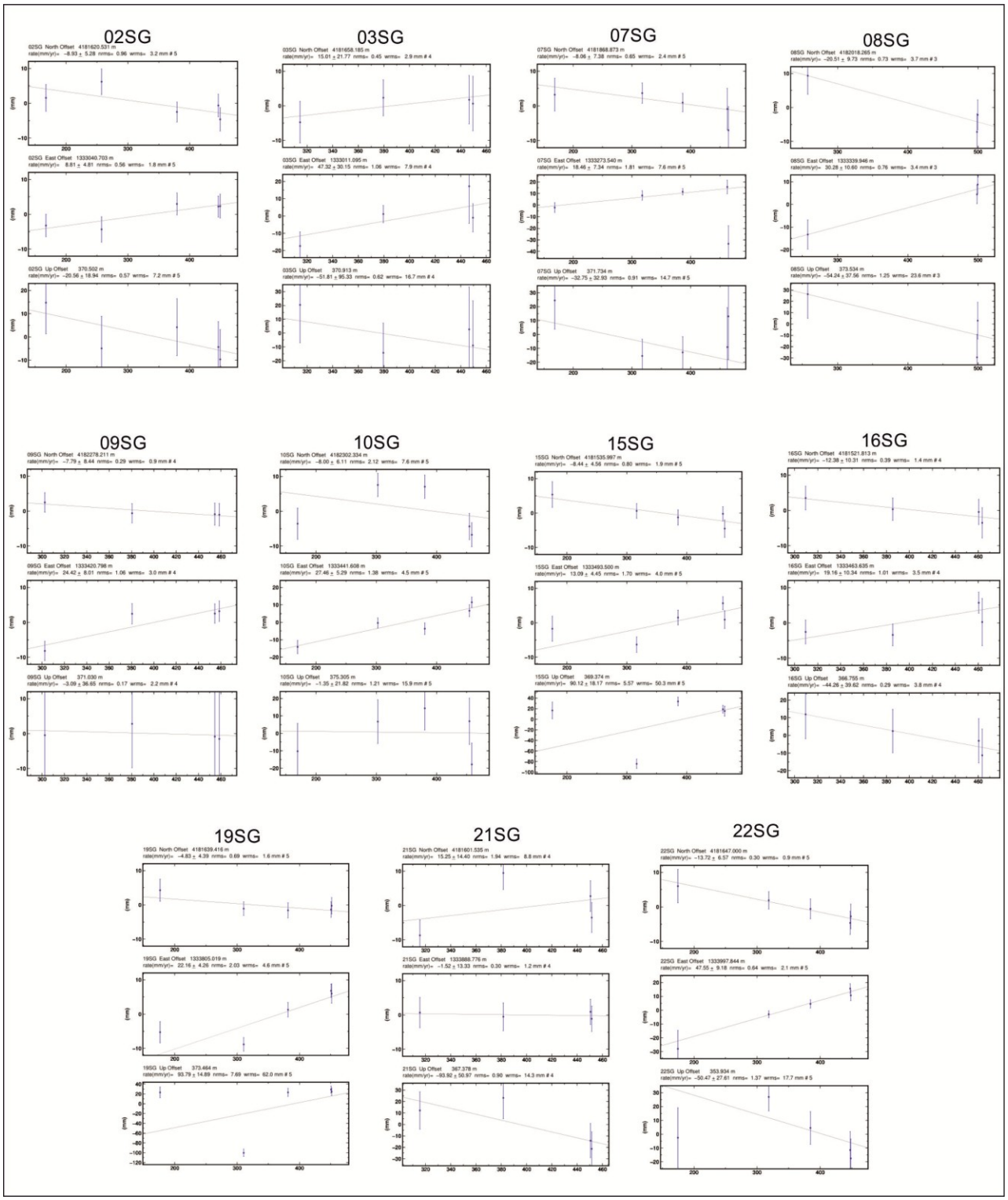

Fig. 6.30. Velocity diagrams for the three components N, E and Up, relating to the 11 measuring stations of the San Gregorio di Catania monitoring network. Observing a single velocity diagram: every point correspond to the value relating to a single measure campaign with associated the error bar, the straight line represent the velocity trend recorded in the period under investigation, it intercepts the value that best fits to its trend

The estimated velocities were further processed with the GLOBEK software; in this software, unlike the GRED software, the velocity field is generated calculating all the time corrections and the corrections between sites. Indeed, the rate values for

the different stations calculated with the GLOBK software, and the relative errors for the three components (Table 6.5), are different from those calculated with the GLRED/ENSUM software (Fig. 6.30). The possibility that the two processing types provide or not the same result is related to the data nature.

Site	Long	Lat	N vel (mm/yr)	N err (mm/yr)	E vel (mm/yr)	E err (mm/yr)	H vel (mm/yr)	H err (mm/yr)	Vettore	Angolo
02SG	15,10678	37,56414	-8,93	5,28	8,81	4,81	-20,56	18,94	12,54436	135
07SG	15,11	37,56637	-4,89	8,57	19,14	8,34	-54,73	37,99	19,75479	104
08SG	15,11133	37,56771	-20,51	9,72	30,27	10,6	-54,23	37,56	36,56409	124
09SG	15,11225	37,57004	-5,9	9,63	17,74	9,21	-7,83	41,42	18,69539	108
10SG	15,11306	37,57026	8,03	8,2	30,48	7,01	19	29,32	31,52001	75
15SG	15,11191	37,56338	-11,21	7,34	1,09	7,2	-59,75	30,83	11,26287	174
16SG	15,11157	37,56325	-11,96	10,88	23,31	10,94	-44,3	40,83	26,19919	117
19SG	15,11544	37,56431	-10,45	6,56	7,27	6,28	-87,46	22,75	12,7301	145
21SG	15,11639	37,56397	15,26	14,4	-1,5	13,33	-93,91	50,97	15,33354	355
22SG	15,11821	37,56437	-13,4	7,59	50,85	12,59	-25,8	32,45	52,58595	104
CTAC	15,07712	37,53228	-9,05	0,62	-6,2	0,6	0,83	2,04		
EBAG	15,161	37,70235	-11,02	0,67	21,54	2,4	-15,29	2,89		
EIIV	15,08208	37,5136	-3,48	0,59	1,13	0,47	-1,49	1,53		
ELAC	15,16641	37,56131	-64,82	8,61	186,87	11,62	263,73	47,4		
ENIC	15,01965	37,61386	-8,1	0,64	5,92	0,7	-4,82	2,33		
EPMN	15,17742	37,82063	-0,29	0,66	3,9	0,92	2,16	1,52		
EPOZ	15,18854	37,67193	-14,02	0,99	34,9	3,05	-7,3	1,6		
ERIP	15,1976	37,72844	-9,74	1,34	31,24	2,04	-5,51	2,05		
ESAL	15,13453	37,75509	-14,29	0,88	23,41	1,63	-6,71	2,58		
ESLA	14,97433	37,69342	-16,66	0,56	3,07	1,18	-1,21	3,25		
MASC	15,19575	37,75897	-12,25	0,95	31,41	1,15	-20,44	2,07		

Table 6.5. The table states velocity vector values for each component (N, E and H) and the associate error relating to the 11 measurement stations located in San Gregorio di Catania urban area; it is also indicated the vector value of Horizontal GPS velocities for each station

The structural survey, discussed above, has allowed to detect the presence of deformation strips, which divide the studied area in three separate blocks (Fig. 6.31). Comparing the values of velocity vectors (Table 6.5), obtained by geodetic monitoring campaigns, concerning the monitoring points which insist on different blocks (Fig. 6.31), it is possible to make some observations concerning the kinematics of fault segments and the relative movement of three blocks.

The difference in the east component of the stations located respectively in blocks 1 (Table 6.6) and 2 (Table 6.7) indicates an extensional movement along the fault segment oriented N-S (**[**09SG - 10SG ≈ 12 mm/a)**]**, **[**07SG,08SG – 22SG ≈ 20-30 mm/a**]**).

Although the vertical component data, need to be further controlled with other measurements, being unrealistic, the data obtained from this geodetic monitoring indicate that the west side of the fault segment (block 1) is lowered (20-30 mm/a).

The comparison between the data relating to the blocks 1 (Table 6.6) and 3 (Table 6.8) ([07SG,08SG – 02SG ≈ 10-20 mm/a]), and that between the blocks 2 (Table 6.7) and 3 (Table 6.8) ([22SG – 15SG,16SG ≈ 30 mm/a]), confirms the right-lateral strike-slip kinematic of the San Gregorio fault.

The 21SG station (block 3), located near the main shear zone, shows an unexpected movement with respect to the other stations, this is probably related to local rotation phenomena, consequence of deformation effects.

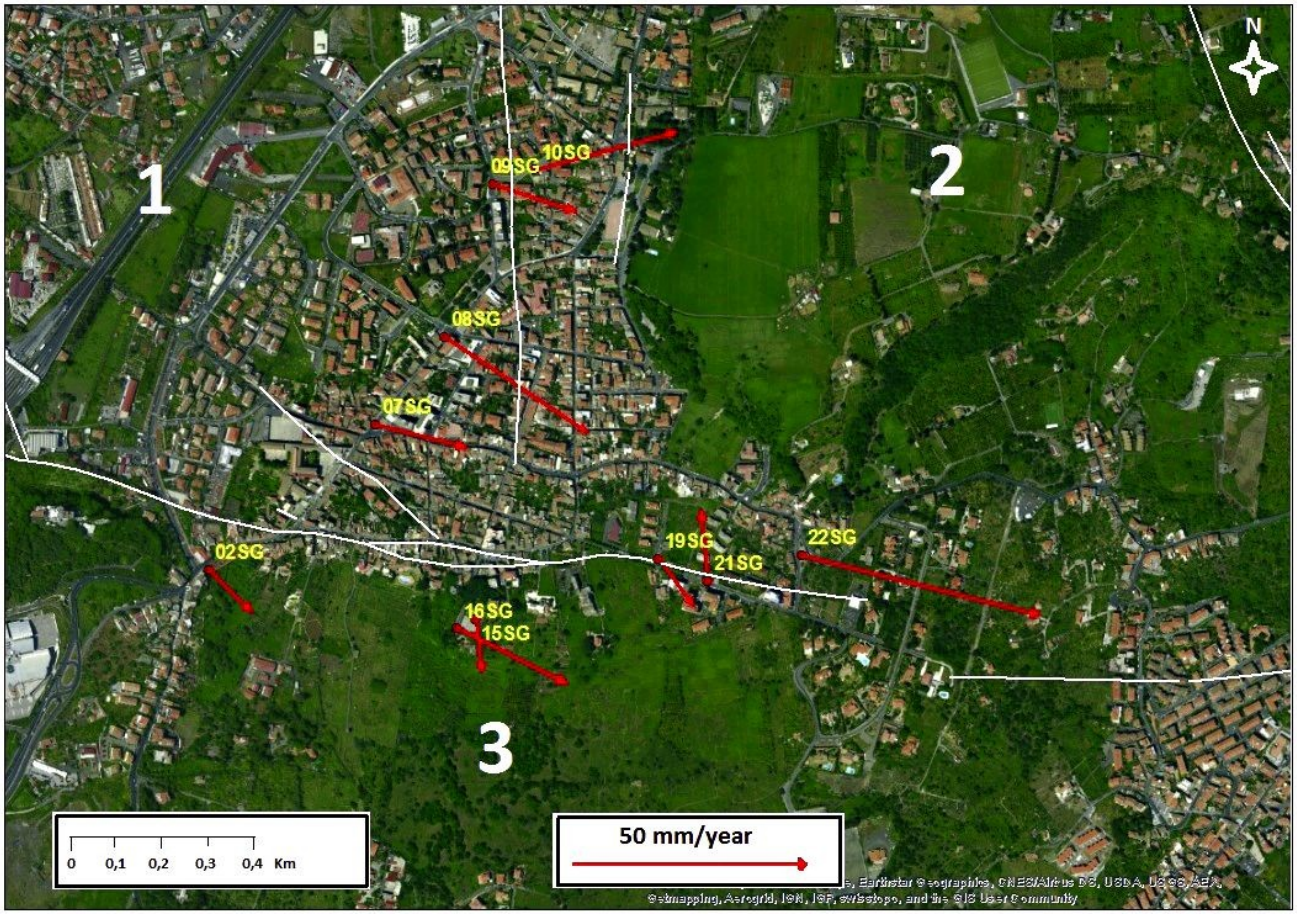

Fig. 6.31. Velocity field of the GNSS stations located in the San Gregorio di Catania area; the red arrows indicate the horizontal velocity vectors; the white lines represents the fault segments which subdivided the area in three blocks

BLOCK 1						
Site	N_vel (mm/a)	E_vel (mm/a)	H_vel (mm/a)	N err (mm/a)	E err (mm/a)	H err (mm/a)
07SG	-4,89	19,14	-54,73	8,57	8,34	37,99
08SG	-20,51	30,27	-54,23	9,72	10,6	37,56
09SG	-5,9	17,74	-7,83	9,63	9,21	41,42

Table 6.6. Velocity vector values for each component (N, E and H) relating to the measurement stations which are located on the block 1

BLOCK 2						
Site	N_vel (mm/a)	E_vel (mm/a)	H_vel (mm/a)	N err (mm/a)	E err (mm/a)	H err (mm/a)
10SG	8,03	30,48	19	8,2	7,01	29,32
19SG	-10,45	7,27	-87,46	6,56	6,28	22,75
22SG	-13,4	50,85	-25,8	7,59	12,59	32,45

Table 6.7. Velocity vector values for each component (N, E and H) relating to the measurement stations which are located on the block 2

BLOCK 3						
Site	N_vel (mm/a)	E_vel (mm/a)	H_vel (mm/a)	N err (mm/a)	E err (mm/a)	H err (mm/a)
02SG	-8,93	8,81	-20,56	5,28	4,81	18,94
15SG	-11,21	1,09	-59,75	7,34	7,2	30,83
16SG	-11,96	23,31	-44,3	10,88	10,94	40,83
21SG	15,26	-1,5	-93,91	14,4	13,33	50,97

Table 6.8. Velocity vector values for each component (N, E and H) relating to the measurement stations which are located on the block 3

6.1.6.3 Topographic monitoring

The topographic monitoring in the urban area of San Gregorio di Catania was carried out along two different polygonal (Fig. 6.32); the scheme used is named "open traverse bounded to extremes", where the endpoints are determined through G.N.S.S. instrumentation.

The first open traverse develops along Corso Umberto (red line - Fig. 6.32) and crosses perpendicularly the San Gregorio fault, it is bounded to extremes by the 02SG and 08SG stations. The main axis of the open traverse is constituted by other five intermediate monitoring points, with reflective prism, and other measurement points, with reflective targets, to increase the precision of the topographic survey.

The second open traverse develops along via Zizzo (blue line; Fig. 6.32); the extreme benchmarks are 11SG and 16SG and there are other four intermediate monitoring points.

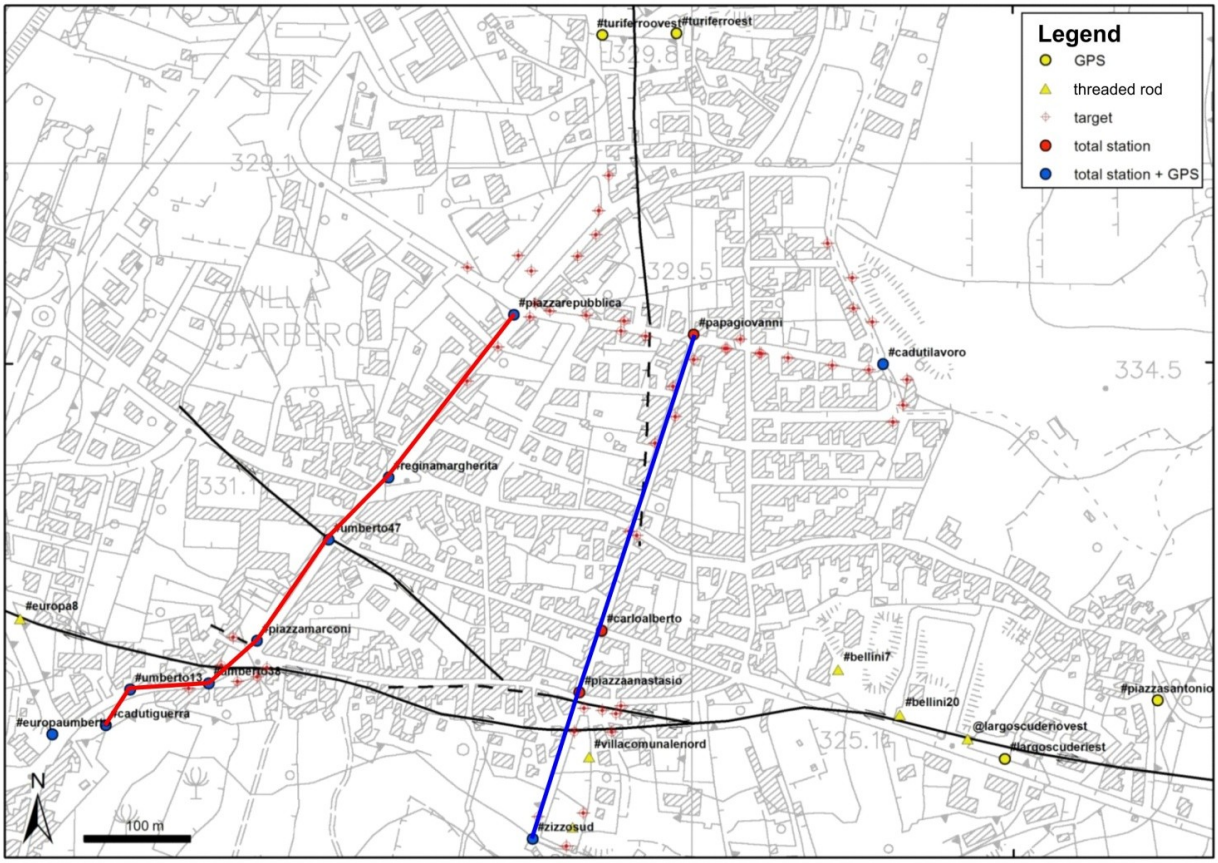

Fig. 6.32. Monitoring network: the black lines represents the fault segments; the two lines, red and blue, show the path of the two open traverses

Two topographic surveys were made, in particular the first during September 2015 and the second in June 2016. The Meridiana software, included within the Total Station used to make the land survey, stores all data in the campaign booklet (Fig. 6.33); these data were elaborated with celerimetric calculation (see Appendix C).

The processing of these two first campaigns, encompassing a very short time, did not provide consistent values to the real surface movements, but they have been crucial for testing the instruments and monitoring the network reliability, as well as to identify what will be considered the "zero point" for subsequent monitoring campaigns, that will be made in the future.

LIBRETTO DI CAMPAGNA

FILE : san_gregorio_def
N. LAVORO : 1
NOME LAVORO : san_gregorio_def
OPERATORE :
STRUMENTO : TS DS103AC
DATA :

NOME STAZIONE : 100
IDENTIFICATIVO :
TEMPERATURA :
PRESSIONE :
ALTEZZA STRUM. : 0.000

Codice Punto	Nome Punto	Altezza Prisma	Distanza Incl.	Angolo Vert.	Angolo Orizz.	Distanza Orizz.	Quota Rel.	Co. Rel. Nord(X)	Co. Rel. Est(Y)
	101	1.000	36.698	100.6898	399.9888	36.696	-1.398	36.696	-0.006
	102	0.000	12.072	97.2558	377.8754	12.061	0.520	11.340	-4.108
	103	0.000	20.705	97.7226	39.8978	20.692	0.741	16.759	12.135
	104	1.000	434.769	100.5700	207.2316	434.752	-4.893	-431.950	-49.279
	200	1.000	43.378	99.6264	126.0372	43.377	-0.745	-17.250	39.800

NOME STAZIONE : 200
IDENTIFICATIVO :
TEMPERATURA :
PRESSIONE :
ALTEZZA STRUM. : 0.000

Codice Punto	Nome Punto	Altezza Prisma	Distanza Incl.	Angolo Vert.	Angolo Orizz.	Distanza Orizz.	Quota Rel.	Co. Rel. Nord(X)	Co. Rel. Est(Y)
	100	1.000	43.380	100.7922	164.6050	43.377	-1.540	-36.843	22.893
	300	1.000	94.456	99.8284	22.4022	94.456	-0.745	88.668	32.557

NOME STAZIONE : 300
IDENTIFICATIVO :
TEMPERATURA :
PRESSIONE :
ALTEZZA STRUM. : 0.000

Codice Punto	Nome Punto	Altezza Prisma	Distanza Incl.	Angolo Vert.	Angolo Orizz.	Distanza Orizz.	Quota Rel.	Co. Rel. Nord(X)	Co. Rel. Est(Y)
	200	1.000	94.458	100.3732	387.5170	94.456	-1.554	92.646	-18.403
	400	1.000	58.455	100.5932	137.1364	58.452	-1.545	-32.196	48.786

Fig. 6.33. Campaign booklet

Processing the data present within the celerimetric booklet, using the trigonometric formulas of right triangles, it was quantified the measurement error between the stations (Table 6.9).

Station		Relative error
From	**To**	
100	200	1 mm
200	300	0,5 mm
300	400	0,5 mm
400	500	2,9 mm
500	600	1,1 mm
600	700	3,2 mm

Table 6.9. Calculated relative error between the stations of topographic monitoring

6.2. Surveys in Tremestieri Etneo area

In the Tremestieri Etneo area some HVSR survey fields were designed and performed in order to define the link between changes in the amplification effects, the directionality of seismic motion and the geological-structural conditions; furthermore MASW surveys were carried out in order to reconstruct the distribution of surface waves velocity in the subsoil. A topographical monitoring network was designed (Fig. 6.34), over a portion of the tectonic structure, in order to assess the deformation rate; the location of monitoring points had been selected following the same criteria used to place the monitoring points of the San Gregorio network; unfortunately due to the lack of agreement with the city administration, such monitoring network, has not been implemented.

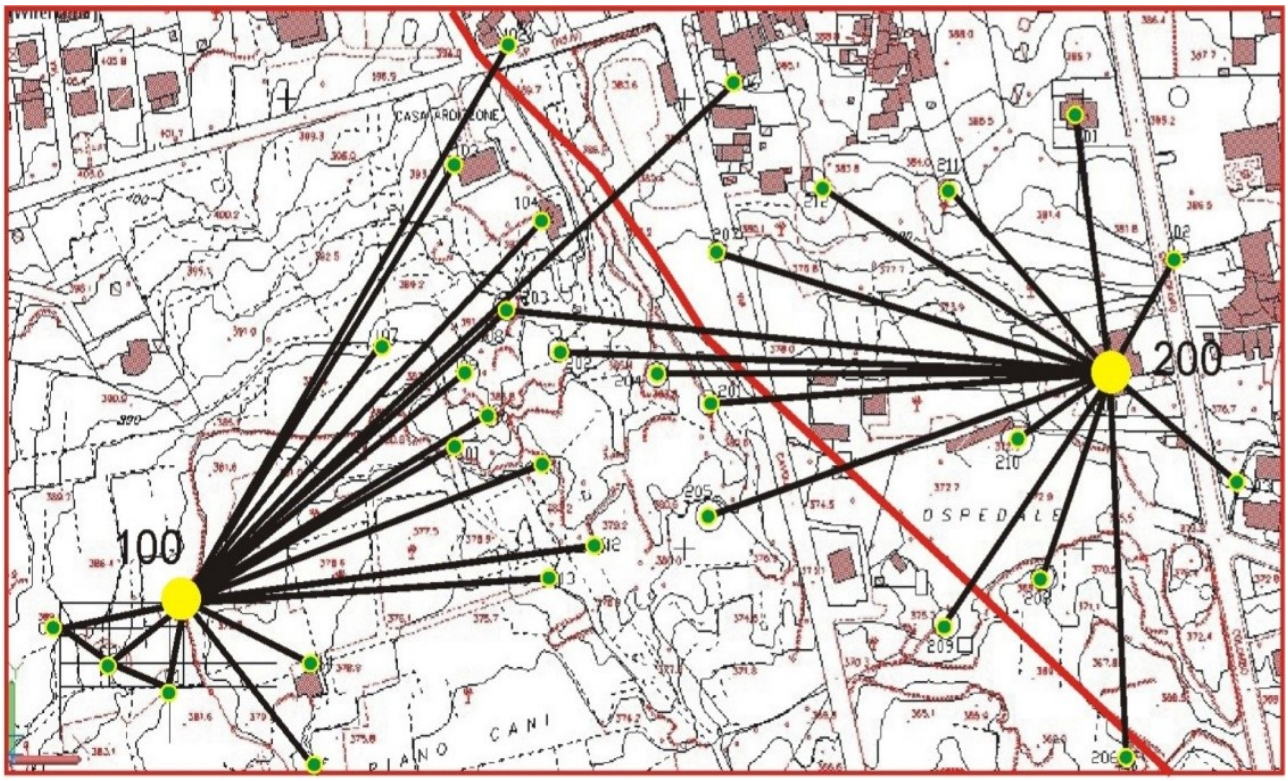

Fig. 6.34. Topographical monitoring network designed to asses the deformation rate across the Tremestieri fault segment.

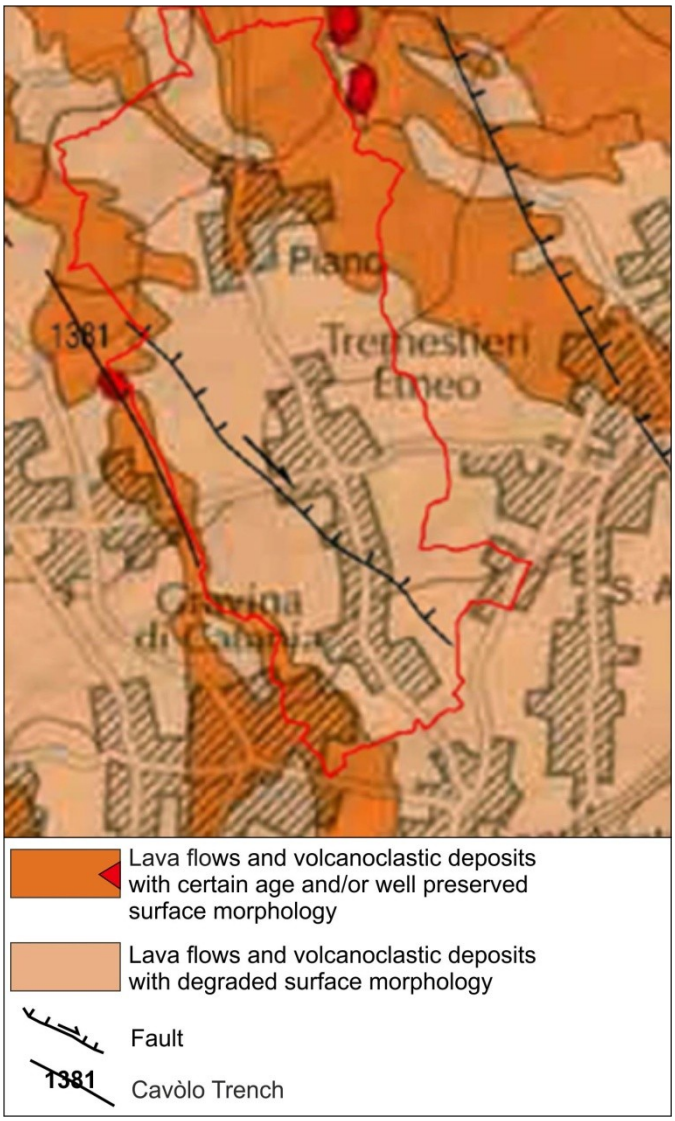

Fig. 6.35. Geologic map of the study area (from Monaco et al. 2010 - modified)

The municipal area of Tremestieri Etneo is characterized by the presence in outcrop (Fig. 6.35) of lava flows and volcanoclastic deposits with well preserved surface morphology and with degraded surface morphology, related to the most recent phase of the eruptive activity (<15 ka - Recent Mongibello) (Monaco et al., 2010); these volcanic products cover a sedimentary substratum formed by marly clays (Middle-Lower Pleistocene). The topography is quite flat, with altitudes ranging from 500 to about 340 m a.s.l. The Tremestieri Etneo village is extensively crossed by a fault segment, with a trend roughly NW-SE, belonging to Tremestieri – Trecastagni - San Gregorio - Acitrezza Fault System. An eruptive fracture, named "Cavòlo Trench" , is present on the border between the Tremestieri and Mascalucia villages, this fracture has a trend roughly parallel to the Tremestieri fault segment.

The segment fault is characterized by a morphological scarp with maximum height of 10 m in its northern sector, and with poor morphologic evidence in the Tremestieri town. The fault releases seismic energy through earthquake swarms as well as aseismic creep phenomena (Lo Giudice and Rasà, 1992; Azzaro, 1999).

6.2.1. HVSR surveys in Tremestieri area

Considering the extension and topography, 235 ambient noise recordings were acquired in the municipal area; in particular, 180 recordings were acquired, along 24 profiles, of which three orthogonal to the fault segment and 21 profiles in the sector to the north of the fault. The others 55 ambient noise acquisitions were performed in different sites of the municipal area (Fig. 6.36).

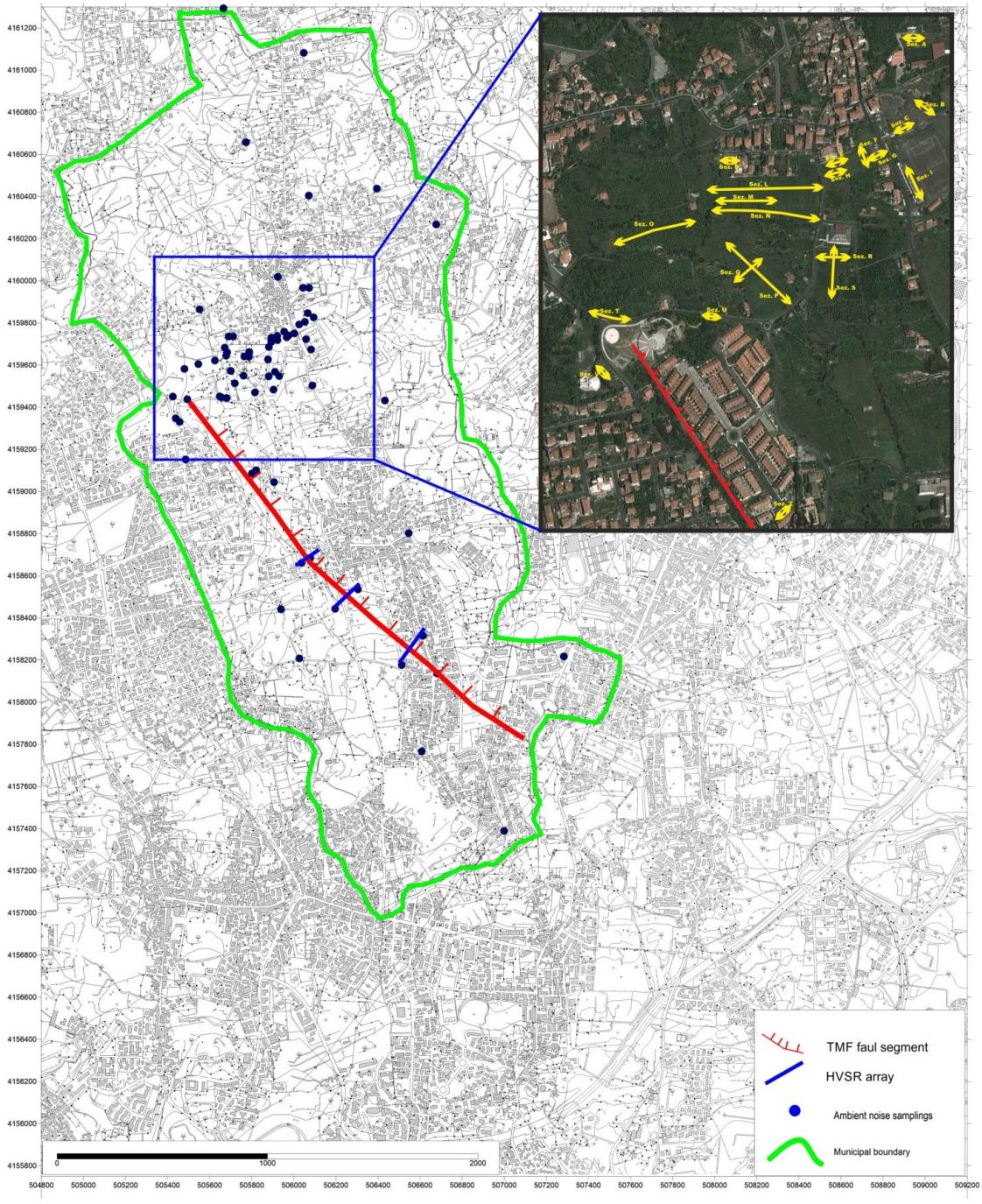

Fig. 6.36. Location of HVSR surveys in Tremestieri Etneo area; the blue lines show the HVSR profiles performed orthogonally to the fault segment; the box to the upper right, shows the location of the 21 HVSR profiles performed in the sector to the north of the fault

The recordings were acquired and processed according to the same procedure described above for the acquisitions made in the San Gregorio di Catania Municipal area. The results of the statistical tests (SESAME guidelines 2004) show also in this case that all measurements meet the criteria of execution goodness, analysis and reliability, while the main resonance peaks were not always significant and clear for all six criteria analyzed.

The resonance frequencies distribution map (Fig. 6.37) and the H/V amplitude distribution map (Fig. 6.38) were reconstructed interpolating the results of 72 ambient noise acquisitions, made in different sites of the municipal area, through a kriging algorithm. For each measuring site the coordinates, the fundamental frequency f_0, in the 0.5-20 Hz frequency range, and the corresponding H/V amplitude, have been considered.

In the area between the fault segment and eruptive fracture, it was observed a distribution of the resonance frequencies within a range, approximately between 1 and 4 Hz; the resonance frequencies for the recordings performed near the fault segment fall within a range between 2 and 6 Hz; variable peak frequencies between 3 and 8 Hz have been identified in the area located north of the fault. In some cases in the spectra are present multiple peaks which also affect higher frequency values. Some spectra are shown as examples in figure 6.39. The analysis of the H/V spectral ratios for the different recording sites has highlighted the presence of major amplification effects (HV amplitude ≈ 4-6) and marked directionality, approximately E-W, for the acquisitions performed to the north of the fault segment (Fig. 6.39), in a not urbanized area. For this reason it was chosen to carry out, in this area, further HVSR surveys aligned along transects. In doing this we found particularly marked directional effects, contrary to what is expected considering the possible attenuation phenomena, which are usually observed away from the fault trace. The strong amplification effects observed could be related either to the lithostratigraphic nature of the subsoil, or to the presence of buried discontinuities.

The systematic directional effect, detected for many of the recordings north of the fault segment, could indicate the presence of buried tectonic structures, probably masked by recent volcanic products; the lack of urbanization and the occurrence of vegetation in this area, have not permitted the execution of a structural survey to detect the possible presence of fractures.

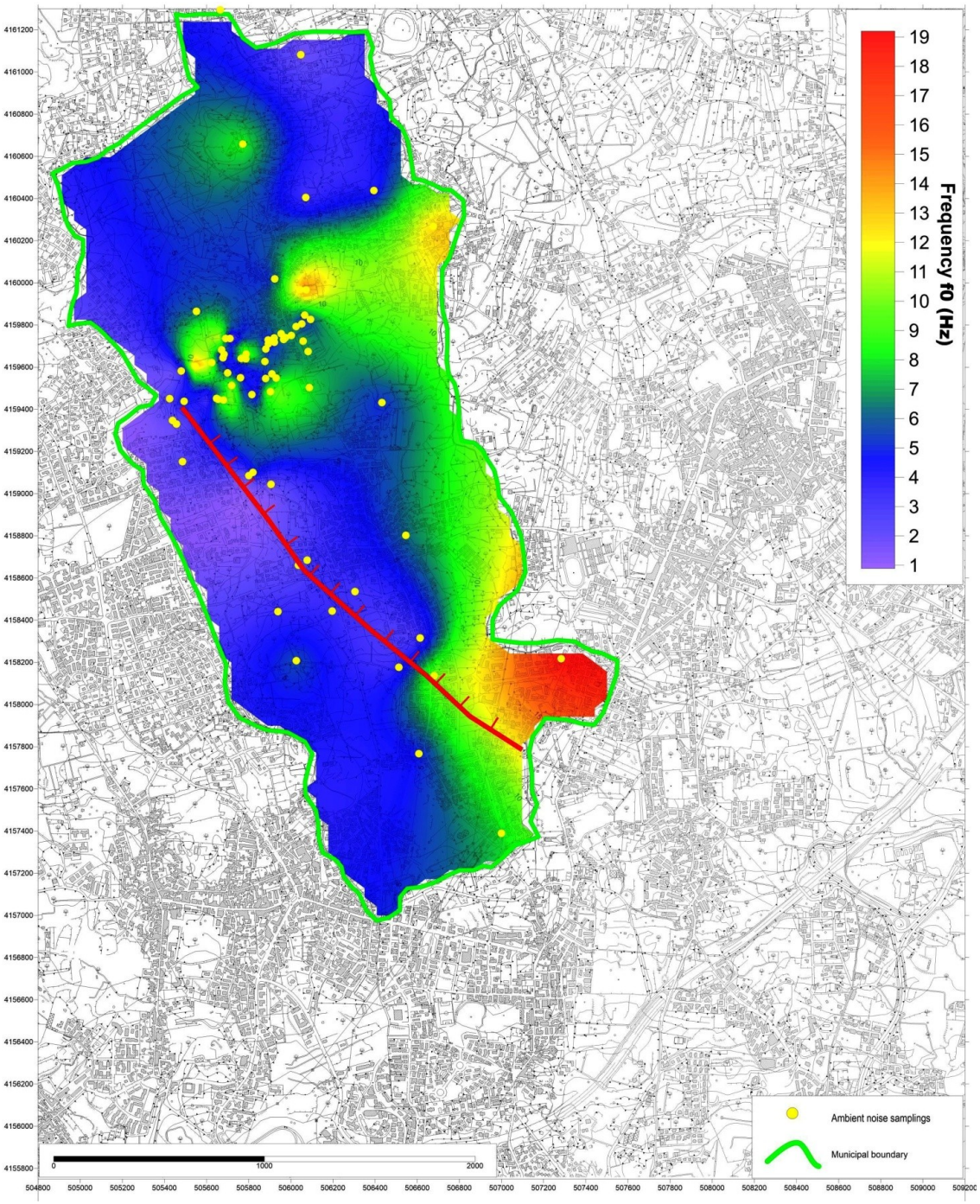

Fig. 6.37. Map of the resonance frequencies distribution

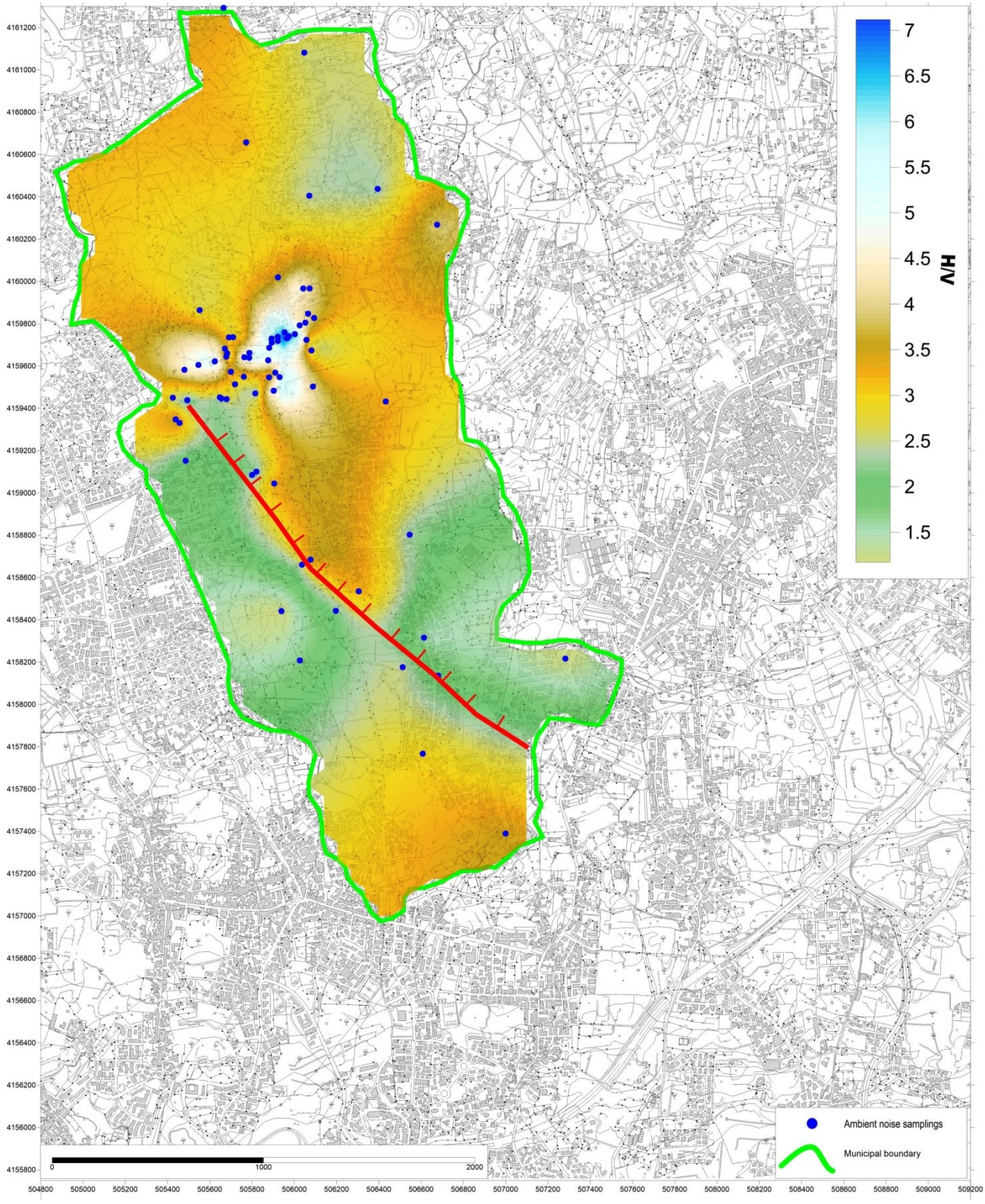

Fig. 6.38. Map of HV amplitude distribution

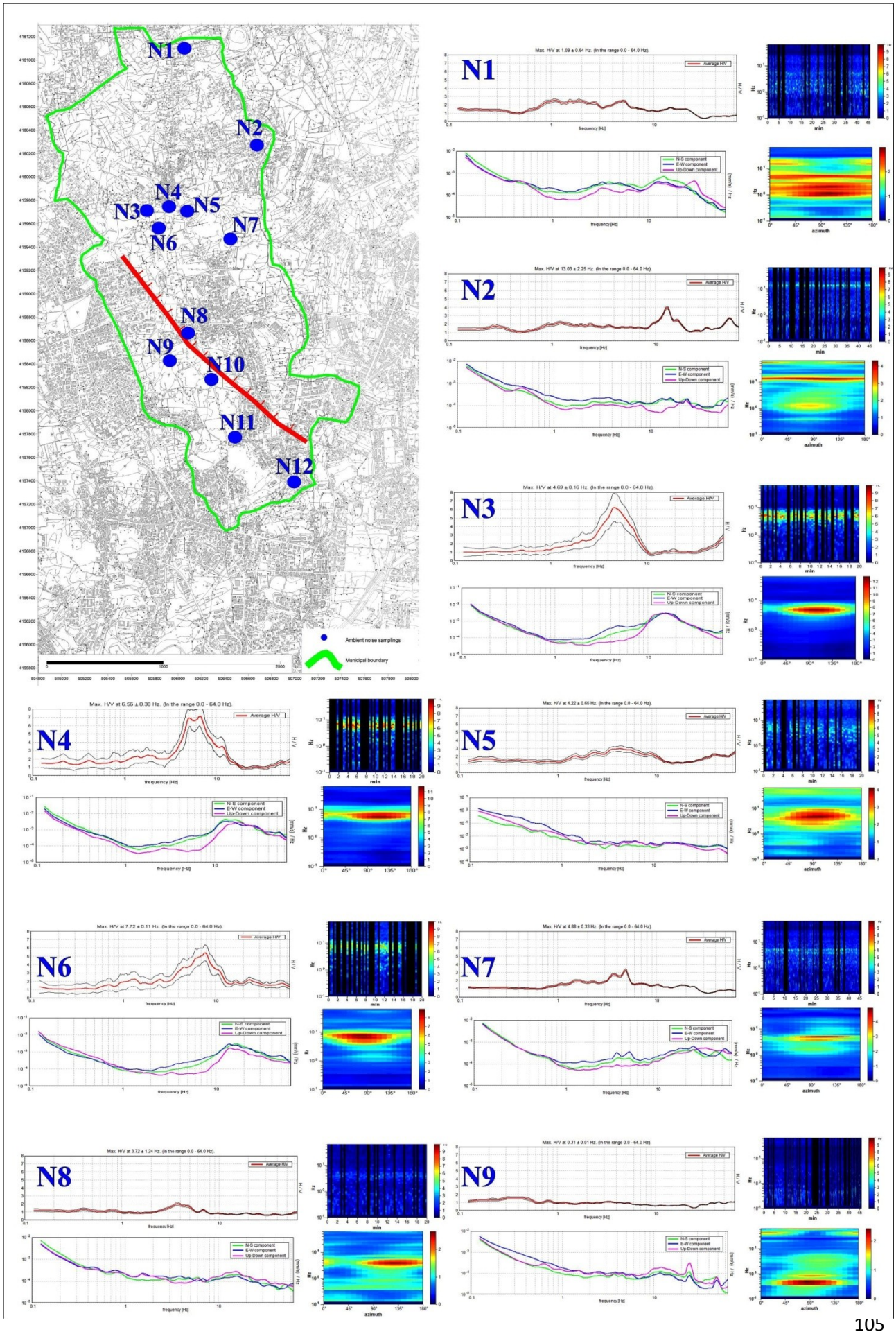
N1
N2
N3
N4
N5
N6
N7
N8
N9
N10
N11
N12
Ambient noise samplings
Municipal boundary
Max. H/V at 1.09 ± 0.64 Hz. (In the range 0.0 - 64.0 Hz).
Max. H/V at 13.03 ± 2.25 Hz. (In the range 0.0 - 64.0 Hz).
Max. H/V at 4.69 ± 0.16 Hz. (In the range 0.0 - 64.0 Hz).
Max. H/V at 6.56 ± 0.38 Hz. (In the range 0.0 - 64.0 Hz).
Max. H/V at 4.22 ± 0.65 Hz. (In the range 0.0 - 64.0 Hz).
Max. H/V at 7.72 ± 0.11 Hz. (In the range 0.0 - 64.0 Hz).
Max. H/V at 4.88 ± 0.33 Hz. (In the range 0.0 - 64.0 Hz).
Max. H/V at 3.72 ± 1.24 Hz. (In the range 0.0 - 64.0 Hz).
Max. H/V at 0.31 ± 0.01 Hz. (In the range 0.0 - 64.0 Hz).
Average H/V
N-S component
E-W component
Up-Down component
frequency [Hz]
A / H
Hz / (km/s)
min
azimuth

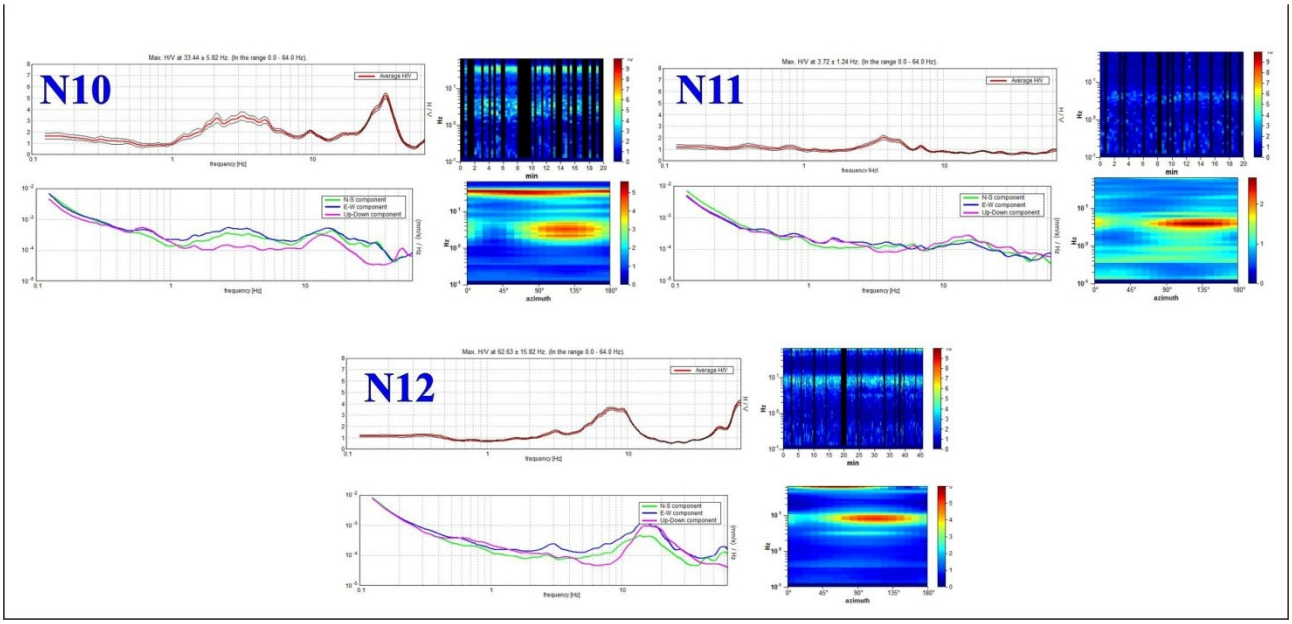

Fig. 6.39. Results of the elaborations of some ambient noise samplings performed in the municipality of Tremestieri Etneo (HV spectra; amplitude spectra of single components N-S, E-W, up-down; H/V stability; directional HVSR)

6.2.2. MASW surveys

MASW (multichannel analysis of surface waves) is an active seismic survey in that it requires an energization source. Experimented by the Kansas Geological Survey (Park et al. 1999), it is based on the study of dispersion of Rayleigh waves. These waves carry about two-thirds of the energy generated by the source and undergo less attenuation as the distance increases compared to body waves. Within the same medium, the velocity of surface waves Vr differs by few percent compared with that of the shear waves Vs (Richart et al., 1970; Achenbach, 2000). For this reason, the MASW method is used to reconstruct the profile of the shear wave velocity with depth in the first meters of the subsoil.

Six MASW surveys were performed (Fig. 6.40) to obtain information on the distribution of the shear wave velocity in the subsoil of the investigated area. The seismic signal was acquired through a digital multichannel array, with 25 channels, SoilSpy Rosina (Micromed S.p.A). The arrays were arranged using geophones with natural frequency of 4.5 Hz and spacing of 3 m. The fall of a heavy body was used as the energization source, with a fixed offset distance from the closest geophone of

about 6 m; to increase the signal-to-noise ratio, several energizations were performed (vertical stacking). In order to distinguish the energy associated with the Rayleigh waves, the acquired signals have been analyzed in the frequency–phase velocity domain.

In the hypothesis of predominant surface waves in the wave field, to obtain the Vs–depth profile for the studied area, once the dispersion spectrum of Rayleigh waves from the MASW elaboration was attained, a joint fit was made between this and one of the H/V spectra acquired near the alignment (Fig. 6.40). Starting from a subsoil model, characterized by values of thickness, Vs, Vp, density and Poisson's ratio, assigned on the basis of geological knowledge of the site, a dispersion curve and a theoretical H/V spectrum have been calculated with the Grilla software rel. 6.5 (Micromed S.p.A.). These are displayed in superposition on the experimental dispersion spectrum of Rayleigh waves and the experimental H/V spectrum, respectively. The model has been modified to ensure that the theoretical curves overlap the experimental ones as much as possible; the model for which there is maximum overlap provides the Vs–depth profile relative to the examined site (Fig. 6.40).

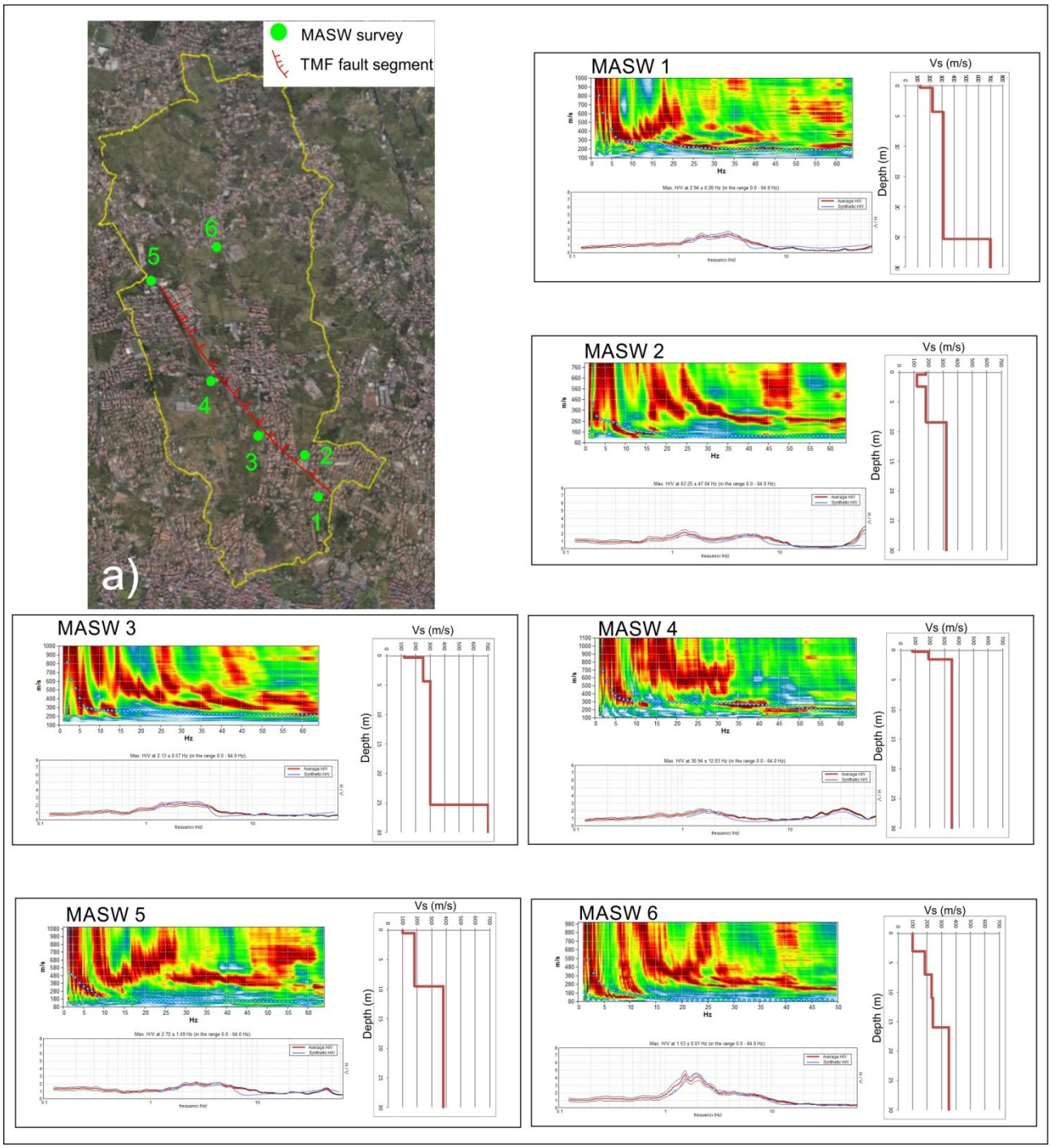

Fig. 6.39. a) Location of MASW surveys; for each survey are shown Rayleigh waves dispersion curve, obtained from the MASW survey, HVSR spectrum, relating to one seismic ambient noise record acquired near the profile and 1D velocity–depth profile obtained from MASW-HVSR joint fit

6.2.3. Impedance contrast sections

By integrating the data from the ambient noise records with information on the velocity–depth distribution from the MASW-HVSR joint fit, the frequency values

have been converted to depth values that enable reconstructing the impedance contrast sections.

The V_0 and α values, which provide a minimum misfit between the function 2 (paragraph 2.2) and the Vs–depth profiles (Fig. 6.41), were obtained with the same procedure used for San Gregorio di Catania area (paragraph 6.1.5), for the Tremestieri area this two parameters are equal to V_0= 129.027 m/s and α=0.349.

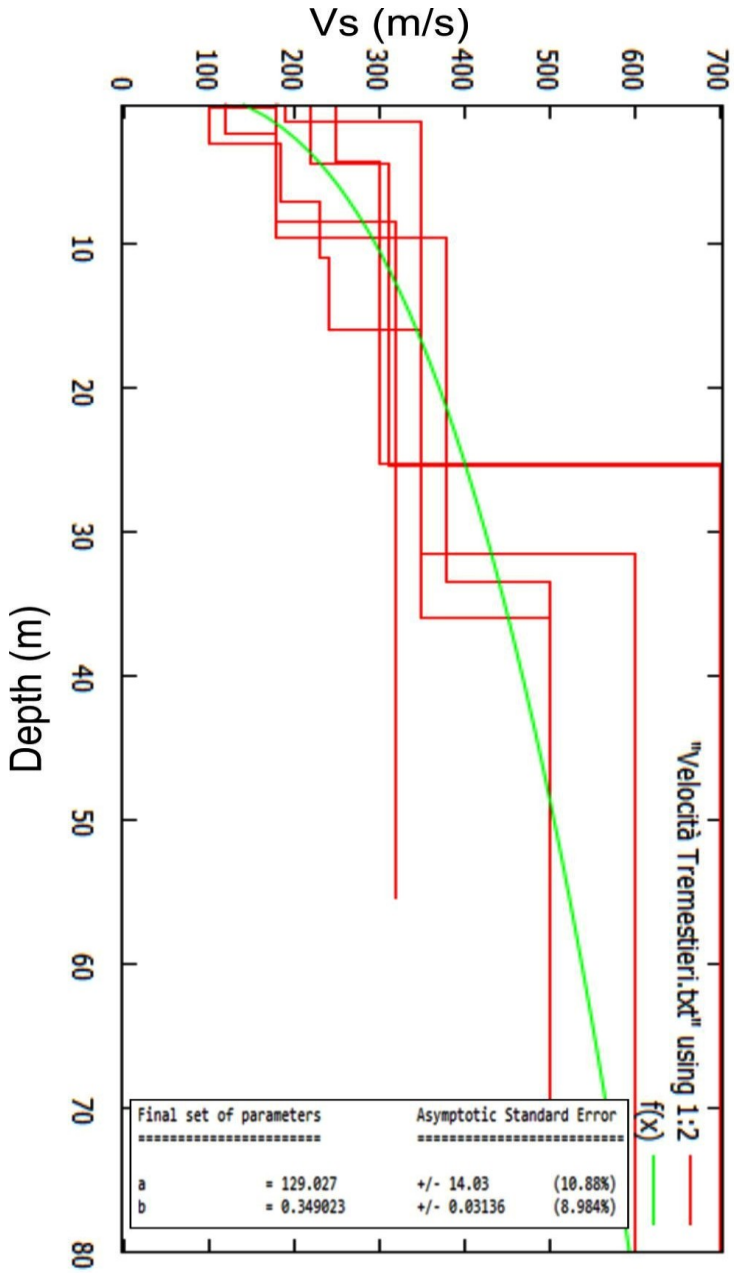

Fig. 6.40. Velocity-depth profiles: the green curve represents the function $V_s(Z) = V_0(1+Z)^{\alpha}$ that has the minimum misfit with the data of the Vs–depth profiles

V_0 and α values were used to convert the spectra frequency values in depth values, through the equation of Ibs-von Seht and Wohlenberg (1999) (paragraph

2.2). In order to reconstruct the impedance contrast sections was taken into account the topography of the profile along which was carried out each alignment, the distance between the measurement points and their relative height. To each frequency value, which has been converted into depth, an amplitude value of H/V spectral ratio is associated. The changes of H/V amplitude values are represented, in the impedance contrast sections, by colors associated with a chromatic scale (Fig. 6.42).

By observing the impedance contrast sections related to the HVSR arrays performed orthogonally to the fault segments (Fig. 6.42a, b), it is possible to note that the main impedance contrast, probably associated with the passage between volcanoclastic coverage and underlying lava flows, is interrupted where the fault segment cross the section.

In section 2 (Fig. 6.42b) the main horizontal impedance contrast seems to be displaced with an apparent fault throw of about 10 m, this information is in agree with the fault kinematics; the impedance contrast that cross the section vertically may be associated with the transition between the fractured zone, affected by the passage of the fault segment, and the surrounding rocks.

The variation of H/V spectral ratio, which is function of impedance contrast, has permitted to distinguish areas with different seismo-stratigraphic characteristics, also in the sections relative to HVSR arrays carried out north of the fault segment (Fig. 6.42c); some of these sections show the main impedance contrast interrupted, just as observed for those performed orthogonally to the fault; this datum together with those obtained from the analysis of directional effects, that show a strong and systematic directionality, suggest the possible presence of potential tectonic structures probably covered by recent volcanic products.

After converting the resonance frequency values of 72 spectra, in depth values using the V_0 and α parameters, a contouring of data was made using the kriging interpolation method thus obtaining the depth map of the layer that causes the resonance peak (Fig. 6.43).

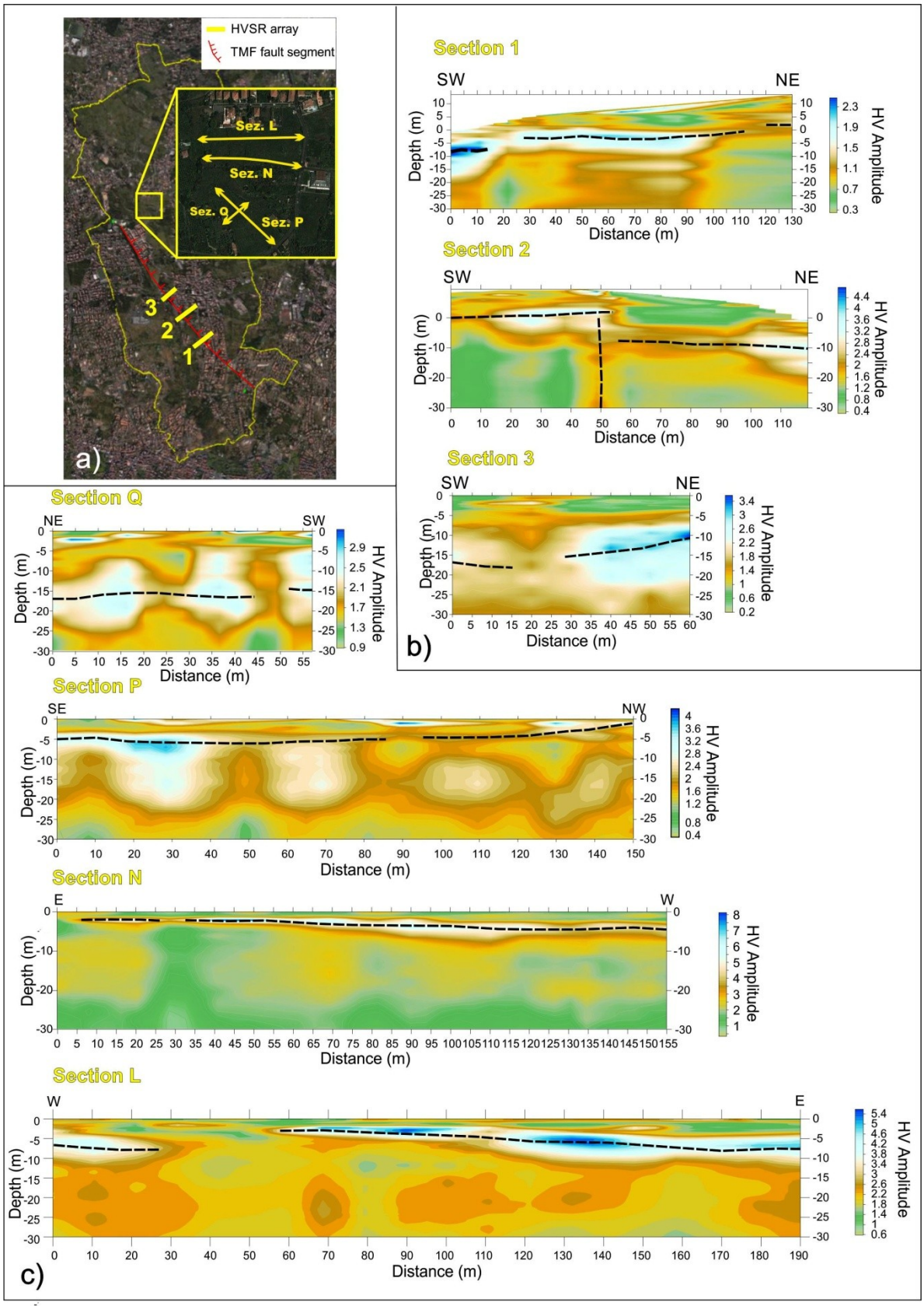

Fig. 6.41. a) Location of some HVSR arrays; b) impedance contrast sections performed orthogonally to the TMF fault segment; c) examples of impedance contrast sections performed to north of the TMF fault segment. The dashed black line highlights the main impedance contrast

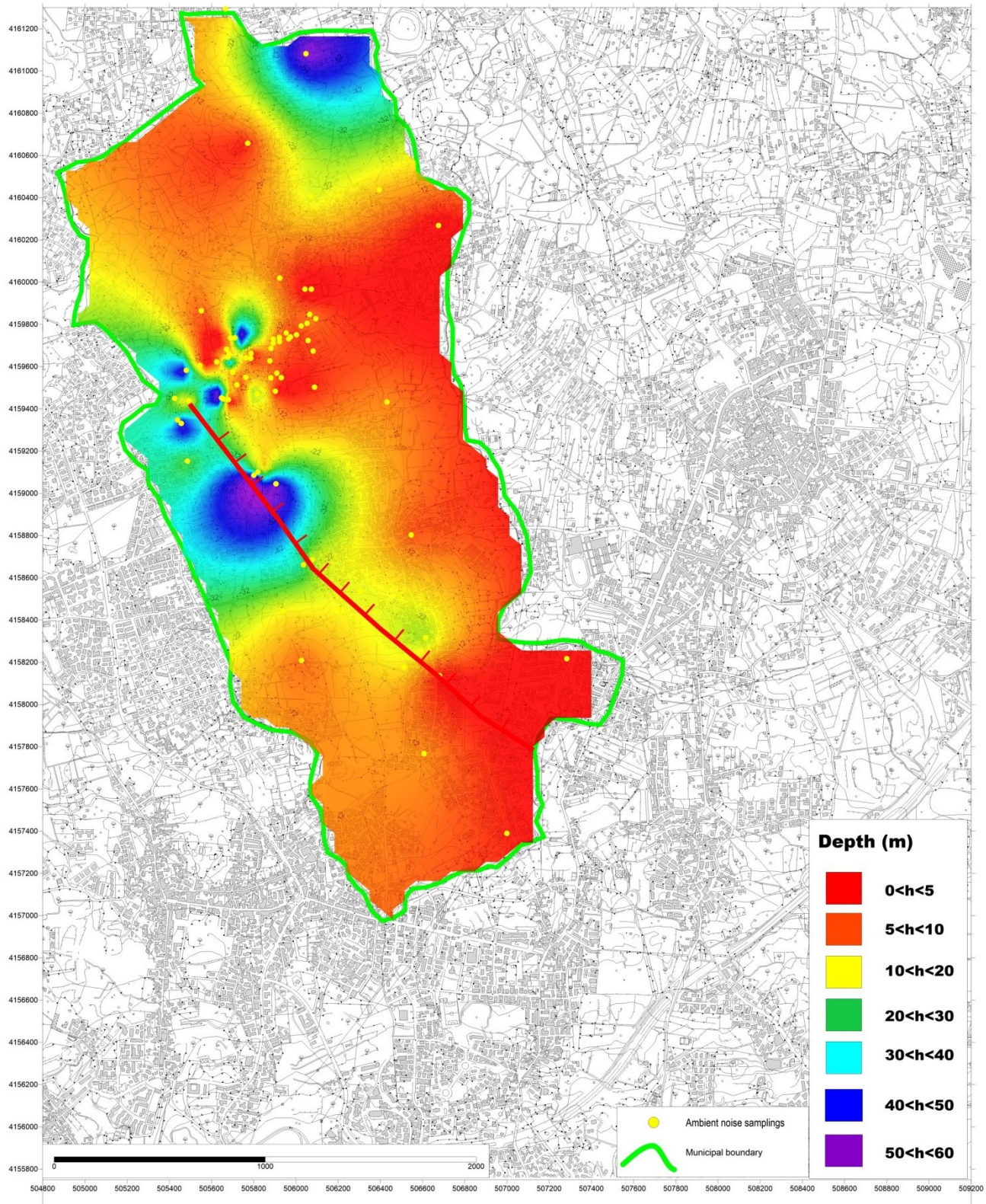

Fig. 6.42. Depth map of the interface that causes the resonance peaks

6.3. Surveys in Aci Castello area

From a geological point of view the Acicastello area can be divided into two zones, in the northern portion outcrop Lower-Middle Pleistocene marly clays and basal tholeiitic volcanics; in the southern sector, the Pleistocene marly clays are totally covered by recent lava flows and volcanoclastic deposits with degraded surface morphology (Fig. 6.44). The northern sector is affected by an active fault segment in the Acitrezza area (ATF), extending with an E-W trend, as reported in several maps (Monaco et al., 2010; Azzaro et al., 2013). Even if the recognition of the fractures in the field was difficult because the clayish substrate outcropping in the area conceals the clues of brittle deformation features, a structural survey was carried out; this survey has permitted to recognize a fracture belt roughly trending E-W for about 1200 m, at about 400 m south of SG-ATF eastern segment (Fig. 6.45).

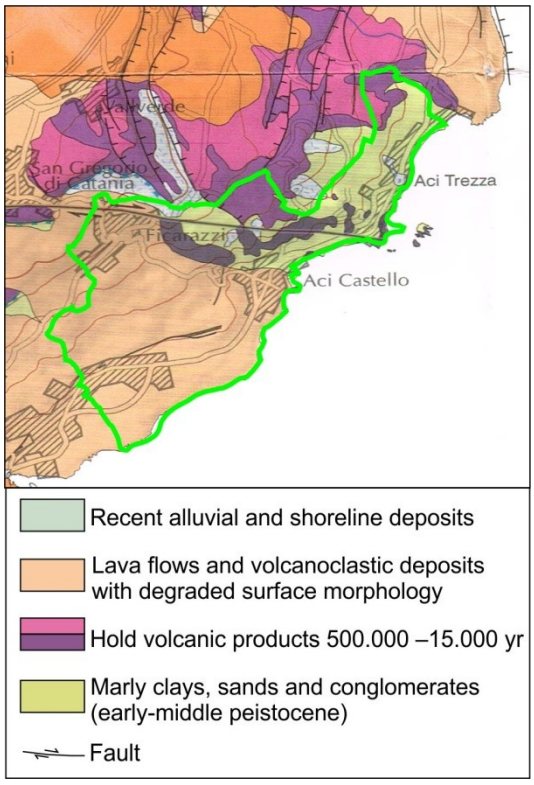

Fig. 6.43. Geologic map of the study area (modified from Monaco et al., 2010)

Were performed several ambient noise samplings, some of them in array configuration along 6 alignments orthogonal to the fault segment and others scattered in the municipal area.

The information relating to the shear waves velocity distribution in the subsoil has been obtained from previous surveys carried out by freelance geologists.

A geodetic monitoring was performed using some of the 46 benchmarks installed previously by the Civil Engineering Office, to monitor the slipping of Vampolieri hill, north of the survey area; this was possible thanks to the drafting of a agreement between the University of Catania and the Civil Engineering Office. The benchmarks consist of concrete pillars where GPS receivers are placed during periodic monitoring campaigns.

6.3.1. HVSR surveys in Aci Castello area

145 ambient noise samplings were acquired and processed according with the same procedure utilized for the other two investigated areas. In particular, 63 recordings were acquired along 6 profiles, and 82 were performed in different positions to uniformly cover the entire municipal area (Fig. 6.45).

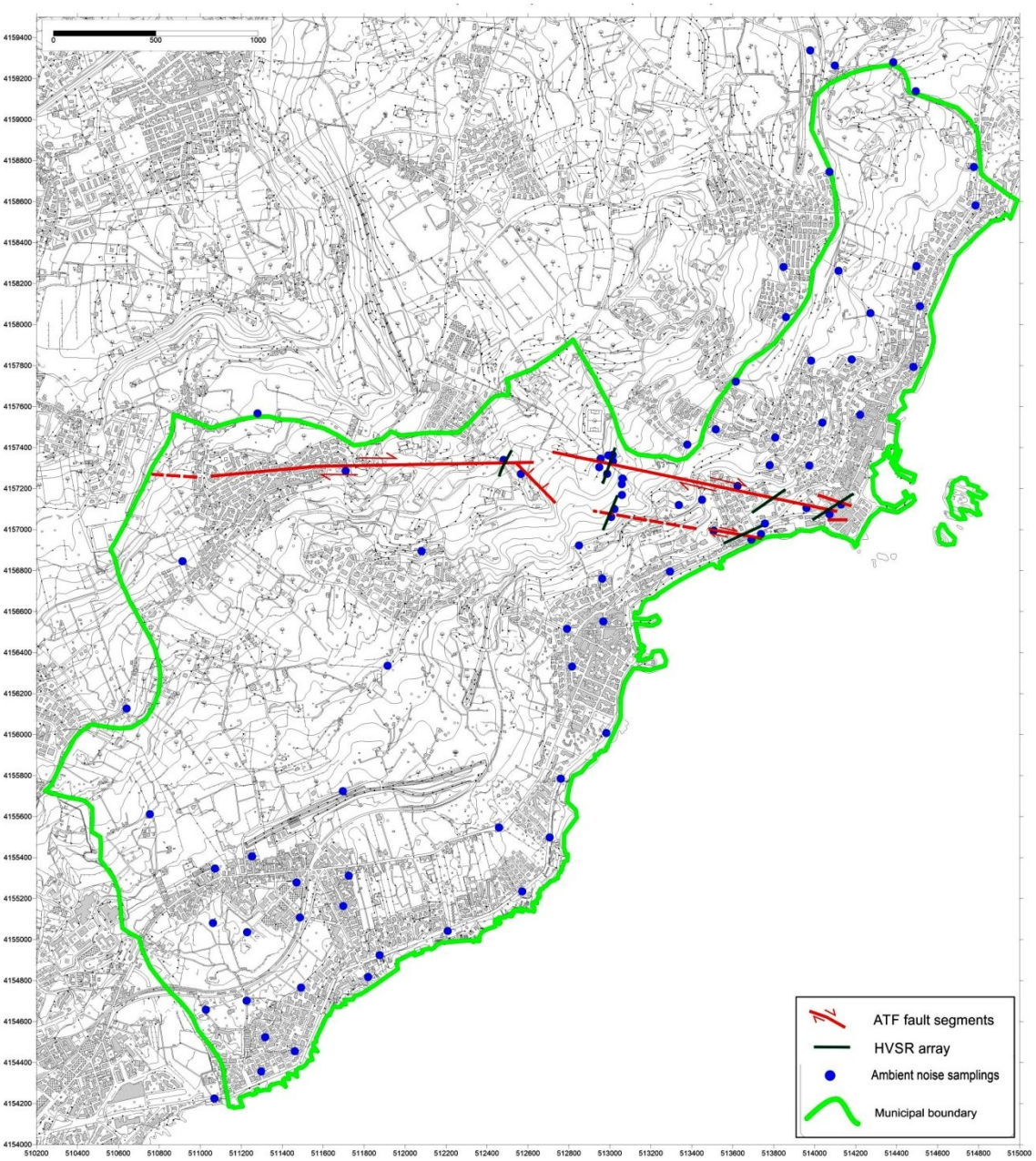

Fig. 6.44. Location of HVSR surveys in Aci Catello area; the green lines show the HVSR profiles performed orthogonally to the fault segments; the red lines show the fault segments detected by the structural survey

In many spectra, the HV spectral ratio value falls below one at high frequencies (> 2.5 Hz) and for a wide frequency range. Observing the single component spectra it

is possible to note that the deamplification of HV curve seems to be caused by the decay of the horizontal components while the vertical component is generally less affected (Fig. 6.46); this can be considered an effect of the presence of a velocity inversion in the first meters of subsoil (Castellaro and Mulargia, 2009). In the southern sector, the stratigraphy of the volcanic soils, that characterizes the first meters of the subsoil cause repeated inversions of velocity seismic waves; the velocity inversion observed in the HV spectra related to the ambient noise samplings acquired in the northern portion of municipal area, could be connected with the presence of water in the first meters of the subsoil.

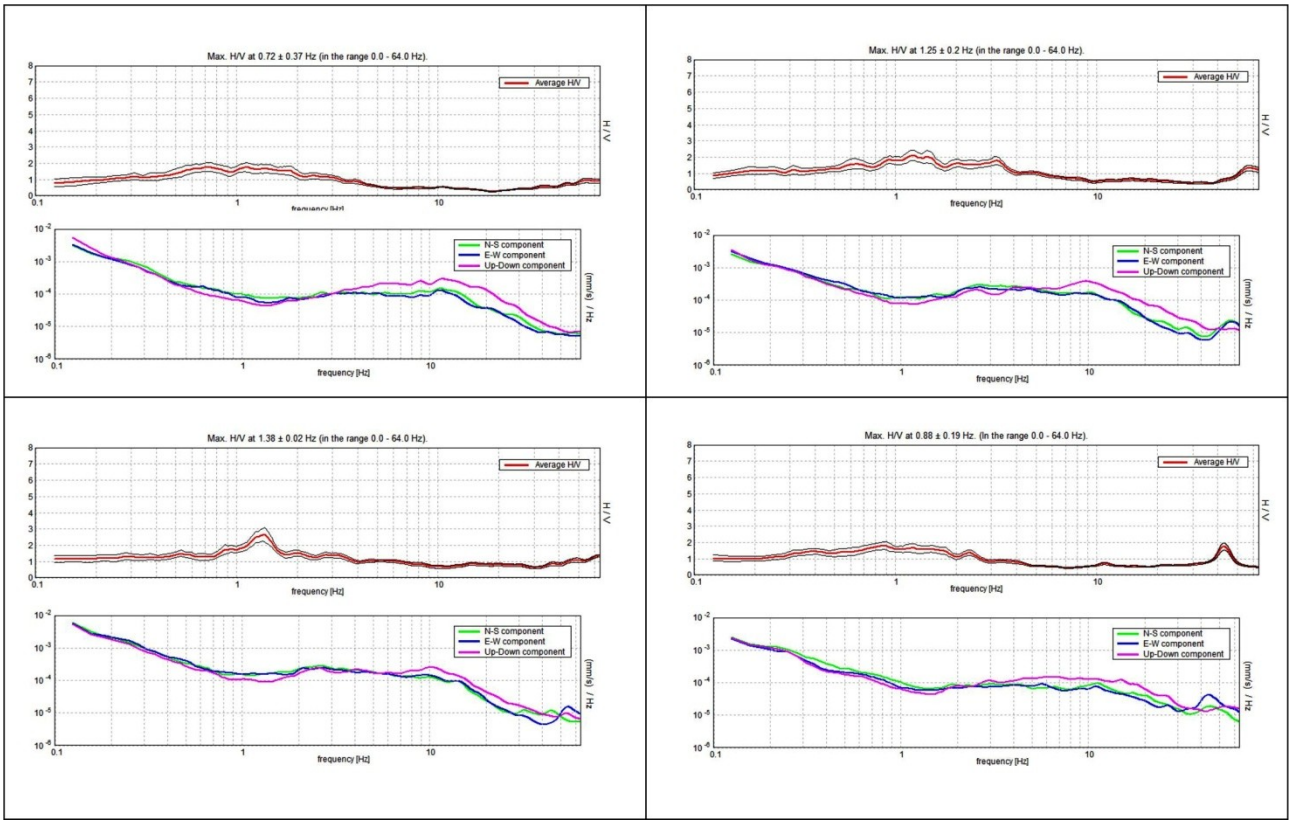

Fig. 6.45. Examples of H/V spectra affected by velocity inversion

For each HVSR measurement, all significant spectral peaks were detected. Through the examination of individual H/V spectra and related components it is possible to distinguish between peaks of anthropogenic origin from those of stratigraphic origin. The stratigraphic peaks were characterized by means of their central frequency value and the related amplitude value.

Based on the above results, a map of the fundamental frequency distributionin the frequency range 0.5 – 20 Hz (Fig. 6.47) has been reconstructed for the entire municipal area. The data contouring was made using the kriging interpolation method; in the same way it was obtained the map of HV amplitude distribution (Fig. 6.48). Observing the map in figure 6.47 it is possible to note the presence of two different areas characterized by different resonance frequency intervals; in particular, the southern sector shows higher resonance frequency values, in the range between 6 and 20 Hz, this suggests that the impedance contrast, which causes the resonant peak, is located at low depth, probably within the succession of lava flows and volcanoclastic deposits that characterize this area. In contrast, most of the northern sector is characterized by lower resonance frequency values, in the range between 0.5 and 3 Hz, which is likely correlated to the possible presence of an impedance contrast at greater depth than the southern sector; this impedance contrast is probably located within the marly clays succession. In this area, only in some measuring sites where debris is present, are observed spectral peaks at higher frequencies, in the range of 6-12 Hz, in this case the impedance contrast is located at low depth, at the interface between debris and the underlying marly clays.

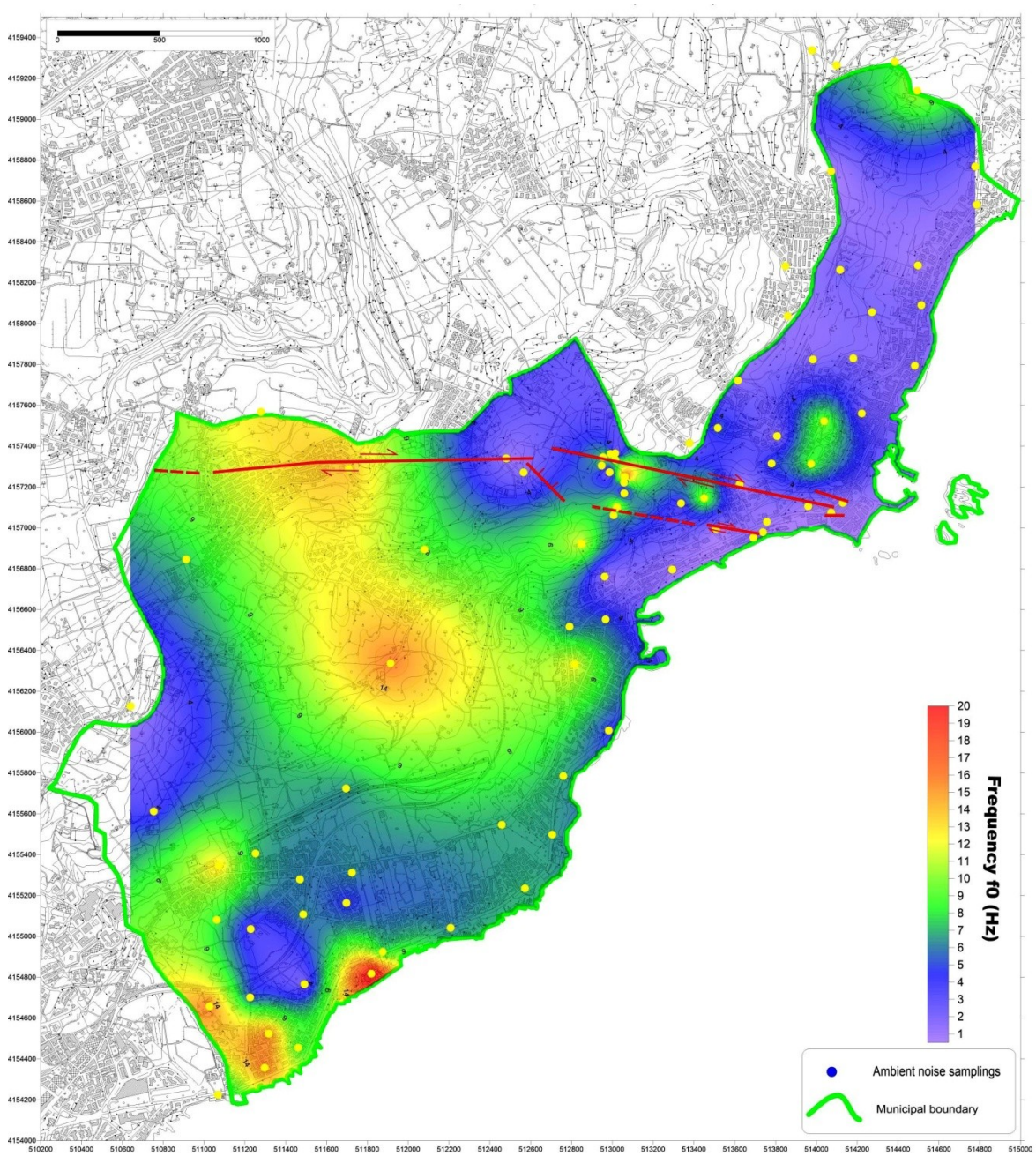

Fig. 6.47. Map of the resonance frequencies distribution

It is interesting to note that the distribution of resonance frequencies is in agreement with the geological characteristics of the area (Fig. 6.44); indeed, different resonance frequency ranges correspond to litotypes with different geological and seismostratigraphic characteristics.

Observing the map of HV amplitude distribution (Fig. 6.48), it is possible to note that the municipal area is mainly characterized by amplitude values of resonance peak between 2 and 3; significant amplification effects are not observed in the north east portion of the municipal area, characterized by the presence of marly clays, and

where most of the spectra show a deamplification of the HV curve, at high frequencies, associated with the presence of a velocity inversion in the subsoil.

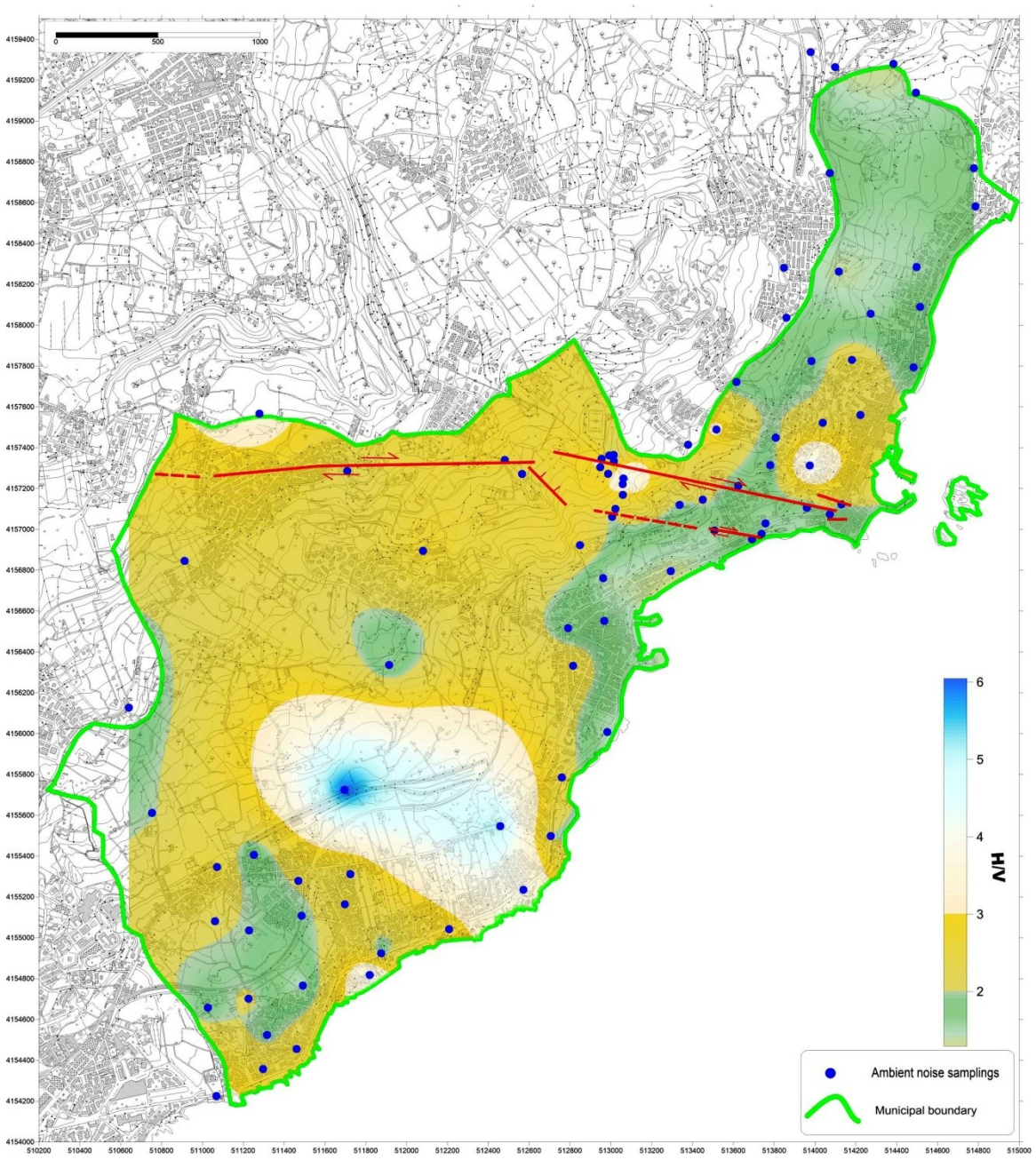

Fig. 6.48. Map of HV amplitude distribution

6.3.2. Impedance contrast sections

In order to reconstruct the impedance contrast sections relating to the ambient noise acquisitions performed, with constant spacing, along seven profiles, it was necessary to obtain information on the distribution of shear waves velocity in the

subsoil of the investigated area. For this reasons we found five 1D Vs profiles obtained by as many MASW surveys previously carried out in areas near the HVSR arrays (Fig. 6.49). In the Table 6.10 are reported the Vs-depth profile values for each survey and the coordinates relative to the center point of each MASW alignment.

Fig. 6.49. Location of MASW surveys

Masw1_AT: 37°33'39.15"N 15° 9'29.77"E – Parallela Via Guarnaccia Lato Ovest			
Interval	**Depth (m)**	**H (m)**	**Vs**
1	0.0-2.0	2.0	175
2	2.0-5.0	3.0	296
3	5.0-8.0	3.0	321
4	8.0-12.0	4.0	296
5	12.0-16.0	4.0	298
6	16.0-26.0	10.0	314
7	26.0-30.0	4.0	327
Vs30			**292**
Masw2_AT: 37°33'38.59"N 15° 9'36.62"E – Parallela Via Guarnaccia Lato Est			
Interval	**Depth (m)**	**H (m)**	**Vs**
1	0.0-2.0	2.0	350
2	2.0-4.0	2.0	255
3	4.0-10.0	6.0	150
4	10.0-25.0	15.0	275
5	25.0-30.0	5.0	480
Vs30			**253**

Masw3_AT: 37°33'33.19"N 15° 9'14.87"E – Lungomare Scardamiano			
Interval	**Depth (m)**	**H (m)**	**Vs**
1	0.0-1.5	1.5	172
2	1.5-3.5	2.0	319
3	3.5-7.0	3.5	254
4	7.0-11.0	4.0	306
5	11.0-15.0	4.0	308
6	15.0-20.0	5.0	378
7	20.0-30.0	10.0	429
Vs30			**332**
Masw4_AT: 37°33'42.71"N 15° 9'15.35"E Residence Ciclope			
Interval	**Depth (m)**	**H (m)**	**Vs**
1	0.0-2.0	2.0	162
2	2.0-5.0	3.0	215
3	5.0-8.0	3.0	305
4	8.0-12.0	4.0	354
5	12.0-26.0	9.0	372
6	26.0-30.0	9.0	360
Vs30			**317**
Masw5_AT: 37°33'41.06"N 15° 8'25.65"E – Zona via Monterosso			
Interval	**Depth (m)**	**H (m)**	**Vs**
1	0.0-4.0	4.0	167
2	4.0-6.0	2.0	417
3	6.0-8.0	2.0	755
4	8.0-10.0	2.0	575
5	10.0-20.0	10.0	830
6	20.0-30.0	10.0	437
Vs30			**431**

Table 6.10. Velocity-depth profiles obtained by MASW surveys

The Vs-depth profiles confirm the presence of a velocity inversion in the subsoil, as assumed from observation of H/V spectral ratios.

Using the same procedure utilized earlier for San Gregorio di Catania and Tremestieri Etneo areas the V_0 and α values were obtained. They provide a minimum misfit between the function $V_s(Z) = V_0(1+Z)^{\alpha}$ and the Vs–depth profiles (Fig. 6.50).

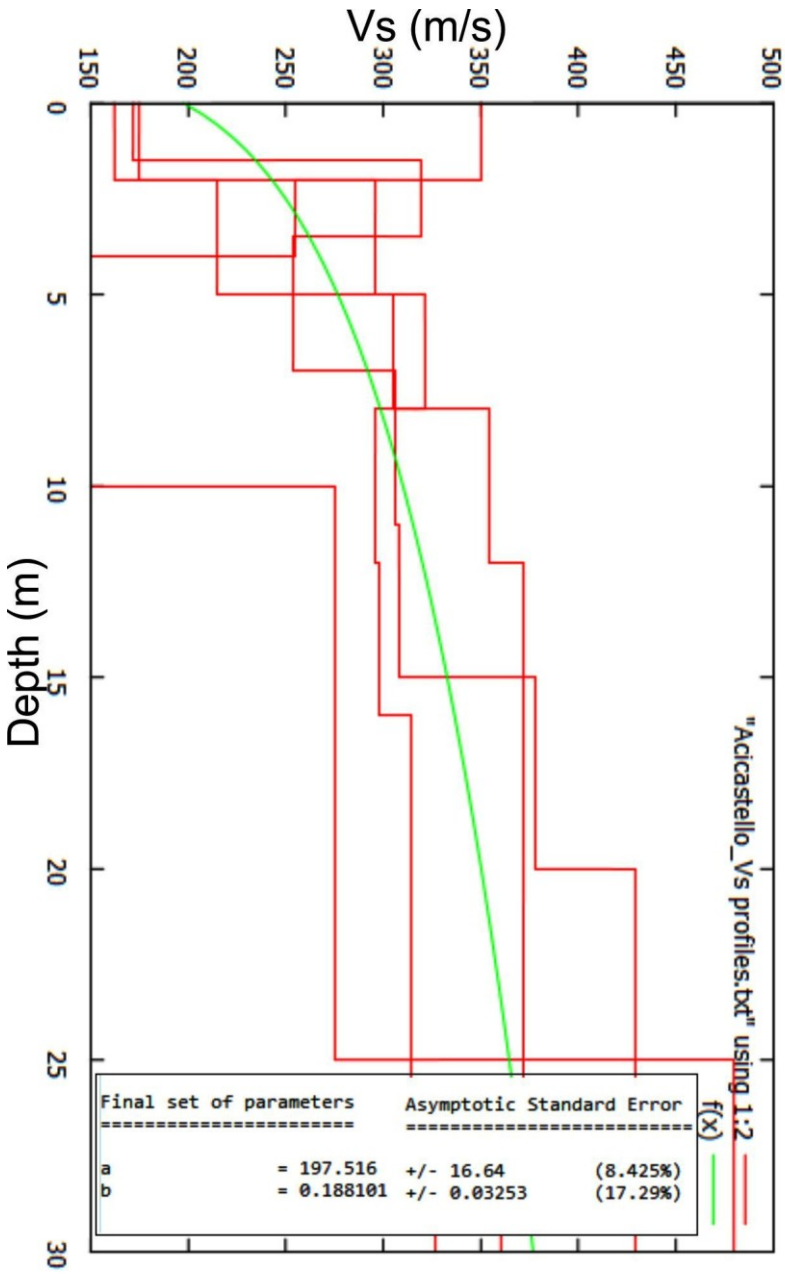

Fig. 6.50. Velocity-depth profiles: the green curve represents the function $V_s(Z) = V_0(1+Z)^{\alpha}$ that has the minimum misfit with the data of the Vs–depth profiles

The V_0 and α values for the northern portion of municipal area, and in particular for Acitrezza area are equal to V_0=198 m/s and α=0.19; substituting these values in the of Ibs-von Seht and Wohlenberg (1999) (equation 3; paragraph 2.2) the frequency values of the HV spectra were converted in depth values. The impedance contrast sections obtained (Fig. 6.51), in this case no clear effects of the presence of the tectonic structure are visible, contrary to what observed in the other two investigated areas. This is probably because the clayish substrate outcropping in the

area conceal the clues of brittle deformation features, or because the effect of velocity inversion hides the possible traces of the tectonic structure. It is evident in some sections the effect of the velocity inversion, in fact in the first meters of depth are observable HV amplitude values less than one.

For the municipal area of Acicastello was not obtained the depth map of the layer that causes the resonance peak; the information on the velocity distribution in the subsurface available concerns only the northern sector where the clay substrate outcrops; it was not considered appropriate to use the V_0 and α parameters obtained for this area to depth convert the resonant frequency values obtained from the acquisitions performed in the southern portion of the municipality, characterized, instead, by outcrops of lava flows and volcanoclastic products with degraded surface morphology; at the same time it was not possible to retrieve information on the velocity distribution in the subsurface in this area in order to get the characteristic V_0 and α parameters for the site.

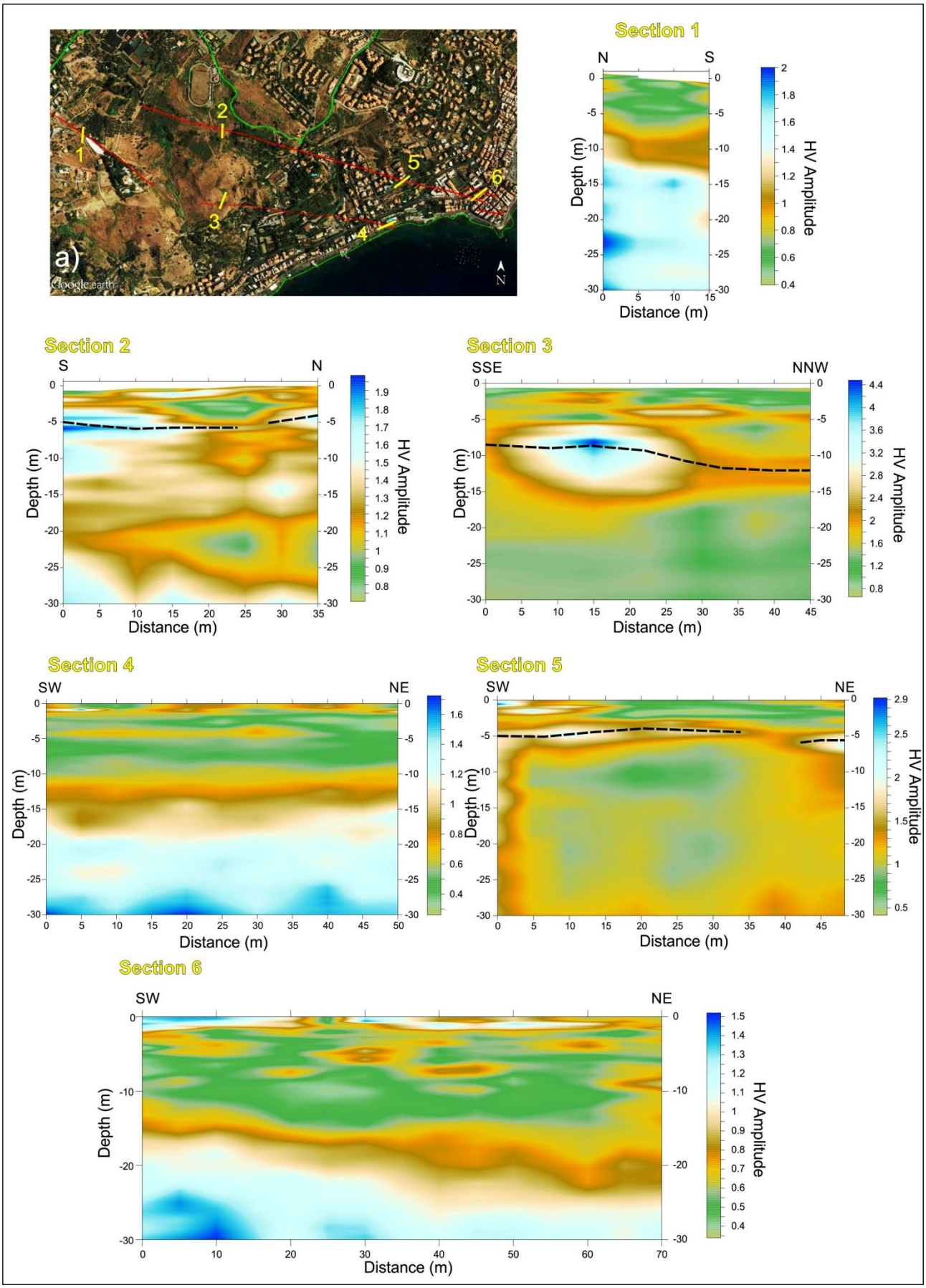

Fig. 6.51. Location of HVSR arrays (a) and impedance contrast sections performed orthogonally to the ATF fault segments. The dashed black line highlights the main impedance contrast

6.3.3. Geodetic monitoring of Acitrezza Fault

In order to analyze the deformation on surface and characterize the kinematic behavior of the area affected by the fault segments, a geodetic monitoring was performed using 9 of the 46 pillars installed previously by the Civil Engineering Office, to monitor the sliding motion of Vampolieri hill.

The nine benchmarks that make up the geodetic monitoring network (Fig. 6.52), used in this study, were selected according with the following criteria:

- absence of physical barriers above the positioning point of GPS antenna;
- proximity to the fault segments.

Fig. 6.52. a) Geodetic monitoring network of ATF fault segments; b) photograph of a monitoring point (45AT)

Four GNSS measurement campaigns were carried out between November 2014 and March 2016; they were performed in static mode, maintaining the receiver fixed on each station for about 5-6 hours, only a few recording were performed for a shorter time due to a wrong operation of the instrument. The measurements were performed by means the same instruments used for geodetic monitoring in San

Gregorio di Catania urban area (two GNSS dual frequency (L1+L2) satellite receiver-TOPCON HiPerV).

The calendar reported in table 6.11 shows all the information related to the measurement campaigns: survey date; reference number of monitoring station; day of the year (DOY); week; day of the week (GPS weekday); acquisition time; receiver type (B-base, R-rover); raw data name (.tps); Rinex file name; GPS and GLONASS precise final orbits; recording time.

The latest measurement campaign has been the most rigorous, have been carried out two recordings of six hours each on two different days, on each monitoring station, in order to get a better estimate and reduce the error.

#	MEASURE-MENT CAMPAIGN	SURVEY DATE	NUMBER OF MONITOR-ING STATION	DOY	WEEK	GPS WEEKDAY	TIIME OF ACQUISITION (h)	BASE 54/ ROVER 44	RAW DATA NAME (.tps)	RINEX FILE NAME
1	nov-14	141113	28	317	1818	4	6	B	541113i.tps	28at317a.14o
2		141210	33	344	1822	3	6	B	541210h.tps	33at344a.14o
3		141210	38				6	R	441210ha.tps	38at344a.14o
4		141217	32	351	1823	3	6	R	441217i.tps	32at351a.14o
5		141217	37				6	B	541217h.tps	37at351a.14o
6		150115	44	15	1827	4	2.5	R 2	rover46.tps	44at015a.15o
7		150115	45				6	B	base45.tps	45at015a.15o
8		150115	46				3	R 1	rover46.tps	46at015a.15o
9	giu-15	150611	28	162	1848	4	6	B	540611ga.tps	28at162a.15o
10		150611	32				4.5	R	440611ga.tps	32at162a.15o
11		150612	33	163	1848	5	6	B	540612ga.tps	33at163a.15o
12		150612	38				4.5	R	440612ga.tps	38at163a.15o
13		~~150619~~	~~44~~	170	1849	5	~~1~~	~~R 2~~	~~440619g.tps~~	~~44at170a.15o~~
14		150619	45				6	B	log0619ga.tps	45at170a.15o
15		~~150619~~	~~46~~				~~1~~	~~R 1 -R 3~~	~~440619g.tps~~	~~46at170a.15o~~
16		~~150619~~	~~41~~				~~1~~	~~R 4~~	~~440619g.tps~~	~~41at170a.15o~~
17		150626	37	177	1850	5	4.5	R	150626_.tps	37at177a.15o
18		150626	39				5	B	150626_.tps	39at177a.15o
19	ott-15	151005	28	278	1865	1	6	B	log1005fa.tps	28at278a.15o

20		151006	32	279	1865	2	5	R	441006f.tps	32at279a.15o
21		151007	33	280	1865	3	6	B	log1007f.tps	33at280a.15o
21		151007	38				5.5	R	441007f.tps	38at280a.15o
22		151008	39	281	1865	4	5.5	B	log1008f.tps	39at281a.15o
23		151013	44	286	1866	2	1.5	R 2	441013g.tps	44at286a.15o
24		151013	45	286	1866	2	6	B	log1013f.tps	45at286a.15o
25		151013	46				1.5	R 1	441013f.tps	46at286a.15o
26		151014	37	287	1866	3	4.5	R	441014f.tps	37at287a.15o
27	mar-16	160307	33	67	1887	1	5.25	B	log0307g.tps	
28		160307	38				6	R	440307g.tps	
29		160307	44				6	SR		
30		160307	45				6	SR		
31		160308	33	68		2	5	B	log0308.tps	
32		160308	38				6	R	440308g.tps	
33		160309	28	69		3	5.25	B	log0309g.tps	
34		160309	32				6	R	440309g.tps	
35		160310	32	70		4	6	R	440310f.tps	
36		160311	44	71		5	6	SR		
37		160311	45				6	SR		
38		160311	46				6	R	440311i.tps	
39		160315	46	75	1888	2	6	R	440315f.tps	
40		160316	39	76		3	6	R	440316f.tps	
41		160317	39	77		4	6	R	440317f.tps	
42		160318	28	78		5	6	R	440318f.tps	
43		160322	37	82	1889	2	6	R	440322f.tps	
44		160323	37	83		3	6	R	440323f.tps	

Table 6.11. Calendar of Aci Trezza geodetic measurement campaigns

The raw data were elaborated a; also in this case, the final result is the estimate of the deformation field (velocity [mm/a]) relative to the Etn@ref reference system (Table 6.12 - Fig. 6.53).

SITE	LONG	LAT	Evel (mm/a)	Nvel (mm/a)	E err (mm/a)	Nerr (mm/a)	Hvel (mm/a)	H err (mm/a)	Vector (mm/a)
28AT	15.15966	37.56146	13.57	-6.34	6.17	5.45	-680.68	26.61	14.978
32AT	15.1553	37.56268	30.38	-10.35	3.82	4.49	23.07	16.43	32.09466
33AT	15.15613	37.56142	41.78	-1.67	3.49	3.91	52.94	18.08	41.81336
37AT	15.15316	37.56103	28.01	-8.59	5.06	4.66	-18.87	23.4	29.29758
38AT	15.15514	37.5601	19.1	-6.29	6.48	5.98	-732.15	28.92	20.10906
39AT	15.14673	37.56373	46.63	-14	3.37	3.37	-4.39	12.78	48.68631
44AT	15.13989	37.56366	33.31	-26.6	5.14	5.89	-3.69	22.13	42.62764
45AT	15.14189	37.56267	16.41	-27.25	3	2.98	49.08	11.65	31.8096
46AT	15.14292	37.56219	48.11	-22.91	13.33	7.41	18.73	26.95	53.2864
CTAC	15.07712	37.53228	-6.2	-9.05	0.6	0.62	0.83	2.04	
EBAG	15.161	37.70235	21.54	-11.02	2.4	0.67	-15.29	2.89	
EIIV	15.08208	37.5136	1.13	-3.48	0.47	0.59	-1.49	1.53	
ELAC	15.16641	37.56131	186.87	-64.82	11.62	8.61	263.73	47.4	
ENIC	15.01965	37.61386	5.92	-8.1	0.7	0.64	-4.82	2.33	
EPMN	15.17742	37.82063	3.9	-0.29	0.92	0.66	2.16	1.52	
EPOZ	15.18854	37.67193	34.9	-14.02	3.05	0.99	-7.3	1.6	
ERIP	15.1976	37.72844	31.24	-9.74	2.04	1.34	-5.51	2.05	
ESAL	15.13453	37.75509	23.41	-14.29	1.63	0.88	-6.71	2.58	
ESLA	14.97433	37.69342	3.07	-16.66	1.18	0.56	-1.21	3.25	
MASC	15.19575	37.75897	31.41	-12.25	1.15	0.95	-20.44	2.07	

Table 6.12. The table states velocity vector values for each component (N, E and H) and the associate error relating to the 9 measurement stations located in the Aci Trezza area; it is also indicated the vector value of Horizontal GPS velocities for each station

Due to the limited number of measurements carried up to this moment, the data relative to the vertical component are not considered, indeed the error on this component is very high (table 6.12).

Comparing the values of the east component of velocity vectors (Table 6.12) related to monitoring points located on opposite sides of the fault segments, it is possible to confirm the right-lateral strike-slip kinematics of the fault segments (e.g. [33AT-38AT ≈ 20 mm/a]).

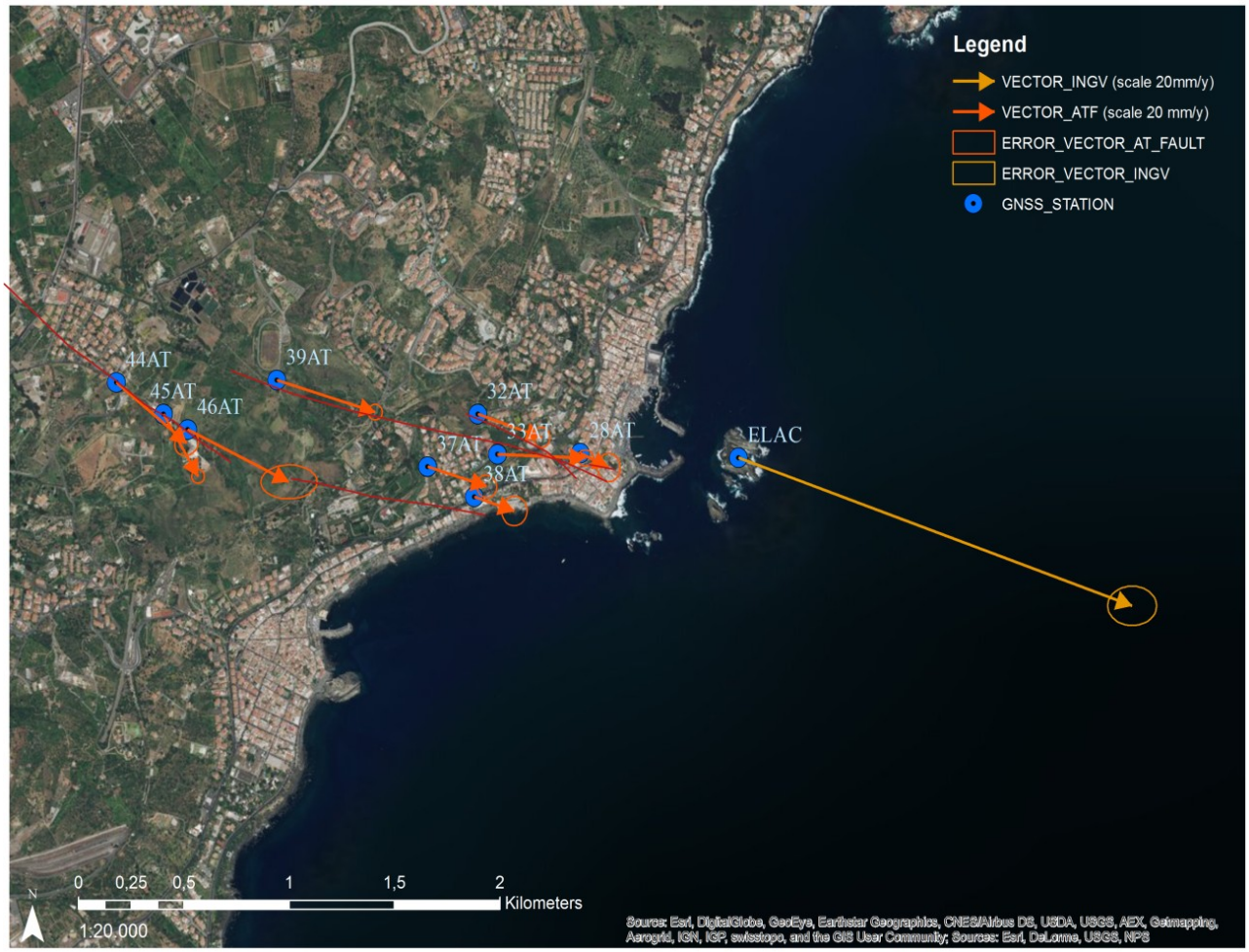

Fig. 6.53. Velocity field (2014– 2016) of the GNSS stations located in the Aci Trezza area; the orange arrows indicate the Horizontal GPS velocity vectors with 95% confidence ellipses in the Etn@Ref reference frame (Palano et al., 2010); it is also shown the Horizontal GPS velocity vector for ELAC permanent station, calculated for the same period (yellow arrow)

Chapter VII

7.0. Modeling of the slip distribution along the southern boundary of Mt Etna unstable sector: general information to fault geometry construction

Fault's geometry and kinematics can be directly inferred either from the long-term fault scarps that reflect the cumulative displacement and are usually well exposed, but also from coseismic (or from slow slip events) ground ruptures. Most normal faults are concave upward, or listric and this shape could be due to geometric constraints, or rheology variations at depth (Jackson and Mckenzie, 1983). If the displacement on faults is driven by gravity alone, the footwall is not deformed by its movement, conservation of mass requires that the downward displacement of the material at the top of the moving body should be balanced by upward movement of the material at its bottom. And hence the displacement surface must intersect the Earth's surface at the base of the moving block as well as at its top, these conditions require growth faults and slip surfaces to be concave upwards (Jackson and Mckenzie, 1983) .

The same conditions do not apply to listric faults when they take up the motion at plate boundaries. In most case the fault plane solutions showed that the fault dips at the foci of the main shocks were approximately 45°. With increasing depth these faults cease to be slip surfaces and become shear zones. Finally, if the crust is sufficiently thick, or at a high enough temperature, the lowest crustal layer creeps homogeneously and aseismically, without any discrete faults being formed. The depths at which these transitions occur must depend on the temperature gradient (Jackson and Mckenzie, 1983). The dip of young normal faults is often very steep at the surface, this is invariably because the top few tens of meters near the ground surface mainly fail in tension, not shear, commonly leaving open fissures and cracks. The surface of an oblique-slip fault may be vertical at depth and convex upward but flattens to horizontal at the surface (Allen, 1965; Lowell, 1972; Wilcox et al., 1973; Sylvester and Smith, 1976), or may be nearly vertical at the surface and concave-

upward but flattens at depth into the main strike-slip fault (Harding, 1983; Harding et al., 1985; Naylor et al., 1986).

Concerning the Etnean volcanic complex a number of geophysical and geological studies focusing on the NE Rift - Pernicana fault system allowed to map on the field and to characterize the different seismic behavior of the various segments composing the fault system, from the summit of the volcano down to the coastal area (Alparone et al., 2013; Acocella and Neri, 2005). In addition, the shallow geometry (~1 km from the surface) has been imaged by geophysical-geochemical and magnetotelluric data (Siniscalchi et al., 2010; 2012) while geodetic inversion models (Bonforte et al., 2007; Currenti et al., 2010; Guglielmino et al., 2011) have provided constraints on the deep geometry (2-3 km) of the fault system. Conversely, little is known about the geometry at depth of the "S Rift-Tremestieri-Trecastagni-San Gregorio-Acitrezza" fault system. Although some fault segments are known with a reasonable detail, the constraints about faults widths are provided only by geodetic inversion models (Azzaro et al., 2013; Palano, 2016).

7.1. Construction of the fault system model

The surface geometry of Tremestieri-Trecastagni-San Gregorio-Acitrezza fault system has been reconstructed by performing geological, structural and geophysical surveys.

The deep geometry of this system was modeled through a complete review of the literature (Monaco et al., 1997; 2010; Neri et al., 1997; Azzaro, 1999; Chiocci et al., 2011; De Guidi et al., 2012; Azzaro et al., 2013; Imposa et al., 2015a; Palano 2016) supported by theoretical modelling (e.g. Allen,1965; Lowell, 1972; Wilcox et al., 1973; Sylvester and Smith 1976; Jackson and McKenzie, 1983; Harding et al., 1985; Naylor et al., 1986).

The pattern of the surface deformation observable by InSAR images and the recent GPS measurements indicate that slip along the studied fault system is not

uniform; to better characterize the kinematics along the fault surfaces an inverse modeling of DInSAR deformation data was carried out.

New detailed field survey allowed to recognize and map new structural lineaments and features. Also the ground displacement observed in DInSAR image well evidenced the dislocation along the fault traces, which is in good agreement with field mapping of surface rupture. DInSAR imageries well constrain the length and strike of fault segments at the surface. In order to simplify the spatial complexity of the fault system, the model was created taking into account seven fault segments, with the characteristics indicated in Table 7.1.

Faults	Length (m)	Average Strike	Avarage Dip	Width (km)	Dominant faulting style
Tremestieri (TMF)	5250	135°	75°	1,6	Dextral, oblique slip
Trecastagni (TCF)	3000	150°	70°	1,6	Dextral, oblique slip
S. Gregorio-Acitrezza (SG-ATF)	7750	102°	90°		Oblique, dextral strike-slip
S. Gregorio_Northern[a] (SGNF)	1080	0°	60°		Normal
Nizzeti_West (NZWF)	3250	0°	70°		Normal, with right-lateral components
Nizzeti_East (NZEF)	3250	0°	70°		Normal, with right-lateral components
Acitrezza (ATSF)	1250	98°	90°		Oblique, dextral strike-slip

[a] Tectonic lineament revealed by structural and geophysical surveys.

Table 7.1. Geometric and kinematic parameters of active faults proposed for modelling kinematics of the southern boundary of Mt Etna unstable sector (modified from Azzaro et al., 2012a);. Note that the most critical definition concerns the dip and width of the faults, which have been inferred from the inversion of ground deformation data; for this reason, in some cases they are not available.

The fault geometry at depth assumed for the modeling was reconstructed taking in account that i) the TMF, TCF and SGNF represent young normal faults and therefore their shear planes are probably very steep; ii) the age of the NZWF and NZEF is 120–100 ka (Monaco et al., 1997), thus their probably tend to develop downdip with an approximate dip angle of 45°; iii) conversely the SGF and ATF are oblique-slip faults and their surfaces can be considered to be nearly vertical both at depth and at the surface (Imposa et al., 2015).

Considering that the seismogenic layer below the eastern flank of Mt. Etna is very thin and most of the earthquakes are confined in the very upper crust (< 6 km depth; Monaco et al., 2005; Patanè et al., 2006; Catalano et al., 2010; De Guidi et al., 2012; Gudmundsson et al., 2013) and that different models have proposed for the sliding of eastern flank of Mt. Etna a decollement surface located at a depth ranging from 1 to 5 km bsl (Lo Giudice and Rasà, 1992; Borgia et al., 1992; Tibaldi and Groppelli, 2002; Palano et al., 2008; Palano 2016), the fault surfaces have been discretized from the free surface down to a maximum depth of 3000 m. It is probably that the faults of the eastern flank of Mt. Etna accommodate at the brittle-ductile transition.

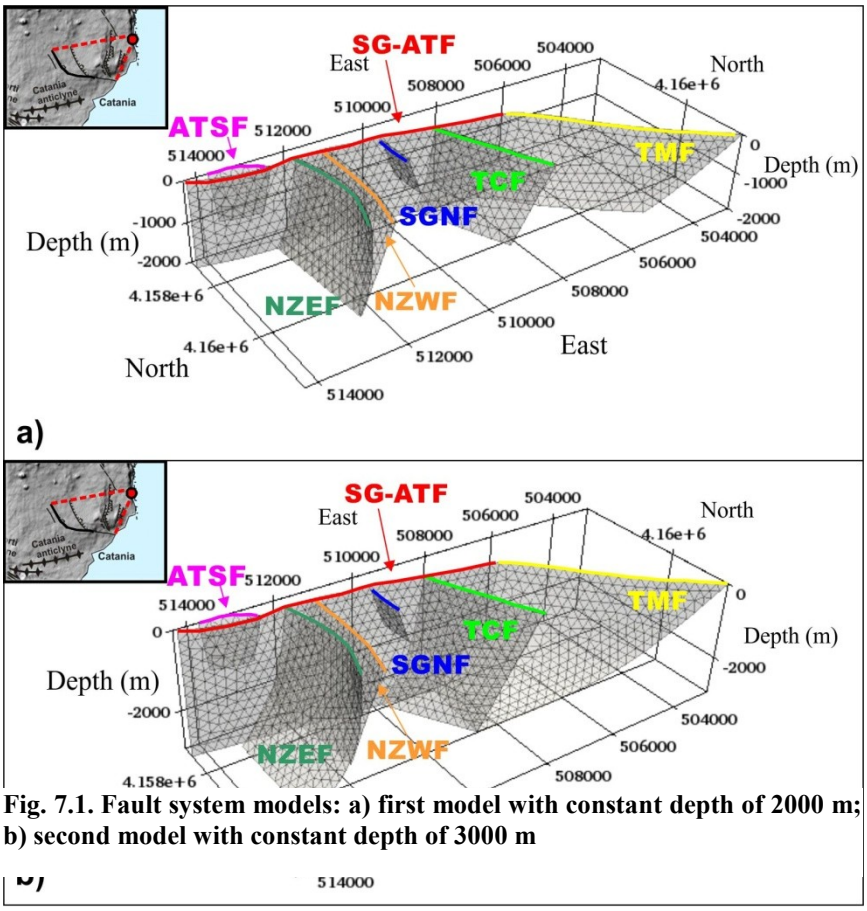

Fig. 7.1. Fault system models: a) first model with constant depth of 2000 m; b) second model with constant depth of 3000 m

The inverse modeling of InSAR deformation was performed using three different fault system models, with same geometry but with a different evolution at depth.

In the first two models the fault surfaces are limited at a depth of 2000 and 3000 m, respectively (Fig. 7.1). In the third model the fault segment SG-ATF has a constant depth of 3000 m from north to south; in order to draw the geometry at depth of the other structures a listric geometry on a hypothetical 10°-dipping surface (not considered in the inversion process) has been considered (Fig. 7.2).

Because of the non-planar geometry of this fault surfaces, the fault system was represented as a set of triangles, which better adapt to the complex geometry. This

meshing process was carried out using CUBIT (2015) software (supplied by INGV, Catania section), a specific software for robust generation of two and three dimensional finite element meshes (grids) and geometry preparation. The fault surfaces were discretized into triangular elements (Figs. 7.1, 7.2), with mesh resolution of 250 m; this discretization allows the construction of three-dimensional fault surfaces that more closely approximate curviplanar surfaces and curved tip lines, consistent with the full extent of available data.

The first two models have been discretized into 1693 and 2388 triangular elements, respectively; the third model with variable depth has been discretized into 2140 triangular elements.

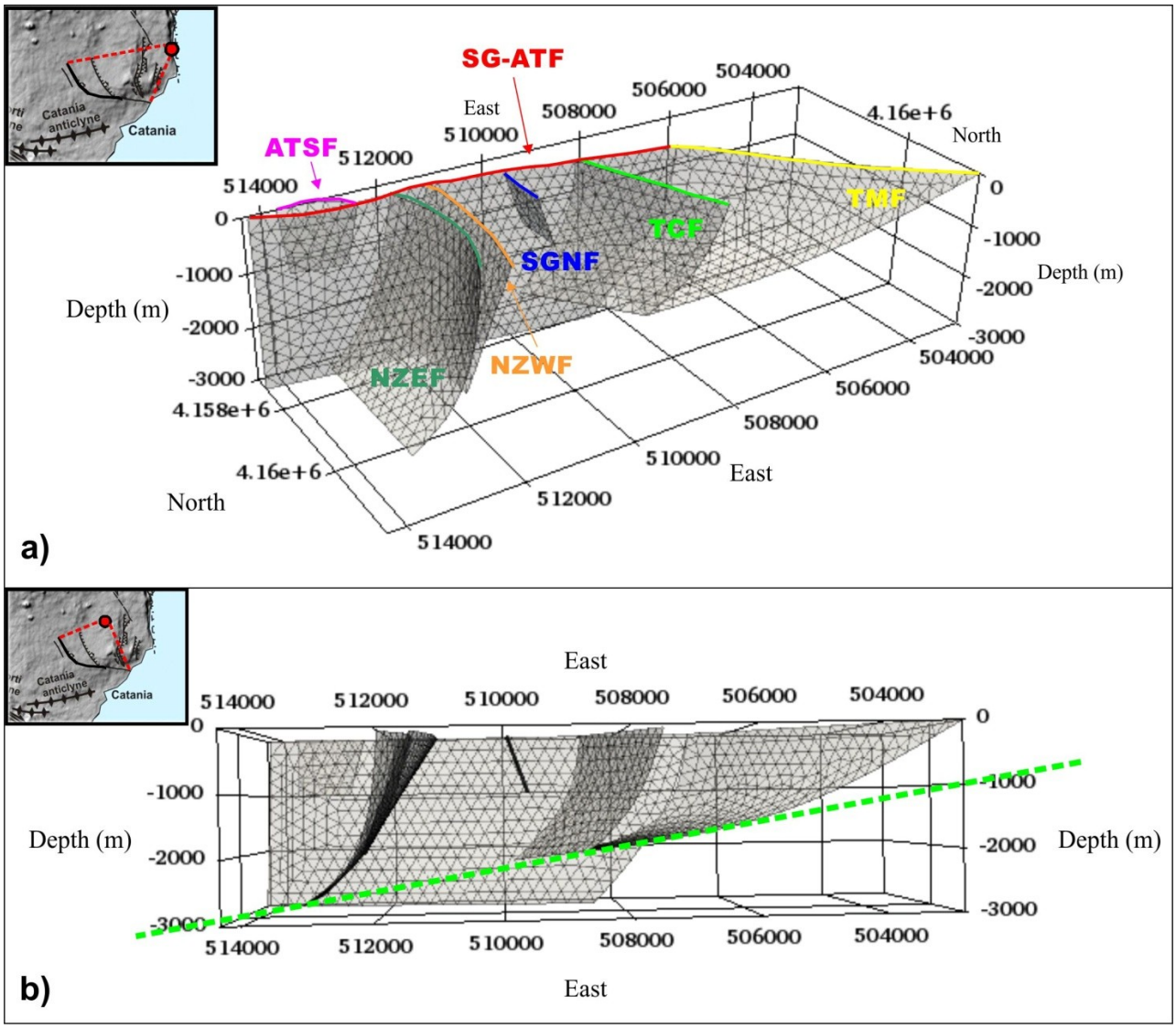

Fig. 7.2. a) Third fault system model; b) the SG-ATF fault segment has a constant depth of 3000m from north to south, the other fault segments have a listric geometry on a hypothetical plan (not considered in the inversion process) 10° tilted, so the model has variable depth (between 1000 m and 3000 m).

7.2.1. DInSAR data

The InSAR deformation was obtained by applying the Small Baseline Subset (SBAS) algorithm (Berardino et al., 2002) on two independent sets of X-band SAR imageries acquired over the volcano from Cosmo-SkyMed (CSK) radar system on ascending and descending orbits. The former was composed of 155 SAR imageries, collected from 12 July 2009 to 5 March 2013 (ascending passes, HH polarization). The latter consist of 87 SAR scenes collected from 23 July, 2011 to 3 March, 2015 (descending passes, HH polarization). From these SAR data, two groups of small

baseline interferometric SAR data pairs were identified. In particular, 356 and 198 differential SAR interferograms from the ascending and descending orbits, respectively, have been generated. For the interferogram generation, a three-arcsec Digital Elevation Model (DEM) of the Mt. Etna area obtained by the Shuttle Radar Topography Mission (SRTM) was used. Moreover, a complex multilook operation with 10 looks both in the range and azimuth direction and twenty looks in the azimuth direction was applied. The SBAS technique allowed the generation of radar line-of-sight (LOS) displacement time series of the investigated area over a set of high coherent pixels (Pepe and Lanari, 2006, Pepe et al., 2011). Residual topographic artifacts as well as the atmospheric phase disturbances were estimated and filtered out from the achieved displacement time-series. The InSAR images that show the deformation along the Line of Sight (LOS) for ascending and descending orbits were supplied by the I.R.E.A. (Istituto per il Rilevamento Elettromagnetico dell'Ambiente) of Neaples.

Depending on the available SBAS-DInSAR time series, the displacement induced by a slow slip event occurred in the investigated area from mid-May 2012 to the end of the month (Palano, 2016) was investigated. In particular, the LOS cumulative deformation from 10 May 2012 to 4 July 2012 for the ascending orbit (Fig. 7.3) and from 7 May 2012 to 2 July 2012 for the descending orbit (Fig. 7.4) were computed.

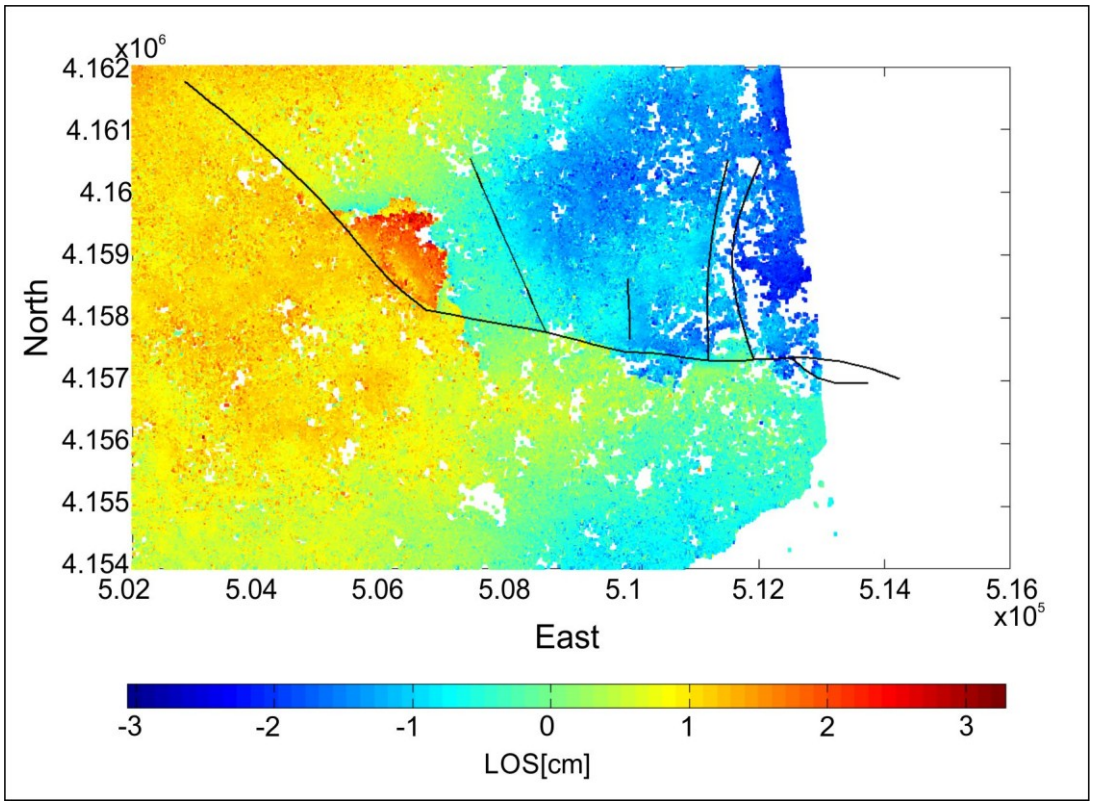

Fig. 7.3. Cumulative LOS displacements obtained by applying the SBAS processing to CSK images acquired along the ascending orbit; the cumulative displacements refer to the period from 10 May 2012 to 4 July 2012. The black lines represents the trace of the model's fault segments

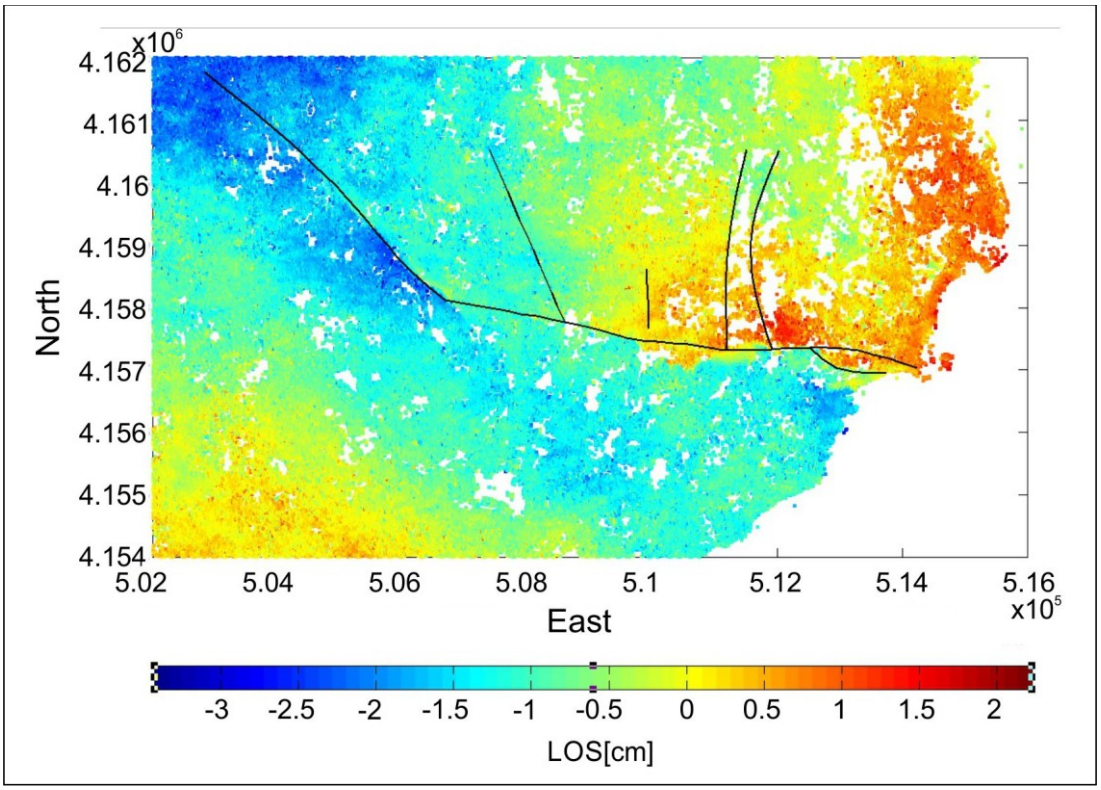

Fig. 7.4. Cumulative LOS displacements obtained by applying the SBAS processing to CSK images acquired along the descending orbit; the cumulative displacements refer to the period from 7 May 2012 to 2 July 2012. The black lines represents the trace of the model's fault segments

In order to limit the computational burden in the modelling inversion, the number of DInSAR observations was reduced by a sub-sampling procedure (Fig. 7.5), ending up with a final dataset of 2089 points for the ascending orbit and 2442 points for the descending orbit. Note that the number of usable ascending points is less than usable descending points because the acquisitions of CSK radar system, in ascending orbit, do not cover the coastal strip; for this reason I decided to exclude from the complete model, created to perform the inversion of DInSAR data, the tectonic structures that fall within the area not covered by InSAR data of ascending orbit.

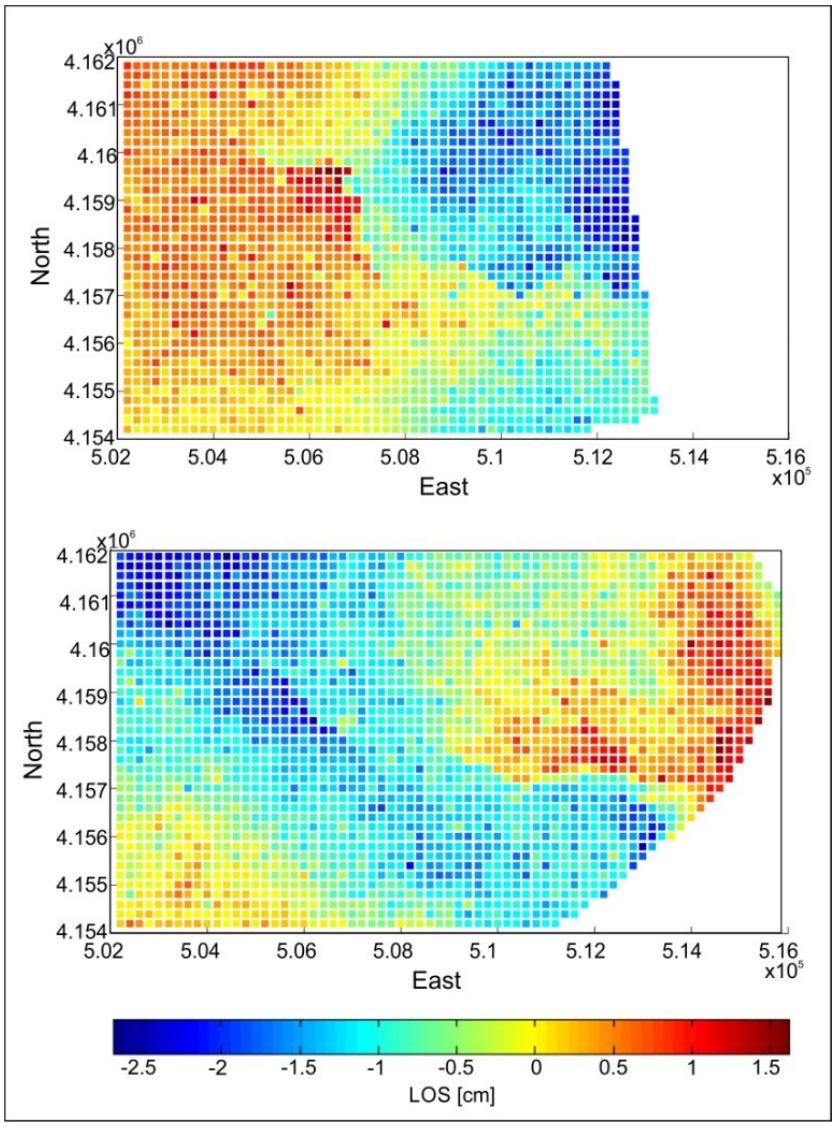

Fig. 7.5. Deformation patterns, projected along the LOS, obtained after applying the sub-sampling procedure - for ascending (top)and descending (bottom) DInSAR data.

7.2.2. DInSAR Kinematic Modeling: slip distribution models

The DInSAR dataset obtained by the sub-sampling procedure were used to derive the slip along the fault surfaces by using a numerical inversion procedure (Currenti et al., 2012). The inversion procedure can be summed up in three main steps:

(i) meshing the computational domain and subdividing the fault surface in a finite number of elements;

(ii) computing the Green's functions for static displacements caused by unit slip over each element;

$$d_i = \sum G_{ij} s_j$$

where d_i= displacement

G_{ij}= Green's function

s_j= slip

(iii) solving an inversion problem constrained by geodetic data to determine the slip distribution.

The first step has been already discussed; the computation of the Green's function of each triangle was performed using the solution devised by Meade (2007) for triangular dislocation elements in a uniform elastic half space. The DInSAR data, which provide a dense spatial resolution able to ensure a robust inversion, were used to calculate the slip in each patch by means of a Quadratic Programming (QP) algorithm with bound and smoothening constraints based on the second order spatial derivative to suppress slip oscillations (Currenti et al., 2010).

The unknowns number of inversion problem, for each fault system model, is the results of the product between the number of triangular elements and the constraint types on slip imposed to the solution. The constraints of the solution were imposed in agreement with the historical activity of the fault segments (Solaro et al., 2010; Bonforte et al., 2011; Chiocci et al., 2011; Azzaro et al., 2012; 2013; Imposa et al.

2015a, b); therefore were imposed right-lateral strike slip, normal dip-slip and small tensile constraints, thus formalizing an inversion problem with 5079 unknowns on slip components for the first model, 7164 for the second model and 6420 for the last model.

The inverse problem can be re-formulated as an optimization problem aimed at finding the unknown slip values that minimize a data misfit and a smoothing functional; as smoothing functional, the Laplacian Operator was used to avoid large variations between neighboring dislocations.

The deformation patterns, projected along the LOS, for ascending and descending DInSAR data, computed from the best-fitting model and the corresponding residual with respect to the observed data (Fig. 7.5) are shown in figures 7.6, 7.7 and 7.8.

The Root Mean Square Error (RMSE) of the residual obtained for the different fault system models is reported in Table 7.2.

Fault System Model	**RMSE[m] (ASCENDING)**	**RMSE[m] (DESCENDING)**	**RMSE[m]**
I° Model	6.216779e-003	7.167591e-003	6.671970e-003
II° Model	5.343583e-003	5.381393e-003	5.361047e-003
III° Model	6.283692e-003	5.878690e-003	6.100316e-003

Table 7.2. Root Mean Square Error (RMSE) of the residual, computed for the different models

The RMSE between the data and the model prediction is slightly lower in the second and third fault system models. The deformation patterns, measured by the DInSAR data are well predicted by the retrieved model. The combination of right-lateral strike slip, normal dip-slip and tensile well reproduces the LOS cumulative deformation, computed in the investigated time interval, for the ascending and descending orbits. The resulting inversions show that the model, closely describing the geometry of the surface ruptures, produces good fit to the geodetic data.

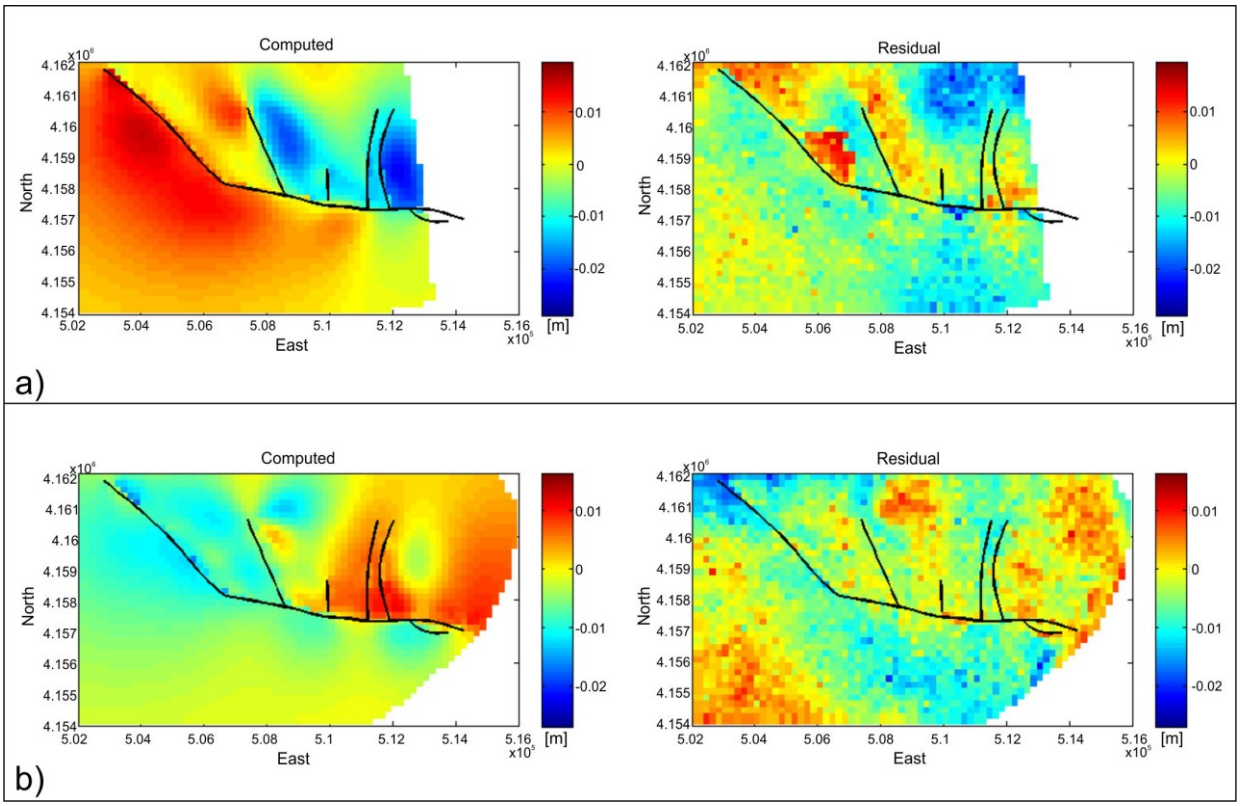

Fig. 7.6. Deformation patterns, projected along the LOS, for ascending (a) and descending (b) DInSAR data, computed (left) from the first fault system model and the corresponding residuals (right) with respect to the observed data

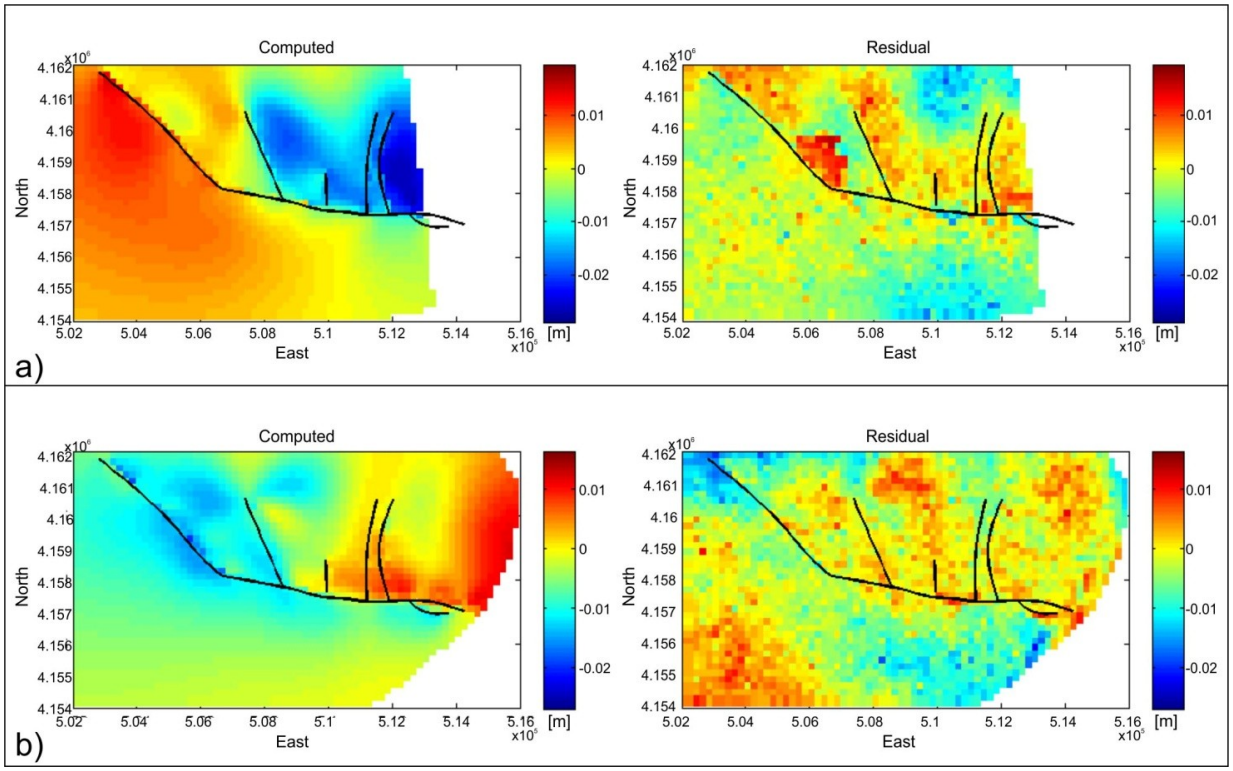

Fig. 7.7. Deformation patterns, projected along the LOS, for ascending (a) and descending (b) DInSAR data, computed (left) from the second fault system model and the corresponding residual (right) with respect to the observed data

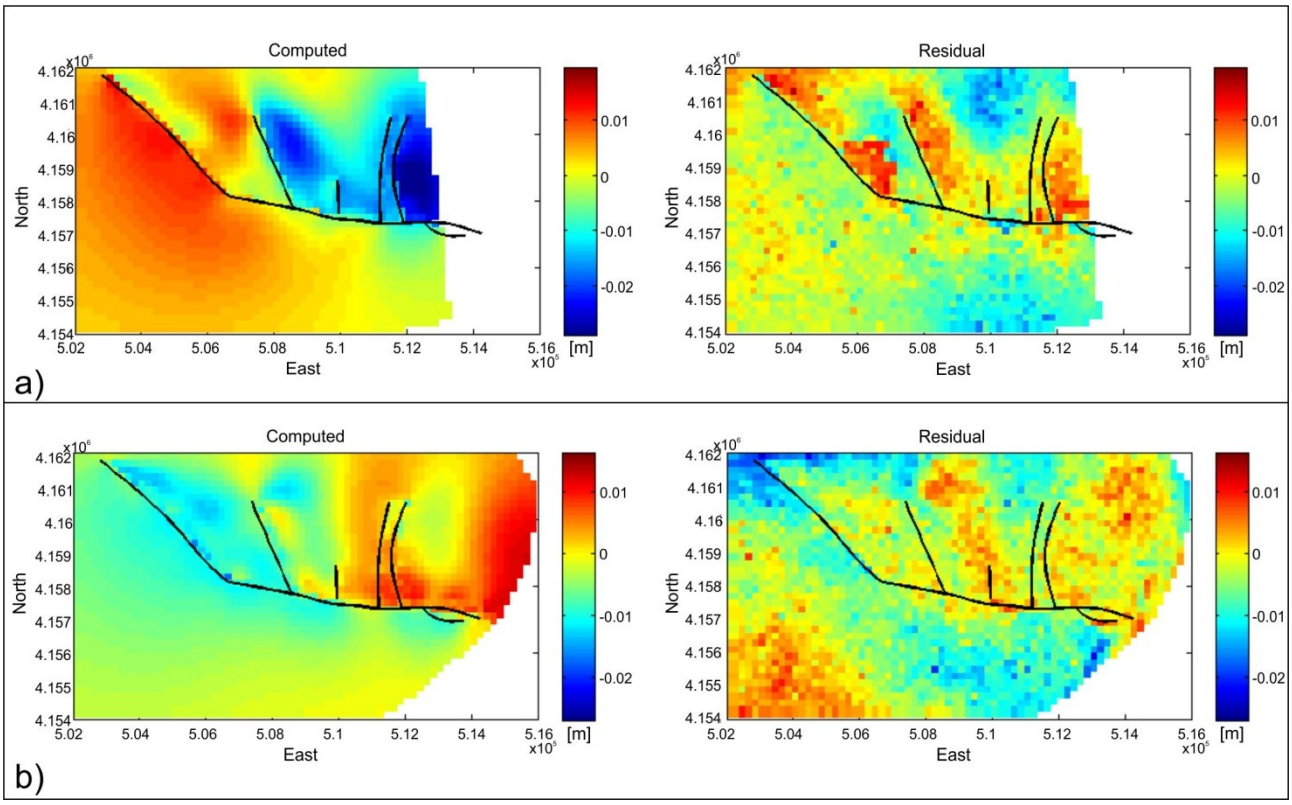

Fig. 7.8. Deformation patterns, projected along the LOS, for ascending (a) and descending (b) DInSAR data, computed (left) from the third fault system model and the corresponding residual (right) with respect to the observed data

Using variable strike–slip and dip–slip fault kinematics, the numerical model highlights a heterogeneous slip distribution along the fault system, characterized by a prevailing right-lateral strike-slip motion, associated with a normal dip–slip component in the fault segments with NNW-SSE trend. Observing the slip distribution models (Figs. 7.9-7.10) obtained with the joint inversion of ascending and descending DInSAR data, it is possible to note that the amplitude of the tensile component is negligible with respect to the strike-slip and dip-slip components, confirming the dominant modes of the fault system.

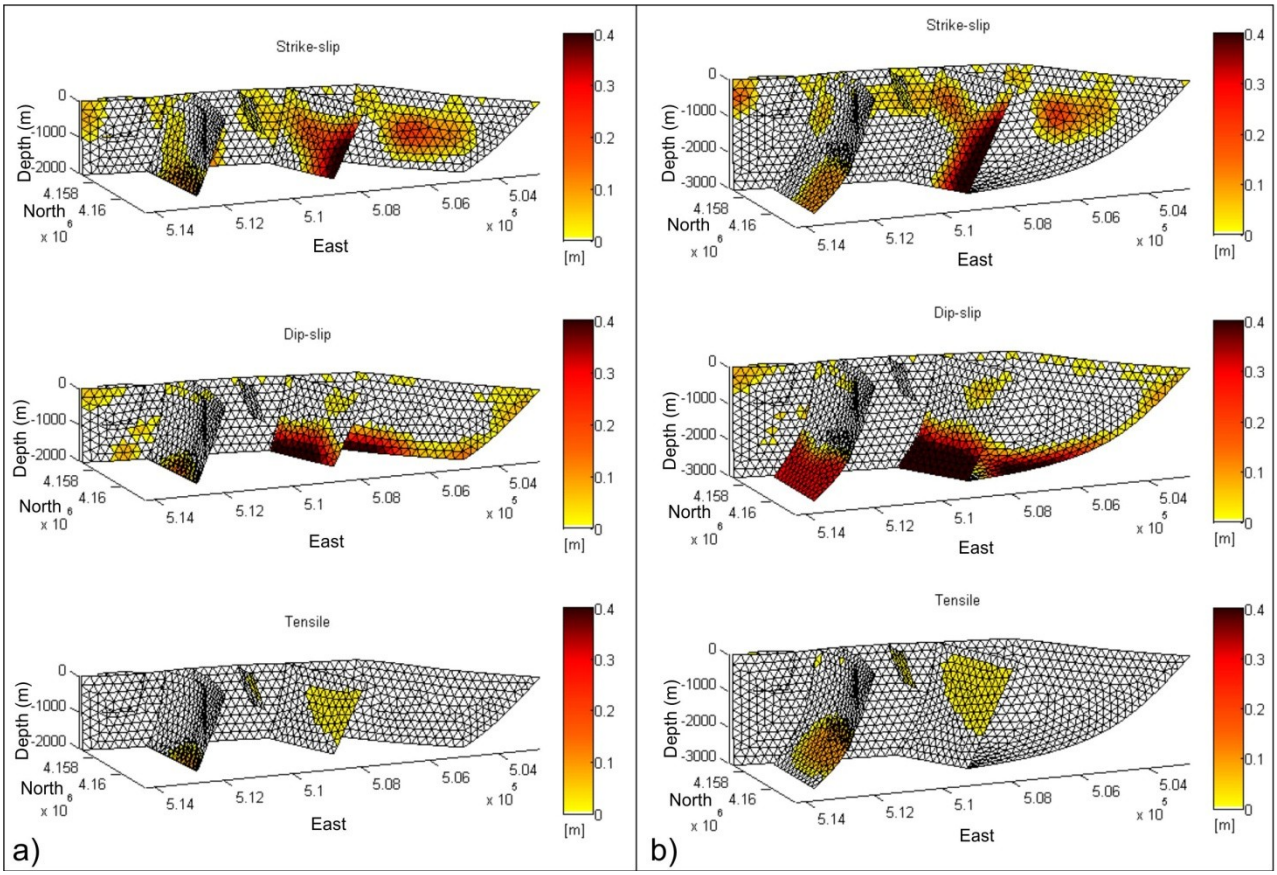

Fig. 7.9. Slip distribution along fault planes for the first (a) and the second (b) models: strike-slip (top), dip-slip (middle) and tensile (bottom)

The third numerical model (Fig.7.10) shows a predominant strike–slip kinematics concentrated in a rather shallow layer, decaying within 1000 m from the topographic surface; only for NFEF the strike-slip component is concentrated at greater depth. The largest strike–slip component (about 0.4 m) is observed in correspondence of the TCF with a longitudinally elongated extension approximately equal to the width of the fault segment. Other significant (0.2-0.3 m) strike-slip components are also concentrated in various portions of the TMF and SG-ATF fault segments with lower longitudinal extension. The amplitude of the normal dip–slip component reaches a maximum of about 0.3-0.4 m at the base of the NZF and TCF fault segments; this can be considered indicative of a kinematic transfer to the base of these fault segments, that may support the hypothesis of the eastward slipping trend along a slightly inclined plane, like the one assumed in this model. Other significant dip-slip components are observed along the TMF fault segment; these are concentrated to lower depth and with minor longitudinal extension. As said before,

the tensile component is found to be negligible with respect to strike-slip and dip-slip components; the tensile component is observable, with low amplitude, only on SGNF, TCF and in the lower portion of the NZF fault segments.

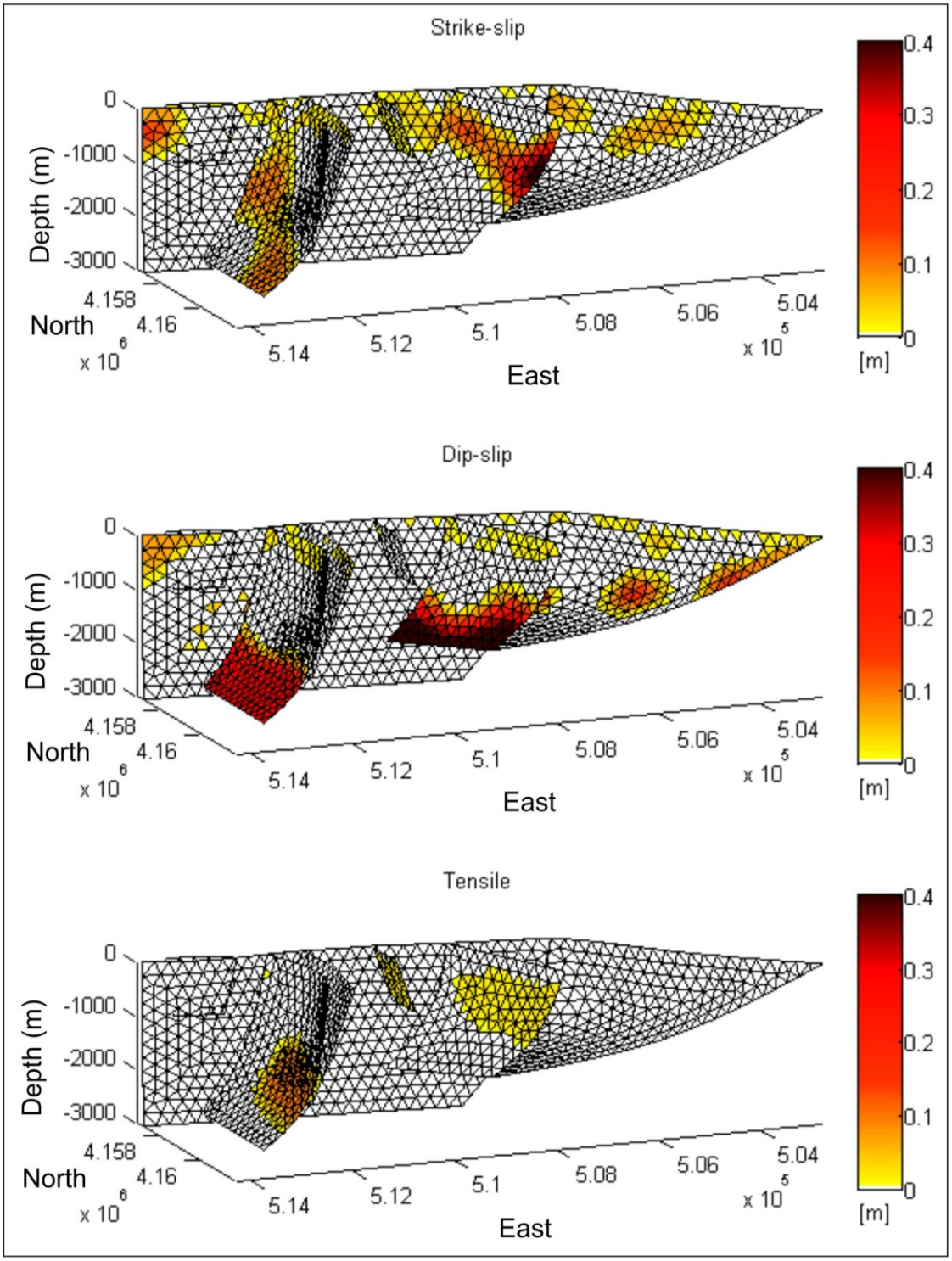

Fig. 7.10. Slip distribution along fault planes for the third model: strike-slip (top), dip-slip (middle) and tensile (bottom)

The slip is often detectable in the model at shallow depth, even if with lower than maximum amounts. This suggests that the slip occurred in the very shallow layers characterized by reduced strength properties, which is indicative of the high degree of cracking along the fault segments as confirmed by the structural and geophysical surveys. It is reasonable to assume that slip occurs in areas where a strong reduction of effective elastic moduli can be expected and interpreted in terms of changes in the micro-crack density or the effective damage parameters.

Discussions and conclusions

The results of several studies carried out recently in the Etnean area, based on geological and geophysical surveys, have shown that the subsoil is characterized by considerable lateral-vertical variability of the seismic waves velocity, probably due to the pronounced anisotropy of lava products with respect to the sedimentary substratum, composed by both allocthonous Triassic formation and Pleistocene marly-clays. The different geo-lithological conditions and the presence of active structural lineaments, strongly influence the local seismic response. The entire edifice of Mt. Etna volcano is deeply conditioned by a network of active tectonic lineaments that control its morphology and kinematics during eruptive or earthquake cycles (Bonforte et al., 2011). This network often intersects and affects infrastructure and urban areas. An active fault whose coseismic displacement can intercept the ground surface is defined as *capable* (Machette, 2000; Galadini et al., 2012), while the corresponding earthquakes are defined as *linear morphogenic events* (Caputo, 2005).

The faults characterized by 'aseismic' slip (creep), either episodic or constant over time, should be considered similar to the capable faults. The surface displacement of such faults can disrupt, rotate or cause structural damage to buildings and infrastructure lines located along, or in proximity of, the fault trace. Consequently, in a densely urbanized area, like the eastern slope of Mt. Etna, surface fault rupture hazard is very high (Azzaro et al., 1998b; Azzaro, 1999; Neri et al., 2004; Blumetti et al., 2007; Imposa et al., 2015b). To optimize the territory management and ensure the best mitigation procedures from the effects of possible rupture events, a detailed study of the active tectonic structures is essential (Imposa et al., 2004; Boncio et al., 2012; Peronace et al., 2013).

In the present research, I investigated the active fault system “Tremestieri-Trecastagni-San Gregorio-Acitrezza” that can be considered the southern boundary of the sliding sector of Mt. Etna. This natural “laboratory” consists of numerous fault segments characterized by different kinematic (from strike-slip to normal dip-slip)

and different modes of strain energy release (coseismic deformation and 'aseismic' creep). Such tectonic structure can be therefore considered as representative of all different kinematics and different strain energy release modes that characterize the active shear structures of the Etnean eastern slope. Furthermore, the northern boundary of lateral sliding (Pernicana Fault System) has been extensively studied and information on the fault planes and their development at depth are already available. Conversely, very little is known about the depth geometry of the Tremestieri-Trecastagni-San Gregorio-Acitrezza fault system. The fault segments associated with the latter were precisely mapped on the basis of detailed geological and geomorphological field work.

In the San Gregorio di Catania area, the multidisciplinary approach combining and integrating the classic surface survey with different geophysical methods, has enabled us to obtain a very accurate model of the geological structure, especially in the first 15 m-depth. It was thus possible to define the areas where the existing artefacts are susceptible to damage as a consequence of surface propagation of the ruptures; this damage zone has a highly variable width, that usually ranges between 5 and 10 m, reaching more than 40 m in the central portion. However, it is not possible to definitively exclude that future displacements could occur outside of the detected zone. The detailed scale of structural survey has also permitted to map a secondary structure in the urban area which extends north of the main fault segment trending approximately N-S. The presence of this secondary tectonic structures was later confirmed on the basis of several passive seismic single station surveys and from the careful analysis of the directional effects.

The seismic site response of the zones affected by the fault segments and of the surrounding areas was characterized by means of several geophysical surveys.

The multidisciplinary approach combining and integrating the classical structural surface survey and geophysical methods, has provided reliable results for the study of fault zones and allowed the identification of fault segments that had not been previously mapped (SGNF- San Gregorio North Fault segment).

The results of HVSR surveys have been used to reconstruct the distribution of resonance frequency for the municipalities affected by the fault system; this have allowed to distinguish areas characterized by different resonance frequencies related to different geological and structural characteristics. The observed resonance frequencies also allowed to identify the zones where the seismic motion would be more amplified in case of seismic shaking, providing an estimate of the minimum amplification value expected at the site. The areas with higher amplification, besides being attributable to the existence of strong impedance contrasts in the subsoil, are often located near the fault segments. The uniform distribution of HVSR investigations, within the municipal territories allows to get detailed information on the values of frequency and amplitude resonance characterizing the investigated areas; this can be considered an important tool that could be used as a base for future microzonation studies.

Furthermore, the obtained results provide important information and indications that can be helpful to plan possible urban expansion as well as an retrofitting to what is already built. The resonance frequency of soil is an extremely important datum that must be considered in the building design phase. Indeed, the building resonance frequency must not match with the soil frequency to avoid the occurrence of double resonance soil-structure phenomena.

The directional analysis of resonance has highlighted the occurrence of systematic effects that appears to be influenced by the predominant fractures direction characterizing the deformation zone, and by dominant faulting style. In the San Gregorio area a directional effect was observed parallel to the azimuth direction of the detected fractures in the fault segments with a strike-to-oblique-slip dextral kinematics. Conversely a directional effect orthogonal to the azimuth direction of the fractures was detected for the fault segments with normal kinematics.

The analysis of directional resonance for the data acquired in the Municipality of Tremestieri Etneo has highlighted the presence of directional effects with systematic orientation, approximately E-W, in an area north and away from the fault segment.

Due to the distance, it is not possible to connect this systematic effect to the presence of the known fault segments, but it could be possibly linked to an extremely fractured area, which could indicate the presence of an additional fault segment. The seismo-stratigraphic structure of the subsoil has been highlighted through the integration between data acquired by HVSR surveys and the information on shear waves velocity distribution obtained by applying other geophysical techniques (e.g. MASW). Such data allowed to reconstruct the impedance contrast sections, which highlight the presence in the subsoil of areas with different seismo-stratigraphic characteristics. It is interesting to note that in some of the sections performed perpendicularly to the fault segments, the main impedance contrast appears interrupted where the fault segment crosses the section, and sometimes it seems to be dislocated by the tectonic structure. This effect is most evident for the impedance contrast sections carried out perpendicular to the fault segments that present normal kinematics, while it tends to fade in the sections performed across the fault segments with strike-slip to oblique-slip dextral kinematics.

The study and monitoring of the deformation that occurs around the fault segments is essential to have a complete picture of the dynamics of these areas. In order to adequately survey the studied fault system and provide complementary information on the dynamics of the main fault segments, a local geodetic monitoring network has been designed and implemented across the identified active deformation zones (GEO-UNICT geodetic network). This network consists of 19 benchmarks and has been measured and checked three times since late 2014. In order to refer to a rigid block, we considered the Etn@ref (Palano et al., 2010), that uses more than a decade of GPS measurements, for calculating the geodetic velocities. Based on filtering by inflection and deflection deformation processes, this allowed to attribute the displacement vectors and velocities to local gravitational processes.

The GNSS measurements carried out on the GEO-UNICT geodetic network show an extensional behavior for the SGNF fault segment and confirm the right-

lateral strike-slip kinematics for SGF and ATF fault segments with deformation rates of 20-30 mm/a (Fig. 1).

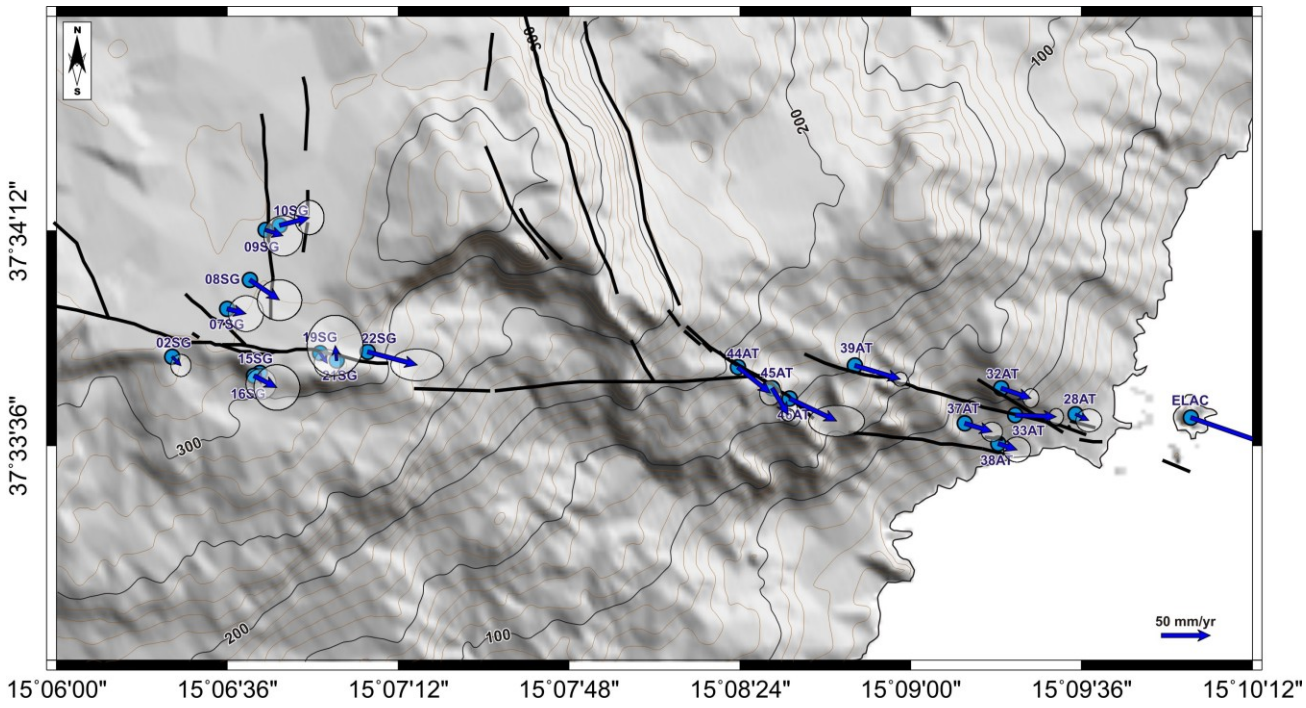

Fig. 1. DTM of the area affected by San Gregorio-Acitrezza Fault System; Blu arrows indicate horizontal GPS velocities (2014– 2016) with 95% confidence ellipses in the Etn@Ref reference frame (Palano et al., 2010)

The east-dipping structures of the lower eastern slope of the volcano, show normal and oblique-slip normal motion compatible with the WNW–ESE regional extension. This process is accompanied, to the north and to the south, by Late Pleistocene to Holocene vertical deformation, characterized by differential uplift reaching rates of 2.5–3.0 mm/a for the last 6–7 ka (Branca et al., 2014).

In a very recent time, it was observed an inversion in the uplift process; in the period 1995–2000, the vertical velocities, expressed in mm/a obtained by interferometric data (Bonforte et al., 2011), indicate that all the footwall blocks within the eastern Etna flank, are not affected by uplift, but by the relative hanging-wall blocks subsidence. These data suggest that the instability of the eastern flank of the volcano is controlled by a complex system given by the iteration of tectonic and volcanic processes that based on the literature data discussed above, can be also considered temporally separated. The active tectonic structures of the eastern slopes of Etna were originally activated from extensional tectonics and now these tectonic

structures are reactivated by the gravitational process that involves the eastern slope of the volcano. The observation of interferometric data emphasizes the subsidence of the hanging-wall block associated with the seaward dragging effect of a large sector of Mt. Etna eastern flank. Such eastward motion is confirmed by GPS and DInSAR measurements as well as geostructural data (e.g. Palano et al., 2008; Solaro et al., 2010; Bonforte et al., 2011; Palano, 2016) and also confirmed by the velocity vectors obtained from GNSS measurements carried out on the GEO-UNICT geodetic network. Moreover the presence of compressional structures (e.g. folds) has recently been observed at the toe of the continental margin, on the Etnean offshore (Fig. 2) (Gross et al., 2015).

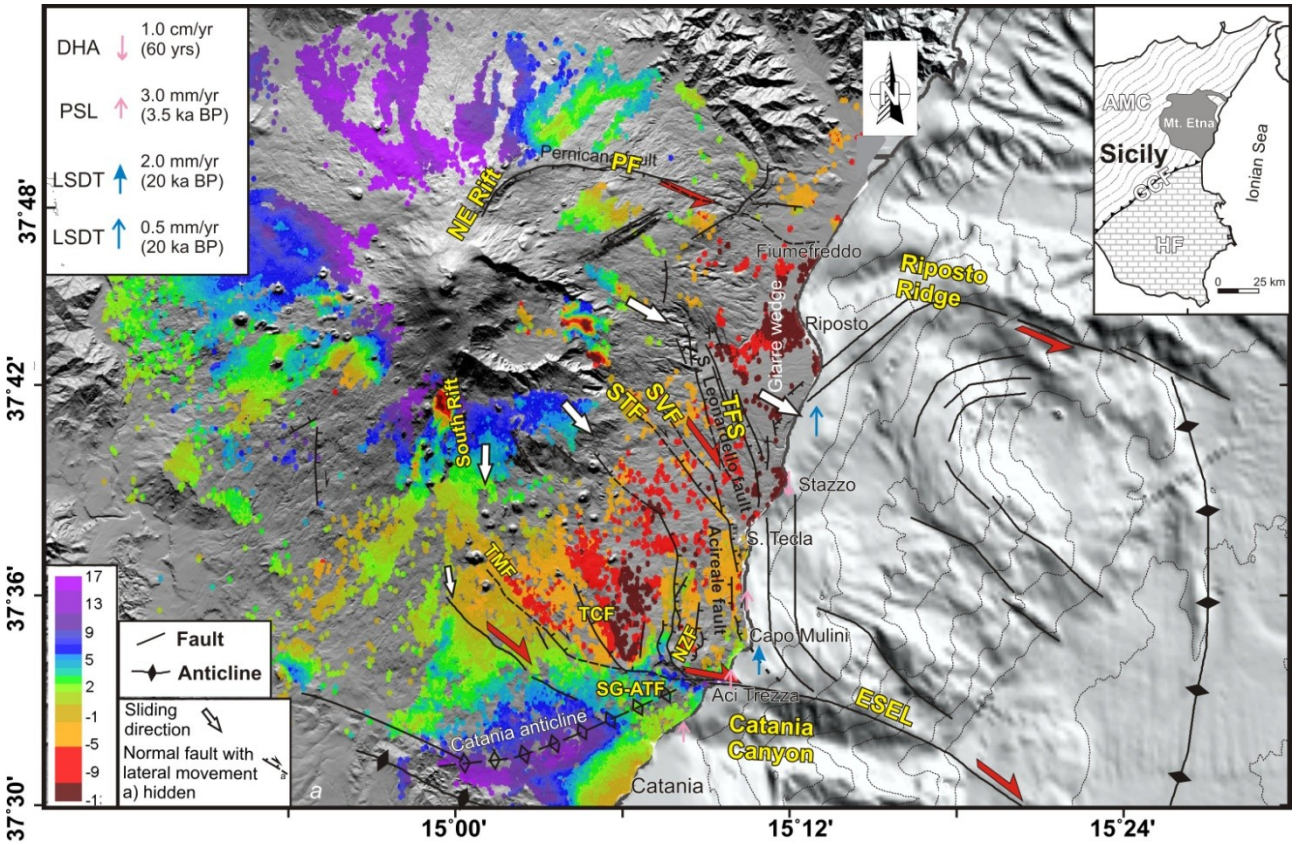

Fig. 2. Simplified tectonic map of Mt. Etna (from Branca et al., 2014) and its eastern off-shore. Bathymetry is from www.emodnet-bathymetry.eu. Tectonic structures are from Branca et al. (2014) and Gross et al. (2015); strike-slip component of motion are indicated with dark arrows. Red and blue scripts show the vertical velocities in mm/a obtained by interferometric data (Bonforte et al., 2011) in the period 1995–2000, and the last 20 ka uplift/subsidence rates observed both along the coast (PSL, palaeo-shoreline; DHA, docks and other manmade structures) and in the offshore (LGM, last glacial maximum platform).

The definition of the basal sliding surface is widely debated and a number of different models have proposed a decollement surface located at a depth ranging from 1 to 5 km bsl (Lo Giudice and Rasà, 1992; Borgia et al., 1992; Tibaldi and Groppelli, 2002; Palano et al., 2008; Palano 2016). The sliding would be confined to the north by the movement of the left-lateral Pernicana Fault, whereas, to the south there is not such clear structural boundary. Some authors proposed the Ragalna Fault (Neri et al., 2007), while others found evidence of active deformation along the Belpasso-Catania lineament and on the Tremestieri-San Gregorio-Acitrezza Fault System (Bonforte et al., 2010), which would accommodate along the southern margin of the eastern slope of Etna, the considerable amount of deformation.

The new geological, geophysical and geodetic datasets obtained and described in the present work allowed to define the geometric and kinematics parameters of Tremestieri-Trecastagni-San Gregorio-Acitrezza Fault Systems. Accordingly, a model of the deep geometry of the Tremestieri-San Gregorio-Acitrezza Fault System has been reconstructed also supported by the results of other theoretical modelling, and the complete review of the literature (Monaco et al., 1997; Neri et al., 2007; Azzaro, 1999; Monaco et al., 2010; Chiocci et al., 2011; De Guidi et al., 2012; Azzaro et al., 2013; Imposa et al., 2015; Palano, 2016).

The morphological and structural analysis of fault segments has provided information about the age and evolution of the vertical deformation as well as the geometry of the fault planes. The TMF and TCF represent Holocene right-lateral to transtensional faults with curve geometry, while the SGF and ATF represent right-lateral faults with planar geometry and approximately vertical setting. The SGNF represents a young normal fault with planar geometry and steeply dipping. The two NZF fault segments represent Late Pleistocene normal faults with some right-lateral component, their setting is very steep near the surface and at depth they decrease the dipping angle to about 45° thus describing an concave upwards geometry.

The pattern of the surface deformation along the investigated fault system, for a time period (spanning from May to July 2012) that encompasses the occurrence of a

slow slip event in the investigated area (Palano, 2016), has been reconstructed based on DInSAR data. This extensive dataset has been exploited to derive the kinematics along the fault surfaces by using a 3D numerical inversion procedure. The numerical inversion process returns a slip distribution pattern along the several fault planes and produces a surface deformation pattern very similar to that obtained by the analyses of the DInSAR imageries. The obtained numerical model shows a heterogeneous slip distribution with a predominant strike-slip motion, associated with dip-slip for the fault segments that have about NNW-SSE trend. The same model also suggests that at shallow depth, these faults flatten on a slightly inclined surface located within the sedimentary basement at a depth between 1000 (west) and 3000 (east) m. It is therefore reasonable to state that the results of several surveys carried out in the frame of the present research together with the constraints supplied by the numerical inversion model allowed to provide new insights about the deep geometry and kinematics of the Tremestieri-San Gregorio-Acitrezza Fault System.

This research has also allowed to design, develop and implement an integrated system of applied geophysical and geodetic monitoring, which could be applied to other tectonic structures of the Etnean eastern slopes, or more generally in all those areas affected by the presence of tectonics structures. Accordingly, it could be considered as an important starting point for a proper urban development planning, having as main purpose the land protection, but especially the population safety.

The results of this thesis will represent an important basic information for the development of a larger research project that aims to carry out the geomechanics characterization, in areas around active structural features. It was in fact, observed how the geomechanical properties of the soil characterizing a fault zone, and in particular the Young's modulus and its space-time variations, could influence the growth and/or the propagation of a tectonic structure (Gudmundsson, 2004; De Guidi et al. 2012; Gudmundsson et al., 2013). The final goal of the present study is to be able to develop a model that includes both the scaling laws (Bonilla et al., 1984;

Wells and Coppersmith, 1994; Pavlides and Caputo, 2004. De Guidi et al., 2012) and the different deformation styles (coseismic deformation and aseismic creep).

Acknowledgement

Firstly, I would like to express my sincere gratitude to my advisor Prof. Sebastiano Imposa for his sustain, patience, motivation and scientific suggestions, as well as for his courtesy and helpfulness. His guidance helped me in all the time of research and writing of this thesis.

My sincere thanks also goes to the co-tutor Prof. Giorgio De Guidi for the continuous support of my Ph.D study, for his insightful comments and encouragement, but also for the stimulating discussions which incited me to widen my research from various perspectives.

I take this opportunity to express gratitude to Dr. Gilda Currenti and Dr. Mimmo Palano, of the INGV Catania Section, for their ever available courtesy and the advises for the software use. Without they precious support it would not be possible to conduct part of this research.

I wish to express my sincere thanks to the IREA of Naples for having supplied InSAR data necessary to develop a part of this research.

I should like to extend my warmest thanks to Dr. Francesco Fazio and to Dr. Giuseppe Rannisi for their kindness and availability, for the interesting discussions and for their help in the field surveys.

I would like to thank all the students who have collaborated during the acquisition phase of geodetic-topographic data.

My heartfelt thanks to my parents, my sisters, Giuseppe and Tiziana for supporting me in this studying career and in my life in general.

Finally, I would express my gratitude to one and all, who directly or indirectly, have lent their hand in this venture.

References

Achenbach, J. D. (2000). Calculation of surface wave motions due to a subsurface point force: An application of elastodynamic reciprocity. *The Journal of the Acoustical Society of America*, *107*(4), 1892-1897.

Acocella, V., & Neri, M. (2005). Structural features of an active strike-slip fault on the sliding flank of Mt. Etna (Italy). *Journal of Structural Geology*, *27*(2), 343-355.

Aki, K., & Richards, P. G. (2002). *Quantitative seismology* (Vol. 1).

Albarello D (2005) Free-field HVSR noise analysis devoted to seismic microzoning: theoretical background and experimental recipes. Procedure manual (Measurements Protocol & Crew Manual). Part A, vol 1, Oct 2005, NATO SfP project 980857

Albarello, D., & Castellaro, S. (2011). Tecniche sismiche passive: indagini a stazione singola. *Ingegneria sismica*, *38*(2), 32-49.

Allen, C. R. (1965). Transcurrent faults in continental areas. *Philosophical Transactions of the Royal Society of London A: Mathematical, Physical and Engineering Sciences*, *258*(1088), 82-89.

Alparone, S., Cocina, O., Gambino, S., Mostaccio, A., Spampinato, S., Tuvè, T., & Ursino, A. (2013). Seismological features of the Pernicana–Provenzana Fault System (Mt. Etna, Italy) and implications for the dynamics of northeastern flank of the volcano. *Journal of volcanology and geothermal research*, *251*, 16-26.

Amorosi, A., Castellaro, S., & Mulargia, F. (2008). Single-Station Passive Seismic Stratigraphy: an inexpensive tool for quick subsurface investigations. *GeoActa*, *7*(10).

Arai, H., & Tokimatsu, K. (1998, December). Evaluation of local site effects based on microtremor H/V spectra. In *Proceeding of the Second International Symposium on the Effects of Surface Geology on Seismic Motion* (pp. 673-680).

Arai, H., & Tokimatsu, K. (2000, January). Effects of Rayleigh and Love waves on microtremor H/V spectra. In *Proc. 12th World Conf. on Earthquake Engineering* (pp. 2232-2240).

Arcidiacono, S. (1901). Il terremoto di Nicolosi dell11 Maggio 1901 e le sue repliche. *Boll. Acc.Gioenia Sci. Nat 70, 2–15 (Luglio).*

Azzaro, R., Lo Giudice, E., & Rasà, R. (1989a). Catalogo degli eventi macrosismici e delle fenomenologie da creep nell'area etnea dall'agosto 1980 al dicembre 1989. *Boll. GNV*, *1*, 13-46.

Azzaro, R., Carveni, P., Lo Giudice, E., & Rasà, R. (1989b). Il terremoto di Codavolpe (basso versante orientale etneo) del 29 gennaio 1989: campo macrosismico e fratturazione cosismica. *Boll. Gruppo Nazionale Vulcanologia*, *1*, 1-12.

Azzaro, R., Branca, S., Giammanco, S., Gurrieri, S., Rasà, R., & Valenza, M. (1998a). New evidence for the form and extent of the Pernicana Fault System (Mt. Etna) from structural and soil–gas surveying. *Journal of volcanology and geothermal research*, *84*(1), 143-152.

Azzaro, R., Ferreli, L., Michetti, A. M., Serva, L., & Vittori, E. (1998b). Environmental Hazard of Capable Faults: The Case of the Pernicana Fault (Mt. Etna, Sicily. *Natural Hazards*, *17*(2), 147-162.

Azzaro, R. (1999). Earthquake surface faulting at Mount Etna volcano (Sicily) and implications for active tectonics. *Journal of Geodynamics*, *28*(2), 193-213.

Azzaro, R., Mattia, M., & Puglisi, G. (2001). Fault creep and kinematics of the eastern segment of the Pernicana Fault (Mt. Etna, Italy) derived from geodetic observations and their tectonic significance. *Tectonophysics*, *333*(3), 401-415.

Azzaro, R. (2004). Seismicity and active tectonics in the Etna region: constraints for a seismotectonic model. *Mt. Etna: volcano laboratory*, 205-220.

Azzaro, R., Branca, S., Gwinner, K., & Coltelli, M. (2012). The volcano-tectonic map of Etna volcano, 1: 100.000 scale: an integrated approach based on a morphotectonic analysis from high-resolution DEM constrained by geologic, active faulting and seismotectonic data. *Italian journal of geosciences*, *131*(1), 153-170.

Azzaro, R., Bonforte, A., Branca, S., & Guglielmino, F. (2013). Geometry and kinematics of the fault systems controlling the unstable flank of Etna volcano (Sicily). *Journal of volcanology and geothermal research*, *251*, 5-15.

Bard, P. Y. (1998). Microtremor measurements: a tool for site effect estimation. *The effects of surface geology on seismic motion*, *3*, 1251-1279.

Bella, D., Carveni, P., Musumeci, C., & Gresta, S. (1996). Aspetti geomorfologici conseguenti all'attività sismica locale sul basso versante orientale del vulcano Etna. *Il Quaternario*, *9*(1), 365-368.

Ben Avraham, Z., Boccaletti, M., Cello, G., Grasso, M., Lentini, F., Torelli, L., & Tortorici, L. (1990). Principali domini strutturali originatisi dalla collisione neogenico-quaternaria nel Mediterraneo centrale. *Mem. Soc. Geol. It*, *45*(1), 453-462.

Berardino, P., Fornaro, G., Lanari, R., & Sansosti, E. (2002). A new algorithm for surface deformation monitoring based on small baseline differential SAR interferograms. *IEEE Transactions on Geoscience and Remote Sensing*, *40*(11), 2375-2383.

Blumetti, A. M., DiManna, P., Ferreli, L., Fiorenza, D., & Vittori, E. (2007). Reduction of environmental risk from capable faults: the case of the Eastern Etna region (eastern Sicily, Italy). *Quaternary International*, *173*, 45-56.

Bock, Y., Abbot, R. I., Counselman III, C. C., & King, R. W. (1986). A demonstration of 1–2 parts in 107 accuracy using GPS. *Bulletin géodésique*, *60*(3), 241-254.

Bodin, P., & Horton, S. (1999). Broadband microtremor observation of basin resonance in the Mississippi embayment, Central US. *Geophysical Research Letters*, *26*(7), 903-906.

Böhm, J., Niell, A., Tregoning, P., & Schuh, H. (2006). Global Mapping Function (GMF): A new empirical mapping function based on numerical weather model data. *Geophysical Research Letters*, *33*(7).

Boncio, P., Galli, P., Naso, G., & Pizzi, A. (2012). Zoning surface rupture hazard along normal faults: insight from the 2009 Mw 6.3 L'Aquila, Central Italy, earthquake and other global earthquakes. *Bulletin of the Seismological Society of America*, *102*(3), 918-935.

Bonforte, A., & Puglisi, G. (2006). Dynamics of the eastern flank of Mt. Etna volcano (Italy) investigated by a dense GPS network. *Journal of Volcanology and Geothermal Research*, *153*(3), 357-369.

Bonforte, A., Branca, S., & Palano, M. (2007). Geometric and kinematic variations along the active Pernicana fault: implication for the dynamics of Mount Etna NE flank (Italy). *Journal of Volcanology and Geothermal Research*, *160*(1), 210-222.

Bonforte, A., Guglielmino, F., Coltelli, M., Ferretti, A., & Puglisi, G. (2011). Structural assessment of Mount Etna volcano from Permanent Scatterers analysis. *Geochemistry, Geophysics, Geosystems*, *12*(2).

Bonforte, A., Carnazzo, A., Gambino, S., Guglielmino, F., Obrizzo, F., & Puglisi, G. (2013). A multidisciplinary study of an active fault crossing urban areas: The Trecastagni Fault at Mt. Etna (Italy). *Journal of volcanology and geothermal research*, *251*, 41-49.

Bonilla, M. G., Mark, R. K., & Lienkaemper, J. J. (1984). Statistical relations among earthquake magnitude, surface rupture length, and surface fault displacement. *Bulletin of the Seismological Society of America*, *74*(6), 2379-2411.

Bonnefoy-Claudet, S., Cotton, F., & Bard, P. Y. (2006a). The nature of noise wavefield and its applications for site effects studies: A literature review. *Earth-Science Reviews*, *79*(3), 205-227.

Bonnefoy-Claudet S, Cornou C, Bard PY, Cotton F, Moczo P, Kristek J, Fa¨h D (2006b) *H/V ratio: a tool for site effects evaluation. Results from 1-D noise simulations*. Geophys J Int 167:827–883

Bonnefoy-Claudet, S., Köhler, A., Cornou, C., Wathelet, M., & Bard, P. Y. (2008). Effects of Love waves on microtremor H/V ratio. *Bulletin of the Seismological Society of America*, *98*(1), 288-300.

Borgia, A., Ferrarit, L., & Pasquarèf, G. (1992). lmportance of gravitational spreading in the tectonic and. *Nature*, *357*, 6375.

Bormann, P., & Wielandt, E. (2002). Seismic signals and noise. *New manual of seismological observatory practice*, *1*.

Boschi, E., & Guidoboni, E. (Eds.). (2001). *Catania, terremoti e lave: dal mondo antico alla fine del Novecento* (p. 414). Bologna: Compositori.

Bousquet, J. C., & Lanzafame, G. (2004). The tectonics and geodynamics of Mt. Etna: synthesis and interpretation of geological and geophysical data. *Mt. Etna: volcano laboratory*, 29-47.

Branca, S., Coltelli, M., & Groppelli, G. (2004). Geological evolution of Etna volcano. *Mt. Etna: volcano laboratory*, 49-63.

Branca, S., Coltelli, M., De Beni, E., & Wijbrans, J. (2008). Geological evolution of Mount Etna volcano (Italy) from earliest products until the first central volcanism (between 500 and 100 ka ago) inferred from geochronological and stratigraphic data. *International Journal of Earth Sciences*, *97*(1), 135-152.

Branca, S., Coltelli, M., Groppelli, G., & Lentini, F. (2011a). Geological map of Etna volcano, 1: 50,000 scale. *Italian Journal of Geosciences*, *130*(3), 265-291.

Branca, S., Coltelli, M., & Groppelli, G. (2011b). Geological evolution of a complex basaltic stratovolcano: Mount Etna, Italy. *Italian Journal of Geosciences*, *130*(3), 306-317.

Branca, S., & Ferrara, V. (2013). The morphostructural setting of Mount Etna sedimentary basement (Italy): Implications for the geometry and volume of the volcano and its flank instability. *Tectonophysics*, *586*, 46-64.

Branca, S., De Guidi, G., Lanzafame, G., & Monaco, C. (2014). Holocene vertical deformation along the coastal sector of Mt. Etna volcano (eastern Sicily, Italy): implications on the time–space constrains of the volcano lateral sliding. *Journal of Geodynamics*, *82*, 194-203.

Caputo R. (2005). Ground effects of large morphogenic earthquakes. *J. Geodyn.*, 40, 2-3, 113-118, doi: 10.1016/j.jog.2005.07.001.

Castellaro, S., & Mulargia, F. (2009a). VS30 estimates using constrained H/V measurements. *Bulletin of the Seismological Society of America*, *99*(2A), 761-773.

Castellaro, S., & Mulargia, F. (2009b). The effect of velocity inversions on H/V. *Pure and Applied Geophysics*, *166*(4), 567-592.

Catalano, S., & De Guidi, G. (2003). Late Quaternary uplift of northeastern Sicily: relation with the active normal faulting deformation. *Journal of Geodynamics*, *36*(4), 445-467.

Catalano, S., Torrisi, S., & Ferlito, C. (2004). The relationship between Late Quaternary deformation and volcanism of Mt. Etna (eastern Sicily): new evidence from the sedimentary substratum in the Catania region. *Journal of Volcanology and Geothermal Research*, *132*(4), 311-334.

Catalano, S., De Guidi, G., Monaco, C., Tortorici, G., & Tortorici, L. (2008). Active faulting and seismicity along the Siculo–Calabrian Rift Zone (southern Italy). *Tectonophysics*, *453*(1), 177-192.

Chiocci, F. L., Coltelli, M., Bosman, A., & Cavallaro, D. (2011). Continental margin large-scale instability controlling the flank sliding of Etna volcano. *Earth and Planetary Science Letters*, *305*(1), 57-64.

Chouet, B., De Luca, G., Milana, G., Dawson, P., Martini, M., & Scarpa, R. (1998). Shallow velocity structure of Stromboli volcano, Italy, derived from small-aperture array measurements of Strombolian tremor. *Bulletin of the Seismological Society of America*, *88*(3), 653-666.

Cocina, O., Neri, G., Privitera, E., & Spampinato, S. (1998). Seismogenic stress field beneath Mt. Etna (South Italy) and possible relationships with volcano-tectonic features. *Journal of volcanology and geothermal research*, *83*(3), 335-348.

Coco, G., & Corrao, M. (2009). Geofisica applicata. *Palermo, Italy*, 198-226.

Cornou, C. (2002). *Traitement d'antenne et imagerie sismique dans l'agglomération grenobloise (Alpes françaises): implications pour les effets de site* (Doctoral dissertation, Université Joseph-Fourier-Grenoble I).

Corsaro, R. A., & Cristofolini, R. (1996). Origin and differentiation of recent basaltic magmas from Mount Etna. *Mineralogy and Petrology*, *57*(1-2), 1-21.

Corsaro, R. A., & Cristofolini, R. (1997). Geology, geochemistry and mineral chemistry of tholeiitic to transitional Etnean magmas. *Acta Vulcanologica*, *9*, 55-66.

Cristofolini, R., & Romano, R. (1982). Petrologic features of the Etnean volcanic rocks. *Mem. Soc. Geol. Ital*, *23*, 99-115.

CUBIT, 15.2 User Documentation, https://cubit.sandia.gov/public/15.2/help_manual/WebHelp/cubithelp.htm

Currenti, G., Bonaccorso, A., Del Negro, C., Guglielmino, F., Scandura, D., & Boschi, E. (2010). FEM-based inversion for heterogeneous fault mechanisms: application at Etna volcano by DInSAR data. *Geophysical Journal International*, *183*(2), 765-773.

Currenti, G., Solaro, G., Napoli, R., Pepe, A., Bonaccorso, A., Del Negro, C., & Sansosti, E. (2012). Modeling of ALOS and COSMO-SkyMed satellite data at Mt Etna: Implications on relation between seismic activation of the Pernicana fault system and volcanic unrest. *Remote sensing of environment*, *125*, 64-72.

D'Agostino, N., & Selvaggi, G. (2004). Crustal motion along the Eurasia-Nubia plate boundary in the Calabrian Arc and Sicily and active extension in the Messina Straits from GPS measurements. *Journal of Geophysical Research: Solid Earth*, *109*(B11).

Dal Moro G (2012) *Onde di superficie in geofisica applicata. Acquisizione e analisi dei dati secondotecniche MASW e HVSR*. D. Flaccovio, Palermo

De Guidi, G., Scudero, S., & Gresta, S. (2012). New insights into the local crust structure of Mt. Etna volcano from seismological and morphotectonic data. *Journal of Volcanology and Geothermal Research*, *223*, 83-92.

De Guidi, G., Caputo, R., & Scudero, S. (2013). Regional and local stress field orientation inferred from quantitative analyses of extension joints: case study from southern Italy. *Tectonics*, *32*(2), 239-251.

De Guidi, G., Imposa, S., Scudero, S., & Palano, M. (2014). New evidence for Late Quaternary deformation of the substratum of Mt. Etna volcano (Sicily, Italy): clues indicate active crustal doming. *Bulletin of volcanology*, *76*(5), 1-13.

De Guidi, G., Barberi, G., Barreca, G., Bruno, V., Cultrera, F., Grassi, S., ... & Scudero, S. (2015). Geological, seismological and geodetic evidence of active thrusting and folding south of Mt. Etna (eastern Sicily): Revaluation of "seismic efficiency" of the Sicilian Basal Thrust. *Journal of Geodynamics*, *90*, 32-41.

Del Gaudio, V., Coccia, S., Wasowski, J., Gallipoli, M. R., & Mucciarelli, M. (2008). Detection of directivity in seismic site response from microtremor spectral analysis. *Natural Hazards & Earth System Sciences*, *8*(4).

Del Gaudio, V., Wasowski, J., & Muscillo, S. (2013). New developments in ambient noise analysis to characterisethe seismic response of landslide-prone slopes. *Nat Hazards Earth Syst Sci 13(8):2075–2087.*

Delgado, J., Casado, C. L., Estevez, A., Giner, J., Cuenca, A., & Molina, S. (2000). Mapping soft soils in the Segura river valley (SE Spain): a case study of microtremors as an exploration tool. *Journal of Applied Geophysics*, *45*(1), 19-32.

Dong, D. N., & Bock, Y. (1989). Global Positioning System network analysis with phase ambiguity resolution applied to crustal deformation studies in California. *Journal of Geophysical Research: Solid Earth*, *94*(B4), 3949-3966.

Duval, A. M., Bard, P. Y., Méneroud, J. P., & Vidal, S. (1996). Mapping site effect with microtremors. In *International conference on seismic zonation* (pp. 1522-1529).

Ellis, M., & King, G. (1991). Structural control of flank volcanism in continental rifts. *Science(Washington)*, *254*(5033), 839-842.

Field, E., & Jacob, K. (1993). The theoretical response of sedimentary layers to ambient seismic noise. *Geophysical research letters*, *20*(24), 2925-2928.

Finetti, I., & Del Ben, A. (1986). *Geophysical study of the Tyrrhenian opening*. Osservatorio Geofisico Sperimentale.

Finetti, I., Lentini, F., Carbone, S., Catalano, S., & Del Ben, A. (1996). Il sistema Appennino Meridionale-Arco Calabro-Sicilia nel Mediterraneo Centrale; studio geologico-geofisico. *Bollettino della Società Geologica Italiana*, *115*(3), 529-559.

Finetti I.R., Lentini F., Carbone S., Del Ben A., Di Stefano A., Forlin E., Guarnieri P., Pipan M. & Prizzon A. (2005) - Geological outline of Sicily and lithospheric tectono-dynamics of its Tyrrhenian margin from new CROP seismic data. In: Finetti I.R. Ed., Deep Seismic Exploration of the Central Mediterranean and Italy, CROP PROJECT, Elsevier, 15, 319-375.

Finetti I.R., Calamita F., Crescenti U., Del Ben A., Forlin E., Pipan M., Rusciadelli G. & Scisciani V. (2005a) - Crustal Geological Section across Central Italy from the Corsica Basin to the Adriatic Sea based on Geological and CROP Seismic Data. In Finetti Eds., CROP PROJECT: Deep Seismic Exploration of the Central Mediterranean and Italy Elsevier, Chapter, 9, 159-197.

Finetti I.R., Lentini F., Carbone S., Del Ben A., Di Stefano A., Guarnirei P., Pipan M. & Prizzon A. (2005b) - Crustal Tectono-Satratigraphy and Geodynamics of the Southern Apennines from CROP and other Integrated Geophysical-Geological Data. In Finetti Eds, CROP PROJECT: Deep Seismic Exploration of the Central Mediterranean and Italy Elsevier, Chapter, 12, 225-263.

Franceschetti, G., & Lanari, R. (1999). *Synthetic aperture radar processing*. CRC press.

Froger, J. L., Merle, O., & Briole, P. (2001). Active spreading and regional extension at Mount Etna imaged by SAR interferometry. *Earth and Planetary Science Letters*, *187*(3), 245-258.

Gabriel, A. K., Goldstein, R. M., & Zebker, H. A. (1989). Mapping small elevation changes over large areas: differential radar interferometry. *Journal of Geophysical Research: Solid Earth*, *94*(B7), 9183-9191.

Galadini, F., Falcucci, E., Galli, P., Giaccio, B., Gori, S., Messina, P., ... & Sposato, A. (2012). Time intervals to assess active and capable faults for engineering practices in Italy. *Engineering Geology*, *139*, 50-65.

Gambino, S., Bonforte, A., Carnazzo, A., Falzone, G., Ferrari, F., Ferro, A., ... & Puglisi, G. (2011). Displacement across the Trecastagni Fault (Mt. Etna) and induced seismicity: the October 2009 to January 2010 episode. *Annals of geophysics*.

Giampiccolo, E., Gresta, S., Mucciarelli, M., De Guidi, G., & Gallipoli, M. R. (2001). Information on subsoil geological structure in the city of Catania (Eastern Sicily) from microtremor measurements. *Annals of Geophysics*, *44*(1).

Gillot, P. Y., Kieffer, G., & Romano, R. (1994). The evolution of Mount Etna in the light of potassium-argon dating. *Acta Vulcanol*, *5*, 81-87.

González, P. J., & Palano, M. (2014). Mt. Etna 2001 eruption: New insights into the magmatic feeding system and the mechanical response of the western flank from a detailed geodetic dataset. *Journal of volcanology and geothermal research*, *274*, 108-121.

Goula, X., Susagna, T., Figueras, S., Cid, J., Alfaro, A., & Barchiesi, A. (1998, September). Comparison of numerical simulation and microtremor measurement for the analysis of site effects in the city of Barcelona (Spain). In *Proceedings of the XIth European conference on earthquake engineering, Paris*(pp. 6-11).

Gresta, S., Bella, D., Musumeci, C., & Carveni, P. (1997). Some efforts on active faulting processes (earthquakes and aseismic creep) acting on the eastern flank of Mt. Etna (Sicily). *Acta Vulcanologica*, *9*, 101-108.

Gresta, S., Peruzza, L., Slejko, D., & Distefano, G. (1998). Inferences on the main volcano-tectonic structures at Mt. Etna (Sicily) from a probabilistic seismological approach. *Journal of Seismology*, *2*(2), 105-116.

Groppelli, G., & Tibaldi, A. (1999). Control of rock rheology on deformation style and slip-rate along the active Pernicana Fault, Mt. Etna, Italy. *Tectonophysics*, *305*(4), 521-537.

Gross, M. R. (1995). Fracture partitioning: Failure mode as a function of lithology in the Monterey Formation of coastal California. *Geological Society of America Bulletin*, *107*(7), 779-792.

Gudmundsson, A. (2004). Effects of Young's modulus on fault displacement. *Comptes Rendus Geoscience*, *336*(1), 85-92.

Gudmundsson, A., De Guidi, G., & Scudero, S. (2013). Length–displacement scaling and fault growth. *Tectonophysics*, *608*, 1298-1309.

Guglielmino, F., Bignami, C., Bonforte, A., Briole, P., Obrizzo, F., Puglisi, G., ... & Wegmüller, U. (2011). Analysis of satellite and in situ ground deformation data integrated by the SISTEM

approach: The April 3, 2010 earthquake along the Pernicana fault (Mt. Etna-Italy) case study. *Earth and Planetary Science Letters*, *312*(3), 327-336.

Harding, T. P. (1983). Divergent wrench fault and negative flower structure, Andaman Sea. *Seismic expression of structural styles*, *3*, 4-2.

Harding, T. P., Vierbuchen R. C., & Christie-Blick, N. (1985). Structural styles, plate-tectonic settings, and hydrocarbon traps of divergent (transtensional) wrench faults.

Herring, T. A., King, R. W., & McClusky, S. C. (2006). Introduction to GAMIT/GLOBK, Release 10.3, Dep. of Earth Atmos. and Planet. *Sci., Mass. Inst. of Technol., Cambridge, Mass*, *28*.

Herring, T. A., King, R. W., & McClusky, S. C. (2010). Introduction to Gamit/Globk. *Massachusetts Institute of Technology, Cambridge, Massachusetts*.

Ibs-von Seht, M., & Wohlenberg, J. (1999). Microtremor measurements used to map thickness of soft sediments. *Bulletin of the Seismological Society of America*, *89*(1), 250-259.

Imbò, G. (1935). *I terremoti etnei*. Le Monnier.

Imposa, S., Coco, G., & Corrao, M. (2004). Site effects close to structural lineaments in eastern Sicily (Italy). *Engineering geology*, *72*(3), 331-341.

Imposa, S., Fazio, F., Grassi, S., & Rannisi, G. (2013). Studio della risposta di sito in un area del versante meridionale del Mt. Etna. *Geofisica Applicata*, *2*, 409-416.

Imposa, S., De Guidi, G., Grassi, S., Scudero, S., Barreca, G., Patti, G., & Boso, D. (2015a). Applying geophysical techniques to investigate a segment of a creeping fault in the urban area of San Gregorio di Catania, southern flank of Mt. Etna (Sicily—Italy). *Journal of Applied Geophysics*, *123*, 153-163.

Imposa, S., De Guidi, G., Scudero, S., & Grassi, S. (2015b). Fault rupture hazard along a sector with aseismic creep in urban area (Eastern Sicily). In *Proceedings of the International Conference: Georisks In The Mediterranean And Their Mitigation Edited by: Galea P., Borg RP, Farrugia D., Agius MR, D'Amico S., Torpiano A., Bonello M. ISBN* (pp. 978-88).

Imposa, S., Grassi, S., Fazio, F. et al. Nat Hazards (2016). *Geophysical surveys to study a landslide body (north-eastern Sicily).* doi:10.1007/s11069-016-2544-1

Imposa, S., Grassi, S., De Guidi, G., Battaglia, F., Lanaia, G., & Scudero, S. (2016a). 3D subsoil model of the San Biagio 'Salinelle'mud volcanoes (Belpasso, SICILY) derived from geophysical surveys. *Surveys in Geophysics*, *37*(6), 1117-1138.

ISIDe working group (2016) version 1.0, DOI: 10.13127/ISIDe

Jackson, J., & McKenzie, D. (1983). The geometrical evolution of normal fault systems. *Journal of Structural Geology*, *5*(5), 471-482.

Kieffer, G. (1971). Dépôts et niveaux marins et fluviatiles de la région de Catane (Sicile). Leurs corrélations avec certains épisodes d'activité tectonique ou volcanique. *Méditerranée*, *2*(5), 591-626.

Kieffer, G. (1975). Existence Of Rift-Zone In Mount Etna (Sicily). *Comptes Rendus Hebdomadaires Des Seances De L Academie Des Sciences Serie D*, *280*(3), 263-266.

King, R. W., & Bock, Y. (2000). Documentation for the GAMIT GPS software analysis version 9.9. *Mass. Inst. of Technol., Cambridge*.

Kudo, K. (1995, October). Practical estimates of site response. State-of-the-art report. In *Proceedings of the fifth Internationnal Conference on Seismic Zonation*.

Lachetl, C., & Bard, P. Y. (1994). Numerical and Theoretical Investigations on the Possibilities and Limitations of Nakamura's Technique. *Journal of Physics of the Earth*, *42*(5), 377-397.

Lanari, R., Mora, O., Manunta, M., Mallorquí, J. J., Berardino, P., & Sansosti, E. (2004). A small-baseline approach for investigating deformations on full-resolution differential SAR interferograms. *IEEE Transactions on Geoscience and Remote Sensing*, *42*(7), 1377-1386.

Latora, V., Vinciguerra, S., Bicciato, S., & Kamimura, R. T. (1999). Identifying seismicity patterns leading flank eruptions at Mt. Etna Volcano during 1981–1996. *Geophysical research letters*, *26*(14), 2105-2108.

Lavecchia, G., Ferrarini, F., de Nardis, R., Visini, F., & Barbano, M. S. (2007). Active thrusting as a possible seismogenic source in Sicily (Southern Italy): Some insights from integrated structural–kinematic and seismological data. *Tectonophysics*, *445*(3), 145-167.

Lay, T., & Wallace, T. C. (1995). *Modern global seismology* (Vol. 58). Academic press.

Lentini, F., Carbone, S., Catalano, S., & Grasso, M. (1995). Principali lineamenti strutturali della Sicilia nord-orientale. *Studi Geol. Camerti*, *2*(1995), 319-929.

Lentini, F., Carbone, S., & Guarnieri, P. (2006). Collisional and postcollisional tectonics of the Apenninic-Maghrebian orogen (southern Italy). *Geological Society of America Special Papers*, *409*, 57-81.

Lermo, J., & Chávez-García, F. J. (1993). Site effect evaluation using spectral ratios with only one station. *Bulletin of the seismological society of America*, *83*(5), 1574-1594.

Lo Giudice, E., Patanè, G., Rasà, R., & Romano, R. (1982). The structural framework of Mount Etna. *Mem. Soc. Geol. It*, *23*, 125-158.

Lo Giudice, E., & Longo, V. (1986). La crisi sismica etnea dell'agosto-settembre 1980. *CNR-IIV Open File Report*, *4*(86), 6.

Lo Giudice, E. L., & Rasà, R. (1992). Very shallow earthquakes and brittle deformation in active volcanic areas: The Eatnean region as an example. *Tectonophysics*, *202*(2), 257-268.

Louie, J. N. (2001). Faster, better: shear-wave velocity to 100 meters depth from refraction microtremor arrays. *Bulletin of the Seismological Society of America*, *91*(2), 347-364.

Lowell, J. D. (1972). Spitsbergen Tertiary orogenic belt and the Spitsbergen fracture zone. *Geological Society of America Bulletin*, *83*(10), 3091-3102.

Machette, M. N. (2000). Active, capable, and potentially active faults a paleoseismic perspective. *Journal of Geodynamics*, *29*(3), 387-392.

Martinelli, G. (1911). Notizie sui terremoti osservati in Italia durante lanno 1908. *App. Boll. Soc.Sism. It. 15.*

Massonnet, D., & Feigl, K. L. (1998). Radar interferometry and its application to changes in the Earth's surface. *Reviews of geophysics*, *36*(4), 441-500.

Mazzuoli, R., Tortorici, L., & Ventura, G. (1995). Oblique rifting in Salina, Lipari and Vulcano islands (Aeolian islands, southern Italy). *Terra Nova*, *7*(4), 444-452.

McGuire, W. J., & Pullen, A. D. (1989). Location and orientation of eruptive fissures and feederdykes at Mount Etna; influence of gravitational and regional tectonic stress regimes. *Journal of Volcanology and Geothermal Research*, *38*(3), 325-344.

McNamara, D. E., & Buland, R. P. (2004). Ambient noise levels in the continental United States. *Bulletin of the seismological society of America*, *94*(4), 1517-1527.

Meade, B. J. (2007). Algorithms for the calculation of exact displacements, strains, and stresses for triangular dislocation elements in a uniform elastic half space. *Computers & geosciences*, *33*(8), 1064-1075.

Mensa, D. L. (1991). High resolution radar cross-section imaging. *Boston, MA, Artech House, Norwood, 1991, 280 p.*, *1*.

Mercier, J., Vergely, P., 1996. Tettonica. *Pitagora editrice, Bologna*.

Monaco, C., & Tortorici, L. (1995). Tettonica estensionale quaternaria nell'Arco Calabro e in Sicilia orientale. *Studi Geologici Camerti*, *2*(special issue), 351-362.

Monaco, C., Petronio, L., & Romanelli, M. (1995). Tettonica estensionale nel settore orientale del Monte Etna (Sicilia): dati morfotettonici e sismici. *Studi Geologici Camerti, volume speciale*, *2*, 363-374.

Monaco, C., Tapponnier, P., Tortorici, L., & Gillot, P. Y. (1997). Late Quaternary slip rates on the Acireale-Piedimonte normal faults and tectonic origin of Mt. Etna (Sicily). *Earth and Planetary Science Letters*, *147*(1), 125-139.

Monaco, C., & Tortorici, L. (2000). Active faulting in the Calabrian arc and eastern Sicily. *Journal of Geodynamics*, *29*(3), 407-424.

Monaco, C., Bianca, M., Catalano, S., De Guidi, G., & Tortorici, L. (2002). Sudden change in the Late Quaternary tectonic regime in eastern Sicily: evidences from geological and geomorphological features. *Boll. Soc. Geol. Ital*, *1*, 901-913.

Monaco, C., Catalano, S., Cocina, O., De Guidi, G., Ferlito, C., Gresta, S., ... & Tortorici, L. (2005). Tectonic control on the eruptive dynamics at Mt. Etna Volcano (Sicily) during the 2001 and 2002–2003 eruptions. *Journal of Volcanology and Geothermal Research*, *144*(1), 211-233.

Monaco, C., De Guidi, G., Catalano, S., Ferlito, C., Tortorici, G., & Tortorici, L. (2008). Carta Morfotettonica del Monte Etna. *Litografia Artistica Cartografica, Firenze*.

Monaco, C., De Guidi, G., & Ferlito, C. (2010). The morphotectonic map of Mt. Etna. *Italian journal of geosciences*, *129*(3), 408-428.

Mora, O., Mallorqui, J. J., & Broquetas, A. (2003). Linear and nonlinear terrain deformation maps from a reduced set of interferometric SAR images. *IEEE Transactions on Geoscience and Remote Sensing*, *41*(10), 2243-2253.

Nakamura, Y. (1989). A method for dynamic characteristics estimation of subsurface using microtremor on the ground surface. *Railway Technical Research Institute, Quarterly Reports*, *30*(1).

Naylor, M. A., Mandl, G. T., & Supesteijn, C. H. K. (1986). Fault geometries in basement-induced wrench faulting under different initial stress states. *Journal of Structural Geology*, *8*(7), 737-752.

Neri, M., Acocella, V., & Behncke, B. (2004). The role of the Pernicana Fault System in the spreading of Mt. Etna (Italy) during the 2002–2003 eruption. *Bulletin of Volcanology*, *66*(5), 417-430.

Neri, M., Guglielmino, F., & Rust, D. (2007). Flank instability on Mount Etna: Radon, radar interferometry, and geodetic data from the southwestern boundary of the unstable sector. *Journal of Geophysical Research: Solid Earth*, *112*(B4).

Nogoshi, M., & Igarashi, T. (1970). On the propagation characteristics of microtremors. *J. Seism. Soc. Japan*, *23*, 264-280.

Ohmachi, T., & Umezono, T. (1998). Rate of Rayleigh waves in microtremors. *The Effects of Surface Geology on Seismic Motion*, *2*, 587-592.

Okada, H. (2003). *The microtremor survey method* (Vol. 12). Society of Exploration Geophysicists with the cooperation of Society of Exploration Geophysicists of Japan [and] Australian Society of Exploration Geophysicists.

Optim L.L.C., 2003. SeisOpt ReMi v2.0 forWindows 95/98/00/NT/Me/XP, Optim Software and Data Services, UNR-MS-174, 1664 N. Virginia St., Reno, Nevada. 89557.

Palano, M., Puglisi, G., & Gresta, S. (2008). Ground deformation patterns at Mt. Etna from 1993 to 2000 from joint use of InSAR and GPS techniques. *Journal of Volcanology and Geothermal Research*, *169*(3), 99-120.

Palano, M., Rossi, M., Cannavò, F., Bruno, V., Aloisi, M., Pellegrino, D., ... & Mattia, M. (2010). Etn@ ref: a geodetic reference frame for Mt. Etna GPS networks. *Annals of geophysics*

Palano, M. (2016). Episodic slow slip events and seaward flank motion at Mt. Etna volcano (Italy). *Journal of Volcanology and Geothermal Research*, *324*, 8-14.

Panou, A. A., Theodulidis, N., Hatzidimitriou, P., Stylianidis, K., & Papazachos, C. B. (2005). Ambient noise horizontal-to-vertical spectral ratio in site effects estimation and correlation with seismic damage distribution in urban environment: the case of the city of Thessaloniki (Northern Greece). *Soil Dynamics and Earthquake Engineering*, *25*(4), 261-274.

Pappalardo, G., Imposa, S., Mineo, S., & Grassi, S. (2016). Evaluation of the stability of a rock cliff by means of geophysical and geomechanical surveys in a cultural heritage site (south-eastern Sicily). *Italian Journal of Geosciences*, *135*(2), 308-323.

Park, C. B., Miller, R. D., & Xia, J. (1999). Multichannel analysis of surface waves. *Geophysics*, *64*(3), 800-808.

Parolai, S., Bormann, P., & Milkereit, C. (2002). New relationships between Vs, thickness of sediments, and resonance frequency calculated by the H/V ratio of seismic noise for the Cologne area (Germany). *Bulletin of the seismological society of America*, *92*(6), 2521-2527.

Patanè, D., Privitera, E., Gresta, S., Akinci, A., Arpalone, S., Barberi, G., ... & Di Grazia, G. (2003). Seismological constraints for the dyke emplacement of the July-August 2001 lateral eruption at Mt. Etna volcano, Italy. *Annals of geophysics*, *46*(4), 599-608.

Patanè, D., Barberi, G., Cocina, O., De Gori, P., & Chiarabba, C. (2006). Time-resolved seismic tomography detects magma intrusions at Mount Etna. *Science*, *313*(5788), 821-823.

Pavlides, S., & Caputo, R. (2004). Magnitude versus faults' surface parameters: quantitative relationships from the Aegean Region. *Tectonophysics*, *380*(3), 159-188.

Pepe, A., & Lanari, R. (2006). On the extension of the minimum cost flow algorithm for phase unwrapping of multitemporal differential SAR interferograms. *IEEE transactions on geoscience and remote sensing*, *44*(9), 2374-2383.

Pepe, A., Euillades, L. D., Manunta, M., & Lanari, R. (2011). New advances of the extended minimum cost flow phase unwrapping algorithm for SBAS-DInSAR analysis at full spatial resolution. *IEEE Transactions on Geoscience and Remote Sensing*, *49*(10), 4062-4079.

Peronace, E., Boncio, P., Galli, P., & Naso, G. (2013). Faglie attive e capaci negli studi di microzonazione sismica: definizioni e procedure di zonazione. *Bull. Seism. Soc. Am*, *95*(5), 1779-1786.

Pullammanappallil, S. K., & Louie, J. N. (1994). A generalized simulated-annealing optimization for inversion of first-arrival times. *Bulletin of the Seismological Society of America*, *84*(5), 1397-1409.

Raines, M. G., Gunn, D. A., Morgan, D. J. R., Williams, G., Williams, J. D. O., & Caunt, S. (2011). Refraction microtremor (ReMi) to determine the shear-wave velocity structure of the near surface and its application to aid detection of a backfilled mineshaft. *Quarterly Journal of Engineering Geology and Hydrogeology*, *44*(2), 211-220.

Rasà, R., Azzaro, R., & Leonardi, O. (1996). Aseismic creep on faults and flank instability at Mount Etna volcano, Sicily. *Geological Society, London, Special Publications*, *110*(1), 179-192.

Richart, F. E., Hall, J. R., & Woods, R. D. (1970). Vibrations of soils and foundations. *Prentice Hall Inc, New Jersey*

Riedel, W. (1929). Zur mechanik geologischer brucherscheinungen. *Zentralblatt für Mineralogie, Geologie und Paläontologie B*, *1929*, 354-368.

Ristuccia, G. M., Di Stefano, A., Gueli, A. M., Monaco, C., Stella, G., & Troja, S. O. (2013). OSL chronology of Quaternary terraced deposits outcropping between Mt. Etna volcano and the Catania Plain (Sicily, southern Italy). *Physics and Chemistry of the Earth, Parts A/B/C*, *63*, 36-46.

Romano, R &. Consiglio nazionale delle ricerche (Italia). Istituto internazionale di vulcanologia, (1982). *Mount Etna volcano: a review of the recent earth sciences studies*.

Rosen, P. A., Hensley, S., Joughin, I. R., Li, F. K., Madsen, S. N., Rodriguez, E., & Goldstein, R. M. (2000). Synthetic aperture radar interferometry. *Proceedings of the IEEE*, *88*(3), 333-382.

Rust, D., & Neri, M. (1996). The boundaries of large-scale collapse on the flanks of Mount Etna, Sicily. *Geological Society, London, Special Publications*, *110*(1), 193-208.

Saastamoinen, J. (1972). Atmospheric correction for the troposphere and stratosphere in radio ranging satellites. *The use of artificial satellites for geodesy*, 247-251.

Scarfì, L., Messina, A., & Cassisi, C. (2013). Sicily and Southern Calabria focal mechanism database: a valuable tool for local and regional stress field determination. *Annals of Geophysics*.

Schaffrin, B., & Bock, Y. (1988). A unified scheme for processing GPS dual-band phase observations. *Bulletin Geodesique*, *62*(2), 142-160.

Scudero, S., De Guidi, G., Imposa, S., & Currenti, G. (2015). Modelling the long-term deformation of the sedimentary substrate of Mt. Etna volcano (Italy). *Terra Nova*, *27*(5), 338-345.

SESAME European project (2003) Nature of noise wavefield. Final Report WP08. http://sesamefp5.obs.ujfgrenoble.fr/Delivrables/D13.08_finalreport.pdf

SESAME European project (2005) Guidelines for the implementation of the H/V spectral ratio technique on ambient vibrations. Measurements, processing and interpretation. WP12. Deliverable D23.12

Silvestri, O., 1886. LEtna nel 1885. *Ann. Met. It., anno I, 192–201.*

Similox-Tohon, D., Sintubin, M., Muchez, P., Verhaert, G., Vanneste, K., Fernandez, M., ... & Waelkens, M. (2006). The identification of an active fault by a multidisciplinary study at the archaeological site of Sagalassos (SW Turkey). *Tectonophysics*, *420*(3), 371-387.

Siniscalchi, A., Tripaldi, S., Neri, M., Giammanco, S., Piscitelli, S., Balasco, M., ... & Rizzo, E. (2010). Insights into fluid circulation across the Pernicana Fault (Mt. Etna, Italy) and implications for flank instability. *Journal of Volcanology and Geothermal Research*, *193*(1), 137-142.

Siniscalchi, A., Tripaldi, S., Neri, M., Balasco, M., Romano, G., Ruch, J., & Schiavone, D. (2012). Flank instability structure of Mt. Etna inferred by a magnetotelluric survey. *Journal of Geophysical Research: Solid Earth*, *117*(B3).

Solaro, G., Acocella, V., Pepe, S., Ruch, J., Neri, M., & Sansosti, E. (2010). Anatomy of an unstable volcano from InSAR: Multiple processes affecting flank instability at Mt. Etna, 1994–2008. *Journal of Geophysical Research: Solid Earth*, *115*(B10).

Spizzichino, D., Margottini, C., Castellaro, S., & Mulargia, F. (2013). Passive Seismic survey for Cultural Heritage landslide risk assessment. In *Landslide Science and Practice* (pp. 483-489). Springer Berlin Heidelberg.

Štěpančíková, P., Dohnal, J., Pánek, T., Łój, M., Smolková, V., & Šilhán, K. (2011). The application of electrical resistivity tomography and gravimetric survey as useful tools in an active tectonics study of the Sudetic Marginal Fault (Bohemian Massif, central Europe). *Journal of Applied Geophysics*, *74*(1), 69-80.

Sylvester, A. G., & Smith, R. R. (1976). Tectonic transpression and basement-controlled deformation in San Andreas fault zone, Salton Trough, California. *AAPG Bulletin*, *60*(12), 2081-2102.

Tapponnier, P. (1977). Evolution tectonique du système alpin en Méditerranée: poinçonnement et écrasement rigide-plastique. *Bull. Soc. Geol. Fr*, *19*(3), 437-460.

Tarabusi, G., & Caputo, R. (2016). The use of HVSR measurements for investigating buried tectonic structures: the Mirandola anticline, northern Italy, as a case study. *Int. J. Earth Sci.*, 1-13, doi: 10.1007/s00531-016-1322-3.

Tibaldi, A., & Groppelli, G. (2002). Volcano-tectonic activity along structures of the unstable NE flank of Mt. Etna (Italy) and their possible origin. *Journal of Volcanology and Geothermal Research*, *115*(3), 277-302.

Tokimatsu K (1997) Geotechnical site characterization using surface waves. In: *Proceedings of the 1st international conference on earthquake geotechnical engineering, vol 3, pp 1333–1368*

Tokimatsu, K., Tamura, S., & Kojima, H. (1992). Effects of multiple modes on Rayleigh wave dispersion characteristics. *Journal of Geotechnical Engineering*, *118*(10), 1529-1543.

Tortorici, L., Monaco, C., Tansi, C., & Cocina, O. (1995). Recent and active tectonics in the Calabrian arc (Southern Italy). *Tectonophysics*, *243*(1), 37-55.

Walter, T. R., Acocella, V., Neri, M., & Amelung, F. (2005). Feedback processes between magmatic events and flank movement at Mount Etna (Italy) during the 2002–2003 eruption. *Journal of Geophysical Research: Solid Earth*, *110*(B10).

Wells, D. L., & Coppersmith, K. J. (1994). New empirical relationships among magnitude, rupture length, rupture width, rupture area, and surface displacement. *Bulletin of the seismological Society of America*, *84*(4), 974-1002.

Wilcox, R. E., Harding, T. T., & Seely, D. R. (1973). Basic wrench tectonics. *Aapg Bulletin*, *57*(1), 74-96.

Yamamoto, H. (2000, January). Estimation of shallow S-wave velocity structures from phase velocities of Love-and Rayleigh-waves in microtremors. In *Proceedings of the 12th World Conference on Earthquake Engineering*.

Yamanaka, H., Takemura, M., Ishida, H., & Niwa, M. (1994). Characteristics of long-period microtremors and their applicability in exploration of deep sedimentary layers. *Bulletin of the Seismological Society of America*, *84*(6), 1831-1841.

Yuan, D., & Nazarian, S. (1993). Automated surface wave method: inversion technique. *Journal of Geotechnical Engineering*, *119*(7), 1112-1126.

Zhao, B., Horike, M., & Takeuchi, Y. (2000, January). Analytical study on reliability of seismic site-specific characteristics estimated from microtremor measurements. In *Proc. 12th World Conf. on Earthquake Engineering* (pp. 1522-1530).

Appendix A. Joint fit MASW-HVSR

Is shown the result of joint fit between a MASW survey, performed in the western portion of the urban area of San Gregorio di Catania village, and a H/V spectrum relating to one of the noise recordings acquired near the alignment. The joint fit procedure MASW-HVSR allowed to obtain the shear waves velocity profile.

TROMINO® *Grilla*
www.tromino.it

MASW San Gregorio_2014_Jun_23 – noise recording N11

START RECORDING: 2014/06/23 10:50:58 END RECORDING: 2014/06/23 11:10:59

TRACE LENGTH: 0h20'00". Analyzed 77% trace (manual selection)

SAMPLING RATE: 128 Hz

WINDOW SIZE: 20 s

SMOOTHING TYPE: Triangular window

SMOOTHING: 10%

CHANNEL LABELS: NORTH SOUTH; EAST WEST ; UP DOWN

ARRAY GEOMETRY (x): 0.0 4.0 8.0 12.0 16.0 20.0 24.0 28.0 32.0 36.0 40.0 44.0 48.0 52.0 56.0 60.0 64.0 m.

MODELLED RAYLEIGH WAVE PHASE VELOCITY DISPERSION CURVE

EXPERIMENTAL DISPERSION SPECTRUM OF RAYLEIGH WAVES
vs.
THEORETICAL DISPERSION SPECTRUM OF RAYLEIGH WAVES

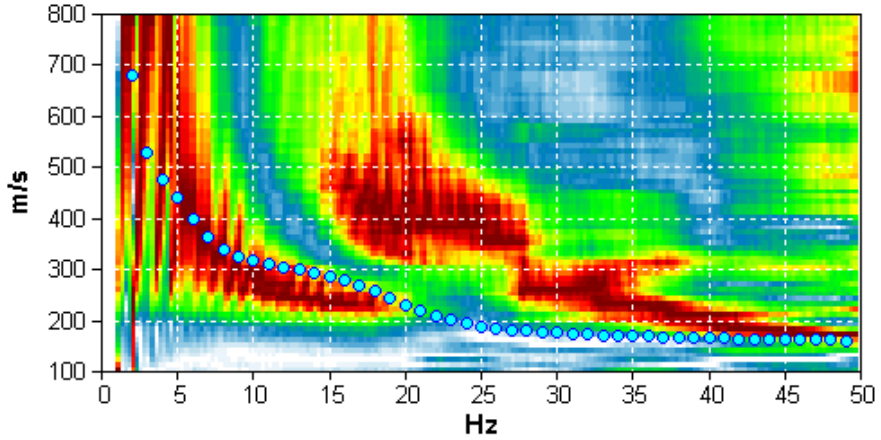

HORIZONTAL TO VERTICAL SPECTRAL RATIO

THEORETICAL H/V SPECTRUM vs. EXPERIMENTAL H/V SPECTRUM

Max H/V at 11.88+/- 0.69 Hz (in the range 0.0 – 0.64 Hz)

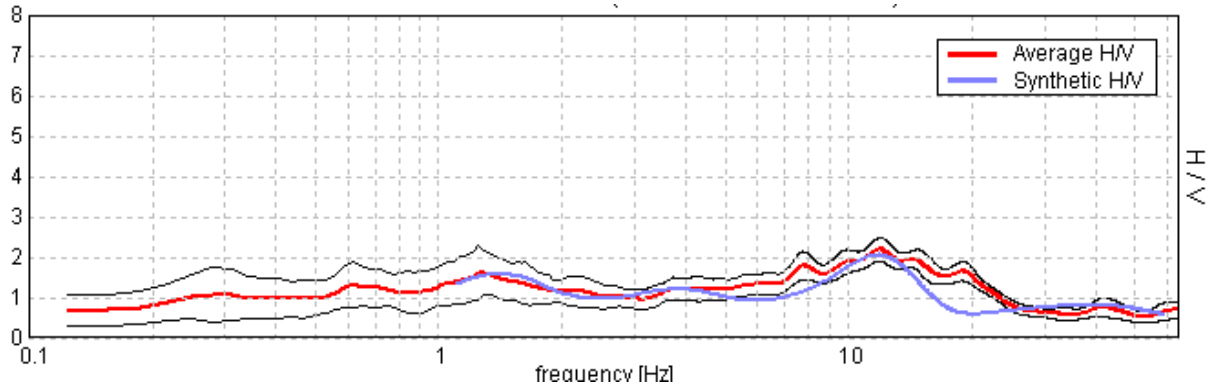

SUBSOIL MODEL

Depth at the bottom of the layer [m]	Thickness [m]	Vs [m/s]	Poisson ratio
0.70	0.70	125	0.35
4.10	3.40	190	0.35
25.10	21.00	370	0.35
100.10	75.00	575	0.30
inf.	inf.	950	0.30

Vs – depth PROFILE

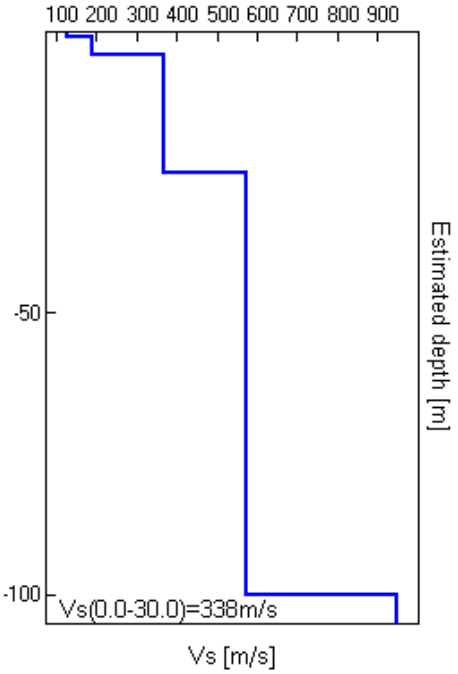

Appendix B. Fit of Vs-depth profiles

Is shown the result of fit process of Vs-depth profiles for San Gregorio area, performed through the gnuplot free software.

```
        G N U P L O T
        Version 4.6 patchlevel 6    last modified September 2014
        Build System: MS-Windows 32 bit

        Copyright (C) 1986-1993, 1998, 2004, 2007-2014
        Thomas Williams, Colin Kelley and many others

        gnuplot home:     http://www.gnuplot.info
        faq, bugs, etc:   type "help FAQ"
        immediate help:   type "help"  (plot window: hit 'h')

Terminal type set to 'wxt'
gnuplot> cd 'C:\Users\tromino\Desktop'
gnuplot> f(x)=a*(1+x)**b
gnuplot> a=100
gnuplot> b=1
gnuplot> fit f(x) "San Gregorio_velocity profiles.dat" using 1:2 via a,b


 Iteration 0
 WSSR        : 7.97623e+007      delta(WSSR)/WSSR   : 0
 delta(WSSR) : 0                 limit for stopping : 1e-005
 lambda   : 3199.04

initial set of free parameter values

a               = 100
b               = 1
/

 Iteration 1
 WSSR        : 7.94551e+006      delta(WSSR)/WSSR   : -9.03867
 delta(WSSR) : -7.18168e+007     limit for stopping : 1e-005
 lambda   : 319.904

resultant parameter values

a               = 99.9989
b               = 0.755885
/

 Iteration 2
 WSSR        : 816922            delta(WSSR)/WSSR   : -8.72615
 delta(WSSR) : -7.12859e+006     limit for stopping : 1e-005
 lambda   : 31.9904

resultant parameter values

a               = 100.022
b               = 0.593571
/

 Iteration 3
 WSSR        : 485543            delta(WSSR)/WSSR   : -0.682492
 delta(WSSR) : -331379           limit for stopping : 1e-005
 lambda   : 3.19904

resultant parameter values

a               = 102.314
b               = 0.530109
```

```
 Iteration 4
 WSSR        : 413611            delta(WSSR)/WSSR   : -0.173913
 delta(WSSR) : -71932.1          limit for stopping : 1e-005
 lambda   : 0.319904

resultant parameter values

a               = 141.813
b               = 0.394893
/

 Iteration 5
 WSSR        : 380484            delta(WSSR)/WSSR   : -0.0870655
 delta(WSSR) : -33127            limit for stopping : 1e-005
 lambda   : 0.0319904

resultant parameter values

a               = 155.513
b               = 0.382097
/

 Iteration 6
 WSSR        : 380422            delta(WSSR)/WSSR   : -0.000160998
 delta(WSSR) : -61.2474          limit for stopping : 1e-005
 lambda   : 0.00319904

resultant parameter values

a               = 155.51
b               = 0.383035
/

 Iteration 7
 WSSR        : 380422            delta(WSSR)/WSSR   : -2.52451e-009
 delta(WSSR) : -0.000960381      limit for stopping : 1e-005
 lambda   : 0.000319904

resultant parameter values

a               = 155.517
b               = 0.383018

After 7 iterations the fit converged.
final sum of squares of residuals : 380422
rel. change during last iteration : -2.52451e-009

degrees of freedom    (FIT_NDF)                        : 62
rms of residuals      (FIT_STDFIT) = sqrt(WSSR/ndf)    : 78.3316
variance of residuals (reduced chisquare) = WSSR/ndf   : 6135.85

Final set of parameters            Asymptotic Standard Error
=======================            ==========================

a               = 155.517          +/- 14.24        (9.157%)
b               = 0.383018         +/- 0.03317      (8.661%)
```

Appendix C. Celerimetric calculation

CALCOLO CELERIMETRICO

FILE : san_gregorio_def

LAVORO : san_gregorio_def

	Nome	Codice Identificativo	Quota	Coordinata Nord(X)	Coordinata Est(Y)	Corr.Ar./Azimut	Distanza Ridotta
Stazione	**100**		**0.00000**	**0.00000**	**0.00000**	**0.0000**	
Punto	101		-1.39763	36.69585	-0.00646	399.9888	36.696
Punto	102		0.52021	11.33974	-4.10765	377.8754	12.061
Punto	103		0.74053	16.75948	12.13542	39.8978	20.692
Punto	104		-4.89267	-431.94967	-49.27890	207.2316	434.752

	Nome	Codice Identificativo	Quota	Coordinata Nord(X)	Coordinata Est(Y)	Corr.Ar./Azimut	Distanza Ridotta
Stazione	**200**		**0.39718**	**-17.25032**	**39.79932**	**0.0000**	

	Nome	Codice Identificativo	Quota	Coordinata Nord(X)	Coordinata Est(Y)	Corr.Ar./Azimut	Distanza Ridotta
Stazione	**300**		**0.80135**	**-108.67742**	**63.52748**	**0.0000**	

	Nome	Codice Identificativo	Quota	Coordinata Nord(X)	Coordinata Est(Y)	Corr.Ar./Azimut	Distanza Ridotta
Stazione	**400**		**0.40589**	**-137.99914**	**114.09298**	**0.0000**	
Punto	401		6.28163	-149.08405	81.29352	279.2520	34.622
Punto	403		3.14499	-93.37484	52.51439	339.9220	76.048
Punto	404		2.61972	-114.03241	80.68034	339.6130	41.119
Punto	405		2.24746	-116.07788	109.24655	386.1482	22.451

	Nome	Codice Identificativo	Quota	Coordinata Nord(X)	Coordinata Est(Y)	Corr.Ar./Azimut	Distanza Ridotta
Stazione	**500**		**0.37262**	**-177.58629**	**224.88745**	**0.0000**	

	Nome	Codice Identificativo	Quota	Coordinata Nord(X)	Coordinata Est(Y)	Corr.Ar./Azimut	Distanza Ridotta
Stazione	**600**		**1.27300**	**-210.40988**	**302.49735**	**0.0000**	

	Nome	Codice Identificativo	Quota	Coordinata Nord(X)	Coordinata Est(Y)	Corr.Ar./Azimut	Distanza Ridotta
Stazione	**700**		**3.12832**	**-277.65790**	**480.14331**	**0.0000**	
Punto	701		5.03600	-220.78123	509.35698	30.2072	63.941
Punto	702		5.05143	-279.55070	523.17880	102.7982	43.077
Punto	703		3.46285	-323.89238	596.72992	124.0352	125.420
Punto	704		3.29024	-328.49378	576.26070	130.9712	108.733
Punto	705		3.80981	-315.60393	548.41913	132.2936	78.112
Punto	706		4.40582	-292.42070	496.47213	146.7962	22.013
Punto	707		3.77778	-308.54287	493.47055	174.0658	33.638
Punto	708		5.14793	-271.03512	446.77713	312.4740	34.017
Punto	709		4.37855	-253.60845	407.17029	320.2672	76.834
Punto	800		1.86948	-445.30423	513.53678	187.4830	170.940